Properties of Highly Nonlinear waves in Compressible Flows

Damien L Bright

A thesis submitted for the degree of
Doctor of Philosophy at
The Australian National University

May 2000

Except where otherwise indicated, this thesis is my own original work.

Damien L Bright
4 May 2000

Acknowledgements

There are many people who have helped me throughout the writing of this thesis. Firstly, I would like to thank those who have been members of my thesis committee, including:

Prof. Brian Kennett, who provided very useful and rapid feedback; always found time to fit me into his schedule and helped with part-time work when my funding expired.

Prof. Ross Griffiths, for his helpful comments and feedback (especially throughout a hectic period for the GFD group).

Dr. Doug Christie, for his initial help before leaving for an overseas appointment in Vienna.

Dr. David Brown, who deserves special thanks for going out of his way to provide much needed help via email from overseas.

Prof. Stewart Turner, for several enlightening conversations about aspects of fluid dynamics which were troubling me.

I would also like to thank the other staff and students at RSES who have provided advice and a friendly environment to work in. This especially includes Jean Braun and Malcolm Sambridge who both helped with questions about numerical modeling.

I would like to acknowledge the support of the ANU supercomputer facility (ANUSF) for providing a world class facility which made this numerical study and its high computational requirements feasible. In particular I would like to thank Judy Jenkinson for her friendly assistance with the technical problems I had.

I have made many friends during the years in Canberra and would like to thank them for their support and for periodically dragging me away from the thesis to remind me that life is not all about numbers and machines. My experiences of being part of a student household were wonderful thanks to my friends Ken and Lynn, who were the best of housemates. Special thanks go to Vern and Anna who provided me with a place to stay over the last few months and to Brian for always being around for a relaxing after work drink on a friday. Of my workmates, I would particularly like to thank Armando for his encouragement over the years and the many relaxing conversations we had over a cup of coffee.

Finally, there are the people who provided me with the closest support of all. To my sister Joanne, thanks for always being there as someone to talk things over with and for your ongoing encouragement. To my girlfriend Lizzii, for providing the inspiration to finish and for putting up with me over a drawn out write-up period during which we had very little time to relax. And to my parents, for their continued support during the difficult moments, their enthusiasm, and their encouragement to finish up. This helped immensely.

Abstract

Solitary waves are increasingly observed phenomena in geophysical environments. Studies of the lower atmosphere often include observations which can be matched by a description in terms of highly nonlinear solitary waves propagating on a low lying waveguide layer with a region of recirculating fluid within the wave. This thesis concentrates on the study of conditions which result in wave formation and decay within the context of highly nonlinear wave theory. Such a study is in part motivated by the discrepancies noted by other researchers between observations and predictions based on weakly nonlinear dispersive wave theory.

The primary tool is a mesoscale numerical model based on a finite difference set of compressible nonlinear governing equations which uses a direct simulation method to represent features of interest. This means that no subgrid parameterizations are made, but instead the model relies on high grid resolution coupled with a second order dissipative operator to remove energy at the smallest scales. A simple test case involving a falling ring vortex shows the ability of this model to represent an appropriate level of fluid dynamics. A free-slip boundary condition represents the ground, and a set of non-trivial wave radiative boundary conditions are applied at the lateral and upper boundaries. The upper boundary requires special care and an approximate radiative condition is chosen (based on the work of Bougealt, 1982; Klemp and Durran, 1982) which is found to be successful in suppressing reflection of wave energy in the numerical model.

A simple model of wave generation from a low level microburst is the impact of a downdraft, of short duration and limited scale, on a suitable waveguide layer. Depending on the conditions this can result in the formation of solitary waves. The impact of a downdraft is found to result in two different mechanisms of wave formation based on whether or not a diverging outflow is produced at the ground. Under suitable conditions a diverging outflow leads to the formation of large amplitude waves which encapsulate some of the outflow fluid. The inclusion of a windshear layer above the waveguide is found to substantially alter the dynamics of the impact and the wave formation process.

For a study of wave decay there is a need for an isolated solitary wave which can be contained within the confines of the numerical domain. This can be achieved via a mapping technique to produce starting wave solutions. Steady solitary wave solutions to the Dubreil-Jacotin-Long (DJL) equation for a time independent incompressible and inviscid stably stratified medium are mapped to the dynamically evolving media of the compressible viscous numerical model. This requires several additional initializations of physical quantities and the

dynamic re-adjustment of the ambient media in order to maintain wave stability. The wave morphology of mapped solutions indicates that highly nonlinear waves with closed circulation have a strong dependence on viscous effects.

A study is then made of the radiative decay of highly nonlinear waves, initially possessing a closed circulation cell, due to the excitation of vertically propagating internal gravity waves in a weakly stratified medium above the waveguide layer. Realistic ambient temperature profiles are included based on measurements by other researchers of conditions present during wave events in the lower atmosphere. The disappearance of closed circulation from within the wave is found not to cause any noticeable deviation from a mostly linear decay of wave amplitude. It is also shown that wave properties exhibit a sensitivity to changes in the ambient environment.

Contents

Introduction

Wave phenomena commonly occur in geophysical environments. The nature of the waves that a given medium will support is dependent on the scales of motion as well as the types of waveguide structure that can exist in such a medium. Waveguide structures in nature take many different forms, from the thermocline region near the surface of stratified lakes and the ocean, to the pycnocline structure of the atmospheric boundary layer. The objective of much research into waves and wave-like phenomenon is to find analytic theories that can describe wave motions in such geophysical environments. Unfortunately most analytic theories to date are only valid under a number of assumptions and therefore have limited applicability to the description of highly non-linear waves in nature. Computational methods offer a chance to model these highly non-linear waves and investigate their properties.

In the work that follows we will be concerned with a fundamentally non-linear class of motions associated with disturbances in stratified environments. This is the internal solitary wave which corresponds to a mathematical solution of the governing equations in remarkably coherent form. Solitary waves exhibit an exact balance between the steepening effects of non-linearity on the wave profile and the broadening effects of wave dispersion. This balance may, at first glance, seem unlikely to occur very often, but solitary wave motions are a commonly occurring feature in geophysical environments. The present study will concentrate on large amplitude waves. Large amplitude internal solitary waves have been observed in the thermocline of the ocean, stratified lakes and in the lower atmosphere. In the ocean, strong sub-surface currents have been associated with large amplitude solitary wave disturbances in the thermocline with sufficient magnitude to disturb oil drilling platforms (eg. Apel et al., 1985; Lui et al., 1985). Large amplitude solitary waves have also been observed in the atmospheric boundary layer. Christie et al. (1978,1979) describe large amplitude disturbances on a nocturnal inversion layer and thunderstorm-generated solitary waves have been observed propagating in a low-lying stable layer (Shreffer and Binkowsi, 1981; Haase and Smith, 1984; Lin and Goff, 1988; Doviak et al., 1991). The later solitary wave disturbances often have severe wind shear associated with them which may pose a serious hazard to aircraft, especially in the vicinity of airports (Christie et al., 1991). Atmospheric waves have also been observed to transport fluid in a recirculating region within the wave.

Solitary waves of modest amplitude can be described mathematically in terms of a model equation that is an asymptotic form of the full set of governing fluid dynamical equations. Al-

though non-linear, equations of this type are exactly integrable (Gardner et al., 1967). Well known examples are the Korteweg-de Vries (KdV) equation (Korteweg and de Vries, 1895) and Benjamin-Davis-Ono (BDO) equation (Benjamin, 1967; Davis and Acrivos, 1967; Ono, 1975). Both of these equations describe the evolution of an initial disturbance into a family of amplitude ordered solitons and an accompanying dispersive wave train. A fundamental consequence of the flow regime is the dispersion relation that governs the dependence of frequency on wavenumber. Internal solitary waves which are described by the KdV equation propagate in shallow fluids with a pycnocline region of depth h that is the same order of magnitude as the total fluid depth H. In contrast, the BDO equation describes internal solitary waves that propagate in a pycnocline region embedded in an unbounded fluid domain. The later equation is useful for describing solitary waves in the atmospheric boundary layer (Christie, 1989). Asymptotic equations of this type are, however, only first order in amplitude and therefore only strictly describe weakly non-linear solitary waves of small but finite amplitude. Observations in both the oceans and atmosphere show that internal solitary waves often have large amplitudes. General second order correction terms (for wave amplitude) have been calculated by Gear and Grimshaw (1983) for shallow fluids and by Grimshaw (1981c) for deep fluids, but these theories only extend the useful range to slightly higher amplitudes. The analytic treatment of this problem rapidly becomes intractable beyond this point.

Because of the complications in extending the analytic results to higher wave amplitudes, the study of highly non-linear waves is usually carried out by numerical integration of the fully non-linear equations. Numerical solutions for solitary waves in continuously stratified fluids have been calculated by Tung et al. (1991), Turkington et. al (1991) and Brown and Christie (1998). These results indicate that, as a/h (where a is the wave amplitude and h the depth of the pycnocline) becomes greater than a non-dimensional value of about 1, closed circulation develops and the wavelength-amplitude relationship is no longer described by weakly non-linear theory.

This project is concerned with the numerical simulation of large amplitude trapped wave motions in atmospheric waveguides. Observations of such waves in the atmosphere indicate that the formation, evolution and decay of these waves are strongly influenced by the structure of the waveguide and the degree to which the overlying tropospheric layer can support energy loss. A very high resolution numerical model has been developed which includes boundary conditions which prevent reflections of both sound and gravity waves at all lateral boundaries and also at the upper boundary of the computational domain. This model has been used to study the evolution of solitary waves on a waveguide in a two layer system representing the lower atmosphere where the upper layer supports varying degrees of energy loss through internal gravity wave radiation.

Several mechanisms of solitary wave generation have been explored numerically. Simulations of solitary wave generation, by the interaction of a modelled descending thunderstorm

microburst with a stable layer, have been carried out and provide insight into the formation process. Such microburst generated wave motions are important atmospheric processes which can lead to hazardous windshear disturbances in the thunderstorm environment. Another mechanism for generating solitary waves numerically is to use as a starting solution a numerical solution of Long's equation (a nonlinear partial differential equation that describes the propagation of stationary two-dimensional finite amplitude wave motions in an incompressible, inviscid and stably stratified fluid - also known as the DJL equation. (Dubreil-Jacotin, 1937; Long, 1953)). Such an approximate starting solution is expected to "relax" rapidly towards a true solution of the compressible model. These starting solutions, which provide a range of different amplitudes and wavelengths, have been used to study the radiative energy loss from solitary waves traveling in the modelled stable layer waveguide. A study of the mechanisms of decay of solitary wave motions provides valuable insight into how long-lived such a disturbance in the atmosphere may be.

A number of computational techniques have been utilized in the course of this project. The properties of evolving large amplitude wave phenomena are detailed from a series of numerical simulations which are based on the integration of the fully nonlinear nonhydrostatic primitive ensemble-averaged equations for compressible fluid flow. The radiative upper boundary condition implements a spectral filtering technique to eliminate Fourier modes that correspond to downward propagating internal gravity waves. Also the generation of starting wave solutions requires the numerical solution of a nonlinear PDE. Calculations of this type require large amounts of memory and are very computationally intensive.

Outline of thesis

The structure of the thesis is as follows:

Chapter One will examine the meteorological context of trapped internal solitary wave motions in the lower atmosphere. Several observations of solitary wave events will be presented to give the reader an idea of the type of forcing mechanisms, such as thunderstorms, which can lead to nonlinear wave formation, as well as the ambient conditions necessary to sustain such motions for extended periods.

Chapter Two presents the mathematical background of nonlinear wave theory in the weakly nonlinear long wave limit where wave amplitude is assumed small but finite and the wavelength is assumed to be long compared to the fundamental scale length of the ambient fluid. Two well known evolution equations are discussed: the KdV equation, which describes wave motions in a shallow fluid regime; and the BDO equation, which describes wave motions in a deep fluid regime. The wave dispersion relation, which relates frequency to wavenumber, is different for each fluid regime, with dispersive effects being stronger in deep fluids. The weakly nonlinear

treatment of radiative damping of waves for a stratified medium which supports loss of energy due to internal wave motions is also presented. Finally the limitations of analytic work are discussed as well as how useful the weakly nonlinear theory is for comparisons with real waves.

Chapter Three is concerned with a description of the fully nonlinear compressible model which has been developed for high resolution modeling of mesoscale processes in the lower atmosphere. A numerical formulation of the prognostic equations for the relevant momentum and thermodynamical variables is given and the energy conserving properties of these equations are examined. Also discussed are the relative merits of using the chosen scheme, which relies on high mesh resolution and second order dissipation to resolve features of interest, versus the use of complicated parameterizations of subgrid processes.

Chapter Four examines the appropriate boundary conditions for the present study. The bottom boundary condition is chosen as an implementation of the free-slip condition often used in atmospheric models. A formulation is given of radiative lateral boundary conditions which allow energy from gravity and sound waves to pass freely out of the numerical domain. A separate formulation is given of an upper boundary radiative condition (which must be treated separately from the lateral boundaries due to the differences in propagation of wave energy between vertical and horizontal directions). This upper boundary condition is tested when the domain represents stratified fluid with constant buoyancy frequency by using an oscillating dipole at the ground to generate an internal wave field. The radiation of wave energy from the dipole source is then confined to a number of rays which pass through the upper boundary and therefore test its suppression of reflection of wave energy. This chapter also includes a formulation of a symmetry condition which is used for some simulations which contain strong symmetry about a lateral boundary and where there is a need to represent substantial horizontal distances using a reasonable computational budget.

Chapter Five explores a scenario for the generation of highly nonlinear waves in the lower atmosphere as the result of a low level microburst of limited spatial extent impacting a ground based stable layer. The term "microburst" (Fujita, 1976) is used here to refer to a form of low altitude wind shear which results from a short-lived thunderstorm downdraft of small diameter (less than 4km) interacting with the ground and producing a strong outflow. In the experiments examined in this chapter there is a stable layer at the ground, modelled as a layer of stable temperature variation in an otherwise homogeneous ambient environment, which can act as a waveguide layer for waves generated as a consequence of the forcing provided by the microburst impact. The simple model chosen to represent a microburst is based on the initialization of an instantaneous "cold pool" of air at a certain height above the stable layer which is then allowed to evolve into a falling axisymmetric thermal (which acts as a simple representation of a downdraft). The effect of varying the volume and peak temperature perturbation associated with the initial cold pool is examined within a parameter range which can result in wave generation. A close examination is made of the processes during impact which

result in wave generation. Realistic atmospheric conditions generally include environmental windshear, therefore some experiments which include windshear above the waveguide layer are also studied. The highly nonlinear solitary waves that are generated in the experiments of this chapter seem to bear close similarity to observations by Doviak et al. (1991) of solitary wave generation due to rapidly moving thunderstorms.

The highly nonlinear waves generated in Chapter Five have limitations (such as the range of amplitude) for use as initial starting solutions in a study of wave decay. Therefore, Chapter Six is concerned with the calculation of more appropriate "ideal" starting solutions which each represent a highly nonlinear isolated solitary wave. A technique is presented which has been developed for the mapping of steady highly nonlinear solitary wave solutions from an incompressible inviscid boundary value PDE problem (the DJL equation) to the fully nonlinear compressible mesocale model of Chapter Three (with the radiative boundary conditions discussed in Chapter Four). Some solutions are calculated to the DJL equation for two cases. The first of these cases involves an appropriate density profile representing a waveguide with homogeneous conditions above. The second involves a two layer case with weaker stratification in the upper layer. Steady state solutions from the first case only are used as mapping solutions. This is because the two layer solutions match the description of trapped modes which are produced by reflection of wave energy from the upper boundary (which is a rigid type condition for the solution of the boundary value PDE problem). Mapped solutions are then tested to ensure they are stable in the compressible numerical model.

In Chapter Seven a study is made of the radiative decay of ducted solitary wave disturbances in an atmospheric waveguide layer when the medium above the waveguide is stably stratified. This ambient configuration is typical of observed atmospheric conditions during solitary wave events. It was decided to model the ambient environment as a two layer system with the lower layer representing the waveguide and the upper layer the region of stable stratification. The upper layer supports internal wave motions which transfer energy away from the ducted solitary wave in the lower layer. This results in the radiative damping of the solitary wave. A study is made of this process using highly nonlinear solitary wave solutions, that were produced as a result of a solution mapping in Chapter Six, as "starting" waves in the compressible numerical model (configured with appropriate radiative boundary conditions). The radiative decay of highly nonlinear solitary waves is then studied for a range of ambient conditions characterised by the value N_2/N_1 representing the ratio of a constant Buoyancy frequency (with value N_1) in the lower layer to a constant Buoyancy frequency with (value N_2) in the upper layer. The change of wave morphology during decay is examined as well as the relative effects of viscous and radiative damping forces. A brief consideration is made of more complicated conditions which can allow solitary waves to propagate for extended periods in the waveguide even when the upper medium supports rapid loss of energy.

Chapter 1

Wave disturbances in the Lower Atmosphere

1.1 Introduction

A detailed study of the physical processes governing general atmospheric phenomenon, would require the consideration of a extremely complex set of processes including gravity, moisture, precipitation, thermodynamics, convection etc, but for the purpose of this study many of these are not of primary significance. The aim here is to study a class of long gravity waves that propagate in the lower atmosphere. Discussion of different types of atmospheric processes will be limited to those that are most important for this class of motions. The lower atmosphere is usually considered to encompass the vertical distance from the ground to the tropopause (approximately 10km vertically) including the troposphere and the atmospheric boundary layer which is generally considered to be the first few hundred meters or so of the atmosphere. Under suitable conditions the lower atmosphere can support a wide range of motions. Those conditions that most readily support gravity waves will be examined here.

In discussing the gravitational stability of a fluid medium a useful abstraction is to consider some form of smoothly varying density or temperature profile that varies vertically but not horizontally so that it is essentially layered. The fluid is then described as being stratified and will either be gravitationally stable or unstable relative to some disturbance. Stable thermal stratification is often encountered in the lower atmosphere and although generally short-lived, under suitable conditions it can persist for long periods (in terms of a time-scale of hours). Favorable topographical and atmospheric conditions such as flat terrain and calm weather lead to the formation of stable layers with a depth of the order of a few hundred meters to a few kilometers. Disruptive atmospheric forces such as strong wind conditions will tend to break up such a layer. Since solar radiation provides the energy source for heating of the ground and production of convective overturning of the air in the lower atmosphere, thermal stratification is most likely to exist at night. Stable thermal stratification where the temperature profile varies most in a finite vertical region at a certain height above the ground is commonly termed by

atmospheric researchers an "inversion layer". A typical inversion layer could exist on top of a stably stratified region which occupies the first few hundred meters near the ground. Nocturnal inversion layers are a common feature of the lower atmosphere, due to favorable nighttime conditions, where the effects of convective turbulent processes are less prevalent. Often a physical process other than solar radiation results in the formation of a stable atmospheric layer. These can take many forms, but an event frequently associated with weather systems is the transformation of an outflow of cold air from thunderstorm activity into a stable layer near the ground. For the work presented here the most important attribute of a stable layer is its ability to act as a waveguide.

Irrespective of the exact form of some source disturbance, the existence of a suitable waveguide layer is necessary for long gravity wave motions to exist (Benjamin 1967; Davis and Acrivos 1967). Waves of this type have been observed traveling on a stably stratified waveguide layer in the lower atmosphere. Such waves can cause large vertical motions and have been observed to propagate over long distances. If they encounter a region that is sufficiently conditionally unstable they can trigger instabilities that lead to convective cloud formation and thunderstorms. In order for these waves to remain coherent over long distances, there must be suitable ambient conditions present above the embedded waveguide layer. If the medium above the waveguide region can be considered homogeneous then energy losses from waves are restricted to frictional forces. However the assumption of homogeneity is rarely appropriate to the atmosphere where it is much more likely that weak stratification will exist above the waveguide. In a stratified medium without some means to trap upward leakage of wave energy, gravity waves rapidly become incoherent and radiate their energy. It is in this situation that the wind shear profile becomes important. Crook (1988) has proposed three mechanisms by which trapping of wave energy within a waveguide layer may occur. These include a low level jet with a suitable velocity profile opposing the wave motion, mid to upper tropospheric winds opposing wave motion, and a mid-tropospheric inversion layer at a suitable height. In examining radiative energy loss from waves, it is important to consider effects such as these in the ambient environment.

1.2 Solitary Waves

A subclass of atmospheric gravity wave that is the focus of the following work is the solitary wave. Solitary waves propagating on an atmospheric waveguide can travel hundreds of miles from their point of origin whilst maintaining a coherent form. This is because of their dynamical balance between the competing effects of frequency dispersion and nonlinear steeping.

The history of solitary waves goes back many years to their discovery by Russell in 1844 and spans many years where they were mostly studied in tank experiments and as a mathematical entity. It is more recently that they have been found to exist in many geophysical systems

and particularly internal solitary waves are common in the thermocline of the ocean, stratified lakes and in the lower atmosphere (Apel (1995), Christie (1989)). It is the internal solitary wave that is of most significance to mesoscale motions in the lower atmosphere and will be examined here. Observations of these type of waves tend to be divided into two classes based on scale height: waves that occupy the entire troposphere, and those that have scale heights bounded by the order of a few kilometers. It is this later group that are of interest here, and which propagate on atmospheric boundary layer waveguides. Waves have been observed in some cases to travel distances of more than 500km. In terms of their dimensions, typical examples have amplitudes spanning the range of 100m to 1km, a width of the order of several hundred meters to 10km and a length that can exceed hundreds of kilometers depending on atmospheric conditions. Typical speeds are in the range of 10-70km/hour.

1.2.1 Large Amplitude Internal Solitary waves

Observations in the atmosphere (eg. Doviak et al 1991) and numerical studies (Tung et al, 1982, Turkington et al, 1991, Brown, 1995) have identified important differences in the wavelength amplitude relationship between large amplitude internal solitary waves and those of modest amplitude which can be described using a weakly nonlinear mathematical theory. It has been shown that in contrast to the predictions of weakly nonlinear theory, the wavelength of highly nonlinear waves decreases to a minimum as the amplitude increases and then increases with further increases in wave amplitude (see Fig 1.1). Weakly nonlinear theory starts to fail as this minimum wavelength is approached and at some point there is the formation of a closed circulation cell that travels with the wave and transports fluid as a first order mass transport effect. This can be thought of as a form of internal 'wave breaking' as the closed circulation cell remains intact and is encapsulated by the wave as it undergoes further increases in amplitude (with a corresponding increase now in wavelength). Brown (1995) shows that the onset of closed circulation occurs just before the minimum wavelength is reached. Highly nonlinear waves of this type occur frequently in the atmosphere. They can produce strong transient winds in the form of a horizontally propagating vortex that travels near the ground. The following work will concentrate on highly nonlinear solitary waves.

1.2.2 Formation of atmospheric solitary waves

It may seem that the exact balance between the steepening effects of nonlinearity and the broadening effects of wave dispersion that give rise to a solitary wave, comprise a relationship that is unlikely to occur very often, but laboratory experiments (Maxworthy (1980), Hammack and Segur (1974)) support the idea that such waves exist under quite general forcing mechanisms. A prerequisite is for the appropriate waveguide conditions in stably stratified flow to exist, but apart from this requirement these studies showed that long lived solitary wave motions could

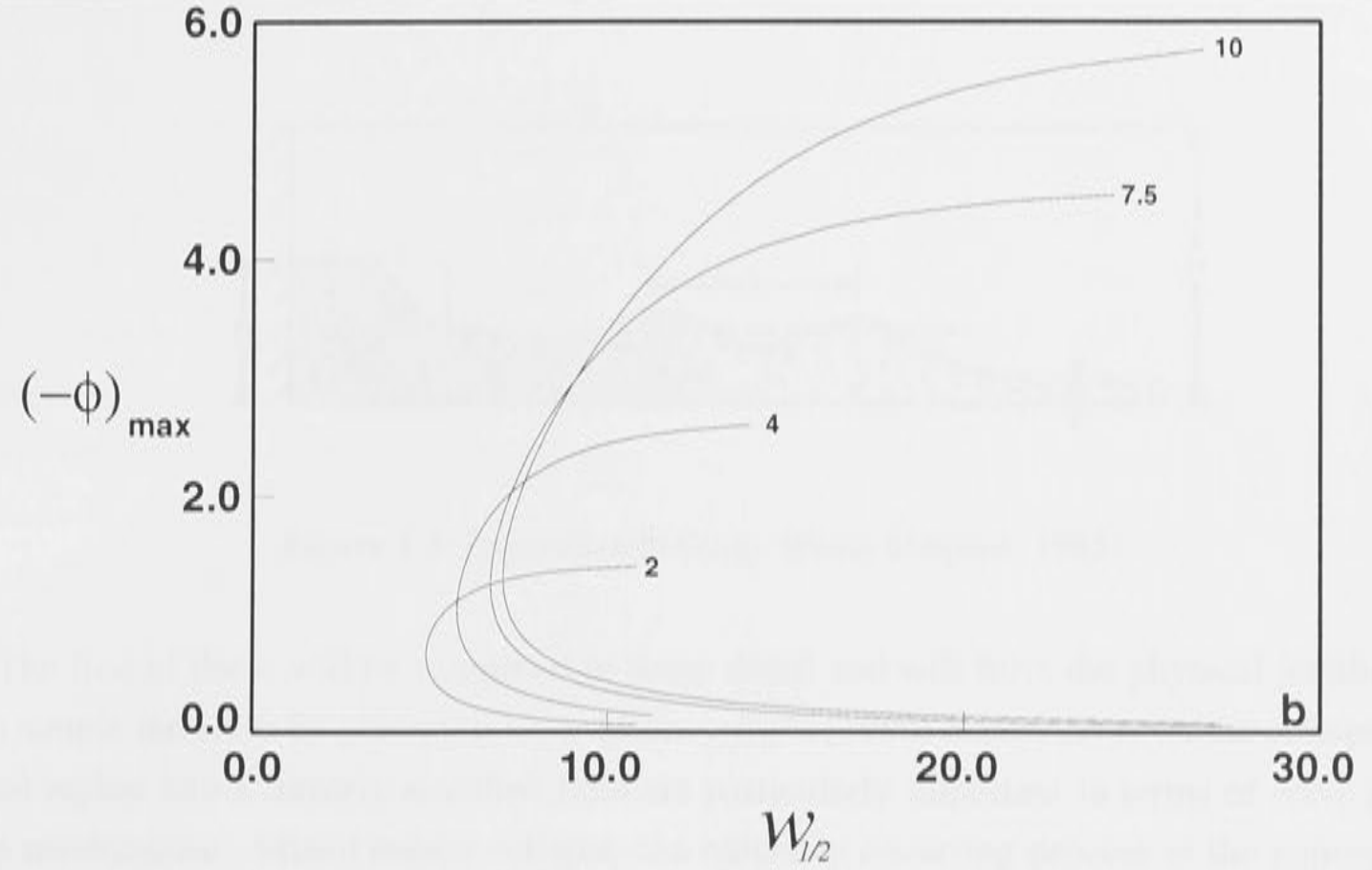

Figure 1.1: Wave amplitude, measured as the maximum value of the negative perturbation streamfunction $(\phi)_{max}$ versus the full width at half maximum amplitude, $W_{1/2}$, (from Brown, 1995) showing how the weakly non-linear prediction of wavelength decreasing with amplitude is valid until the vicinity of a minimum wavelength at which point the wavelength begins to increase with amplitude and we are in the fully non-linear regime. (The numbers indicate different values of total fluid depth).

result from a broad range of initial disturbances. The significance of these results for the atmosphere is supported by observations of large amplitude solitary waves formed in the lower atmosphere. Christie et al. (1978,1979) describe large amplitude disturbances on a nocturnal inversion layer and thunderstorm-generated solitary waves have been observed propagating in a low-lying stable layer (Shreffer and Binkowsi, 1981; Haase and Smith, 1984; Lin and Goff, 1988; Fulton et al., 1990; Doviak et al., 1991). The morning glory roll clouds that appear in spring time in the Gulf of Carpentaria, which have been extensively studied (see Smith, 1988) have been interpreted as an example of a family of large amplitude solitary waves (Christie, 1992). Many mechanisms that lead to the formation of such waves are still not well understood. Generation of a wave disturbance in the atmosphere can be attributed to a wide variety of processes including:

- Intense thunderstorm activity
- deeply penetrating interacting sea breeze fronts
- activity from cold fronts which occurs at mid-latitudes.
- Movement of cold air down a mountain range (Katabatic flow)

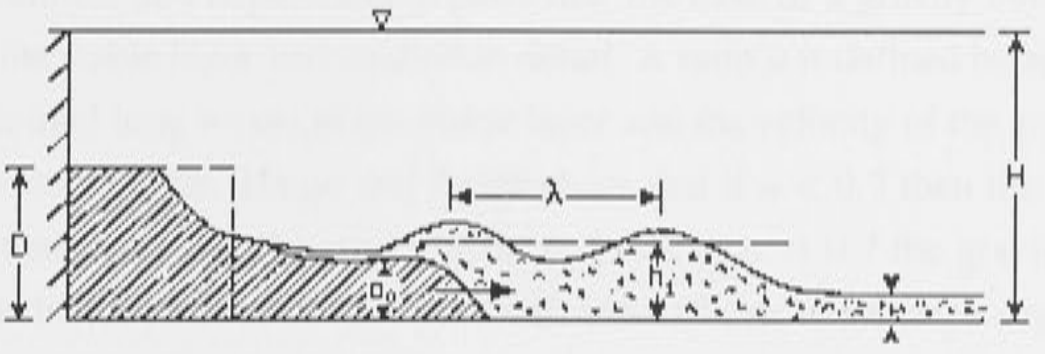

Figure 1.2: Experimental Setup. (From Simpson, 1985)

The first of these will be examined in some detail and will form the physical justification for a simple model to be presented later. Maxworthy's (1980) experiments on the collapse of a mixed region into a linearly stratified fluid are particularly important in terms of wave generation mechanisms. Mixed region collapse is a naturally occurring process in the atmosphere. Maxworthy defined the fundamental parameters for his experiments as the ratios of the height and length of the mixed region to a characteristic height h of the ambient stratification. Using a series of general forcing mechanisms, he was able to produce large amplitude solitary waves with closed circulation cells that advected fluid as a first order mass transport process.

1.2.3 Gravity currents and solitary waves

The generation of internal bores and solitary waves by advancing gravity currents has been studied in laboratory experiments (e.g., Rottman and Simpson (1989), Monaghan (1996)). In such experiments a gravity current is allowed to interact with a stable layer of slightly less dense fluid. Wave generation in the stable layer is linked to the relative height of this intruding current to the depth of the stable layer and its speed of propagation. If the height of the inflow is greater than or comparable to the depth of the stable layer it is likely to give rise to an internal bore which may then evolve into a family of amplitude ordered solitons. If the height of the inflow is considerably less than the depth and its propagation speed is greater than the maximum allowable speed of (small) internal waves on the interface of the stable layer, the flow is supercritical and no waves can form. If it is less, then the flow is subcritical and solitary waves of finite amplitude can be generated ahead of the density current. Laboratory experiments of this type generally use a setup as shown in Fig 1.2 where an isolated mass of fluid (initial height D) is instantaneously released, in a tank with a shallow stable layer of slightly less dense fluid, to generate an intruding current which can produce a wave disturbance on the stable layer. This mechanism of wave generation is important in the study of thunderstorm outflows.

Haase and Smith (1989) have conducted numerical simulations of gravity currents of cold air propagating into stable atmospheric boundary layers. The stable layers were created with

different static stabilities and depths and in particular the case of a gravity current with depth exceeding that of the stable layer was studied in detail. A ratio μ is defined between the critical velocity of infinitesimal long waves in the stable layer and the velocity of the gravity current in the absence of the stable layer. Haase and Smith show that if $\mu < 0.7$ then the gravity current propagates faster than waves on the stable layer, and that as $\mu \to 0.7$ the gravity current head is observed to detach from the feeder flow and will form one or more large amplitude solitary wave which advect a mass of cold air (originating from the gravity current) ahead of the gravity current. As $\mu > 0.7$ the detached gravity current head(s) are able to propagate away from the parent gravity current.

1.2.4 Detection of atmospheric solitary waves

Solitary waves cause variations in atmospheric pressure which can be detected at ground level by ultra-sensitive infrasonic arrays (such as the Warramunga array at Tennant Creek, NT, Australia). They also have visible profiles using Doppler and acoustic radar. The surface pressure perturbation can be used as a measure of the nonlinearity of the disturbance. Boundary layer solitary waves have a unique surface pressure perturbation and it has been found (Christie (1989)) that large amplitude solitary waves often exhibit a bi-modal character that is not predicted by weakly non-linear theory. This bi-modal character is a manifestation of recirculation in the relative streamline flow. A set of surface perturbation pressure traces from the work of Brown (1995) is shown in Fig 1.3 for a range of non-linear wave amplitudes.

1.3 The role of Thunderstorms

Outflows from thunderstorms often interact with and form stable layers in the atmosphere. Solitary wave disturbances have been observed to propagate on spatially and temporally varying waveguides created by these cold thunderstorm outflow currents. Of particular interest for this study is the generating mechanism and evolution of such waves. Thunderstorm-generated outflows of this type are gravity currents with a well defined structure consisting of a head and trailing flow. Within the head region the airflow is supported by a rapid feeder flow near the ground which is advected vertically upwards by the updraft at the nose of the current, bringing cold air to the top of the head. Often the trailing edge of the head consists of turbulent eddies which result from shear flow instability. Ambient air encountered by the head is swept upwards and results in a return flow aloft above the trailing flow of the density current. Such a density current can act as a time varying inhomogeneous waveguide layer for solitary waves which may be created by the interaction of another thunderstorm downdraft outflow with the stable layer.

A multisensor observation of an atmospheric undular bore has been documented by Mahapatra et al. (1990). A bore of this type propagates as a disturbance in the form of a sudden

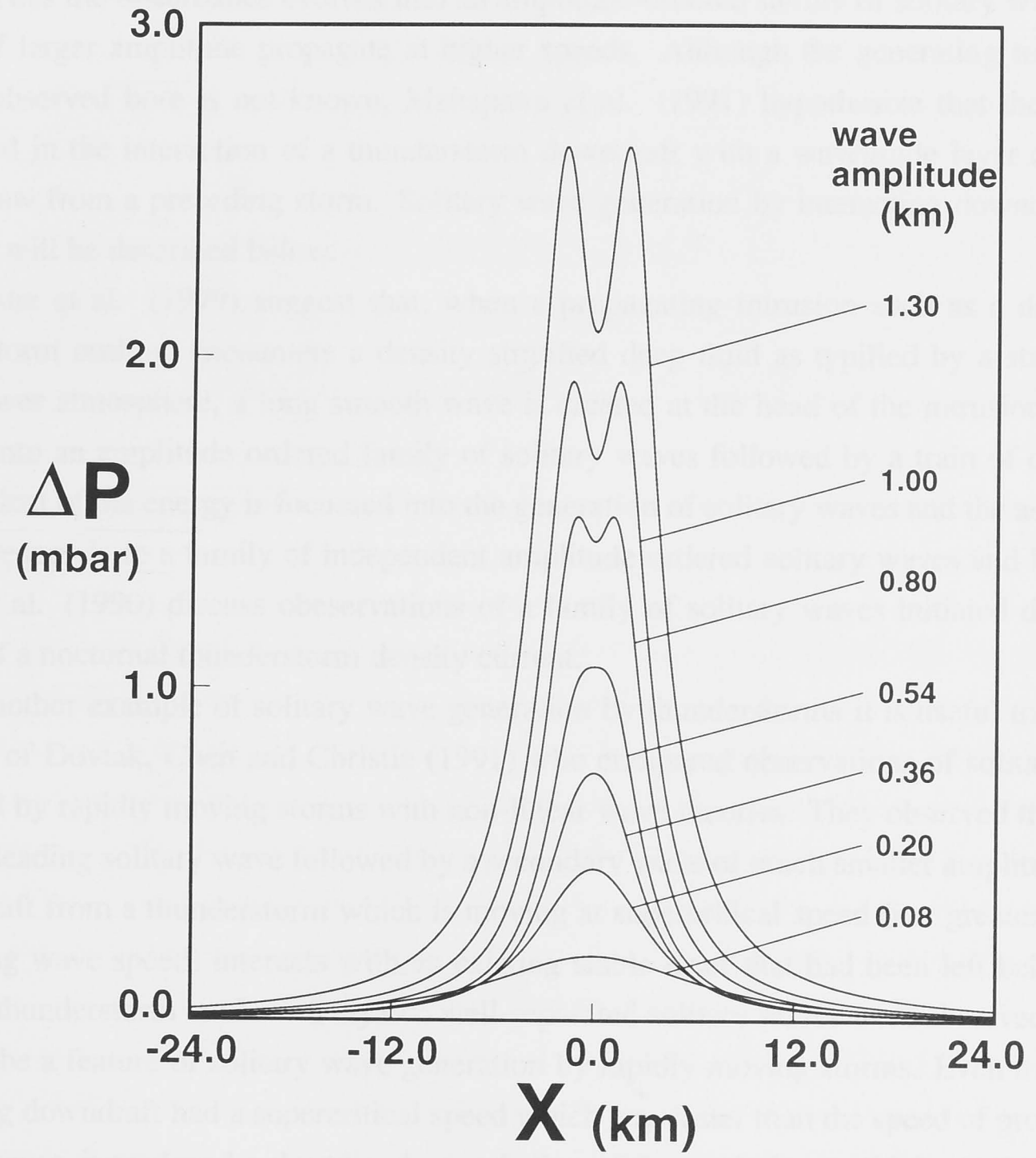

Figure 1.3: The surface perturbation pressure for non-linear waves of different amplitudes. There is a characteristic bimodal shape for waves of very large amplitude. Taken from Brown (1995).

increase in the depth of the stable layer which slowly becomes undular as an ever increasing number of solitary waves develop along the leading edge of the disturbance. The propagation velocity of the waves was measured by using successive Doppler radar scans to record the displacement of the wave front, allowing the speed at different points in the wave train to be calculated. It was found that the speed of propagation was highest for the leading wave in the solitary wave packet formed by the bore in agreement with predictions from weakly non-linear theory. Thus the disturbance evolves into an amplitude-ordered family of solitary waves since waves of larger amplitude propagate at higher speeds. Although the generating mechanism for the observed bore is not known, Mahapatra et al. (1991) hypothesize that these waves originated in the interaction of a thunderstorm downdraft with a waveguide layer created in the outflow from a preceding storm. Solitary wave generation by interacting downdrafts and outflows will be described below.

Christie et al. (1979) suggest that, when a propagating intrusion such as a dissipating thunderstorm outflow encounters a density stratified deep fluid as typified by a stable layer in the lower atmosphere, a long smooth wave is created at the head of the intrusion and this evolves into an amplitude ordered family of solitary waves followed by a train of dispersive waves. Most of the energy is focussed into the generation of solitary waves and the asymptotic state corresponds to a family of independent amplitude-ordered solitary waves and little else. Fulton et al. (1990) discuss obeservations of a family of solitary waves initiated during the demise of a nocturnal thunderstorm density current.

As another example of solitary wave generation by thunderstorms it is useful to examine the work of Doviak, Chen and Christie (1991) who compared observations of solitary waves generated by rapidly moving storms with non-linear wave theories. They observed the formation of a leading solitary wave followed by a secondary wave of much smaller amplitude when a downdraft from a thunderstorm which is moving at supercritical speed (i.e. greater than the linear long wave speed) interacts with an existing stable layer that had been left behind by a previous thunderstorm outflow. Only two well-separated solitary waves were observed and this seems to be a feature of solitary wave generation by rapidly moving storms. Even though the generating downdraft had a supercritical speed which was faster than the speed of propagating solitary waves, it produced a short lived perturbation of the stable layer with limited horizontal dimension (about 5 km) which led to the generation of nonlinear curved wave fronts aligned at an angle to the storm path. The wave energy is then directed away from the storm along a ray path (see Fig 1.4).

These observations were compared with both weakly non-linear theory and the numerical work done by Tung et al. (1982) on strongly non-linear waves in environments without shear. It was found that the weakly non-linear theory provided a relationship between amplitude and wave speed that was in good agreement with the strongly non-linear numerical solutions up to values of $a/h_s = 1.3$ (h_s being the scale of stratification). For larger amplitude disturbances,

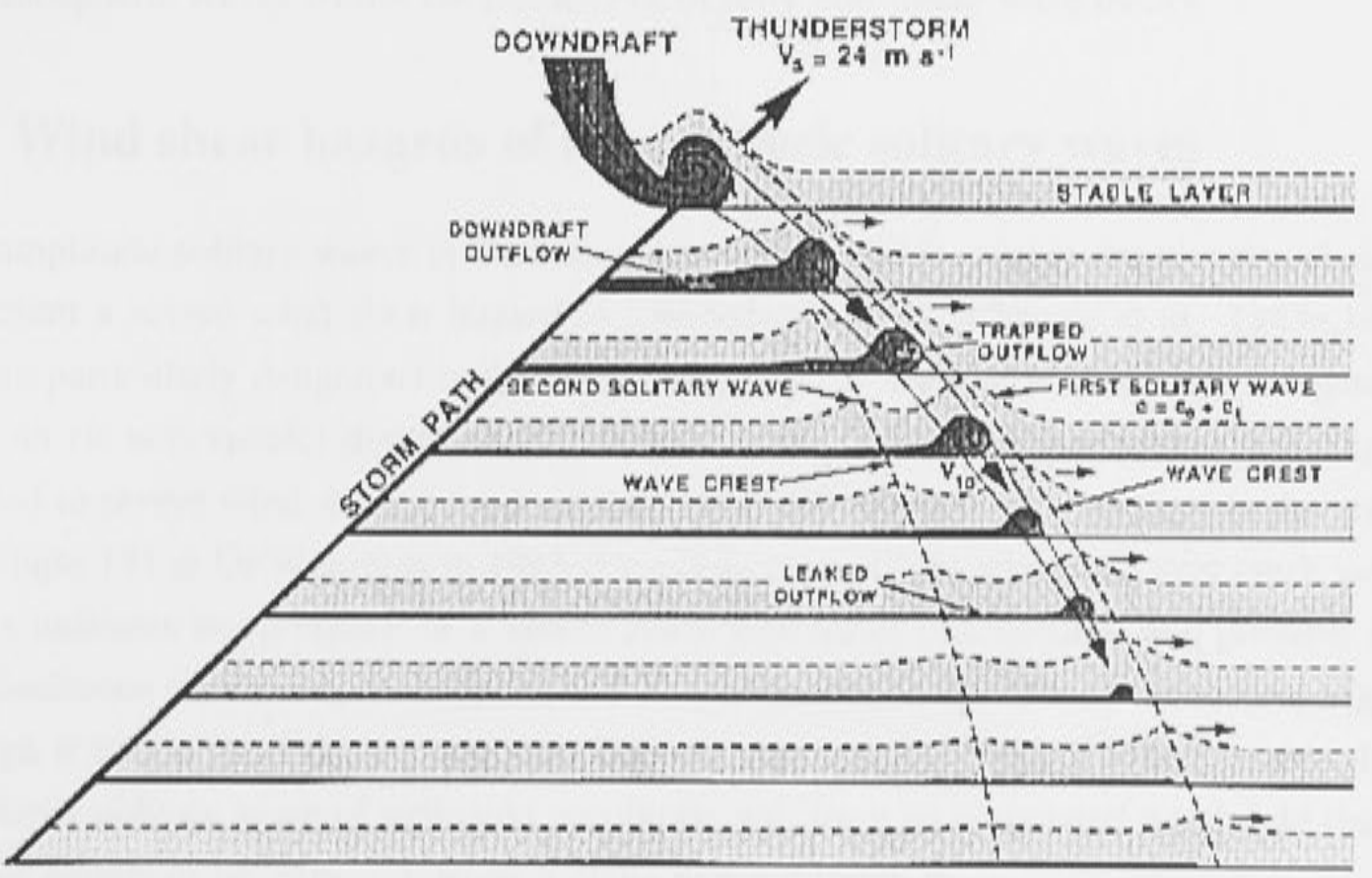

Figure 1.4: *Observed evolution process for thunderstorm generated solitary waves (from Doviak, Chen and Christie, 1991)*

the wave speed predicted by both theories were faster than those observed, but the values from the strongly non-linear solutions were closer to the observed values. Weakly non-linear theory gave poor estimates of wave half-widths as opposed to reasonable predictions from strongly non-linear solutions. Of particular interest was the observation of trapped recirculating thunderstorm air in the evolving solitary wave. Trapped air was observed to leak slowly from the back of the wave leaving behind a shallow layer of denser air. It was suggested that if radiative and frictional losses can be ignored, then the disturbance will eventually become a wave of permanent form when all trapped fluid is lost from the interior of the wave.

Observations of boundary layer oscillations at Sydney airport propagating ahead of a thunderstorm have been attributed to a train of solitary waves by Manasseh and Middleton (1993). The passage of three very smooth amplitude-ordered boundary layer oscillations was observed. These authors attribute these observations to a family of amplitude ordered solitary waves created in the interaction of a thunderstorm outflow with a stable layer. These authors found that the propagation speed was adequately described by linear theory but that the wave half-width was smaller than that predicted by weakly non-linear theory. They also found that the trapping mechanism (inhibiting upward propagation of wave energy at some height and forming a trapped layer below) for such a weakly-non linear solution was not strong enough to account for the observations. Hence, it was concluded that highly non-linear waves were observed.

All of the above observations highlight the need for a theoretical treatment of large ampli-

tude atmospheric waves within the framework of fully non-linear wave theory.

1.4 Wind shear hazards of atmospheric solitary waves

Large amplitude solitary waves in the lower atmosphere which exist in the vicinity of airports can present a severe wind shear hazard to low flying aircraft (Christie et al. 1983a,1983b). They are particularly dangerous in that they usually occur without warning and are generally a clear air (ie non-visible) disturbance. There have been several plane crashes that might be attributed to severe wind shear from a solitary wave disturbance. One of these is the crash of Delta Flight 191 at DFW airport in 1985 (Caracena et al. 1986) where the post crash weather analysis indicates the presence of a severe storm downdraft (microburst) and possible stable layer conditions which may have given rise to a large amplitude solitary wave (see Fig 1.5). Although it is not possible to prove conclusively this was the case, it is undeniable that an atmospheric solitary wave of sufficient amplitude will have an associated wind field that will effect the degree of lift experienced by a plane flying through it.

An aircraft which encounters a solitary wave from the front at low altitude will experience a sudden increase in lift due to increased horizontal winds and the vertical updraft at the leading edge of the wave. This will then be followed by a sudden loss of lift as the plane experiences the combined effects of a rapidly decreasing headwind and the effect of the downdraft at the trailing edge of the wave. Obviously this unexpected and sudden change in the lift experienced by the plane could have disastrous consequences for a plane landing where the pilot would naturally try to correct any deviation from the usual glide path. Normal procedure would result in a reduction of speed on encountering the added lift, and combined then with the sudden loss of lift this would mean a potential undershoot of the glide path - with potentially fatal consequences at low altitude. Figure 1.6 shows a possible solitary wave encounter by a low flying aircraft.

1.5 Observed Atmospheric Solitary Wave Events

Due to the inherent difficulty in making measurements of the vertical structure of the atmosphere (where instruments are usually located on ground based towers, balloons and aircraft), it is not surprising that only widely scattered data exists from a few studies of ambient conditions present before the observed passing of a large amplitude solitary wave disturbance. Relevant studies include Clarke, Smith and Reid (1981), Cheung and Little (1990), Doviak, Chen and Christie (1991). The first two of these offer the most detailed measurements of the ambient conditions, and ambient conditions chosen for much of the work to follow will be loosely based on measurements provided by these two studies.

Clarke, Smith and Reid (1981) investigate the structure and origin of the "morning glory".

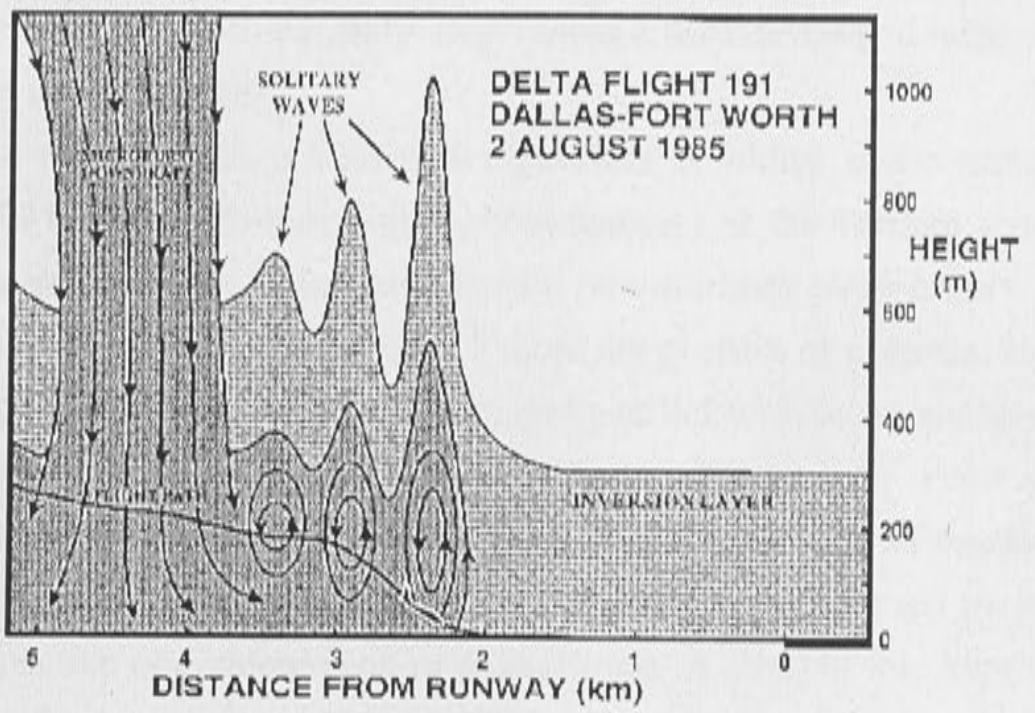

Figure 1.5: Analysis of weather data indicates a possible cause of the crash of Delta Flight 191 was the generation of a set of large amplitude solitary waves by a thunderstorm downdraft. (from)

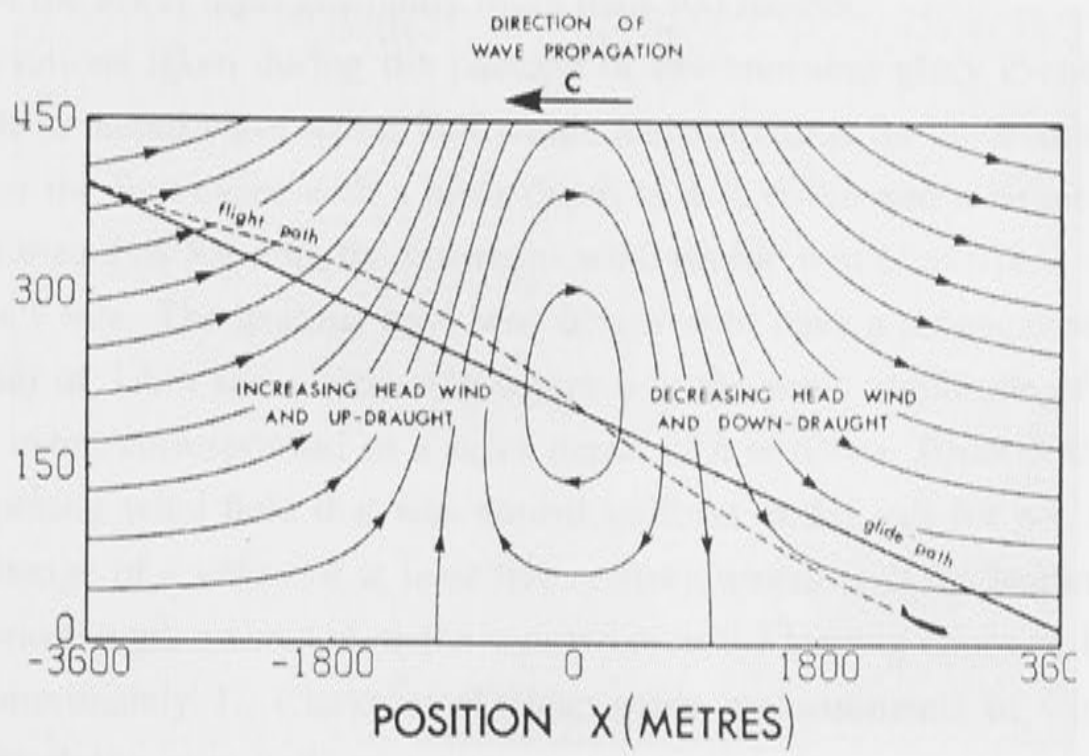

Figure 1.6: Possible scenario for a solitary wave encounter with a low flying aircraft (from Christie and Muirhead, 1983b)

This line wind squall observed in the Gulf of Carpentaria in far northern Australia often appears as a visible disturbance marked by a long roll cloud or series of such clouds. Measurements were made of a pressure jump at the surface which marks the passage of the disturbance. These support the view that the "morning glory" represents a well developed large amplitude solitary wave or group of solitary waves.

Using a light aircraft with a Väisäla temperature-humidity probe mounted in the nose, Clarke et al. (1981) made pre-morning glory soundings of the vertical wind and thermodynamical structure of the lower atmosphere before two morning glory events. The first of these measurements is shown in Fig 1.7. In Fig 1.7 there are profiles of potential temperature θ_v, the wind components u and v measured normal to and parallel with the cloud lines, and total static energy E (where total static energy is defined by $E = c_pT + gz + Lq$ where c_p is specific heat at constant pressure, T is temperature, g is gravity, L the latent heat of condensation and q the water vapor mixing ratio). The total static energy E is exactly conserved for steady frictionless air motions irrespective of condensation or evaporation. A straight line approximation is fitted to the data points for two segments of the potential temperature profile. These line segments are used to calculate a characteristic Brunt-Väisäla period (BVP) defined by:

$$\text{BVP} = 2\pi[(g/\theta_v)\frac{\partial\theta_v}{\partial z}]^{-\frac{1}{2}} \tag{1.1}$$

for a lower and upper layer. The lower layer for these data sets has a characteristic period of 4-6 min and corresponds to the nocturnal inversion layer. The upper, much deeper, layer consists of less stable air with a characteristic period of approximately 14 mins. It can be seen that the depth of the lower layer is slightly more than 500 meters.

From observations taken during the passage of two morning glory events, Clarke et al. (1981) were able to record wave speed, half width, and amplitude for the leading solitary wave disturbance. For the first event with a layer depth of $h \approx 690$m and a Brunt-Väisäla period in this layer estimated as 5.9 min, the upstream wind profile was $U = U_1 z/h - U_2$ with $U_1 =$ 8 m/s and $U_2 = 1$ m/s. The leading wave was observed to have a propagation speed of 10.8 m/s, a half width of 3 km and a ratio a/h where a is the wave amplitude of approximately 1. The second event corresponded to a layer depth of $h \approx 630$m, Brunt-Väisäla period 5.1 min and an opposing wind field that was almost uniform at 2.2 m/s for $z < h$. Instruments recorded the passage of a series of at least five solitary waves with the leading wave having speed 9 m/s, a wavelength estimated on the separation of the leading crests as 10km and again a ratio a/h approximately 1. Clarke et al. also made measurements of wind components using double theodolite pilot-balloon ascents at intervals before and after the arrival of the leading disturbance. The wind components, measured relative to the center of the propagating disturbance for each event, are denoted by $u - c$ where c is the speed of the disturbance and u is the fluctuating wind field. For one of these events the relative streamlines are calculated

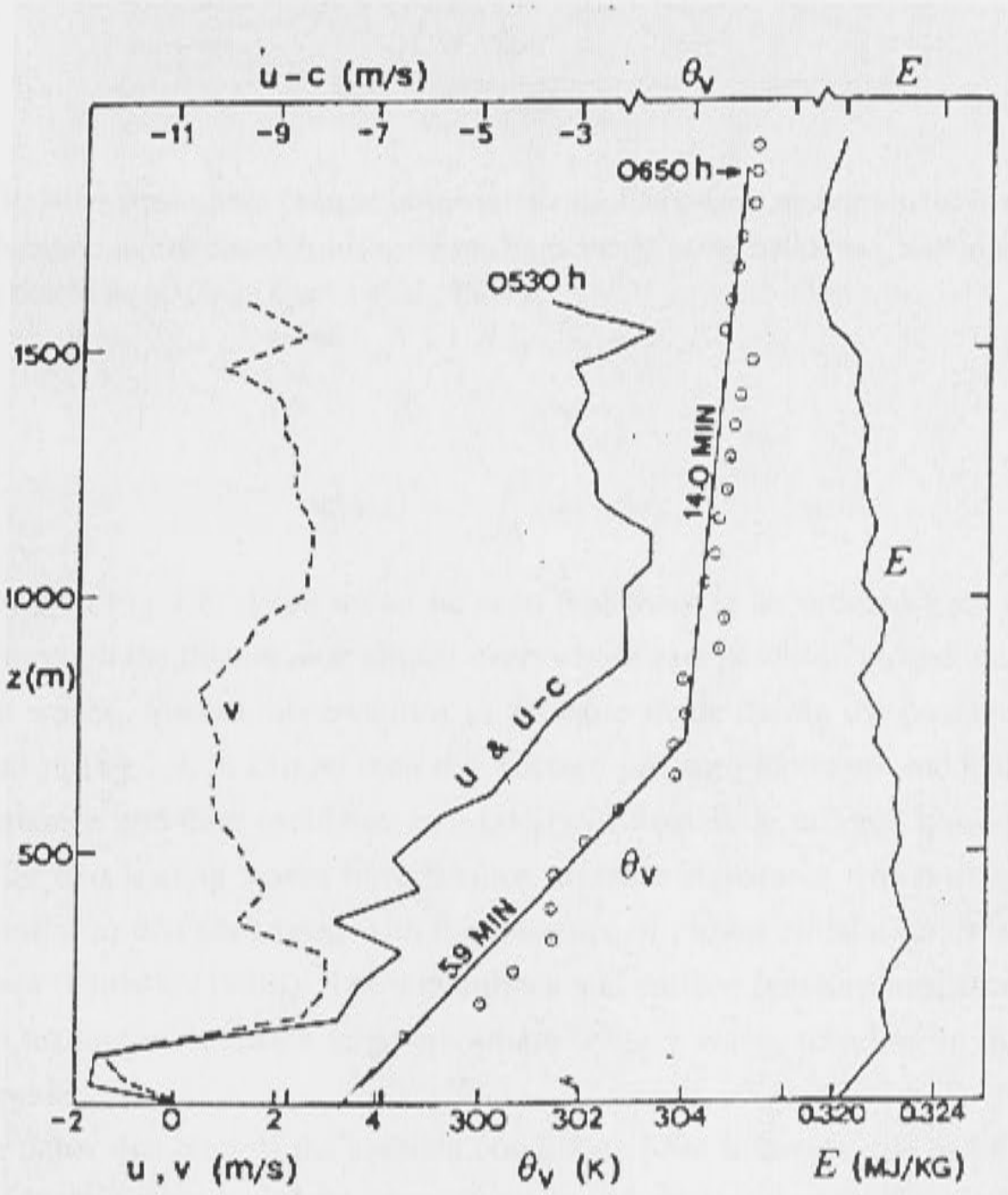

Figure 1.7: Atmospheric measurements of potential temperature from Clarke et al. (1981)

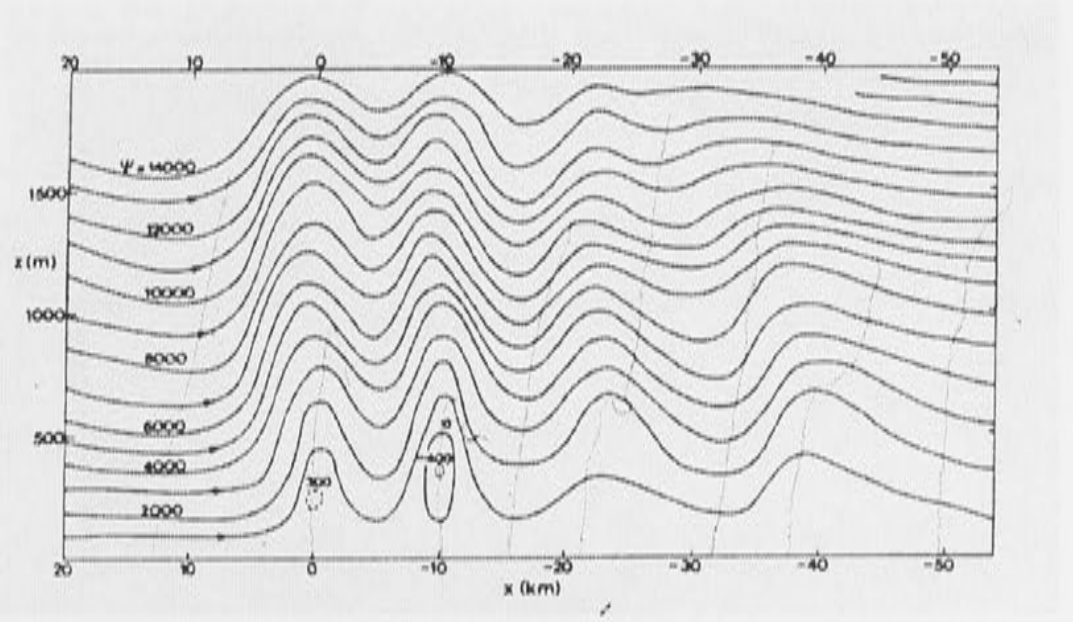

Figure 1.8: Relative streamlines from an observation of solitary wave motions in the lower atmosphere. The streamfunction is calculated from wind readings made using balloons. Balloon trajectories are shown using dotted lines. (from Clarke et al., 1981)

using:

$$\psi(x,z) = -\int_0^z (u-c)dz \tag{1.2}$$

and are shown in Fig 1.8. Here it can be seen that there is an ordered train of waves with air flowing through the disturbance almost everywhere except within closed cells enclosed by the first two waves. Surface observations of pressure made during the passage of the waves are displayed in Fig 1.9. It can be seen that surface pressure increases suddenly at the onset of the disturbance and then oscillates as a family of amplitude ordered quasi-periodic wave motions. The two leading waves have surface pressure signatures which display a bimodal character similar to that associated with the presence of closed circulation in large amplitude solitary waves (Christie (1989)). The streamlines and surface pressure measurements suggest that the two leading waves were large amplitude solitary waves traveling in the lower stable layer waveguide.

Another paper that records the ambient conditions prior to events that had the characteristics of strongly nonlinear deep fluid internal solitary waves is that of Cheung and Little (1990). The physical size of events observed is quite small but their observations cover a range of large a/h values. Cheung and Little also observe the waves transporting and recirculating cold air. The data shows that the maximum observed negative temperature perturbations are typically larger than expected from the lifting of cool air from the pre-disturbance ambient profile. They note that this implies the observed large negative $\Delta\theta$ must be due to the advection of recirculating cool air by the observed solitary waves. Cheung and Little also report evidence of "leakage" of some of the recirculating fluid from behind the waves, as has been observed in laboratory experiments.

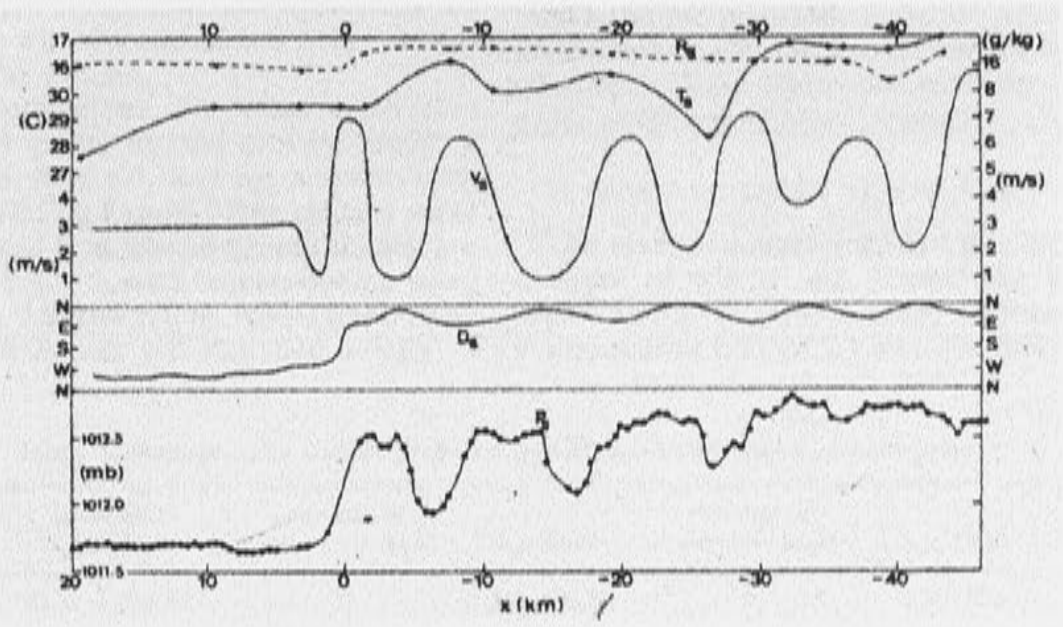

Figure 1.9: Surface observations of mixing ratio R_s, temperature T_s, wind direction D_s, speed V_s and corrected pressure P_s (corrected by subtracting the diurnal changes obtained by averaging over hourly pressure readings for a large number of days) recorded for a morning glory event. The time axis has been transformed to distance relative to the leading edge of the morning glory for comparison with aircraft data. (from Clarke et al., 1981)

1.6 Concluding remarks

The above background material provides a context and some motivation for the work that follows. It would seem clear that large amplitude solitary waves are significant and commonly occurring events in the lower atmosphere. Because of the suddenness with which they can occur and the intensity of the localized disturbance which they can produce, such waves are potentially hazardous events for aircraft at low altitude. It is therefore of interest to study models of atmospheric events that can lead to formation of large amplitude solitary waves. In this thesis this will lead to the study of a model for wave generation from a sinking localized mass of cold air (which can be used to represent an atmospheric "microburst") similar to conditions that can occur during and in the aftermath of thunderstorm activity. Given a method of generating large amplitude solitary waves it is then of interest to study under what conditions a large amplitude wave disturbance can propagate for a significant distance without losing its form (or energy). This will lead to a study of the radiative decay of large amplitude solitary waves. It will be assumed that the upper medium above the waveguide layer is weakly stratified (as is common in the atmosphere) and can support internal wave motions that can carry away wave energy from the large amplitude solitary wave.

To achieve these aims a suitable modeling environment is necessary. This will take the form of a numerical finite difference model with appropriate boundary conditions that will represent the lower atmosphere. Details of this model will be explained below.

Chapter 2

Weakly Nonlinear wave theory

2.1 Introduction

Attempts to provide a theoretical description of the evolution of non-linear waves, such as those encountered in geophysical environments, generally result in analytic problems that are intractable. As such, a comprehensive analytic description of fully non-linear waves does not exist. There is, however, a well-developed theory in the weakly non-linear limit for which wave amplitude is assumed to be small-but-finite. This restriction applies to most of the theoretical work that has been carried out on non-linear waves. The mathematical analysis of weakly nonlinear waves usually divides the problem into the treatment of two flow regimes; one dealing with shallow fluids and the other deep fluids. A dispersion relation that is dependent on the particular regime leads to the development of a mathematical equation in terms of wave amplitude (or some other dependent variable). For shallow fluids this class of equation is known as the Korteweg-de Vries (KdV) equation (Korteweg and de Vries, 1895) and for deep fluids the Benjamin-Davis-Ono (BDO) equation (Benjamin, 1967; Davis and Acrivos, 1967; Ono, 1975). Both of these equations can be solved directly for N soliton solutions using a technique known as the inverse scattering transform (Gardner et al., 1967). This method was discovered in the derivation of analytic solutions to the KdV equation and can be applied to the BDO equation and the more fundamental Whitham integro-differential equation (for a discussion see for instance, Ablowitz and Clarkson, 1991). The details will not be presented here. It is more appropriate for the atmosphere to consider the description of internal solitary waves in a deep fluid with density stratification. Therefore this chapter will review the first order perturbation analysis of Benjamin (1967) derived for small but finite wave amplitude. A perturbation analysis to higher order has been derived by Grimshaw (1981b) for continuously stratified deep-fluids. The theory presented in this chapter will be used for comparisons to the results of later chapters.

2.2 Governing Equations

The following review of weakly non-linear theory will be restricted to inviscid, incompressible and homogeneous flow which leads immediately to the Euler equations. Later we will discuss more general approaches that include spatially and temporally varying waveguides, ambient shear, compressibility, vertically propagating internal waves and energy loss due to turbulent frictional dissipation.

The starting point for analysis is the set of general equations for a Newtonian fluid in two dimensions:

$$\frac{\partial u}{\partial t} + \left(u\frac{\partial}{\partial x} + v\frac{\partial}{\partial y} \right) u = -\frac{1}{\rho}\frac{\partial p}{\partial x}, \tag{2.1}$$

$$\frac{\partial v}{\partial t} + \left(u\frac{\partial}{\partial x} + v\frac{\partial}{\partial y} \right) v = -\frac{1}{\rho}\frac{\partial p}{\partial y} - g, \tag{2.2}$$

$$\frac{\partial u}{\partial x} + \frac{\partial v}{\partial y} = 0, \tag{2.3}$$

with appropriate boundary conditions.

Generally, non-dimensional parameters are introduced using the undisturbed depth, h, a typical measure of wave amplitude, a, and a typical horizontal length scale, l. The parameters used here are:

$$\varepsilon = \frac{a}{h}, \qquad \kappa = \frac{h}{l}, \tag{2.4}$$

and in what follows we focus on small amplitude long waves in the limits $\varepsilon \to 0$ and $\kappa \to 0$. The key factor which distinguishes between different flow configurations will be the dispersion relation which links the frequency, ω, and wave-number, k, of infinitesimal waves. By assuming that every dependent variable φ satisfies a harmonic wave solution of the form

$$\varphi = \hat{\varphi} \exp i(\omega t - kx), \tag{2.5}$$

where x is the direction of propagation, then we can derive a dispersion relationship $\omega(k)$ between ω and k for waves which travel at speed $c = \omega/k$.

2.3 Flow Regimes

Weakly non-linear theories have been developed for fluids of any depth, but most treatments to date focus on shallow fluids with total depth H or unbounded fluids. A distinction needs to be made between the total fluid depth H and a layer of depth h which will be defined as the pycnocline region in which the density variations take place. The solutions that will be examined here will be for internal solitary waves. For a solitary wave solution there is an exact balance between the steepening effects of non-linearity (which causes energy transfer to higher frequency harmonics) and the effects of wave dispersion. Dispersion is present because the phase velocity $c = \omega/k$ depends on wavenumber. This implies that wave components of different wave number will propagate at different velocities, thus causing a spreading of the wave profile as energy is transfered to lower frequency harmonics.

Waves in shallow fluid

In this case $l/H >> 1$ and h/H is $O(1)$. For k small enough, we will have the long wave dispersion relation

$$\omega(k) = kc_0(1 - \beta k^2), \tag{2.6}$$

where c_0 is the linear phase speed (c obtains a maximum value c_0 at $k = 0$) and β is a constant ($\beta > 0$) which depends on the actual system being solved. A harmonic wave solution $A(x,t)$ representing vertical displacement will now satisfy the equation:

$$\frac{\partial A}{\partial t} + c_0 \frac{\partial A}{\partial x} + c_0 \beta \frac{\partial^3 A}{\partial x^3} = 0. \tag{2.7}$$

The third (odd) order derivative term represents a dispersive term resulting in real $\omega(k)$ for real k. If a second (even) order term is included as well then we get complex $\omega(k)$ and a solution which exhibits dissipative properties. Non-linear small amplitude wave effects can be incorporated by adding a quadratic term of the form $\alpha A \partial A/\partial x$ (with constant α) which results in the well known Korteweg-deVries (KdV) equation,

$$\frac{\partial A}{\partial t} + c_0 \frac{\partial A}{\partial x} + \alpha A \frac{\partial A}{\partial x} + c_0 \beta \frac{\partial^3 A}{\partial x^3} = 0. \tag{2.8}$$

This equation was derived by Korteweg and de Vries in 1895 and used to describe small, but finite amplitude surface waves in shallow water. It also describes the evolution of internal small amplitude wave evolution in shallow fluids (Benjamin, 1966).

Waves in deep fluids

Now $l/h >> 1$ and $l/H \to 0$. It can be shown that for a fluid of infinite depth where the density varies only in a limited depth h, the long wave dispersion relation has leading terms given by (Benjamin, 1967):

$$\omega(k) = kc_0(1 - \nu|k|). \tag{2.9}$$

where ν is a positive non-zero constant which is dependent on the particular system under consideration. The pioneering work for internal solitary wave solutions for deep fluid was done by Benjamin (1967) and Davis and Acrivos (1967) who both proposed the following evolution equation including dispersive effects (with coefficient of dispersion δ) and non-linear effects

$$\frac{\partial A}{\partial t} + c_0\frac{\partial A}{\partial x} + \nu A\frac{\partial A}{\partial x} + \delta\left(\frac{\partial^2 \mathcal{H}(A)}{\partial x^2}\right) = 0, \tag{2.10}$$

where the dispersive term is defined in terms of the Hilbert Transform $\mathcal{H}$[1]

$$\mathcal{H}(A(x)) = \frac{1}{\pi}\mathcal{P}\int_{-\infty}^{\infty}\frac{A(x')}{x'-x}dx, \tag{2.11}$$

and it is assumed that $A(x)$ vanishes at $x = \pm\infty$. The first rigorous derivation of this equation was provided by Ono (1975). This equation is now generally referred to as the Benjamin-Davis-Ono (BDO) equation.

2.4 Internal solitary wave solutions

As discussed by Benjamin (1966, 1967) the height y of individual streamlines may be taken as the dependent variable in a traveling frame of reference for which the wave motion to be examined is at rest. The independent variables are taken as the horizontal displacement, x, and the original height, μ, of the individual streamlines in appropriate stretched coordinate systems. Thus $y - \mu = z(x,\mu)$ defines a streamline displacement $z(x,\mu)$ and the vertical displace-

[1] where $\mathcal{P}\int$ denotes a Cauchy principal value integral

ment of an interface at $\mu = h$ can be considered as a surface defined by $z(x,\mu) = f(x)$. Assuming the fluid is incompressible and non-diffusive with constant density along each streamline, a second order dynamical equation in y (known as the Dubreil-Jacotin-Long, or DJL, equation) can be derived. This equation is quite general and there are no assumptions at this stage on wave amplitude. Benjamin solves this equation for approximate solutions in the weakly non-linear limit subject to the restraints $y = 0$ for $\mu = 0$ and $y - \mu \to 0$ for $\mu \to \infty$. These approximate solutions are perturbations of the undisturbed state $y = \mu$, derived by dividing the flow into two regions: (I) a lower region $\mu \leq h$ which allows a long wave approximation and (II) an upper region $\mu \geq h$ where constant density allows a term from the dynamical equation to be discarded. Solution matching must be applied between the regions.

For the deep fluid case, the upper homogeneous region with ρ constant has a flow field described to leading order by Laplace's equation. In this case $\mathcal{H}(-f_x)$ which appears in the BDO equation represents a streamfunction $\psi(x,\mu = 0)$ solution to the Dirichlet problem for the upper half plane ($\mu \geq h$) given by Laplace's equation (with the boundary condition $\psi = f(x)$ on $\mu = h$) for unit density and velocity. This means $\mathcal{H}(-f_x)$ can be interpreted as the hydrodynamic pressure on an infinitesimal hump ($\mu = f(x)$) over which there is an irrotational flow field in an infinitely deep fluid. For the lower region there is a separable solution to leading order with $z(x,\mu)$ given by,

$$z(x,\mu) = f(x)\phi(\mu). \tag{2.12}$$

where $\phi(\mu)$ is a vertical modal function and satisfies a linear eigenvalue equation.

Applying solution matching between regions leads to the time independent BDO equation (Benjamin, 1967), for stationary wave solutions, in terms of $f(x)$

$$B_1 f - B_2 f^2 + \mathcal{H}(-f_x) = 0, \tag{2.13}$$

where x is a traveling frame of reference, B_1 and B_2 are functions and $\mathcal{H}$ again represents a Hilbert transform. The functions B_1, B_2 are defined as:

$$B_1 = \frac{(c^2 - c_0^2)}{c_0^2} \frac{1}{\rho(h)} \int_0^h \rho(\frac{d\phi}{ds})^2 ds, \tag{2.14}$$

$$B_2 = \frac{3}{2\rho(h)} \int_0^h \rho(\frac{d\phi}{ds})^3 ds, \tag{2.15}$$

where h represents the depth over which there is significant variation of density (ie the lower region discussed above) and s is an intrinsic variable representing variation of ϕ vertically. For the BDO type equation given above Benjamin (1967) found symmetrical single-crested solitary wave solutions in the long wave limit $\lambda/h \to \infty$ of the form:

$$f(x,t) = \frac{a\lambda^2}{(x-ct)^2+\lambda^2}, \tag{2.16}$$

where 2λ is the full width of the wave profile at half-amplitude. The scaling relationship for waves in unbounded fluids is given by

$$a\lambda = O(h^2). \tag{2.17}$$

Benjamin has also shown that the propagation speed of solitary waves is given by

$$c = c_0[1+\nu(a/h)]^{\frac{1}{2}}, \tag{2.18}$$

where ν is determined from B_1 and B_2 in (2.13). Thus c is larger than the linear phase speed c_0 by an increasing function of a/h.

For the shallow fluid case, there is also a $\phi(\mu)$ which satisfies a modal equation and an equation for $f(x,t)$ can be derived, which turns out to be a time independent form of the KdV equation. Korteweg and de Vries found stationary non-periodic solitary wave solutions to this equation, in a frame of reference moving at the wavespeed c, of the form:

$$f(x,t) = a\,\mathrm{sech}^2\left[\left(\frac{a\alpha}{12c_0\beta}\right)^{\frac{1}{2}}(x-ct)\right], \tag{2.19}$$

and Benjamin (1966) showed that solutions for these classical shallow fluid waves are generally governed by the scaling relationship:

$$a\lambda^2 = O(h^3). \tag{2.20}$$

2.5 Properties of KdV and BDO solitary waves

It is important to stress some important properties of the solutions of these fundamental equations. Dispersive effects are stronger in deeper fluids and we expect there to be major differences between these solutions. An important general property of the solitary wave solutions of these two equations is that they preserve their identity under non-linear interaction. These solitary wave solutions are therefore solitons. One key difference between the solitary wave solutions is that solitons that satisfy the KdV equation undergo a phase shift after collision whereas those derived from the BDO equation do not. The wave-length amplitude scaling is

also fundamentally different for the two equations. In addition, soliton solutions to the KdV equation have an exponentially decaying sech^2 profile while those of the BDO are algebraic. However, there are also common properties, such as the fact that solutions for both equations that develop from arbitrary initial disturbances of finite extent evolve asymptotically into a family of amplitude-ordered solitons followed by a dispersing wave train.

2.6 Limitations of weakly nonlinear theory

Long atmospheric gravity waves usually fall into the deep fluid wave category. As it stands the BDO equation (2.10) is directly applicable to the description of small amplitude waves in a homogeneous waveguide embedded in a neutrally stratified fluid of infinite extent. Realistic flow conditions in the atmosphere usually involve spatially and temporally varying waveguides, wave amplitudes that can exceed the limitations of weakly non-linear theory and effects such as variable background shear. Some brief comparisons between observed phenomena and the theory outlined above will be provided in the next section. It has been found that for small amplitude solitary waves in the atmospheric boundary layer the BDO equation provides a reasonable description. What is surprising, however, is that it still provides a reasonable approximation to observed features even in many cases where the equation is used outside its domain of validity. However there are many non-linear processes in the atmosphere that have strong effects on wave morphology and are not included in the BDO description.

One of these processes is the important effect of turbulent frictional damping. As described by Christie (1989) frictional dissipation can be expected to play an important role in the evolution of long wave disturbances in the lower atmosphere. Also there will be a radiative damping effect due to energy loss into the upper atmosphere which occurs when the region above the waveguide is weakly stratified and supports internal waves. Solitary waves in the atmosphere are generally not stationary and so some account of their temporal evolution is necessary for any realistic analysis. Christie (1989) provides the following general evolution equation (a generalization of the BDO equation) for non-linear wave propagation in an inhomogeneous waveguide subject to turbulent frictional dissipation and long wave radiation

$$\frac{\partial A}{\partial t} + c_0 \frac{\partial A}{\partial x} + \alpha(x,t) A \frac{\partial A}{\partial x} + \delta(x,t) \frac{\partial^2}{\partial x^2} \mathcal{H}(A) = \mu(x,t) \frac{\partial^2 A}{\partial x^2} - \frac{\delta(x,t)\,\text{sgn}(u_\infty - c_0)}{\pi} \int_{-\infty}^{\infty} A(x')\,dx' \int_0^{\hat{\alpha}} k(\hat{\alpha}^2 - k^2)^{\frac{1}{2}} \cos[k(x-x')]\,dk, \tag{2.21}$$

where $A(x,t)$ describes the wave amplitude, $\hat{\alpha}$ is a cutoff wavenumber defining the allowable wavenumber spectrum of ducted modes, and $\alpha(x,t)$, $\delta(x,t)$ represent coefficients of nonlinearity and dispersion respectively which depend on the ambient environment (so that they will vary in (x,t) due to changes in the inhomogeneous waveguide layer). This equation (2.21)

represents a combination of the BDO-Burgers equation (including viscous effects through the RHS term with Burgers eddy diffusivity coefficient μ) and the effects of radiative damping through the RHS forcing term which is dependent on a integral defined using the cutoff wavenumber $\hat{\alpha}$. Christie (1989) shows using numerical solutions to the BDO-Burgers equation that the degree of turbulent boundary friction influences the development of an initially smooth finite-length wave of elevation into a family of amplitude ordered solitions. The theory of radiative damping of weakly nonlinear waves has been treated by Maslowe and Redekopp (1980) and Grimshaw (1981a) and is outlined in more detail below.

Laboratory experiments (Davis and Acrivos (1967); Maxworthy (1980)) and numerical experiments (Davis and Acrivos, 1967; Tung et al., 1982; Brown, 1995) suggest that the morphology of nonlinear internal solitary waves changes at large amplitude. Also the second order in amplitude correction terms that have been calculated to extend the analytic theory (Grimshaw, 1981c; Gear and Grimshaw, 1983) indicate that, as amplitude increases, there is a point at which there will be an increase in wavelength with increasing amplitude (i.e. wave broadening). This has been observed in laboratory experiments (Koop and Butler, 1981; Segur and Hammack, 1982). In particular as a/h increases beyond 1 (Tung et al., 1982), there is generally an onset of closed circulation in the interior of a solitary wave and the wave transports fluid as a first order process. This effect has been observed in the atmosphere (Christie, 1989). The wavelength increases with increasing amplitude in strongly non-linear waves of this type in contrast with the predictions of weakly nonlinear theory. Also, the phase velocity for strongly non-linear waves increases with amplitude at a slower rate than that indicated by weakly nonlinear theory.

Some of these non-linear effects will be covered in more detail at a later stage but the above remarks illustrate the complexity of real geophysical flows. This provides the justification for adopting a numerical model that is fully nonlinear, fully compressible and non-hydrostatic as a means to examine long wave propagation under more realistic conditions such as those mentioned above. Very little work has been done on fully non-linear waves in the atmosphere, yet waves of large amplitude are routinely observed in the lower atmosphere. Numerical experiments offer a chance to study fully non-linear waves and their evolution in detail.

2.7 Weakly nonlinear radiative damping of long waves

Consider finite-amplitude wave motions in a pycnocline region of an unbounded fluid. We assume a weakly stratified upper region above the pycnocline. As in Benjamin's (1967) analysis for the neutrally stable case it is necessary to consider an upper and lower region for the solution and to match the respective solutions. The lower region has a separable solution

where to first order the stream function can be represented as

$$\psi = A(\xi, \tau)\phi(z). \tag{2.22}$$

For small amplitude two-dimensional disturbances we require that $\phi(z)$ satisfy an eigenvalue problem for the allowable wave modes. Synge (1933) provides a generalized form of the Taylor-Goldstein equation for non-Boussinesq flow and shear profile $U(z)$:

$$(\bar{\rho}\phi')' + \left[\frac{(\bar{\rho}U')'}{c-U} - \frac{g\bar{\rho}'}{(c-U)^2} - k^2\bar{\rho}\right]\phi = 0, \tag{2.23}$$

which has associated boundary conditions for the deep-fluid case of

$$\phi(0) = 0, \qquad \lim_{z\to\infty}\phi(z) = 0, \tag{2.24}$$

This reduces in the Boussinesq approximation to a Helmholtz equation of the form

$$\phi'' + (l^2(z) - k^2)\phi = 0, \tag{2.25}$$

where

$$l^2(z) = \frac{N^2}{(U-c)^2} - \frac{U''}{U-c}, \tag{2.26}$$

is the Scorer parameter (Scorer, 1949) and upward radiation of energy is possible only if $l^2 > k^2$.

Maslowe and Redekopp (1980) and Grimshaw (1980, 1981) solve the eigenvalue problem for the Boussinesq case in the long wave limit $k \to 0$ with constant background shear in the upper region. They require that the amplitude part of the separable solution in the lower region satisfy the evolution equation

$$A_\tau + \gamma A A_\xi + \delta(D(A))_\xi = O(\varepsilon), \tag{2.27}$$

where γ and δ represent constant coefficients of nonlinearity and dispersion dependent on the ambient environment and where the operator $D(A)$ is determined by matching with the non-separable solution in the upper region and $0 < \varepsilon \leq 1$ is a perturbation representing a ratio between vertical and horizontal scales. In the upper region internal wave motions are described to leading order by a Helmholtz equation in ϕ with cutoff wavenumber, defining the wavenumber spectrum for ducted modes, given by

$$\hat{\alpha} = \frac{N_\infty}{|U_\infty - c|}, \tag{2.28}$$

where N_∞ is the constant Brunt-Väisälä frequency in the upper region, U_∞ is the constant background wind and c is the linear long wave phase speed at which the coordinate system is moving. A radiation condition $\phi \to 0$ in the limit $z \to \infty$ is applied.

An important result from the work of Maslowe and Redekopp, which is directly related to the definition of $\hat{\alpha}$, is that for a waveguide layer with characteristic frequency N_0 beneath an unbounded domain with characteristic frequency N_∞ when shear is absent (or sufficiently weak so that $U'' \approx 0$), ducting of long waves is only possible when

$$a/L \geq O(N_\infty/N_0), \tag{2.29}$$

where a is the wave amplitude and L the length scale of the waveguide (ie scale linear long wave speed in the waveguide is $N_0 L$). When a wave amplitude becomes too small to satisfy (2.29) it will be dispersed.

Making use of appropriate stretched spatial and time coordinates ξ, ζ and τ, moving at the linear long wave speed c_0, usually defined by

$$\xi = \varepsilon(x - c_0 t), \qquad \tau = \varepsilon^2 t, \qquad \zeta = \varepsilon z, \tag{2.30}$$

where ε is a small perturbation, wave solutions that include radiative decay can be found in terms of a streamfunction ψ by defining the following problem

$$\begin{aligned} (\partial^2_{\xi\xi} + \partial^2_{\zeta\zeta} + \hat{\alpha}^2)\psi &= 0, \\ \psi(\xi, \zeta = 0, \tau) &= A(\xi, \tau), \end{aligned} \tag{2.31}$$

where $A(\xi, \tau)$ represents a localized wave packet, and $\hat{\alpha}$ is a cutoff wavenumber as defined above by (2.28) (so that the problem is limited to a shear free ambient wind profile). This is then solved by specifying a radiation condition for ψ. This radiation condition requires $\psi \to 0$ as $\zeta \to \infty$ and that there is no incoming wave energy from infinity. The later requirement can be achieved by eliminating all Fourier components of a wave motion that correspond to downward energy transfer. The equations defined by (2.31) define a well known problem in 2D stratified flow over topography (see Baines (1996) for details). This problem can be solved using Fourier methods where a transform function $\hat{\psi}$ is defined as

$$\hat{\psi}(k, \zeta, \tau) = \int_{-\infty}^{\infty} \psi(\xi, \zeta, \tau) e^{-ik\xi} d\xi, \tag{2.32}$$

$$\psi(\xi, \zeta, \tau) = \frac{1}{2\pi} \int_{-\infty}^{\infty} \hat{\psi} e^{ik\xi} dk. \tag{2.33}$$

Maslowe and Redekopp (1980) give a solution to the problem (2.31), where the boundary condition at $\zeta = 0$ is defined for $c < U$ (for $c > U$ the opposite choice of sign in the exponents

for $-\hat{\alpha} < k < \hat{\alpha}$ applies), that also satisfies the radiation condition such that

$$\hat{\psi}(k,\zeta,\tau) = A(k,\tau)\begin{cases} \exp[-\zeta(k^2-\hat{\alpha}^2)^{\frac{1}{2}}] & \text{if } |k| > \hat{\alpha} \\ \exp[i\zeta(\hat{\alpha}^2-k^2)^{\frac{1}{2}}] & \text{if } 0 < k < \hat{\alpha} \\ \exp[-i\zeta(\hat{\alpha}^2-k^2)^{\frac{1}{2}}] & \text{if } -\hat{\alpha} < k < 0 \end{cases} \tag{2.34}$$

Applying the inverse transform and a limit $\zeta \to 0$ Maslowe and Redekopp derive the following matching condition[2]

$$\begin{aligned} \lim_{\zeta\to 0}\psi \;=\; & A(\xi,\tau) - \frac{\hat{\alpha}\zeta}{2}\,{}^{*}\!\int_{-\infty}^{\infty}\left\{\frac{Y_1(\hat{\alpha}|\xi-\xi'|)}{|\xi-\xi'|} + \operatorname{sgn}(U-c)\frac{\mathbf{H}_1(\hat{\alpha}|\xi-\xi'|)}{\xi-\xi'}\right\}A(\xi',\tau)d\xi' \\ & + \frac{1}{2}\zeta^2(A_{\xi\xi}+\hat{\alpha}^2A) + O(\zeta^3), \end{aligned} \tag{2.35}$$

The first term in the integrand contains $Y_1(x)$ which is a Bessel function of the second kind of order 1. From (2.34) decay in the outer region occurs for $|k| > \hat{\alpha}$. The solution for $|k| > \hat{\alpha}$ with $\hat{\alpha}$ very small is similar to the potential like flow that would exist if $N_\infty = 0$. The function $Y_1(x)$ describes potential like flow in the outer region when the solution matching is imposed. Maslowe and Redekopp assume that the dominant contribution comes from the neighborhood of the singularity and then apply the approximation

$$\frac{\hat{\alpha}}{2}\,{}^{*}\!\int_{-\infty}^{\infty}\frac{Y_1(\hat{\alpha}|\xi-\xi'|)}{|\xi-\xi'|}A(\xi',\tau)d\xi' \approxeq \frac{\partial}{\partial\xi}\left\{\mathcal{H}(A(\xi,\tau))\right\}, \tag{2.36}$$

where the approximate term is the same solution that would exist if the outer region is homogeneous (hence the disappearance of $\hat{\alpha}$) with the radiation condition applied. The error in this approximation is given as $O(\hat{\alpha})$ by Maslowe and Redekopp for weak stratification in the outer region.

The second term in the integrand contains $\mathbf{H}_1(x)$ which is a Struve function of order 1. This second term takes account of the wave drag that is present due to internal waves supported by the ambient medium. As described by Baines (1996) for fixed topography, there is a horizontal drag force due to the pressure acting along the surface defined by $A(\xi,\tau)$. When $0 < k < \hat{\alpha}$ the total pressure is increased on the upslope side of the surface and decreased on the downslope side. In the solutions represented by (2.34) the topographic surface is a wave profile $A(\xi,\tau)$ that may depend slowly on time. There is no direct coupling of the effect of reduction of wave speed by a horizontal drag force and the corresponding change in wave amplitude. The contribution of the second term in the integrand is proportional to $\hat{\alpha}$ and vanishes when there is no stratification in the outer region.

It is now possible to derive an evolution equation for wave amplitude under radiation by evaluating the matching operator $D(A)$ in equation (2.27). Maslowe and Redekopp give D(A)

[2] ${}^{*}\!\int$ is the Hadamard finite part of the integral (see Hadamard, 1923)

as:

$$D(A) = \frac{\partial}{\partial \xi}\mathcal{H}(A) - \frac{\hat{\alpha}}{2}\mathrm{sgn}(U_\infty - c)\int_{-\infty}^{\infty} \frac{\mathbf{H}_1(\hat{\alpha}|\xi - \xi'|)}{\xi - \xi'} A(\xi', \tau)d\xi'. \tag{2.37}$$

Replacing the Struve function $\mathbf{H}_1$ with its integral representation allows the equation to be expressed as

$$A_\tau + \gamma A A_\xi + \delta \frac{\partial^2}{\partial \xi^2}\mathcal{H}(A) = \tag{2.38}$$
$$-\frac{\delta}{\pi}\mathrm{sgn}(U_\infty - c)\int_{-\infty}^{\infty} A(\xi', \tau)\int_0^{\hat{\alpha}} k(\hat{\alpha}^2 - k^2)^{\frac{1}{2}}\cos[k(\xi - \xi')]dkd\xi'.$$

This evolution equation can be seen as a generalization of the BDO equation and reduces to the standard BDO equation when the RHS is zero.

For radiative damping of solitary waves Maslowe and Redekopp assume that $A(\xi, \tau)$ represents a localized wave packet which satisfies (2.37) and define the volume of the wave packet (because the calculation is 2D the volume here is only defined in 2 dimensions and is not the physical volume) as $< A >$ and show that it is subject to the conservation identities:

$$\frac{\partial}{\partial \tau} < A > \;=\; \frac{\partial}{\partial \tau}\int_{-\infty}^{\infty} A(\xi, \tau)d\xi \qquad = 0, \tag{2.39}$$

$$\frac{\partial}{\partial \tau} < A^2 > \;=\; \frac{-2|\delta|}{\pi}\int_0^{\hat{\alpha}} k(\hat{\alpha}^2 - k^2)^{\frac{1}{2}}|F(k, \tau)|^2 dk, \tag{2.40}$$

where $F(k, \tau)$ represents the Fourier transform of $A(\xi, \tau)$. The first corresponds to volume conservation and the second gives an energy decay law. This second conservation terms corresponds to the term used to described a wave drag force on fixed topography in Baines (1996). In Baines (1996) it is explained that obstacle shapes which have a significant part of their wavenumber spectrum close to $k \approx \hat{\alpha}/\sqrt{2}$ tend to be subject to relatively large drag and that long objects (such that $\hat{\alpha}a/h \gg 1$ with $|F(k, \tau)|$ small unless $k \ll \hat{\alpha}$) experience relatively small wave drag.

Maslowe and Redekopp (1980) find a solitary wave solution to a special adiabatic deep fluid case governed by the above conservation identities and show that deep fluid solitary waves decay linearly (with $a/h \propto \tau$) for modest wave amplitude and asymptotically approach an algebraic decay (with $a/h \propto \tau^{-1}$) as wave amplitude becomes small (see Appendix A for solution details). It must be remembered that τ represents a slow time coordinate so that any analysis is made under the assumption that the time scale of decay will be long relative to the time taken for a wave to travel a distance comparable to one wavelength. Pereira and Redekopp (1980) present some solutions to an initial value problem for a special adiabatic case derived from (2.39) and (2.40) with $\delta = 1$. Their results are subject to a number of approximations. This includes a small perturbation approximation in terms of ε, the special adiabatic case de-

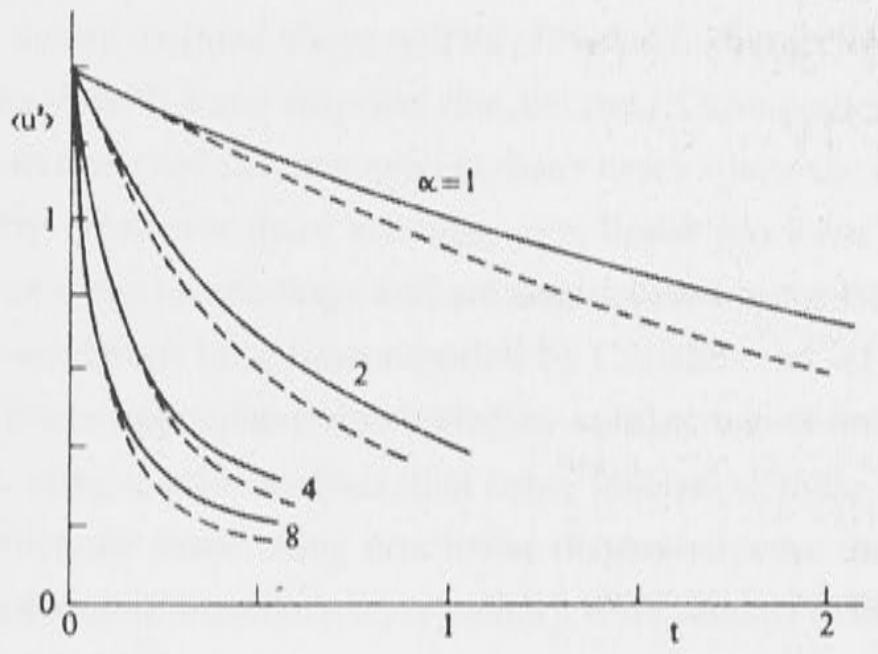

Figure 2.1: Radiative decay curves for different values of $\hat{\alpha}$ (Pereira and Redekopp, 1980)

scribed above, and the assumption that each Fourier mode (ie in the wavenumber spectrum) of a solitary wave profile is independently affected by the degree of damping. Given these approximations their results indicate that a value of α corresponding to strong damping can cause the solitary wave shape to undergo distortions in its shape and to form into several waves where according to the dispersion relation for weakly nonlinear waves the wave amplitude of each wave will be proportional to the wave speed. Their amplitude decay solutions to the initial value problem are displayed in Fig 2.1.

A limitation of results such as those of Pereira and Redekopp (1980) presented above is that there must be a fixed scaling relationship between the wave amplitude a and wavelength λ, for the special adiabatic case solved, to reduce the relevant equations to an initial value problem. Although an approximate relation between these wave properties can often be specified for cases within the framework of weakly non-linear theory (generally with a set of constraints), such an approach is limited in its application to waves in geophysical environments and is not expected to apply to highly non-linear waves where the relationship between amplitude and wavelength is more complicated.

2.8 Mathematical models compared to observations

Long atmospheric gravity waves usually fall into the deep fluid wave category. As it stands the BDO equation (2.10) (described above) is directly applicable to the description of small amplitude waves in a homogeneous waveguide embedded in a neutrally stratified fluid of infinite extent. Realistic flow conditions in the atmosphere usually involve spatially and temporally varying waveguides, wave amplitudes that can exceed the limitations of weakly non-linear the-

ory and effects such as variable background shear. Some brief comparisons between observed phenomena and the theory outlined above will be provided in this section. As mentioned earlier researchers have found, with some surprise, that the the BDO equation can provide a reasonable approximation to observed features even in many cases where the equation is used outside its domain of validity. However there are many non-linear processes in the atmosphere that have strong effects on wave morphology and are not included in the BDO description.

A number of observations have been reported by Christie et al. (1979) of nonlinear wave disturbances in the lower troposphere dominated by solitary waves initiated from density currents. They showed, using a scale analysis, that many features of these waves are in qualitative agreement with predictions made using non-linear dispersive wave theory. In particular they observed that the evolution of boundary layer solitary waves seems to be described by the BDO equation.

Another noteworthy comparison of Benjamin's theory for internal solitary waves with observations of atmospheric solitary waves has been reported by Noonan and Smith (1984). They assumed a waveguide layer (depth h) of stably stratified Boussinesq fluid which lies beneath an unbounded upper layer which is neutrally stable. Noonan and Smith extend Benjamin's theory to include a shear term $U(z)$ in the lower layer and define the upper layer as a uniform flow $U(h)$. Calculations of the wave speed were made by numerically integrating the vertical modal function ϕ and these were then compared to their observational data. They investigated the sensitivity of the linear long wave speed to changes in h both with and without wind shear. They conclude that the value of h that one would choose based on a visual inspection of the stability profile provides a prediction of linear long wave speed that is considerably less than the observed value. This was taken by Noonan and Smith to imply that the calculated wave speed is sensitive to h in this range and the static stability immediately above this region is not negligible. With a value of h greater than that based on a visual assessment the calculated linear long wave speed gives good agreement with the observed speeds and weakly non-linear theory gives values that are no improvement. They conclude that the inclusion of the wind data gives only slight improvements to the theoretical predictions. Prediction of wave half-widths yielded values 2-3 times those observed, but there was some uncertainty in the determination of wave half-widths from observations. Thus the overall conclusion was that the BDO theory, although providing results that where reasonable to some degree, failed to predict the wave half-width with any accuracy using the chosen h. This suggests that the observed waves where highly non-linear in nature.

Rottman and Einaudi (1993) consider two well-documented observations of atmospheric solitary waves. In the first case, the waves propagate on boundary layer waveguides in the lower troposphere and in the second case, the solitary waves have scales which are comparable to the depth of the entire troposphere. They compare these observations with idealized weakly non-linear models of the respective flow configurations and focus on the importance of properly

determining properties of the waveguide layer such as effective depth. This is a difficulty that has been commented on by many authors (e.g., Noonan and Smith (1984)). Although weakly nonlinear BDO theory appears to be accurate up to wave amplitudes of about half the waveguide depth, in practice, it is hard to determine accurate waveguide properties from field data.

Rottman and Einaudi (1993) also examine the effect of wave trapping in the atmosphere. Crook (1986,1988) uses the Scorer parameter (2.26) to examine three different mechanisms of trapping of low-altitude gravity waves. The relevant equation is the familiar Taylor-Goldstein equation (under the Boussinesq approximation) governing wave motion in a continuously stratified fluid: $d^2w/dz^2 + m^2w = 0$. Here, it is assumed that since $m^2 = l^2 - k^2$ (where k is the horizontal wavenumber, and l is the Scorer parameter) must be positive for upward propagation of energy, at some height it becomes negative so that wave energy from lower-levels will be reflected thus trapping energy below a certain height. The three mechanisms are (i) the case when N^2 (N is the buoyancy frequency) above the waveguide layer decreases with height, (ii) there is an opposing flow that increases vertically in strength and (iii) the curvature in the wind profile decreases vertically. Crook (1988) provides numerical simulations of these different cases and attributes the long life-time of the Morning Glory solitary waves to the third case. Skyllingstad (1991) studied the effect of critical layers (where the background wind speed is equal to the wave speed) on solitary and cnoidal gravity wave propagation and found that if a region with strong stratification exists below the critical layer, then the wave energy will be dissipated. Skyllingstad (1991) shows that for a gradient Richardson number above but in the vicinity of the well known critical stability value of 0.25 (from linear theory for instability of a shear flow), there is a reflection of the wave energy and thus energy is trapped below the height of the critical layer. If the stability below the layer has Richardson number less than 0.25 then over-reflection can occur and the wave can actually gain energy. Rottman and Einaudi (1993) propose that the trapping mechanism that allows large scale atmospheric solitary waves to propagate for long distances is due to internal wave critical layers that reflect wave energy. Rottman and Einaudi (1993) also found that weakly non-linear theory provides only an approximate description of the properties of atmospheric solitary waves.

Meteorological observations of solitary-like waves in the nocturnal boundary layer have also been made by Cheung and Little (1990). They investigated the properties of solitary waves propagating on a stable nocturnal boundary layer inversion. Such stable layers commonly act as waveguides for solitary waves in the atmosphere. It was found that although BDO theory provided a satisfactory description for non-dimensional amplitudes $a/h < 1$, when a/h increases beyond 1 the waves became strongly non-linear and BDO theory begins to break down. Four of the five short duration disturbances observed by Cheung and Little (1990) appeared to be solitary waves with recirculating fluid ($a/h > 1$) and this supports the need for a fully non-linear treatment of these types of wave disturbances.

Chapter 3

A fully compressible, non-hydrostatic numerical model

3.1 Origins and model philosophy

The numerical model which will be presented in this chapter is designed to represent two-dimensional fully compressible, non-hydrostatic flow in the atmosphere. The governing equations of this model provide an relatively accurate representation of atmospheric flow at the typical pressures, densities and length scales of mesoscale dynamics. Finite difference methods are used to formulate a stable numerical representation of these equations. In designing the finite difference form of this model the governing philosophy has been to make no unnecessary approximations (beyond 2-dimensionality), favoring an algorithm that is computationally expensive but free of complicated parameterization schemes. The finite difference methods used to achieve this have a long history of development in atmospheric numerical models presented by previous researchers. Many features of the model chosen have origins in the numerical atmospheric models formulated by Mitchell and Hovermale (1977), Klemp and Wilhelmson (1978), Droegemeier and Wilhelmson (1987) and Brown (1995). Like these predecessors, the model described here solves a set of finite difference equations on a mesh representing a particular flow domain with imposed boundary conditions. The following gives a brief genealogy of the key features that are utilized in of the numerical algorithm.

Mitchell and Hovermale (1977) chose to use a general non-hydrostatic fully compressible model with parameterized evaporation to simulate a severe thunderstorm gust front. They included linear diffusivity to provide stability but no explicit formulation for turbulent processes. In contrast, the numerical model developed by Klemp and Wilhelmson (1978) to model three-dimensional convective storm dynamics implemented an explicit parameterization of the subgrid microphysics to represent turbulence. They solved a time-dependent turbulence energy equation which depends on local buoyancy, shear and dissipation and to which they applied first order closure. Their model used a splitting process for the timestep which treated sound waves (for reasons that will be explained below) separately. Droegemeier and Wilhelmson

(1987), following Mitchell et al. (1977), performed a numerical simulation of thunderstorm outflow dynamics using effectively inviscid equations with numerical damping which behaves as a first order approximation to eddy viscosity. Thus, the model is not truly inviscid and this, coupled with high spatial resolution, allowed them to explicitly represent turbulent processes without the use of subgrid parameterizations. They performed most of their numerical experiments using a quasi-compressible model that treats sound waves separately, and made a few comparisons of computational accuracy with a fully compressible model finding large integrated differences in domain averaged kinetic energy but minor qualitative differences. The approach implemented here inherits its formulation from this technique. The method will rely on sufficiently high spatial resolution to resolve large scale turbulent processes and use a linear eddy diffusivity term to ensure stability at the smallest scales. The fully compressible non-hydrostatic equations will then be solved numerically without any further approximations. A key advantage of this type of model, in terms of computational efficiency, over that of many other atmospheric models, is that it avoids a Poisson type equation in the formulation of a governing equation for pressure. Instead all governing equations are of prognostic form (ie a system of equations in terms of the time derivatives of the variable fields) and thus it is not necessary to have to solve a complicated elliptic PDE equation at each time step which can be very costly for a numerical scheme.

Turbulent processes in atmospheric models are often parameterized using some form of closure scheme based on the turbulent kinetic energy, vorticity, or local velocity deformation. What must be kept in mind in the use of such schemes is that they only provide rough approximations to the real physical small scale processes and generally require a substantial increase in the number of prognostic equations. The increase in the number of equations leads to an increased computational demand which can be very restrictive especially when considering the accuracy of the underlying approximations. These questions in relation to the accuracy of a turbulence modeling scheme and its ability to faithfully represent the small scale physical mixing processes in the atmosphere, are particularly relevant in 2D models where there is a upscale propagation of turbulent energy as apposed to the downscale transfer in 3D models (there are some experiments by Maxworthy (1980) which seem to verify this upscale transfer in the laboratory). The problems inherent in the numerical representation of energy transfer by sub-grid processes must be considered in the choice of grid resolution. A judicious choice of grid resolution based on the scales of interest attempts to provide reasonable accuracy under the assumption that smaller scales (subgrid) will contain relatively small amounts of energy. However dissipation due to thermodynamical terms present in the numerical model used here will eventually lead to downscale transfer of energy. To remove this energy from the model and avoid numerical instability some form of weak subgrid dissipation is required. Because of the problems associated with sub-grid parameterization, it has been decided here to make no unnecessary approximations of this type and instead rely on the high spatial resolution of

the numerical scheme and a weak subgrid dissipation term to represent the effects of turbulent processes. By adopting such an approach it is necessary to have a clear idea of the scales of motion that are of interest and to realize that there will be smaller scales which will remain unresolved in the numerical model. The choice to avoid parameterization of sub-grid turbulent processes is discussed further in Section 3.6 which examines the role of sub-grid dissipation in the model.

No mention has been made so far of moisture and precipitation, both of which may play important roles in real thunderstorm downdrafts and outflows. It is assumed that dynamical processes have the most influence on the evolution of the outflow, dominating the moist microphysical processes that are generally more important in the formation process for outflows and other surface flow phenomenon. Hence, moisture and precipitation processes will not be included at this stage and the model represents a dry atmosphere. Because a fully three dimensional model is impractical under the computational resources available at the present time, and a purely two dimensional study is considered, slab symmetry has been chosen which allows the inclusion of wind shear processes. It also provides added simplicity by eliminating the effects of geometric distortion on wave morphology. Furthermore, thunderstorm downdrafts that are approximately slab symmetric do occur on occasion.

3.2 Governing equations

In the derivation of a set of governing equations the following terms are used to describe the relevant variables:

$\mathbf{u}$ is the ensemble averaged velocity,

p is the pressure,

ρ is the density,

θ is the potential temperature,

S_θ is a thermodynamic heat source term,

$\mathbf{F}$ is a term representing any external body force (per unit mas s),

T is the absolute temperature,

R is the gas constant of dry air,

χ is a term representing any net internal frictional forces including molecular and turbulent viscosity.

The governing equations have been chosen as follows: we start with the following formulation of the full ensemble-averaged Navier-Stokes equations:

$$\frac{\partial \mathbf{u}}{\partial t} = -\mathbf{u}\cdot\nabla\mathbf{u} - \frac{1}{\rho}\nabla p + \mathbf{F} + \frac{1}{\rho}\chi, \tag{3.1}$$

together with the mass continuity equation,

$$\frac{\partial \rho}{\partial t} + \nabla\cdot(\rho\mathbf{u}) = 0, \tag{3.2}$$

a relationship for the thermodynamic conservation of heat,

$$\frac{d\theta}{dt} = S_\theta, \tag{3.3}$$

and an equation of state,

$$p = \rho RT \tag{3.4}$$

The numerical form of the above equations will only be able to represent a finite range of scales. Because of the limitation of this finite grid size, ensemble averaging has been used for the governing flow equations, so that the model can be statistically independent of small scale random variations due to turbulent or molecular effects.

These equations are now recast in a more computationally efficient form. Prognostic fully compressible equations are used that describe both sound and gravity wave solutions. Such a set of equations requires restrictions on the timestep imposed by the sound wave modes (which are of limited interest for larger scale meteorological studies but important for computational stability), but allows the set of governing equations to be written in flux-conservative form. Fully prognostic equations are particularly useful in that changes to boundary conditions and grid structure can be made without changing the set of solution equations.

In the formulation used here it was decided to retain three components of the velocity field, but with a 2-D flow field. Thus only the two dimensional properties of the flow need to be treated directly. This means that all variables are assumed independent of the third dimension (this idea has been used by Holloway, 1984), but allows the treatment of the effects of rotation in terms of the Coriolis force without the computational expense of fully three dimensional modeling. In the simulations presented here, the Coriolis force is set to zero, but may be incorporated in future work.

In order to transform (3.1) into flux conservative form, the continuity equation (3.2) is used to write (3.1) as a set of equations:

$$\frac{\partial u}{\partial t} = -\frac{\partial(uu)}{\partial x} - \frac{\partial(uv)}{\partial y} - \frac{\partial(uw)}{\partial z} - \frac{1}{\rho}\frac{dp}{dx} - fv + \frac{1}{\rho}\chi_1, \tag{3.5}$$

$$\frac{\partial v}{\partial t} = -\frac{\partial (uv)}{\partial x} - \frac{\partial (vv)}{\partial y} - \frac{\partial (wv)}{\partial z} - \frac{1}{\rho}\frac{dp}{dy} + fu + \frac{1}{\rho}\chi_2, \tag{3.6}$$

$$\frac{\partial w}{\partial t} = -\frac{\partial (uw)}{\partial x} - \frac{\partial (vw)}{\partial y} - \frac{\partial (ww)}{\partial z} - \frac{1}{\rho}\frac{dp}{dz} + \kappa g + \frac{1}{\rho}\chi_3, \tag{3.7}$$

where f has been used to represent the Coriolis forces, and κg the gravitational force.

It remains therefore to find conservative forms of (3.3) and (3.4). This will result in the use of an equation for pressure (as implemented from the outset by some researchers in place of an energy equation) coupled to an equation for temperature. A compromise on strict conservation must be made in the formulation of the equation for pressure to achieve a complete set of prognostic equations. This approach also eliminates the need for an explicit equation for density, relying on (3.5), (3.6), (3.7) and the coupled equations for temperature and pressure to define the governing set of equations.

It becomes necessary at this point to differentiate between a variable's base state (for this model, hydrostatic) and its perturbation field. Apart from the velocity variables, the other variables in this model are expressed as a sum of their hydrostatic component and their perturbation component. This means we have density, potential temperature and pressure defined as follows:

$$\rho = \bar{\rho} + \rho', \tag{3.8}$$

$$\theta = \bar{\theta} + \theta', \tag{3.9}$$

$$p = \bar{p} + p'. \tag{3.10}$$

Potential temperature θ is defined as the temperature assumed by an air parcel if compressed adiabatically to the reference pressure $p_0 = 1000$ mb. Using the equation of state gives

$$\frac{\theta}{T} = \left(\frac{p_0}{p}\right)^{\frac{R_d}{C_p}}, \tag{3.11}$$

where C_p is the specific heat of dry air at constant pressure, and R_d is the gas constant for dry air. For potential temperature the perturbation field can be expressed as a prognostic equation as follows:

$$\frac{\partial \theta'}{\partial t} = -u\frac{\partial \theta'}{\partial x} - v\frac{\partial \theta'}{\partial y} - w\frac{\partial \theta'}{\partial z} - w\frac{\partial \bar{\theta}}{\partial z} + S_\theta. \tag{3.12}$$

It should be noted that this equation is written in advective form. This is done out of necessity to provide independence from the pressure equation to be formulated in flux conservative form (the two being mutually exclusive). To this end it is convenient to define pressure in terms of

the Exner function:

$$\Pi = \left(\frac{p}{p_0}\right)^{\frac{R_d}{C_p}}. \tag{3.13}$$

In terms of potential temperature we now have the equation of state,

$$\Pi = \left(\frac{R_d \rho\theta}{p_0}\right)^{\frac{R_d}{C_v}}, \tag{3.14}$$

where C_v is the specific heat of dry air at constant volume. This allows us to write the pressure gradient terms as:

$$\frac{\partial p}{\partial(.)} = \rho\theta C_p \frac{\partial \Pi}{\partial(.)}. \tag{3.15}$$

A common governing equation for pressure used by many previous modelers (eg. Kentzner, 1970b, Roache, 1985) is

$$\frac{\partial p}{\partial t} = -\mathbf{u}\cdot\nabla p - \gamma p\,(\nabla\cdot\mathbf{u}). \tag{3.16}$$

Together with the above equation of state, this allows a prognostic equation for the perturbation Exner function Π' valid for an adiabatic fluid to be written as

$$\frac{\partial \Pi'}{\partial t} = -\mathbf{u}\cdot\nabla\Pi' - (\gamma-1)(\bar{\Pi}+\Pi')\nabla\cdot\mathbf{u} + \frac{c_s^2}{C_p(\bar{\theta}+\theta')^2}\left(\frac{d\theta'}{dt} + w\frac{\partial\bar{\theta}}{\partial z}\right) - w\frac{\partial\bar{\Pi}}{\partial z}, \tag{3.17}$$

where $c_s = \sqrt{C_p R_d \Pi\theta / C_v}$ is the local sound speed and $\gamma = C_p/C_v$ is the ratio of specific heats. As a result of the above steps, it is now possible to present the following set of governing prognostic equations:

$$\frac{\partial u}{\partial t} = -\frac{\partial(uu)}{\partial x} - \frac{\partial(uv)}{\partial y} - \frac{1}{\bar{\rho}}\frac{\partial(\bar{\rho}uw)}{\partial z} - C_p\theta\frac{\partial\Pi'}{\partial x} - fv, \tag{3.18}$$

$$\frac{\partial v}{\partial t} = -\frac{\partial(uv)}{\partial x} - \frac{\partial(vv)}{\partial y} - \frac{1}{\bar{\rho}}\frac{\partial(\bar{\rho}wv)}{\partial z} - C_p\theta\frac{\partial\Pi'}{\partial y} + fu, \tag{3.19}$$

$$\frac{\partial w}{\partial t} = -\frac{\partial(uw)}{\partial x} - \frac{\partial(vw)}{\partial y} - \frac{1}{\bar{\rho}}\frac{\partial(\bar{\rho}ww)}{\partial z} - C_p\theta\frac{\partial\Pi'}{\partial z} + g(\frac{\theta}{\bar{\theta}} - 1), \tag{3.20}$$

$$\frac{\partial \theta'}{\partial t} = -u\frac{\partial\theta'}{\partial x} - v\frac{\partial\theta'}{\partial y} - w\frac{\partial\theta'}{\partial z} - w\frac{\partial\bar{\theta}}{\partial z} + S_\theta, \tag{3.21}$$

$$\frac{\partial \Pi'}{\partial t} = -\mathbf{u}\cdot\nabla\Pi' - (\gamma-1)(\bar{\Pi}+\Pi')\nabla\cdot\mathbf{u} - w\frac{\partial\bar{\Pi}}{\partial z} \tag{3.22}$$

$$+\frac{c_s^2}{C_p(\bar{\theta}+\theta')^2}\left(\frac{d\theta'}{dt}+w\frac{\partial\bar{\theta}}{\partial z}\right),$$

where the inclusion of $\bar{\rho}$ in the vertical derivative terms is made to improve flux conservation (see Chen, 1980).

3.3 Conservation properties

With the exception of the equation for potential temperature, the governing equations have now been recast with their advective components in flux conservative form. The properties of this new form can be demonstrated by considering the advective components of the velocity equations. Consider,

$$\frac{\partial u_i}{\partial t}=-\frac{\partial(u_i u)}{\partial x}-\frac{\partial(u_i v)}{\partial y}-\frac{1}{\bar{\rho}}\frac{\partial(\bar{\rho}u_i w)}{\partial z}, \tag{3.23}$$

which can be written as $\partial(\bar{\rho}u_i)/\partial t=-\nabla\cdot(\bar{\rho}\mathbf{u}u_i)$. Integrating over some closed volume V gives

$$\int_V\frac{\partial(\bar{\rho}u_i)}{\partial t}dV=\int_V-\nabla\cdot(\bar{\rho}\mathbf{u}u_i)dV. \tag{3.24}$$

Using Gauss's theorem, this can be expressed as

$$\frac{\partial}{\partial t}\left(\int_V(\bar{\rho}u_i)dV\right)=-\int\int_S(\bar{\rho}\mathbf{u}u_i)\cdot\mathbf{n}dS. \tag{3.25}$$

This states that the rate of change of the quantity $\bar{\rho}u_i$ over the closed volume V is equal to the net advective flux rate of the same quantity through the surface S which bounds V. In other words, this can be taken as a statement of conservation of momentum in any of the respective i-th coordinate directions. In terms of energy conservation, after the transformation to a flux conservative form of the appropriate equations, total energy is almost conserved by the resulting system but not necessarily for the finite difference approximation. The finite difference equations exhibit a quasi-quadratic conservation of the spatial difference terms for a closed or periodic domain. However, for the boundary conditions described in the next chapter the total energy is not completely conserved due to the use of open rather than closed or periodic boundaries and also due to energy loss from the domain as a result of diffusion processes (to be outlined below). The property of conservation of momentum in the individual coordinate directions does hold however for the finite difference form of the equations. Flux conservative forms also have benefits in terms of computational stability. Use of quadratic conservation terms is advantageous from this perspective using the idea that stability can be maintained if finite difference forms are designed to conserve the integral of the quadratic quantities (Piacsek and Williams, 1970). The use of diffusivity terms (defined below) means

that the scheme used here is not strictly conservative in this sense, but together with a method of dissipating subgrid energy the conservative forms help in successfully suppressing growth of computational instability without damping wave amplitudes. However it should be noted that relaxation of strict conservation in this fashion will possibly result in small phase errors.

3.4 Finite difference form

With the preceding ideas in mind, second order centered finite difference operators will be used to represent all the spatial differences in the model. This means there will be a discretization of equations onto a mesh defined by the discrete set of points:

$$x_i = x_0 + i\Delta x, \qquad i = 0,..,nx \tag{3.26}$$

$$z_j = z_0 + j\Delta z, \qquad j = 0,..,nz \tag{3.27}$$

which will result in a 2D nx by nz mesh with grid spacing given by Δx and Δz. A staggered mesh will allow variables to be assigned at points that are defined using half grid spacing. (eg $\Delta x/2$) In the choice of mesh structure, it has been decided here to utilize a standard Cartesian staggered mesh of the type commonly deployed in atmospheric cloud models (see Fig 3.1), with the thermodynamic variables (θ, Π) in the center and the velocity variables (u,v,w) on the side corresponding to the direction they act in. This choice of grid orientation provides increased accuracy for mass variables compared to an unstaggered grid, which can be an important consideration for the types of atmospheric flow studied. However the stability criteria for the timestep, on this staggered grid, is restricted by an additional factor of two over that for the unstaggered case.

A finite difference operator notation has been developed by Lilly (1965):

$$\partial_{n\xi}\phi(\xi) = \frac{\phi(\xi + n\Delta\xi/2) - \phi(\xi - n\Delta\xi/2)}{n\Delta\xi}, \tag{3.28}$$

$$\overline{\phi(\xi)}^{n\xi} = \frac{\phi(\xi + n\Delta\xi/2) + \phi(\xi - n\Delta\xi/2)}{2}, \tag{3.29}$$

where ϕ is the dependent variable field, ξ is a independent variable and $n\Delta\xi$ is the mesh interval over which differencing takes place. This means that, for example, $\partial_{2x}\phi(x,z)$ describes finite differencing based on the RHS of (3.28) with the choice of $n = 2$ so that differencing takes place over a mesh interval of $2\Delta x$. In using the above operators the staggered grid arragement shown in Fig 3.1 must be taken into account so that relative to variables θ, Π and v at a mesh point ξ, the horizontal velocity u is offset by $\xi - \Delta x/2$ and the vertical velocity w by $\xi - \Delta z/2$.

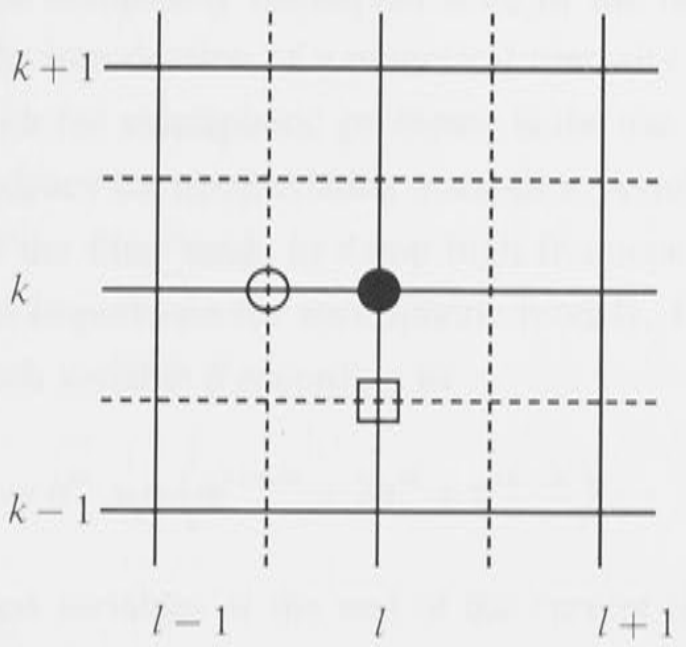

Figure 3.1: Structure of a mesh cell; $\diamond$ is $w_{i,j}$, $\circ$ is $u_{i,j}$, $\bullet$ is $\theta_{ij}, \Pi_{i,j}, v_{i,j}$.

Using this notation, the finite difference equations to be solved are

$$\partial_{2t} u + \partial_x(\bar{u}^x \bar{u}^x) + \partial_z\left(\frac{\overline{\bar{\rho} w}^x \bar{u}^z}{\bar{\rho}}\right) + C_p(\bar{\theta} + \frac{\Delta x}{2}\partial_x\theta')\partial_x\Pi' + f\bar{v}^x = 0, \qquad (3.30)$$

$$\partial_{2t} v + \partial_x(\bar{u}^x \bar{v}^x) + \partial_z\left(\frac{\overline{\bar{\rho} w}^x \bar{v}^z}{\bar{\rho}}\right) - f\bar{u}^x = 0, \qquad (3.31)$$

$$\partial_{2t} w + \partial_x(\bar{u}^z \bar{w}^x) + \partial_z\left(\frac{\overline{\bar{\rho} w}^z \bar{w}^z}{\bar{\rho}}\right) + C_p(\bar{\theta} + \frac{\Delta z}{2}\partial_z\theta')\partial_z\Pi' - g\frac{\overline{\theta'}^z}{\bar{\theta}} = 0, \qquad (3.32)$$

$$\partial_{2t}\theta' + \overline{u\partial_x\theta'}^x + \frac{\overline{\bar{\rho} w \partial_z\theta'}^z}{\bar{\rho}} + \bar{w}^z\frac{d\bar{\theta}}{dz} = 0, \qquad (3.33)$$

$$\partial_{2t}\Pi' + \bar{u}^x\partial_{2x}\Pi' + \bar{w}^z\partial_{2z}\Pi' + (\gamma - 1)(\bar{\Pi} + \Pi')[\partial_x u + \partial_z w] + \qquad (3.34)$$
$$\frac{R(\bar{\theta} + \theta')(\bar{\Pi} + \Pi')}{C_v(\bar{\theta} + \theta')^2}[\partial_t\theta' + \bar{w}^z\frac{d\bar{\theta}}{dz}] - \bar{w}^z\frac{g}{C_p\bar{\theta}} = 0.$$

A higher than second order finite difference scheme would have provided greater accuracy and a reduction of phase errors (which may be important at smaller scales) but does not seem to justify the increase in complexity and large increase in computational resources.

3.5 Time stepping in a compressible model

Leapfrog time differencing, which has been proven in many models to be reliable, has been chosen for all numerical simulations. When dealing numerically with non-linear equations, the leapfrog method for second order time differencing may become unstable for large gradients.

This instability is due to the completely decoupled state of the odd and even mesh points, and is usually handled by the introduction of a numerical viscosity term that couples the two meshes. A common approach for atmospheric problems is the use of the Robert (1966) time filter which removes any tendency for mesh drifting instability. Asselin (1972) and Schlesinger et al. (1983) also note that the filter tends to damp high frequency sound waves which are generally of limited physical importance for atmospheric models. Each timestep is smoothed in our model by updating each variable ϕ according to:

$$\phi^t = \phi^{*t} + \alpha\left(\phi^{*t+\Delta t} - 2\phi^{*t} + \phi^{*t-\Delta t}\right), \tag{3.35}$$

where ϕ^* are the unsmoothed variables at the end of the current time step and α is a small positive number (0.1 is chosen for all simulations that follow).

In the use of time differencing, it is important to have some idea of the stability of the scheme based on the magnitude of the finite differencing resolution selected. Most numerical schemes are evaluated on the basis of time and spatial differencing errors for a propagating sinusoidal wave. The relative importance of each is usually represented by the Courant number $|\mu|$ which represents the ratio of the temporal resolution to the spatial resolution for a wave propagating at speed c. A well known stability condition is that $|\mu| \leq O(1)$ for any explicit difference scheme (Courant-Friedrichs-Lewy (CFL) stability condition). The fastest moving waves in the system determine the size of the largest allowable timestep. In this model the limiting wave speed is that of the sound waves. A CFL linear stability condition governing sound wave motion for the leapfrog scheme in a 2D finite difference model is:

$$\Delta t <= \frac{1}{2c}\left(\frac{1}{(\Delta x)^2} + \frac{1}{(\Delta z)^2}\right)^{-1/2}, \tag{3.36}$$

where c is the average sound speed (approx 350 m/s). For all the numerical simulations performed in this thesis a value of $\Delta t = 0.04$s was used which is well within the CFL stability regime. Time truncation errors become more significant when the stability provided by the faster moving wave modes is removed by the use of filtering. Durran (1990) proves that for oscillatory systems second order time differencing produces second-order phase speed errors and fourth-order amplitude errors. He shows that the Robert-Assellin filter reduces the accuracy of the truncation error of the unfiltered leapfrog scheme from $O[(\Delta t)^2]$ to $O(\Delta t)$ and that compared with the Adams-Bashford method which damps the solution in proportion to $(\omega\Delta t)^4$, Asselin time filtering results in $O[(\omega\Delta t)^2]$ dissipation. This means that for a sinusoidal traveling wave with $\omega\Delta t = \mu k\Delta x$ the use of such a temporal filter is equivalent to spatial damping of second order. Such a result indicates that when using a spatial damping term to suppress computational aliasing errors, use of a higher than order two operator (such as the fourth order operators commonly used in atmospheric models) to dampen the shortest wavelengths can

have its scale selectively reduced by Asselin time filtering. However, even though the leapfrog scheme is not ideal it is a reliable method that is generally faster and easier to implement than Adams-Bashford and other more complicated schemes. The most relevant aspect of the above results for this model, is that choice of higher than order two damping operator does not seem justified. Additional arguments are presented below to further support the choice of a second order operator in the model presented here.

The most significant factors in the choice of timestep are the restrictions imposed by the presence of different wave modes in the model. Most general disturbances to the model radiate a combination of sound and gravity wave modes. The most restrictive influence on the timestep are acoustic waves which have significantly higher propagation speeds than any other wave mode in the model. Though sound waves may be of limited importance for large scale atmospheric modeling they need to be included, for mesoscale models, to maintain stability and flux conservation. This means that a much smaller time step (often a factor of ten) must be used even though the wave motion being simulated can be adequately resolved with a larger timestep. Fast moving sound waves have strong implications for the boundary conditions used with the model (the subject of the next chapter). Such waves must be prevented from reflecting from boundaries to avoid an unphysical build up of energy inside the domain. This will be discussed in detail in the formulation of the lateral and upper boundary conditions.

3.6 Subgrid dissipation and suppression of aliasing

There is rarely high enough resolution because of computational limitations to cover the entire range of important spatial scales. This problem is generally dealt with by the addition of some form of sub-grid parameterization or dissipation in order to remove the smallest scale energy from the model. However this inevitably causes spurious computational aliasing instabilities which arise from the growth of computationally induced modes (usually the result of spurious nonlinear interaction of low wavenumber modes creating high wavenumber structure).

The two main approaches to this problem involve the use of sub-grid parameterization of the turbulence equations which describe the dissipation of energy at the smallest scales, or the use of some form of spatial background damping term. Without the use of some form of numerical background damping, energy is built up in the smallest scales and causes the whole model to become unstable. With sub-grid parameterization the aim is to account for the effects of sub-scale motion on the resolvable scales used in the model. This is generally achieved through the use of sub-grid turbulence equations. Often these turbulence equations are simplified with the aim of retaining the important features of the turbulence statistics. A common approach is to retain a time dependent turbulence energy equation that might depend on such things as local buoyancy, shear and dissipation. It is also necessary to have some sort

of closure scheme. Klemp and Wilhelmson (1978) use a first-order closure scheme applied to nearly conservative variables with eddy coefficients based on the computed turbulence energy. These closure techniques for sub-grid equations depend on the grid scale being within the inertial subrange (something that is often difficult to achieve!). The specification of the sub-grid turbulent kinetic energy usually takes the form of a prognostic equation, and the eddy mixing coefficients can be derived from this kinetic energy relation. Prognostic equations can also be derived for the sub-grid turbulence transport and variance, but this can mean a large number of prognostic equations and the physical validity of the approximations involved makes the extra complication seem like wasted effort. So it would seem that attempts to provide more realism in sub-grid processes can involve a substantial increase in the computational requirements whilst providing dubious gains in physical accuracy.

The second approach to the problem of computational aliasing, namely that of background damping also has advantages and disadvantages. Firstly it has the advantage of simplicity, being easy to implement, but this simplicity also implies a first order approximation to physical processes. A background damping term such as a diffusive operator (in a 2-D model this operator can have different coefficients for each coordinate direction) can be used to inhibit the growth of nonlinear instabilities and act as a filter to suppress spurious very short wavelength modes whilst also providing a first approximation to the eddy viscosity parameterization associated with turbulence (like an eddy viscosity term with constant coefficient). Unfortunately this sort of damping term can remove important low wavenumber structure as well as the high wavenumber noise. A technique used to overcome this problem is the use of a higher order hyperdiffusive operator (Klemp and Wilhelmson (1989) use a 4th order operator) which is supposed to strongly attenuate high wavenumber noise without substantially affecting the low wavenumber modes, but it has been found in practice that such an operator can change the low wavenumber behaviour (Macaskill and Bewick, 1995) and that there is a tradeoff between increasing the order of the operator and truncation errors.

3.7 Representation of viscous effects in the model

For the current model a simple Fickian diffusion term of second order has been chosen to provide spatial background damping. This involves the addition of the following diffusion term

$$K^x_{(\phi)} \frac{\partial^2 \phi}{\partial x^2} + K^z_{(\phi)} \frac{\partial^2 \phi}{\partial z^2}, \tag{3.37}$$

to the right-hand side of the prognostic equation for each variable ϕ (except the Exner pressure equation). The use of a Fickian diffusion term as a first order approximation for eddy diffusion/viscosity has become popular in recent years (Skylingstad, 1991) as a compromise between the competing requirements of computational efficiency and accuracy and avoids use of complicated and physically dubious subgrid parameterization schemes. The diffusivity terms represented by (3.37) also provide numerical stability by dissipating the energy which accumulates in short wavelengths due to aliasing of nonlinear terms in the governing equations. Use of the diffusive terms in (3.37) requires special consideration at the boundaries of the numerical domain. For the rigid type free-slip condition applied at the bottom boundary, the diffusion term normal to the boundary is set to zero (ie $K_\phi^z = 0; z = 0$). When wave radiation type boundary conditions are used, the coefficients K_ϕ^x, K_ϕ^z are set to zero at the relevant boundary to avoid possible amplification of certain harmonics (Shapiro, 1970).

It is useful at this stage to consider the implications of the use of different vertical and horizontal coefficients (K_ϕ^z and K_ϕ^x respectively) in the damping operator represented by (3.37) in the context of atmospheric problems. It has been shown by Droegemeier and Wilhelmson (1987) in the study of atmospheric outflows that shearing instabilities at the top of such outflows are sensitive to the relative magnitude of the vertical mixing coefficient but not particularly sensitive to the horizontal mixing coefficient. For these type of outflow problem they note that excessive vertical smoothing rapidly spreads out the shear interface and this suppresses the development of Kelvin-Helmholtz instabilities. A couple of observations are relevant here. One, that Droegemeier and Wilhelmson compare the results of their numerical simulations to tank experiments and that it is difficult to interpret such comparisons given the difference in Reynolds number of the flow regimes. It is not certain that large billows of this type can be expected in the atmospheric case, which suggests caution in the assignment of values. Secondly, in discussing the magnitude of the coefficients it must be remembered that there is implicit dependence of each coefficient on the horizontal or vertical mesh resolution. The most important requirement in the choice of each coefficient is to have a high enough value of smoothing to damp the smallest scale aliasing induced modes, but at the same time the value needs to be small enough so that there is minimal suppression of turbulent dynamics. The use of different diffusive coefficients has dynamical implications. For one thing, different coefficients means that the turbulent mixing is not homogeneous and isotropic (which is generally desirable).

The fact that eddy viscosity does not feature explicitly in the model suggests that the Reynolds number should be infinite. However, because the background damping acts as a crude form of eddy viscosity, a Reynolds number can be calculated by using the background damping coefficients to take the place of the kinematic viscosity term. The magnitude of this Reynolds number will vary for simulations which follow due to different choices of damping coefficients but the typical range will be $\mathrm{Re} \approx 10^2 \rightarrow 10^3$ which is different from that associated with physical atmospheric flows by several orders of magnitude. It should be noted that

this method of calculating a Reynolds number does not take into account the fact that the flow regime of a numerical model will always be affected in some way by the chosen spatial resolution. The difference between the Reynolds number calculated for the numerical model and that calculated for physical atmospheric flows is due to the differences in kinematic viscosity. The calculation for an observed atmospheric event will be based on the kinematic viscosity of air ($\mu \approx 10^{-5}\mathrm{m}^2/s$) whereas, for the model used here, the calculation of Reynolds number must be based on a numerical damping coefficient with typical magnitude $K \approx 0.5(10^2)\mathrm{m}^2/s$.

An attempt to produce a Reynolds number closer to the physical value will lead to a more restrictive choice of grid resolution. This is because reductions in the magnitude of a damping coefficient will require a higher grid resolution in order to avoid numerical instability. These constraints mean that a grid resolution, in the chosen model, of $\approx 10-40\mathrm{m}$ would be needed to achieve the physical Reynolds number. Because this choice of grid resolution is too restrictive for the computational resources available, the aim has been to achieve a grid resolution as close as possible to this range whilst still addressing other requirements, such as the size of the numerical domain, which are equally important for the type of simulations to be performed. It has also been found by many numerical modelers (eg. Droegemeier and Wilhelmson, 1987) that a more relaxed choice of grid resolution is sufficient to resolve the scales of interest for many atmospheric flows. Because many of the experiments which follow examine processes influenced strongly by the vertical transfer of energy, the value of the vertical grid resolution in particular is chosen to be as high as possible (generally $\Delta z = 50\mathrm{m}$) in all simulations.

3.8 Initialization of the Ambient Background

The primary application of this model will be the study of highly nonlinear wave motions in the lower atmosphere. Much of the pioneering work (eg Long, 1965) on a mathematical description of nonlinear waves in a deep fluid regime (as is appropriate for the atmosphere) derives the formulation of such wave motions, in their fundamental form, for essentially two layer density profiles. It is therefore useful to consider a two layer simplified ambient environment in modeling such waves in the lower atmosphere. In this two layer case, the bottom layer will be strongly stratified so that it can represent an atmospheric waveguide layer and the upper layer is chosen as either homogeneous or weakly stratified depending on weather wave radiation by upward propagation of wave energy is supported in the choice of background state. An attempt will be made to choose ambient temperature profiles that are similar to those recorded in observations of large amplitude wave disturbances in the lower atmosphere.

3.8.1 Ambient Temperature Profiles

Using the field data of Clarke, Smith and Reid (1981)[1] as a guide, the ambient temperature profiles used extensively in what follows will be based on the assumption of a two layer model of the lower atmosphere. The upper layer will be defined as either stratified or homogeneous as needed, and the lower layer will always be assumed stratified. It is convenient at this point to start by defining these layers in terms of potential temperature profiles.

Stratification in the atmosphere is usually described using the Brunt-Väisälä (or Buoyancy) frequency defined in terms of potential temperature as:

$$N = (\frac{g}{\theta}\frac{\partial\theta}{\partial z})^{\frac{1}{2}}. \tag{3.38}$$

It will be assumed that the choice of a constant N (corresponding to a linear stratification) within a layer is not restrictive.

Starting with the case of two stratified layers it is assumed that the potential temperature in each layer can be defined as exponential, depending on a constant Brunt-Väisälä frequency N:

$$\frac{\theta}{\theta_0} = \exp(N^2/g)z, \tag{3.39}$$

where θ_0 is defined as the temperature at the ground.

If it is now assumed that the Brunt-Väisälä frequency will be N_1 in the lower layer and N_2 in the upper layer. This allows the potential temperature profile to be written as:

$$\frac{\theta}{\theta_0} = \begin{cases} \exp[(N_1^2/g)z] & \text{if } (z < d), \\ \exp[(N_2^2/g)(z - d + \frac{N_1^2}{N_2^2}d)] & \text{if } (z > d) \end{cases}$$

where d defines the depth of the lower layer. Such a two layer profile will be used for ambient temperature initialization to give a lower waveguide layer and a weakly stratified upper layer. Typical values that are chosen based on Clarke, Smith and Reid (1981) are $N_1 = 2\pi/(6 * 60)$ (6 min period) and $N_2 = 2\pi/(14 * 60)$ (14 min period).

An alternate ambient temperature profile will be used to study the case when the upper layer is homogeneous (ie $N_2 = 0$ above). This is defined as

$$\frac{\theta}{\theta_0} = 1/(1 - \sigma\text{Tanh}(z/d)),$$

where σ is a dimensionless parameter representing the degree of variation in temperature over depth d. This profile will be discussed in more detail in later chapters.

---

[1] This refers to the linear line segment fits used by these researchers to denote two stratified layers in the lower atmosphere. This data has been presented and discussed in Chapter 1

3.8.2 Hydrostatic Stability

When discussing the stability of a fluid relative to buoyancy forces, it is usual to look at the vertical force balance for a displaced air parcel. In terms of the potential temperature θ the appropriate stability criteria are:

$$\frac{d\theta}{dz} > 0, \quad \text{stable,} \tag{3.40}$$

$$\frac{d\theta}{dz} = 0, \quad \text{neutral,} \tag{3.41}$$

$$\frac{d\theta}{dz} < 0, \quad \text{unstable.} \tag{3.42}$$

To consider stability in terms of Brunt-Väisälä frequency it is only necessary to substitute N^2 for $d\theta/dz$ in the above.

Hydrostatic stability of vertical motions controls the environments ability to support convective and turbulent processes. For instance, convective overturning and turbulent mixing are favored in regions of negative stability. For the study of wave motions, positive values of N are considered, corresponding to regions of positive stability that are capable of sustaining such motions. Furthermore, for the ambient environments considered here, the background pressure is assumed to be in hydrostatic balance with the potential temperature field. In terms of the Exner pressure function Π, this means the ambient hydrostatic condition is given by:

$$\frac{d\Pi}{dz} = -g/(C_p\theta), \tag{3.43}$$

where $\Pi = \Pi_0$ at $z = 0$. Both temperature and pressure will be considered from now on as consisting of a hydrostatic base state and a perturbation quantity that represents departure from the base state.

3.9 Comments on the model chosen

In summary, this numerical model relies on high grid resolution and simple energy dissipation at the smallest scales to provide adequate representation of turbulent processes. There are a few more items of interest associated with this model and its properties that are worth mentioning. Among the assets of this model are its high accuracy, its conservation of energy (which is exact in a closed or periodic domain and equivalent to semi-conservation in a domain with open boundary conditions), and its formulation from the fundamental form of the Navier-Stokes equations. In discussing potential aliasing effects, it must be kept in mind that the finite difference averaging of the algorithm itself produces a degree of numerical smoothing. Lastly it is important to consider the relative importance of turbulent eddy terms on the basis of the first order energy dissipation scheme chosen as the grid resolution is increased. Droegemeier

and Wilhelmson (1987) examine the diminishing importance of eddy terms by comparing their simulations to results using a Smagorinsky (1963) eddy viscosity parameterization (where the eddy coefficient K in this case is proportional to $(\Delta x \Delta z)^2$), for progressively refined grid resolution. They show that for high enough resolution the model seems to perform almost the same with or without turbulence parameterization. These results further support the use of the numerical model described above for high resolution simulation of mesoscale atmospheric disturbances.

Chapter 4

Boundary Conditions

4.1 Introduction

Computational domains must be of finite extent with the spatial limitations governed by the computer resources available. This naturally calls for the selection of appropriate boundary conditions to be defined for the solution domain. The numerical model defined in the previous chapter falls into the class of a boundary value problem. The governing equations are evaluated in the interior of the domain subject to conditions imposed on the boundaries of the domain.

Boundary conditions for this class of problem are usually selected from three common generic types: Neumann conditions, which specify the values of the normal gradients of variables on the boundary, Dirichlet conditions which specify the value at boundary points as a function of time (including constant values) and outgoing wave boundary conditions. For the approximate model of the atmosphere adopted here, the lower boundary is of Dirichlet type and involves a simple free-slip condition, but outgoing wave conditions are applied at the other boundaries. This is necessary because in a model which simulates atmospheric disturbances, sound and gravity waves that are radiated by the disturbance must eventually reach a boundary. If reflection of such waves is allowed there will be an unphysical build up of energy in the model domain and errors introduced into the solution.

Thus, some means must be incorporated into the model which allows such waves to propagate out of the domain. This obviously does not apply to the lower boundary which will be the ground, but is applicable to both the lateral and upper boundaries. The approach adopted here is the formulation of what are commonly known as "open boundary conditions" which involve an alteration of the finite difference equations at the boundary points of the domain. Other formulations that do not fall into this class include, for instance, methods that extend the domain using "artificial" grid points to create some sort of "sponge" zone. Two types of open boundary condition are used; one for the lateral boundaries and another for the top boundary. Reasons for the necessity of making a distinction between the lateral and top boundaries and a description of each type of boundary condition are outlined below. First however we formulate a boundary condition for the lower boundary.

4.2 Lower boundary

The lower boundary represents the surface of the Earth with a fluid-solid contact. The appropriate condition is simply an implementation of the rigid free-slip condition that is commonly used as an approximation to the surface of a solid object in modeling physical flows in the atmosphere. Such a condition does not take account of any boundary layer effects. Momentum and heat is transfered to the surface by the Fickian diffusion terms, described in the last chapter, which are added to the finite difference form of the governing equations in order to maintain computational stability. At the surface there is also horizontal spreading of momentum and heat due to the Fickian diffusion term acting tangential to the boundary which is retained (at $z = 0$) but the term which acts normal to the boundary is set equal to zero (for $z = 0$). The lower boundary condition requires that $\partial_z u = 0$ ($z = 0$) and that vertical velocity w is assigned to zero on the lowest row of the domain (ie $z = 0$). All other variables are updated along the lower boundary using modified prognostic equations where the vertical derivative terms have been replaced by one-sided difference terms of the form

$$\frac{df(\xi)}{d\xi}|_{\xi=\xi_n} \approx \frac{1}{2\Delta\xi}(A_0 f(\xi_0) + A_1 f(\xi_1) + A_2 f(\xi_2)), \tag{4.1}$$

where $f(\xi)$ is the variable in question and the A_i vary with n. One-sided difference forms are most useful in numerical boundary conditions which allow no motion to pass through the boundary. If motion through the boundary is allowed then such formulations are effective only for motions characterized by strong advection or a smooth form at the boundary.

4.3 Lateral boundaries

For the lateral boundaries a scheme is adopted which is based on a linear wave equation in one dimension and which uses an extrapolation procedure to calculate the phase velocity of a wave disturbance propagating through the boundary. This type of wave equation method was originally proposed by Orlanski (1976) and falls into the class of a Sommerfeld type radiation condition.

It has been demonstrated by many authors including Orlanski (1976), Miller and Thorpe (1981) and Durran et al. (1992) that implementation of a Sommerfeld type radiation condition for lateral boundaries allows gravity and sound waves to radiate from a numerical domain with minimal reflection. A Sommerfeld radiation type condition is derived from a general elliptic differential equation which has been recast in the form of a reduced wave equation and where the wave solutions are assumed simple harmonic in time with a certain frequency.

The general solution of such an equation is represented as the sum of two components, where one component satisfies the Sommerfeld condition for outward radiation which characterizes net loss of wave energy (ie negative total energy flux through the boundary). In numerical terms this boundary condition is implemented by forcing a prognostic variable ϕ to satisfy a wave equation which matches the dispersion characteristics needed by waves to satisfy the Sommerfeld radiation equation:

$$\frac{\partial \phi}{\partial t} + c\frac{\partial \phi}{\partial x} = 0, \tag{4.2}$$

where c is the effective phase speed for disturbances advected out of the domain. Assigning a suitable value of c becomes the fundamental issue. The local phase velocity of the disturbance in question is generally not known for the nonlinear sets of equations representing typical realistic mesoscale flows. Some researchers have solved this problem by using a fixed value of c, but reflections at the boundary will occur in this case for wave modes with phase velocities not well approximated by the chosen fixed value c. A better approach is to use a numerical scheme that dynamically calculates a propagation velocity using the neighboring grid points at the domain boundary. Using a centered time difference form of (4.2) compatible with leapfrog time differencing, the finite difference relation is (Orlanski 1976):

$$\frac{(\phi_b^{n+1} - \phi_b^{n-1})}{2\Delta t} = -\frac{c}{2\Delta x}\left[\phi_b^{n+1} - 2\phi_{b-1}^{n} + \phi_b^{n-1}\right], \tag{4.3}$$

where n is the time index and b is a mesh point on the boundary. Introducing the variable $r = c\Delta t/\Delta x$ and rewriting the previous equation in terms of r gives a numerical method of calculating r using interior mesh points at preceding times:

$$r = (\phi_{b-1}^{n-2} - \phi_{b-1}^{n})/(\phi_{b-1}^{n} - 2\phi_{b-2}^{n-1} + \phi_{b-1}^{n-2}). \tag{4.4}$$

The necessary radiation condition is then expressed as:

$$\phi_b^{n+1} = \left(\frac{1-r}{1+r}\right)\phi_b^{n-1} + \left(\frac{2r}{1+r}\right)\phi_{b-1}^{n}. \tag{4.5}$$

This finite difference form is used in all calculations to provide a lateral radiation condition.

Orlanski (1976) tests the above radiation condition for a simulation of a mixed region collapsing in a stratified fluid using a formulation in two dimensions of the Navier Stokes equations in terms of stream function and vorticity. Although derived from an essentially one-dimensional relation, the radiation condition performs well at the lateral boundaries. Given that for the type of modeling proposed in this study it is expected that horizontal advection will dominate at the lateral boundaries, the one-dimensional nature of the radiation condition is not considered limiting.

Klemp and Lilly (1978) apply the technique of Orlanski to a hydrostatic atmospheric model. Outward propagating wave energy is removed from the domain by advecting outward going disturbances through the lateral boundary at their horizontal phase speeds. However, in addition to Orlanski's basic formulation, a distinction is made between inward and outward going wave energy[1] in terms of the advective properties of the boundary condition. Under this assumption, the horizontal velocity u becomes the governing parameter controlling propagation of wave energy and conditions of positive and negative horizontal velocity correspond to outgoing and incoming wave energy. For open boundary conditions, each boundary value of u that has sign corresponding to wave energy leaving the domain, is assigned an estimate of c, the phase velocity for the one dimensional (horizontal) wave advection equation (4.2) at that point. For boundary values of u corresponding to incoming wave energy, horizontal advective terms are set to zero (under the assumption of no external forcing). A similar method of specifying the advective properties of a lateral boundary condition is used for the formulation of lateral boundary conditions applied to the model adopted here.

4.4 Symmetry Boundary Condition

In many of the experiments to follow, the flow field can be considered symmetric about some vertical set of mesh points. This will apply for a certain period of time after startup before nonlinear interactions are able to lead to a strong departure from symmetry. If the object is to study only one part of a solution resulting from a symmetric source[2], then it is only necessary to use a mesh that represents one side of the symmetric solution domain with the axis of symmetry being chosen as one of the lateral boundaries. The left lateral boundary has been chosen as the axis of symmetry when such a boundary condition is applied. At some point it is expected that the symmetry of the flow field will break down, but this effect will be minimal over substantial time periods for many of the flows considered. The statement of the basic condition used here is numerically equivalent to:

$$u_{\xi-\Delta x} = -u_{\xi+\Delta x}, \tag{4.6}$$

$$\phi_{\xi-\Delta x/2} = \phi_{\xi+\Delta x/2}, \tag{4.7}$$

$$u_{\xi} = 0, \tag{4.8}$$

[1] In the lateral boundary case (horizontal motion) the direction of wave energy given by the group velocity is the same as the direction of propagation. (Linear wave theory)

[2] The right-going solution is chosen for simulations here, with the symmetric source centered on a line through the origin at the left most part of the mesh

where u is the horizontal velocity field, ϕ represents the other fields and ξ represents an appropriate set of vertical grid points. For the model adopted here, the effectiveness of a symmetric lateral boundary condition is coupled to the performance of the radiation condition at the upper boundary. There will be problems with accurate transfer of energy through the upper boundary if the boundary condition at that level is not modified (as outlined below) to take account of the LHS symmetry.

4.5 Upper boundary

For the types of atmospheric disturbance to be considered in this work, it is important to have an upper boundary condition that allows the radiation of gravity waves so that reflected vertically propagating wave energy does not interfere with the simulation of disturbances inside the domain. Sound waves are not physically significant for the atmospheric disturbances considered here but are important for stability of the algorithm. Therefore the boundary condition presented here will focus entirely on gravity wave modes. Linear internal wave theory shows that individual wave components with phase velocity directed upwards result in the transfer of wave energy downwards. This means that for an open type boundary condition it will be necessary to use a spectral method to eliminate appropriate Fourier components. The basis of the radiation condition will be that under the assumption of no sources of energy at infinity, a condition is imposed that insures that wave motions will not contain Fourier components that correspond to downward transfer of energy (ie upward propagating components).

The condition derived here is based on that of Bougeault (1982) and Klemp and Durran (1982) who use linear internal wave theory to formulate a radiation condition that only requires instantaneous values of the flow field at the boundary. A number of restrictions apply to this formulation. It is derived for a set of linear, hydrostatic, Boussinesq equations which exclude Coriolis effects. Horizontal homogeneity is assumed for the mean state conditions at the top boundary, and there is an implied periodicity for disturbances at the upper boundary due to the use of Fourier transforms. The major advantages of this type of boundary condition lie in its simplicity and the fact that the key relationship is not dependent on frequency (the conventional form even for the same governing equations depends on phase speeds of individual modes and time integrals at the boundary) or the time history of the flow field at the boundary. Also, although the boundary condition is derived with many assumptions, it has been applied with success to more general governing equations, including non-linear equations. There are however questions with regards to accuracy when this method is applied outside its domain of strict validity. This method imposes a limited spectrum of horizontal wavenumbers for which the derivation is valid and so there are questions in regards the degree of reflectivity for wave modes outside this range. Given that nonlinear interactions tend to transfer wave energy to

higher wavenumbers over time, it is expected that a high horizontal grid resolution will be important in minimizing reflections when the condition is applied in a nonlinear model.

The system of equations that apply under the assumptions of linear, Boussinesq and hydrostatic 2D flow, without any consideration of Coriolis effects, are given by:

$$\frac{\partial u}{\partial t} + U\frac{\partial u}{\partial x} + \frac{\partial \phi}{\partial x} = 0, \tag{4.9}$$

$$\frac{\partial \theta}{\partial t} + U\frac{\partial \theta}{\partial x} + \frac{d\bar{\theta}}{dz}w = 0, \tag{4.10}$$

$$\frac{\partial \phi}{\partial z} - g\frac{\theta}{\theta_0} = 0, \tag{4.11}$$

$$\frac{\partial u}{\partial x} + \frac{\partial w}{\partial z} = 0, \tag{4.12}$$

where ϕ represents the pressure field.

Assuming solutions of this set of equations represent a general linear disturbance which is periodic in both space and time, they can be expressed in the form:

$$\xi(x,z,t) = \tilde{\xi}(k,n,\omega)\exp[i(kx+nz-\omega t)]. \tag{4.13}$$

If we consider plane wave solutions in a coordinate system moving with the mean wind U, we can define an intrinsic frequency $\sigma = \omega - Uk$, which is the frequency of a wave as seen by an observer moving with the local mean wind. It is then possible to Fourier transform (using k,n,σ) the dependent variables of the above set of equations to end up with the following set of transformed equations, defined for the coordinate system moving with the mean wind:

$$-i\sigma\hat{u} = -ik\hat{\phi}, \tag{4.14}$$

$$in\hat{\phi} = \beta\hat{\theta}, \tag{4.15}$$

$$\hat{w}\frac{\partial\bar{\theta}}{\partial z} = i\sigma\hat{\theta}, \tag{4.16}$$

$$k\hat{u} = -n\hat{w}. \tag{4.17}$$

By manipulating this set of equations the following further set of relations may be derived:

$$\hat{u} = \frac{k}{\sigma}\hat{\phi}, \tag{4.18}$$

$$\hat{\theta} = i\frac{n}{\beta}\hat{\phi}, \tag{4.19}$$

$$\hat{w} = -\frac{k^2}{n\sigma}\hat{\phi}. \tag{4.20}$$

Using the Brunt-Väisälä frequency [N=$(g\theta/\theta_0\partial\theta/\partial z)$] and this set of transformed equations

(4.18), (4.19), (4.20), it is now possible to derive a dispersion relation relating frequency to horizontal and vertical wavenumbers for this class of wave motion:

$$k^2N^2 = n^2\sigma^2. \tag{4.21}$$

If the hydrostatic approximation had not been applied the dispersion relation would be:

$$\sigma^2 = k^2N^2/(k^2+n^2), \tag{4.22}$$

which is the general dispersion relation governing linear internal waves in a continuously stratified 2D medium. The hydrostatic approximation can be seen to only be applicable for waves with $k << N/U$ (ie not acoustic waves).

Linear wave theory states that energy will travel with the local group velocity which can be represented in 2D vector form as:

$$(\partial\sigma/\partial k, \partial\sigma/\partial n). \tag{4.23}$$

The dispersion relation states that this vector is parallel to the local phase velocity vector $(\sigma/k, -\sigma/n)$. It is clear from these relations that the vertical fluxes of wave energy and momentum are of opposite sign. For wave energy to be carried upwards momentum must be transfered downwards with $\sigma/n < 0$. Using eqns (4.18),(4.19),(4.20) it is possible to derive an invariant relation (with respect to coordinate transformations) between the transformed pressure and vertical velocity:

$$\tilde{\phi} = \tilde{w}N/k \tag{4.24}$$

This is the fundamental form of the radiation condition to be implemented here. A physical interpretation of this relation can be compared to the physical behaviour of a passive upper stratified layer at the top of the model. There will be a positive pressure response when the flow is disturbed upwards and a negative one when the flow is disturbed downwards.

In the atmosphere, internal wave solutions are strongly influenced by the presence of a mean wind field. Eliassen and Palm (1960) analyse the properties of stationary internal wave solutions described by the wave equation:

$$\hat{w}_{zz} + (l^2 - k^2)\hat{w} = 0, \tag{4.25}$$

where $l^2 = N^2/U^2 - U_{zz}/U$ is defined in terms of the mean wind field U. In a layer of constant l^2 internal wave solutions ($k^2 < l^2$) are described by:

$$\hat{w} = A\exp(i\lambda z) + B\exp(-i\lambda z), \tag{4.26}$$

where $\lambda^2 = l^2 - k^2$ and $\lambda > 0$.

The solution represented by $\exp(i\lambda z)$ which corresponds to a wave with lines of constant phase tilted upwards ($U > 0$) results in upward energy transport, whereas that represented by $\exp(-i\lambda z)$ corresponds to waves with lines of constant phase tilted downwards and downward energy transport. This allows the complete wave solution to be represented as an incident and reflected wave (with respect to higher layers). It can be shown that the radiation condition (4.24) is equivalent to requiring the coefficient B to be equal to zero and only considering the solution that represents upward flux of wave energy.

For the application of the boundary condition (4.24) to non-hydrostatic models where vertically propagating waves can have amplitudes that vary with height due to density variations, it has been suggested (Gutman, 1991) that density variations in the continuity equation should be kept or the characteristics of the wave propagation may be altered. Klemp and Durran (1983) find that non-linearity significantly alters the interpretation of gravity wave radiation and raises many questions about the applicability of such a simplified radiation condition. When non-hydrostatic and rotational effects are included in the derivation of the radiation condition, the resulting relation becomes more complicated but still reduces to a transform relation between w and ϕ. For non-Boussinesq models where mean density variation is included (which is necessary in a model with vertical scale motions over a substantial depth of the atmosphere), the radiation condition between w and ϕ now has a complex number as the scaling factor between terms, with a dependence on frequency ω. However, since the non-Boussinesq contribution is the imaginary part, it does not effect the transfer of vertical energy but has been found by Klemp and Durran (1983) to have a small effect on the amplitudes of the vertically propagating wave modes. It is therefore likely to have only limited influence on the effectiveness of the radiation condition. Klemp and Durran (1983) found that the radiation condition was still effective in its basic form for a non-linear non-Boussinesq mountain lee wave problem. It was found to give similar results to the use of multiple "sponge" layers, but with obvious benefits in terms of computational runtime. Strictly accurate or not, the reason this method is chosen here over others is that it seems to be able to radiate most of the wave energy through the upper boundary when subjected to the tests described below. Furthermore, the condition is simple to apply and is computationally efficient.

4.5.1 Implied periodicity

When the radiation condition is restated in physical coordinates by applying the convolution theorem, we have

$$\phi(x, z_t, t) = \frac{N}{\pi} \int_{-\infty}^{\infty} w(x', z_t, t) \ln|x - x'| dx'. \tag{4.27}$$

A finitely bounded domain in x means that the integral with infinite bounds cannot be evaluated without points outside the domain unless there is an implied periodicity with the finite x domain length being taken as the periodic length scale. If the major source region of upward propagating disturbances is toward the center of the domain then this restriction should not overly affect the radiative properties of the upper boundary condition. Klemp and Durran (1983) point out that the assumption of periodicity is acceptable given that the radiation condition itself is only an approximation. As noted above, a radiation condition that only requires a finite lateral domain length has been formulated by Bennett (1976) but requires the complete time history of the flow field at the boundary.

4.5.2 Numerical implementation

The basic radiation condition (4.24) depends on a relationship between horizontally transformed variables that is numerically equivalent to a filtering technique where a transform of the variable w is scaled by a factor depending on horizontal wavenumber to yield a value of $\hat{\phi}$ in transform space that can then be inverse transformed. It is the finite difference form of terms containing horizontal derivatives in the governing equations that will determine the effective numerical representation of horizontal wavenumbers. Consider a second-order central difference form such as :

$$\frac{\partial u}{\partial x}|_{j,n} = \frac{u^n_{j+1} - u^n_{j-1}}{2\Delta x} + O(\Delta x^2). \tag{4.28}$$

At a numerical timestep we imagine the coefficients of the difference equations to be so slowly varying that we can consider them constant and assume eigenmodes of the difference equations of the form,

$$u^n_j = \xi^n \exp ik_x \pi/(j\Delta x), \tag{4.29}$$

corresponding to linear sinusoidal wave modes with k_x, the real horizontal wavenumber and $\xi = \xi(k_x)$, a complex number that depends on k_x. This implies a discrete set of numerical wavenumbers given by:

$$k_a = \sin\left(\frac{k_x \pi}{\mathrm{M}}\right), \tag{4.30}$$

where M represents the length of the FFT used to transform to a discrete wavenumber space. For the model used in this study we have a fully compressible non-hydrostatic set of nonlinear governing equations. However for the basic radiation condition it will only be the finite difference forms of the horizontal derivative terms associated with gravity wave propagation

(i.e., based on a linear sinusoidal disturbance) that will influence the numerical form of k_x. For the staggered mesh which is used here (where the velocity variables are one-half grid interval removed from the thermodynamic variables), this implies a numerical horizontal wavenumber given by,

$$k_w = \frac{2}{\Delta x} \sin\left(\frac{k_x \pi}{\mathrm{M}}\right), \tag{4.31}$$

and the approximate radiation condition for our model will take the form:

$$\hat{\Pi} = \frac{N}{C_p \bar{\theta} |k_w|} \hat{w}. \tag{4.32}$$

Updating of the model under the radiation condition is straightforward. The vertical velocity w is updated along the top of the domain according to the usual prognostic equation but with vertical derivative terms replaced with one sided differences and with the vertical mixing coefficients set to zero. It is then transformed with a fast Fourier Transform (FFT) and the radiation condition applied to each Fourier coefficient yielding a transformed $\hat{\phi}$ along the upper boundary. ϕ is then recovered using an inverse FFT. The updating of the prognostic equations for the other variables requires an extrapolated value of w one mesh space in the vertical for stability of the finite difference scheme.

To avoid the restriction of the number of horizontal grid points having to be equivalent to the length M of the FFT (and therefore a power of two), arrays of field values corresponding to a set of horizontal grid points (with length less than M) were padded with zeros up to length M. This padding can lead to a sharp discontinuity if the field variables have large nonzero values at the point padding is applied, resulting in Gibbs phenomenon in the transformed signal. Such effects are reduced by the use of a windowing function applied to a set of points prior to the padding and ensuring a smooth drop off to zero. It was found that by using a half cosine windowing function applied to a number of points near the padded region that the boundary condition using a padded array performed equally well as the condition applied to an array with a length equal to a power of two. However, this equivalent performance was dependent on the choice of a suitable minimum number of points, just prior to the padded region, as the set on which the windowing function operates. A typical minimum number of points was a set of 10 points for an FFT of length 256 and a windowing function defined using a Tanh function that varies between 1 and 0 over this set of points.

4.5.3 Implementation of the boundary condition under Symmetry

For the symmetry boundary condition introduced above, a change must be made in the implementation of the upper boundary condition given by (4.24). This is necessary to have the

symmetry reflected in the discrete wavenumber space represented by an FFT of the horizontal w field at the upper boundary. This is achieved by artificially extending the top row of grid points for each time step. The new artificial top row is double the length of the original and is made up of a mirror image of the relevant flow field values (vertical velocity w_i) reflected around the LHS boundary. These are stored in a temporary array which is double the size of that needed to store the original top row and can be considered as being made up of two sections. The front section of the new double length array holds the LHS reflected mirror image and the old values then follow in the remaining (back) section. An FFT is then applied to this new array and the spectral filtering corresponding to the upper boundary is applied before the data is inverse transformed. The returned pressure field values Π_i are then taken from the back section of the temporary array (now storing the inverse FFT data) and applied to the top row of grid points.

This modified upper boundary condition has been found to be very effective for flow conditions where the symmetry boundary condition described above can be applied. A test case is shown here where a symmetric mixed region of fluid is allowed to collapse under gravity. It can be seen that a symmetric vortex ring develops and falls towards the ground where it impacts and forms a symmetric outflow centered on the point of impact. This is shown in Fig 4.1 without imposed symmetry and in Fig 4.2 for the same flow conditions with symmetry imposed. The same grid resolution has been used in both cases (with $\Delta x = \Delta z = 50$ m) and the Fickian diffusion coefficients are $K^x = K^z = 20\text{m}^2/s$. The non-symmetric case uses a [200x400] point mesh representing a 10km by 20km domain. For the symmetric case a [200x200] mesh is used. The starting blob is initially ($t = 0$) released at a height of 5km where it is defined using a potential temperature perturbation of -1 K . The axes in the figures represent grid points and not physical distances. Analysis of the vertical velocity field at the axis of symmetry found that the vertical velocity field at $z = 0$ matches for both simulations. This simple test can be compared to the many laboratory studies that exist for vortex ring motions (see eg. Barker and Crow, 1977) and also provides a test of the chosen numerical models ability to resolve an appropriate level of fluid dynamics.

4.6 Tests of upper boundary condition

A useful test of the effectiveness of the upper boundary condition to radiate wave energy has been selected which has been used previously by Bougeault (1982) to test his formulation of the upper boundary condition. This is in the form of an internal wave field, generated by an oscillating source, in a stratified fluid of uniform buoyancy frequency. It was found that wave energy is passes freely out of the domain through the upper boundary without reflection. Further it was found comparisons were possible between this test case and results for the "St

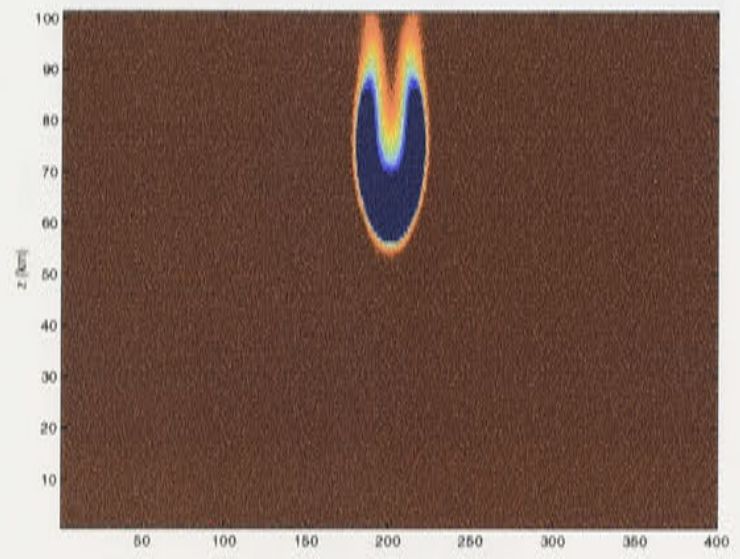

(a) blob at 6 mins

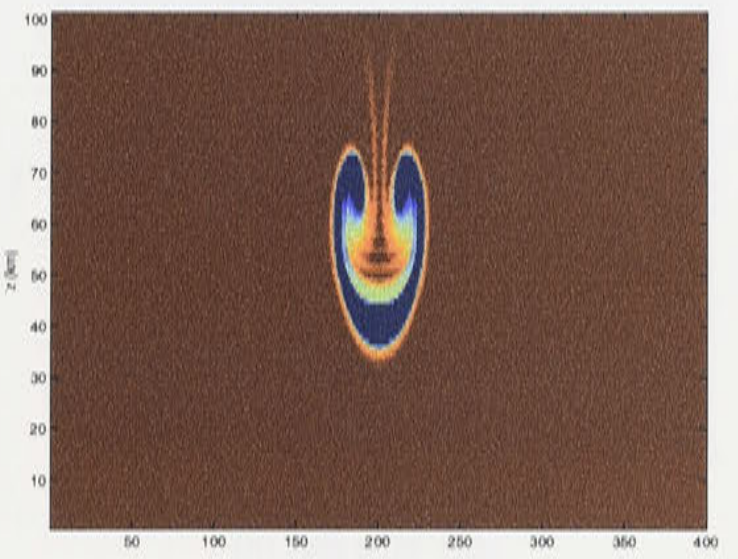

(b) blob at 10 mins

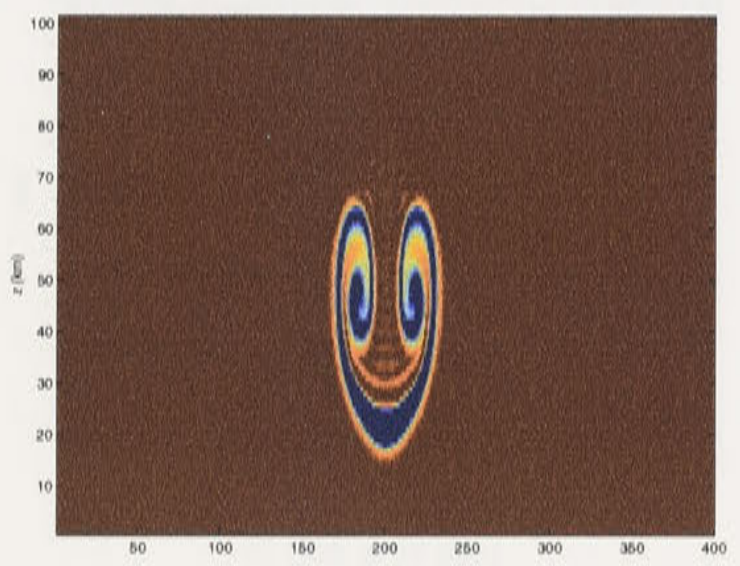

(c) blob at 14 mins

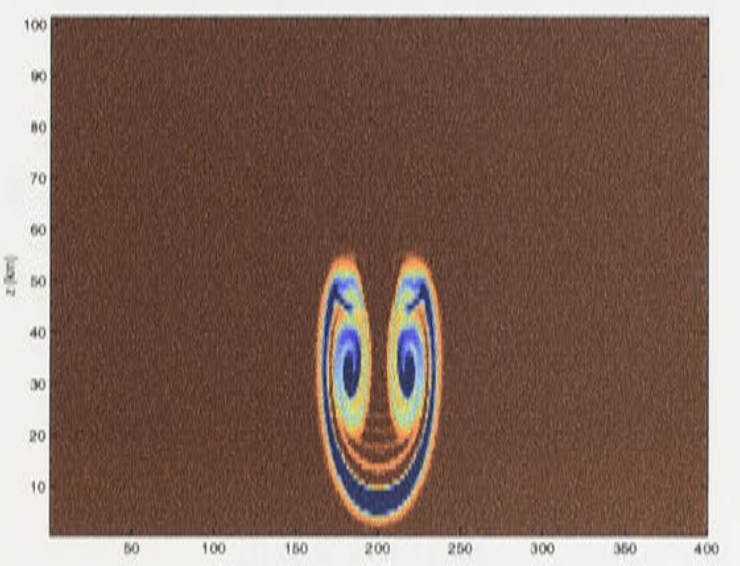

(d) blob at 18 mins

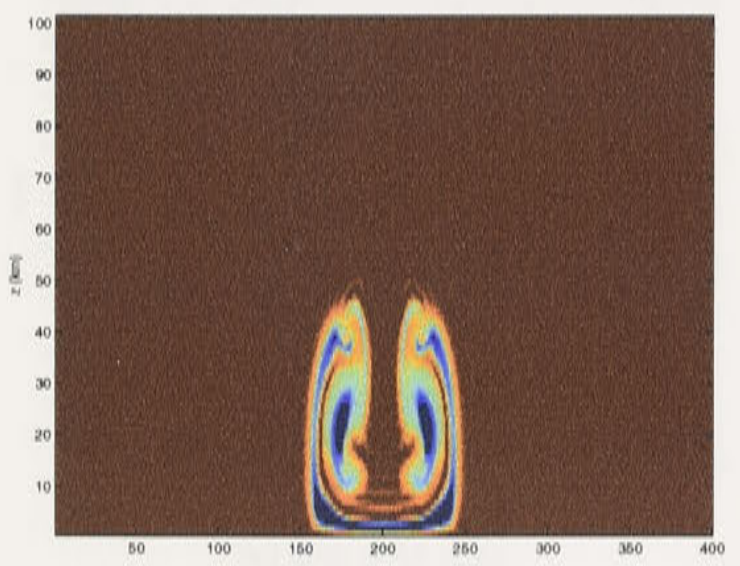

(e) blob at 22 mins

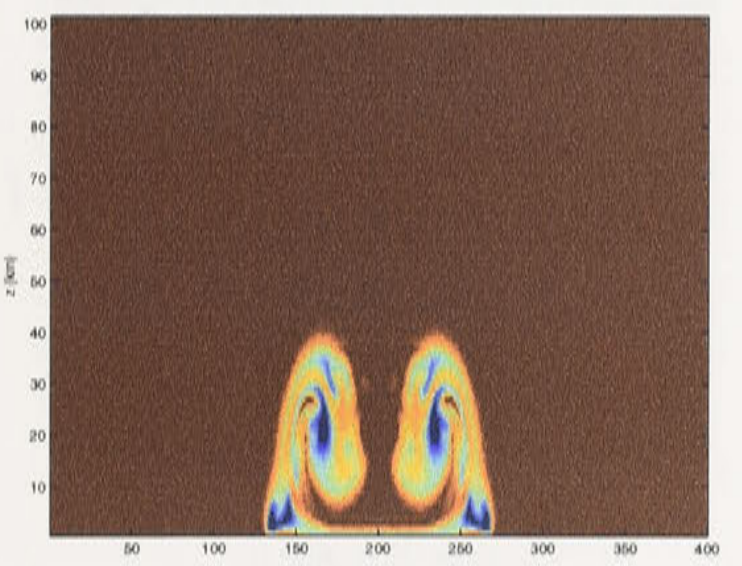

(f) blob at 26 mins

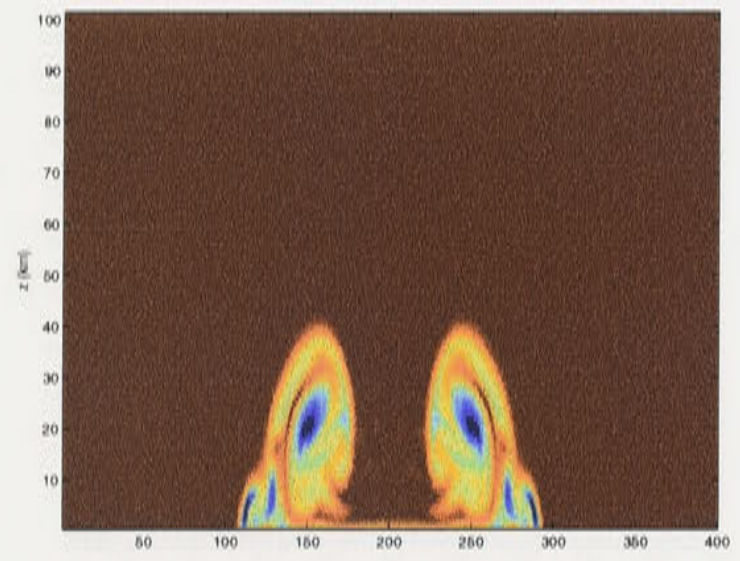

(g) blob at 30 mins

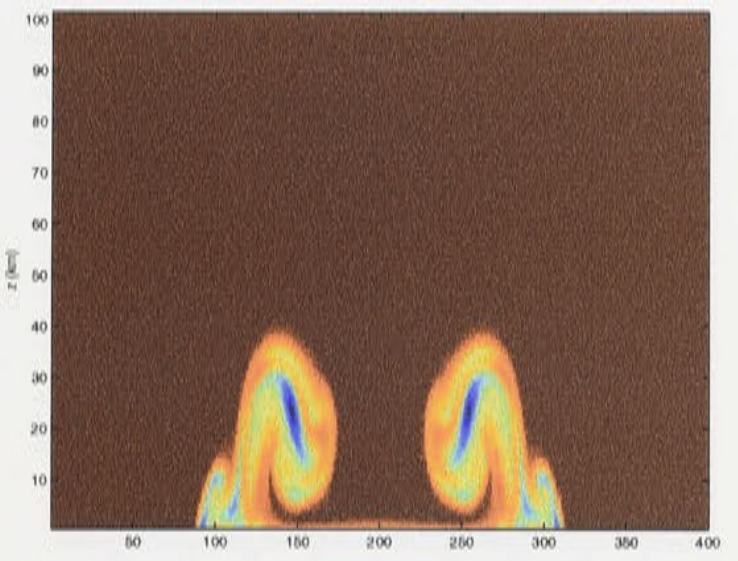

(h) blob at 34 mins

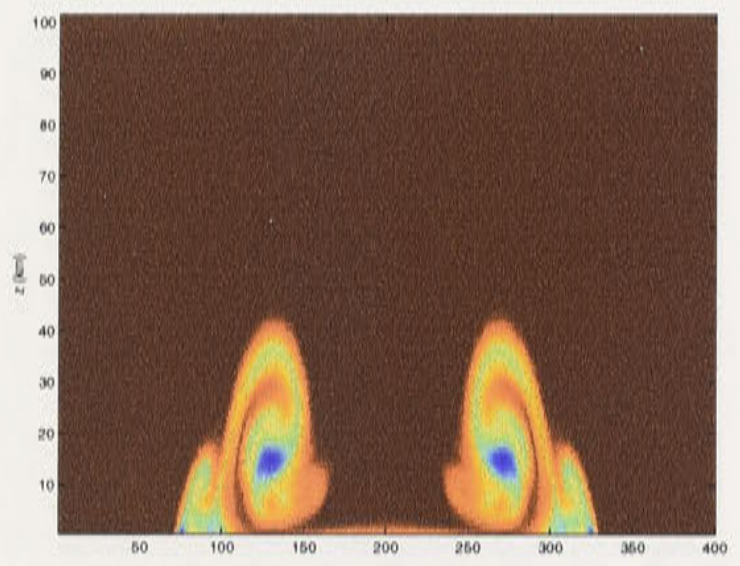

(i) blob at 38 mins

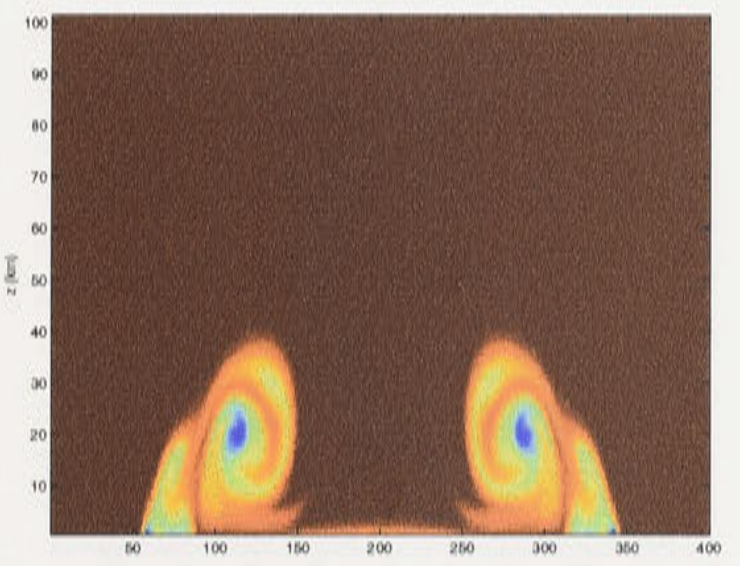

(j) blob at 42 mins

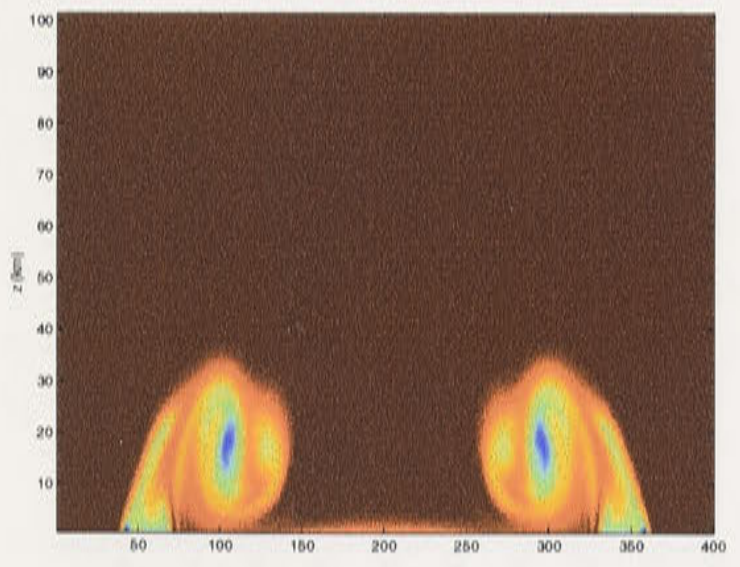

(k) blob at 46 mins

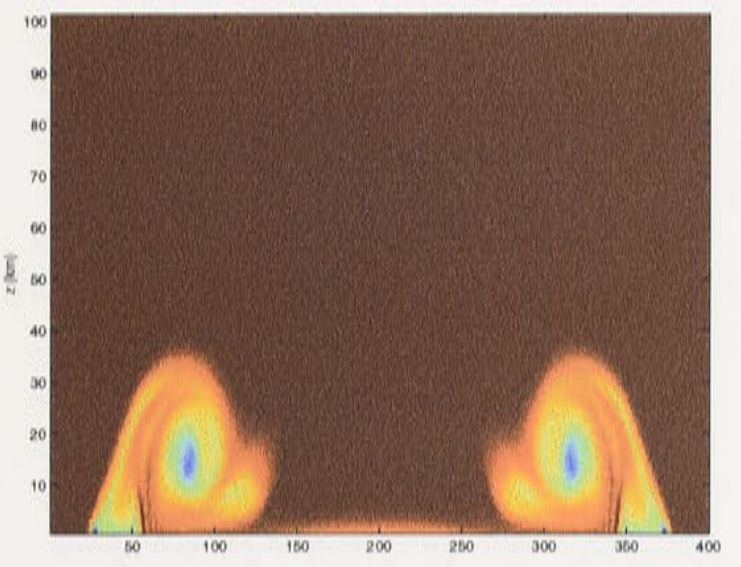

(l) blob at 50 mins

Figure 4.1: Evolution of a falling Blob using wave radiative type boundary conditions at the lateral and top boundaries. The perturbation potential temperature field is displayed using a contour scale that varies between -1K (blue) and 0K (red).

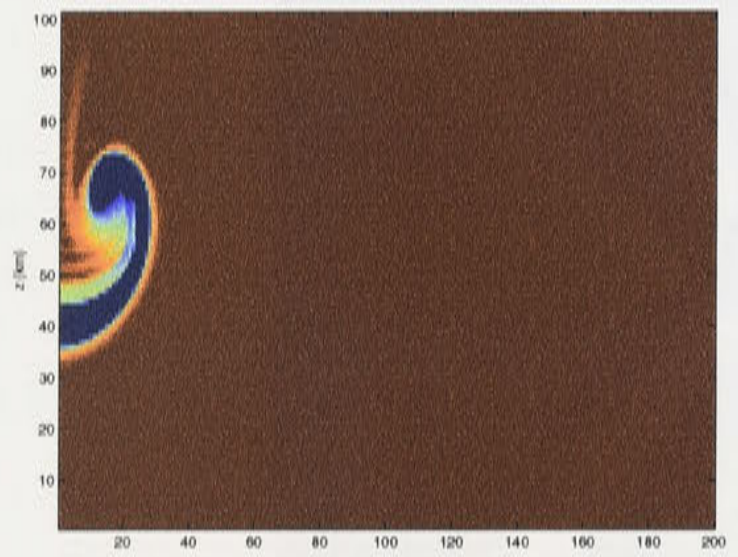

(a) blob at 10 mins

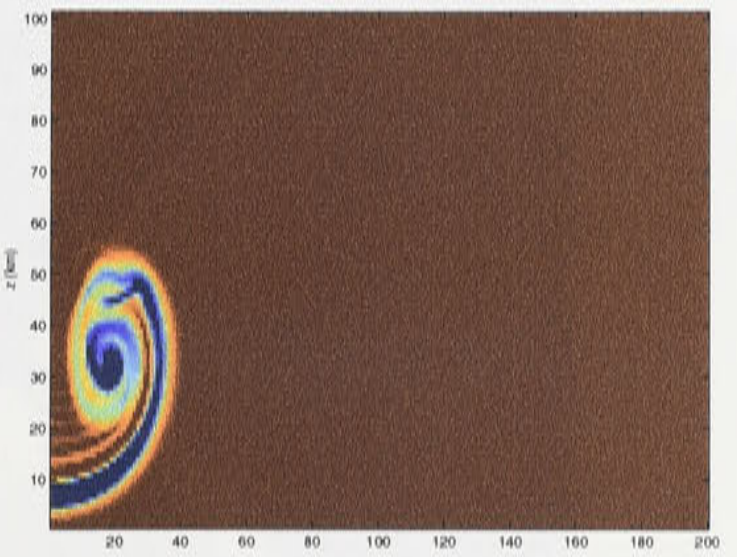

(b) blob at 18 mins

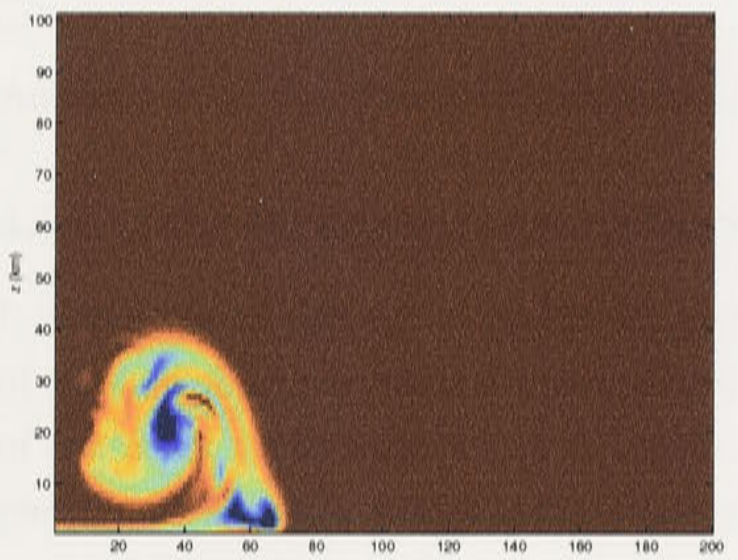

(c) blob at 26 mins

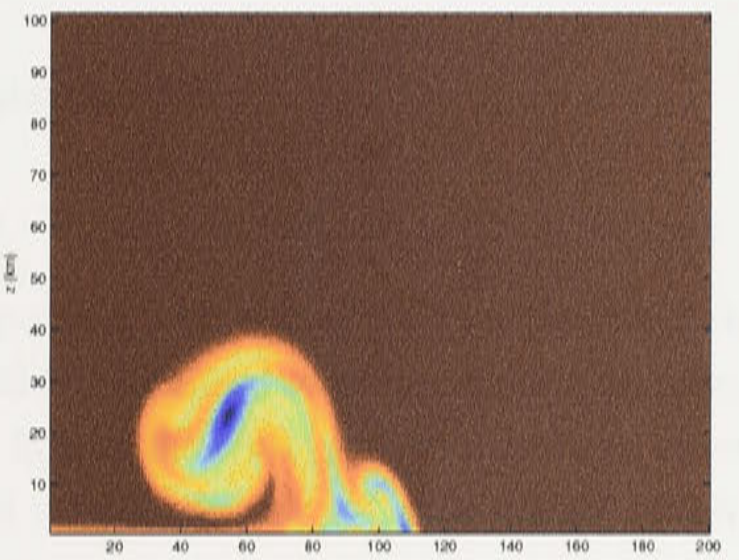

(d) blob at 34 mins

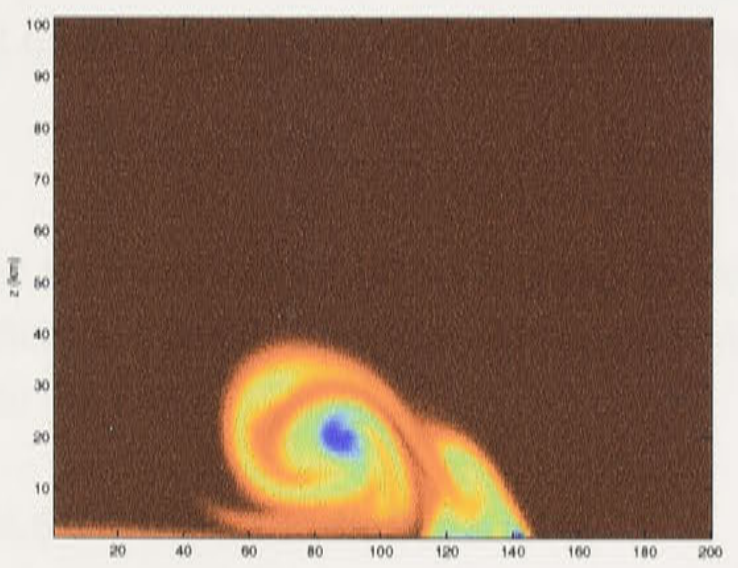

(e) blob at 42 mins

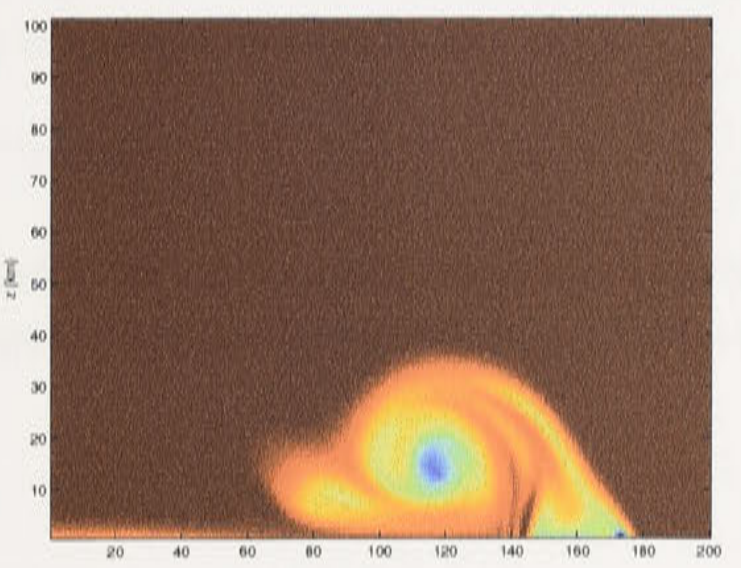

(f) blob at 50 mins

Figure 4.2: Evolution of falling blob under symmetry boundary condition. The figures show the perturbation potential temperature field using a contour scale that varies between -1K (blue) and 0K (red).

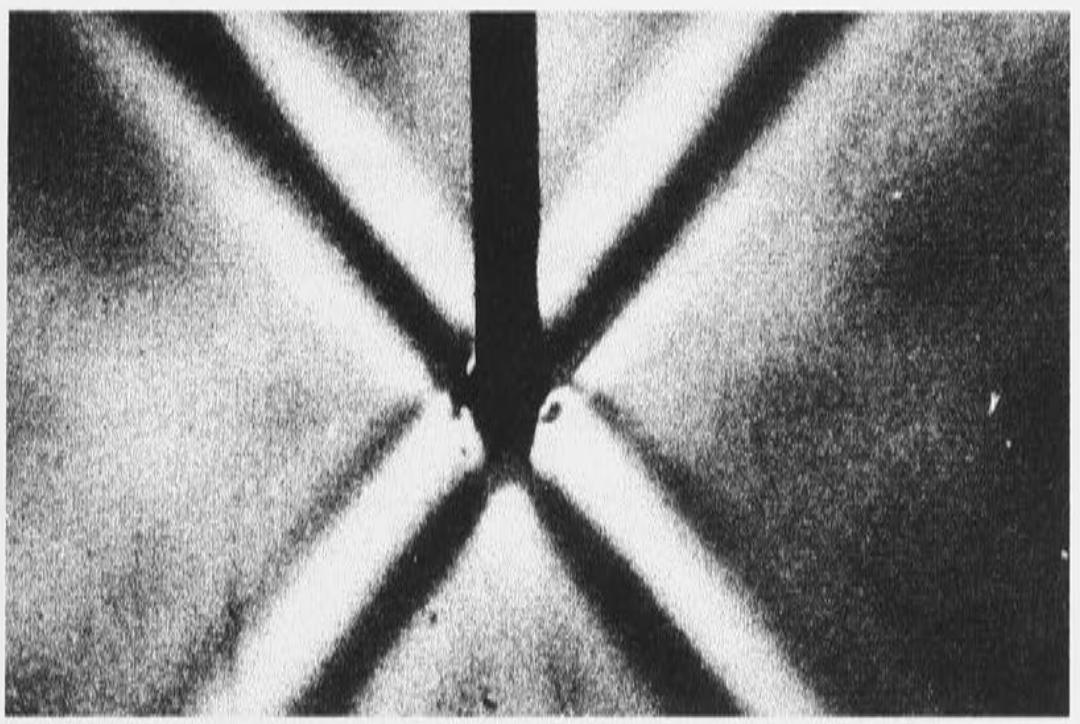

Figure 4.3: Schlieren photo of experiment (Taken from Lighthill, 1978)

Andrews cross" experiment described by Lighthill (1978).

4.6.1 Internal gravity wave radiation

It is well known that due to the fact the group velocity of internal waves is parallel to surfaces of constant phase any internal waves generated by a localized source never have the appearance of concentric crests centered on the source. Instead the crests and other surfaces of constant phase can be seen to stretch radially outward from the source and wave energy travels along rays parallel to these surfaces.

Lighthill describes an experiment where waves are generated in a uniformly stratified fluid by vertical oscillation of a cylinder at frequency ω (where $\omega \leq N$ the buoyancy frequency). Lighthill shows that for this case the surfaces of constant phase all lie at an angle

$$\theta = \cos^{-1}(\omega/N) \tag{4.33}$$

to the vertical axis. All wave energy generated in the source region propagates outward confined to a double cone with semi-angle θ. A typical Schlieren photo of the wave field is shown in Fig 4.3.

4.6.2 Dipole radiative source

A numerical condition that produces a radiation field that is comparable to the oscillating cylinder in a fluid (which is quite complicated to model realistically) is that of an oscillating dipole source. The dipole radiative source is specified by selecting two grid points (along the ground ie $z = 0$) in the center of the mesh and applying a vertical velocity at these points given

by:

$$w_{\text{ground}}(t) = w_0 \sin(2\pi t/\mathrm{T}), \tag{4.34}$$

where w_0 is the peak magnitude of the oscillation and T is the period of oscillation. For the test cases shown here a value of $w_0 = 0.16$ was chosen with the period chosen as either $T = 24$ mins or $T = 14$ mins.

4.6.3 Results of test

In making comparisons between the experiment and the numerical test case, it was necessary to take into account a transient response time, dependent on the vertical domain length, before the rays representing the direction of travel of wave energy approached steady state. This was because the source function produced a range of wave modes, all of which traveled at different speeds depending on their wavenumber. A sufficient time period was required before a superposition of wave modes in the radial surfaces of constant phase approached a steady state form. A plot of the vertical velocity field is shown in Fig 4.4 which is taken at a time when steady state has been reached. It can be seen that this plot bears a close resemblance to the Schlieren photos of density variation from the experiment referred to in Lighthill. Taking into account the grid scaling, it was found that the angle of the rays in the plot matched closely the expected value given by equation (4.33). For $\omega/N \approx 0.3386$ this was calculated to be $\theta = 70.2$ degrees (note that the scaling of the grid for the plots of the radiation field will affect the apparent angle in the plots). As can be seen clearly in Fig 4.4 there is no visible reflection from the upper boundary and it appears that the wave energy is radiated without reflection.

The symmetry boundary condition is also examined for the dipole radiation field with the dipole located at the axis of symmetry. A plot of the vertical velocity field after a suitable time period is shown in Fig 4.5. As can be seen the radiation field is the same as the non-symmetric case and there is no visible reflection of wave energy. If the upper boundary condition (4.24) is only applied to part of the wavenumber space (after an FFT) then there is visible partial reflection of wave modes from the upper boundary. This case is shown in Fig 4.6.

4.6.3.1 Vertical Energy Flux

The mean vertical energy flux is commonly represented as $\overline{pw}$ where the over-bar is an average over one horizontal wavelength. It is also possible to consider total vertical energy flux as represented by the integral:

$$\mathrm{Flux}_e = \int_{-\infty}^{\infty} p'w'\mathrm{d}x. \tag{4.35}$$

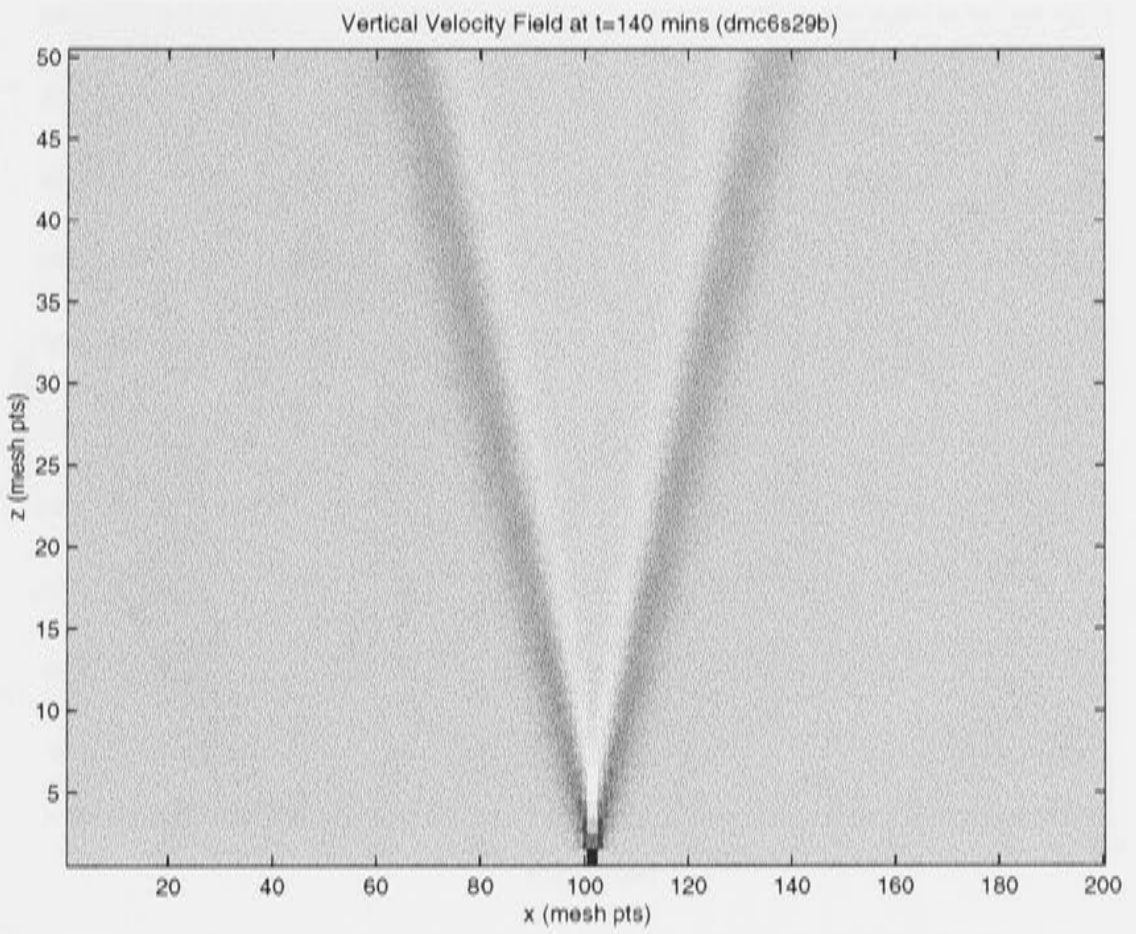

Figure 4.4: Plot of vertical velocity field for radiating dipole experiment

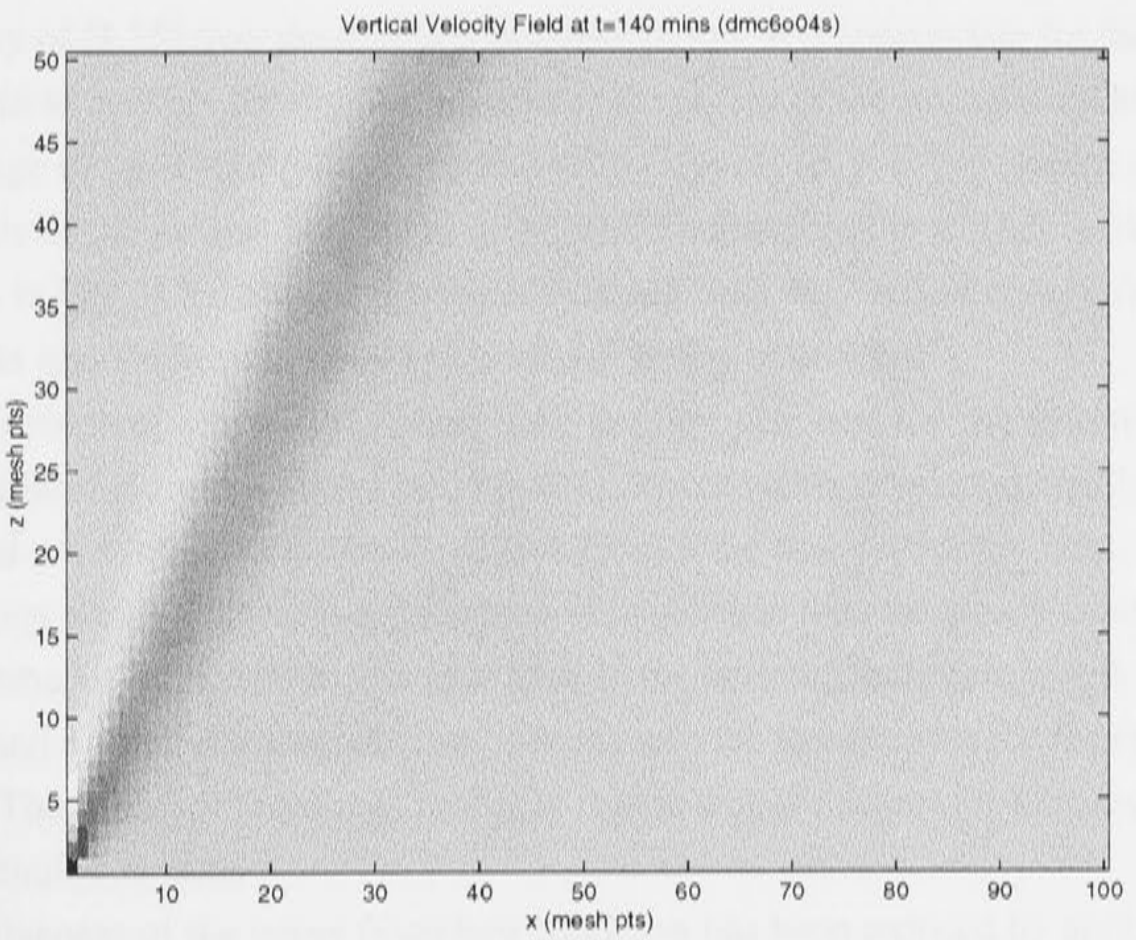

Figure 4.5: Plot of vertical velocity field for symmetry half plane

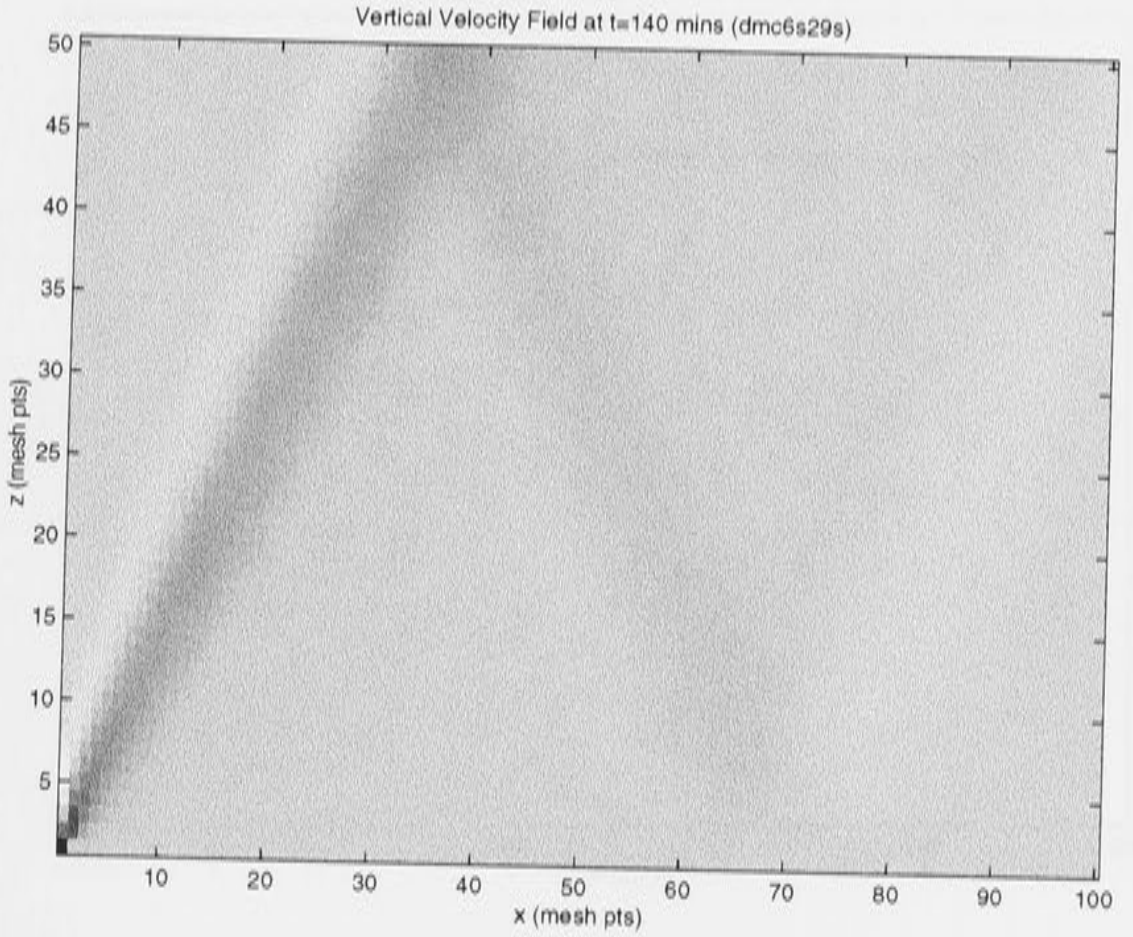

Figure 4.6: Plot of vertical velocity field for symmetry case with partial reflection from upper boundary

With a finite horizontal domain length we are restricted to an approximate version of this integral. To test the effectiveness of the upper boundary condition it is necessary to examine the time history of (4.35) over the duration of a simulation. It is appropriate for the "St Andrews Cross" problem to average the time samples over the period of the source oscillation. A plot of the time average of (4.35) for a dipole source with ($w_0 = 0.16, T = 24$) and measured at three different values of the vertical height ($nz = 20, 30, 40$ corresponding to 1km, 1.5km, and 2km). It can be seen in Fig. 4.7 that after a transient startup time the vertical energy flux at all three vertical heights approaches the same approximate steady state value.

The time evolution of vertical energy flux is also examined for the symmetry boundary condition measured at $z = 20, 30, 40$ (see Fig 4.8). These values also approach the same steady state value and when compared directly (Fig 4.7) with the non-symmetric case, it can be seen that they are very similar. There is a difference in magnitude with the steady state value being a factor of two smaller in the symmetric case (due to the horizontal domain length being a factor of 2 smaller) and a slight (almost constant) deviation in the three curves for the symmetric case at long time. This small difference is probably due to a slight departure from exact symmetry after a long simulation time.

The effectiveness of the upper boundary condition has been reduced by applying the spectral method to only part of the wavenumber spectrum for one run of the numerical model. This has been done so that a comparison can be made to a case where there is visible reflection

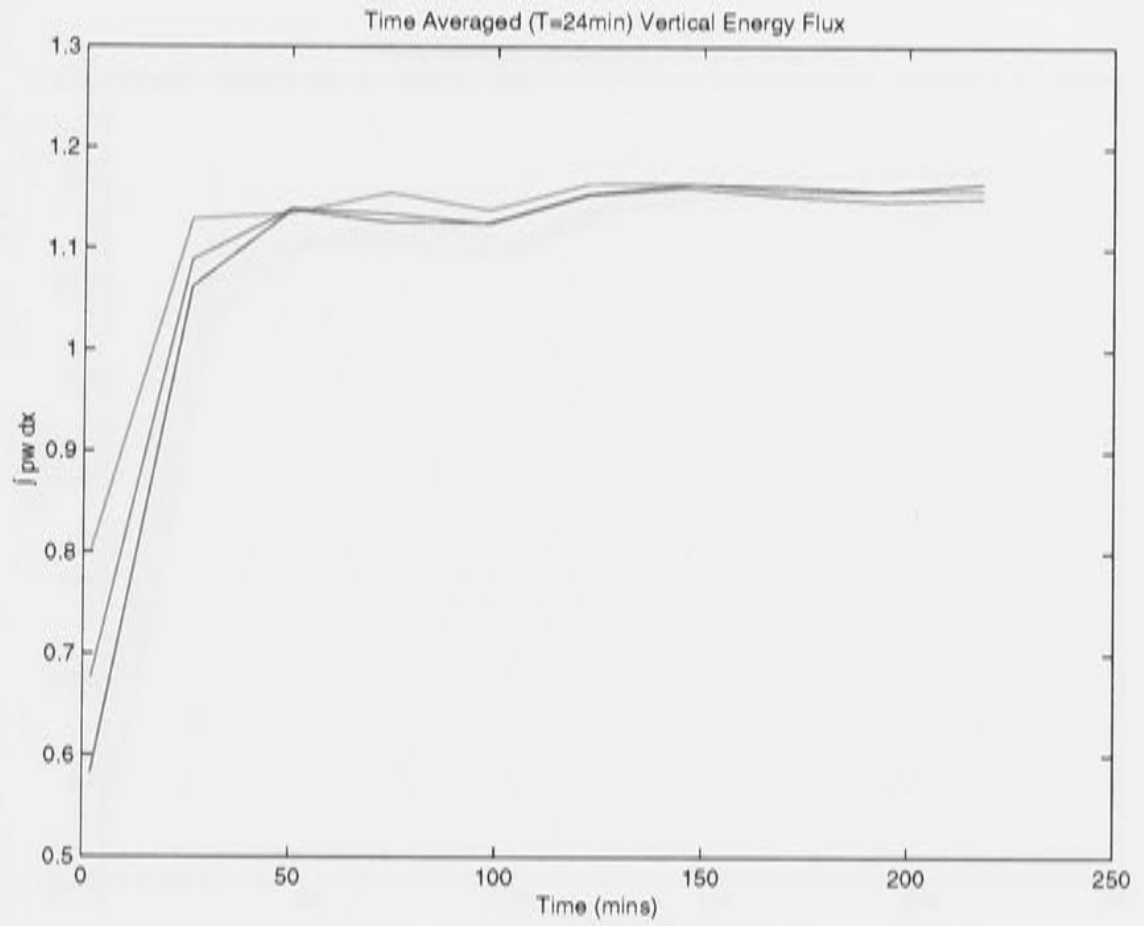

Figure 4.7: Time averaged vertical energy flux measured at 3 values of z (non-symmetric domain).

from the upper boundary (as mentioned above). The vertical energy flux at $z = 20, 30, 40$ for the reflective case, shown in Fig. 4.9, reveals that there is no longer convergence to a common steady state value and also fluctuations in the source averaged vertical energy flux.

The convergence to a single steady state value of the vertical energy flux evaluated at three different heights in the model domain, within a time period that accounts for the vertical propagation of the slowest wave modes, verifies that the upper boundary condition does indeed radiate internal wave energy without reflection.

4.6.3.2 The limited wavenumber spectrum

Due to the dependence of the source wave radiation and the upper boundary condition itself on the horizontal grid resolution it is expected that there will be a limited range of horizontal wavenumbers that can be represented by the numerical model. Using the well known Welch's method of estimating the power spectral density for the horizontal wavenumber spectrum, it can be shown that at a suitable time from startup (after any transient effects) there is a limited wavenumber spectrum that corresponds to the wavenumbers of wave modes emitted by the source (which is dependent on horizontal resolution). It can be seen in Fig 4.10 that non-symmetric and symmetric cases match closely, showing clearly that the limited spectrum of the source radiation is adequately represented in the symmetric case.

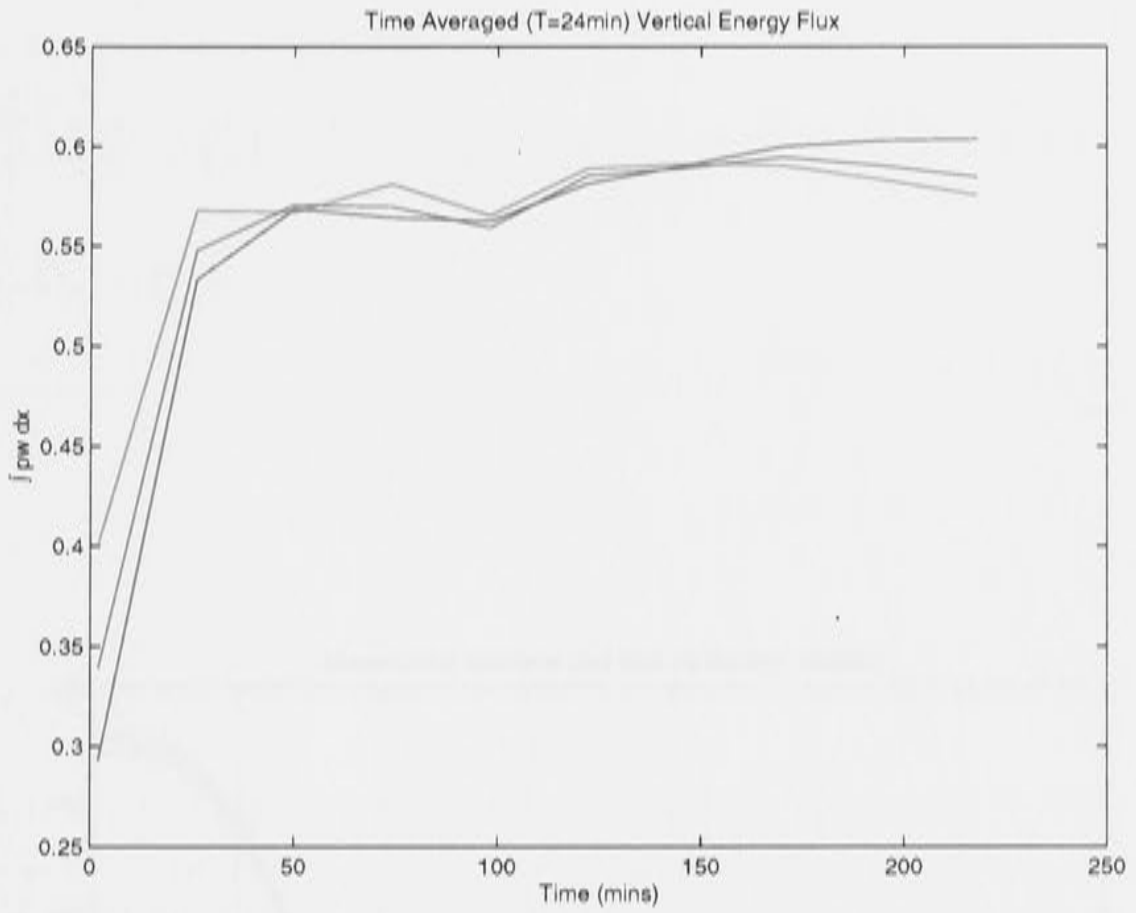

Figure 4.8: Time averaged vertical energy flux measured at 3 values of z (symmetric domain).

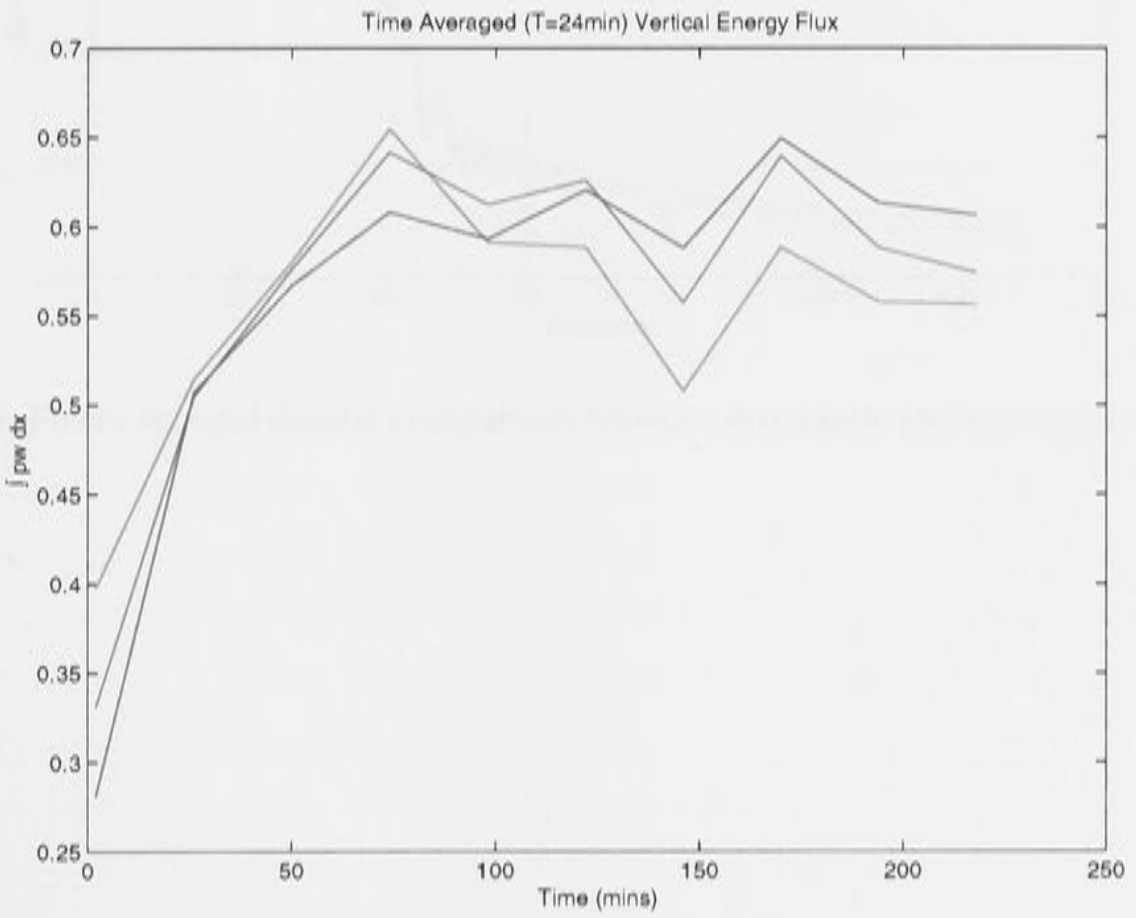

Figure 4.9: Time averaged vertical energy flux measured at 3 values of z (symmetric domain with partial reflection at upper bc).

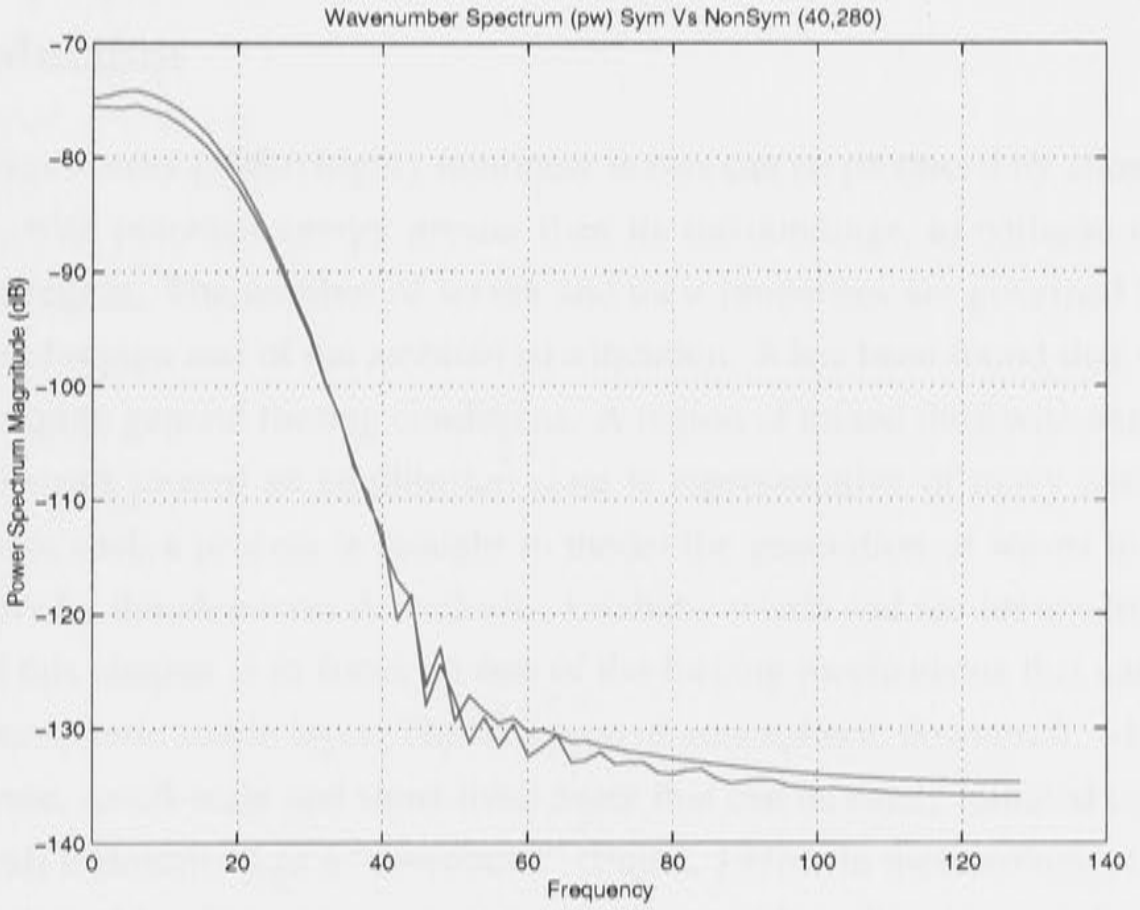

Figure 4.10: Power spectral density comparison between symmetric and non-symmetric cases.

Chapter 5

The Microburst as a Wave Generation mechanism

5.1 Introduction

As shown by Maxworthy (1980) highly nonlinear waves can be produced by allowing a region of mixed fluid, with potential energy greater than its surroundings, to collapse under gravity into a stratified region. The number of waves and their properties are governed by the initial state of the mixed region and of the ambient stratification. It has been found that waves can be produced under quite general forcing conditions. A region of mixed fluid with excess potential energy that collapses toward an equilibrium state is representative of many natural systems. In the atmosphere such a process is thought to model the generation of waves in atmospheric waveguide layers by thunderstorm downdrafts, katabatic winds and sea breeze fronts.

The aim of this chapter is to focus on one of the forcing mechanisms that can give rise to waves in an atmospheric stable layer. This is a type of atmospheric downdraft, which takes the form of an intense, small-scale and short-lived event that can be easily initiated in simulations. Such a downdraft is described as a "downburst" (Fujita, 1976). In meteorological terminology the word "microburst" has become associated with a form of low altitude wind shear that results from a thunderstorm downburst of relatively small diameter (less than 4km) interacting with the ground and producing a strong outflow. Microburst type downdrafts have been observed to generate strong vortex motions in outflows that are produced as a result of an impact with the ground or a low-lying stable layer. Some downdrafts have also been observed to generate vorticity, in the form of a vortex ring, at the leading edge of the descending flow, prior to contact with any low level atmospheric structure.

For wave motions to be produced as the result of a microburst impact, suitable atmospheric conditions must exist. As mentioned previously such conditions usually take the form of a ground-based lower layer which is stably stratified. The primary effect of the stable layer is to absorb or transfer the momentum of the microburst and produce stretching of vorticity. The boundary at the ground can cause dissipation of vorticity if the disturbance penetrates to the

ground. The stable layer therefore provides a conduit for the transfer of kinetic energy from the downdraft into wave energy. It is possible to roughly categorize the different types of possible impact as belonging to one of three states; non-penetrating, if the downdraft does not penetrate to the ground; diverging or non-diverging, depending on whether or not an outflow is produced after impact with the ground. Young and Lane (1989) have studied these three regimes in the laboratory for descending thermals of dyed fluid with different buoyancy deficits and minimal initial vortex rollup. A Richardson number is assigned as a parameter to predict which of these three conditions is likely to occur. Many other studies have been made of thermals in the laboratory and these are reasonable approximations to many types of short duration limited-area downdrafts. Laboratory studies have examined thermals formed by the sudden release of a buoyant mass of fluid (eg Scorer, 1957; Turner, 1963). The motion of such thermals in two dimensions for a homogeneous fluid has been shown to fit that of a vortex pair (Lilly, 1964; Turner 1973). There have also been laboratory studies of a vortex ring impinging on a density interface far away from any boundary (Linden, 1973; Dahm et al., 1989), but these studies have not examined the generation of secondary flows after the disturbance of the density interface.

In a two layer system, the interaction of a thermal with a stably stratified layer is expected, for a suitable Richardson number based on downflow speed, to produce a gravity current along the layer (eg Britter and Simpson, 1981). The disturbance generated is similar to that formed as a result of mixed region collapse in a stratified fluid. Studies of the mixed region case (Maxworthy 1989; Wu, 1969) have shown that it is possible to generate internal waves in the stratified fluid and in Maxworthy's experiments highly nonlinear waves with closed circulation were generated.

It is well known that density currents in stratified fluids will evolve, after sufficient time, into a family of amplitude ordered solitary waves at the leading edge of the flow (eg Maxworthy, 1980; Christie, 1989; Simpson, 1987). A sufficiently strong gravity current in a stratified medium, will undergo a process by which the gravity current head separates from the feeder flow and travels as an independent mass of fluid. This process may occur many times. The internal waves that are generated in the stratified medium and encapsulate the propagating detached fluid masses are comparable to those observed in the experiments of Davis and Acrivos (1967) and Maxworthy (1989) who relate them to highly non-linear solitary wave solutions with closed streamline flow within the waves. Laboratory studies of Noh et al. (1992) and Manasseh et al. (1998) examine the important transition from a flow governed by the advective motion of buoyant fluid, to a wave dominated flow, after a buoyant parcel has impacted a shallow stratified layer.

Although they have been a focus of laboratory studies, there are no detailed numerical studies of large amplitude solitary waves generated by the impact of a negatively buoyant fluid parcel onto a stably stratified layer. Because of its usefulness as a simplified model for wave formation as the result of microburst events and also as a means of producing suitable large

amplitude solitary waves for study, we study this process using the numerical model described in previous chapters. The use of a numerical model has many advantages in such a study. It is possible to generate high resolution data for the velocity and thermodynamic fields which would be difficult to obtain in field or laboratory experiments.

5.2 Description of observed microburst features

A microburst event is characterized by a strong localized downdraft that produces strong horizontally spreading winds after impacting the ground. Microbursts commonly occur within the thunderstorm environment or during rainshowers. In these cases the formation of the microburst is precipitation-driven, as cooling accelerates a moisture-laden mass of air downwards. Microbursts are often observed to produce a ring vortex at the leading edge of the horizontal outflow. This vortex motion is often visible due to dust or rain advected by the strong circulation. Meteorological definitions of a microburst vary. The first definition of a microburst was given by Fujita (1981,1985) who also subdivided microbursts into either "wet" or "dry" types based on the amount of precipitation measured at the ground. This definition has presented some problems since it is often difficult to accurately determine the amount of precipitation. Therefore, microbursts are alternatively classified as "low reflectivity" or "high reflectivity" based on their peak radar reflectivity (Roberts and Wilson, 1986). The aim here will be to present those features of observed microbursts that are not strongly linked to microphysical processes and can be compared to a simple model of a microburst to be presented in the next section.

In examining precipitation-driven downdrafts it is important to note that no obvious precipitation may be visible by the time the downdraft reaches the ground. It is the structure of the parent storm that dictates the form of a thunderstorm outflow. Most downdrafts that are associated with significant precipitation and surface rain have parent storms with a low cloud base (between a few hundred meters to around 3000 meters), whereas those with a high cloud base (around 4000 meters) generally have any precipitation limited to a region directly below the cloud base and the downdraft falls through a significant height before reaching the ground with little or no rain observed at the surface. This type of microburst is often referred to as "virga" (in reference to the precipitation visible just below cloud base), dry or low reflectivity. The principal forcing mechanism for any of these cases is the buoyancy (precipitation) driven evolution of a convective cell.

Another mechanism that can account for a more localized small scale turbulent downdraft is that of the "penetrative downdraft" which is driven by evaporative cooling. The entrainment of dry air into a penetrative downdraft generally occurs at mid-levels (approx 4-6km) and not through the cloud top. In mature thunderstorms, entrainment of air at mid-levels to compensate for the displaced air of any accelerating downdraft of cold air, can set up strong gradients

in the vertical profile of potential temperature which can then support an intense penetrative downdraft drawn from the updraft core of the storm.

In observations of the "virga" type downdraft, the downward acceleration begins below a high altitude cloud base and the large vertical distance that such a downdraft traverses often allows for the evolution of vortex rings around the descending downdraft. As air converges into the downdraft, it is seen to narrow (from observations of the visible virga shaft) and as the downward acceleration decreases the frontal area is seen to broaden into a "mushroom" style cap. This bears a strong similarity to the formation of spherical vortex rings from a sinking thermal and the transfer of kinetic energy into the internal circulation (Scorer, 1957; Richards, 1963; Lilly, 1964; Turner, 1973). This divergence of the flow at the leading edge of a descending downdraft has only been observed for virga type downdrafts from high cloud-based dry thunderstorms. However laboratory experiments suggest that such vortex ring formation can occur at low levels as well and horizontally propagating vortex rings are commonly associated with microbursts that have impacted with the ground (described as "rotor vortices") after low-level generation from a thunderstorm downdraft.

5.3 A simplified model

A simple method of generating waves in a simulated stable layer is to allow a thermal to fall under gravity and impact a stably stratified layer. An important issue here will be the transition from advection to wave dominated flow. Such a simulation provides a simple parallel to wave generation mechanisms in the thunderstorm environment. The pre-existing stable layer on the ground may, in some cases, be the remains of the outflow of an earlier thunderstorm.

Before defining the experimental setup, there are several issues to resolve. The first is the form of the thermal or buoyant plume. Here we would like something that can roughly approximate a descending thunderstorm downdraft. For this reason a spherical blob of fluid is chosen to represent a volume of air that is colder than its surroundings at a height D above the ground. When the blob is allowed to fall under gravity it assumes the familiar form of a descending plume with an axisymmetric vortex ring at the leading edge.

5.4 Dynamics of Thermals

The evolution of the cold mass of fluid has a configuration that resembles a ring vortex. However at the moment of release it does not possess any circulation, kinetic energy or forward momentum. Instead the circulation is generated as it descends (the vortex roll up). Hence it is best described as a cold "thermal" in atmospheric terminology. As the thermal starts to descend the circulation increases as a hydrostatic buoyancy force acts on the column of buoyant fluid located along the central axis.

As described by Scorer (1957), when a thermal has achieved its final configuration, the circulation round the thermal is proportional to wz_f and therefore constant. Here w is the vertical velocity of the front of the thermal and z_f is the distance fallen. Scorer (1957) presents the following approximations to the average frontal width l, downward frontal velocity w, and mean buoyancy b of a descending axisymmetric thermal:

$$l = \alpha z_f, \tag{5.1}$$

$$w = C_1 Q^{\frac{1}{2}} z_f^{-\frac{1}{2}}, \tag{5.2}$$

$$b = C_2 Q z_f^{-2}, \tag{5.3}$$

where Q is the total released buoyancy and α, C_1, C_2 are constants determined empirically for a particular flow regime.

5.5 Dimensional Analysis

The experiments of Noh et al. (1992) and Manasseh et al. (1998) examine several parameters of interest in a transition from advection to wave dominated flow. These parameters include the initial total buoyancy of the thermal, the descent velocity of the thermal, the penetration depth into the lower layer, the speed of any resulting gravity current and the speed/amplitude parameters for any resulting internal waves.

The initial buoyancy deficit of an region of volume V_0 and potential temperature θ_0 is defined as:

$$Q_0 = \frac{\theta_0 - \bar{\theta}}{\bar{\theta}} g V_0, \tag{5.4}$$

where $\bar{\theta}$ is the potential temperature of the surrounding air. Q_0 is treated as essentially a 2D entity due to the 2D nature of the numerical model.

The parameters governing the ambient environment are illustrated in the diagram of Fig 5.1. H_0 is the initial height of the blob (from the ground), h is the depth of the lower waveguide layer, and $\bar{\rho}(z)$ is the ambient density profile. This diagram represents a two layer system where N_1 is the buoyancy frequency of the lower layer and N_2 is the buoyancy frequency of the upper layer (zero for neutral stability). If σ, a dimensionless parameter representing the degree of stratification over the scale depth h, is defined as

$$\sigma = hN_1^2/g, \tag{5.5}$$

then the density profile in Fig 5.1, representing a smooth transition from the upper layer with

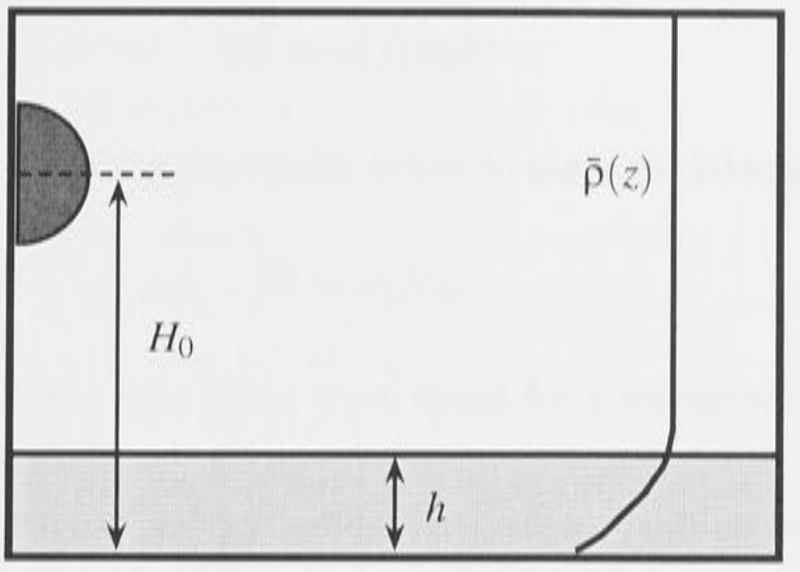

Figure 5.1: Model setup for falling blob experiment

$N_2 = 0$ to the lower layer with N_1, can be defined as

$$\bar{\rho}(z) = \rho_0(1 - \sigma \mathrm{Tanh}(z/h)), \tag{5.6}$$

where ρ_0 is the density at the ground. Using potential temperature, the corresponding ambient profile is

$$\bar{\theta}(z) = \theta_0/(1 - \sigma \mathrm{Tanh}(z/h)), \tag{5.7}$$

where θ_0 is a reference temperature at the ground. It is assumed that calculations fall within the deep fluid category and are independent of the depth of the domain. Dimensional scales will be non-dimensionalised using the depth of the waveguide layer h.

A Richardson number or inverse square internal Froude number is defined for the interface between upper and lower fluid regions. This is calculated using the downflow speed of the thermal at the height of the interface but calculated without taking into account any interaction with the interface. If Q_0 is used to represent the buoyancy deficit of a blob released instantaneously at height H_0 above the ground in a model with a lower stable layer of scale depth h (so that the downflow speed is w_1 after the blob has fallen through the height $z_f = H_0 - h$) a Richardson number can be defined as

$$\mathrm{Ri} = N_1^2 h^2 / w_1^2, \tag{5.8}$$

where $N_1 h$ represents the scale speed of linear long waves in the waveguide layer. The inverse

Richardson number or Froude number squared Fr^2 can be written in terms of σ,h and w_1 as

$$\mathrm{Fr}^2 = w_1^2/(\sigma g h). \tag{5.9}$$

It will be convenient in analyzing the results below to use a modified definition of Fr as

$$\mathrm{Fr} = w_1/c_0. \tag{5.10}$$

where $c_0 = \sqrt{(\sigma g h/2)}$ is the long linear wave speed for a waveguide layer defined using the ambient profile given by (5.7).

Considering the transfer of energy within the system, the blob initially has potential energy which is transfered into kinetic energy as it falls and this is ultimately transfered by the waveguide layer into kinetic energy of wave motion. The initial potential energy of the blob is dependent on z_f/h a non-dimensional measure of the distance through which the thermal falls. To allow a clear relation to be formulated between Q_0 and the amplitude a and speed c of a resulting wave, z_f/h will be treated as a independent parameter. A slightly different approach from that of Mannaseh et al. (1998) will be adopted. Mannaseh et al. used a definition of Ri that intrinsically depended on Q_0 through the use of (5.2). Instead the downflow speed w_1 at $z = h$, for each choice of Q_0, will be taken directly from the numerical data.

In deriving a set of non-dimensional parameters to analyze subsequent data there are two main aims. The first is the derivation of a Richardson number to relate the downflow speed of the thermal at height $z = h$ to $N_1 h$, the scale speed of linear long waves for the stable layer. As shown in the experiments of Young and Lane (1989), the Richardson number or inverse internal Froude number can be used as a parameter predicting the type of impact. In the following experiments the Froude number has been used to establish a parameter range for which large amplitude internal wave motions can be generated in the stable layer. The second aim is to derive a relation between the non-dimensional amplitude and the speed of a generated wave (denoted by a/h and c, respectively), the initial state of the blob (represented by the non-dimensional parameters z_f/h, $Q_0\bar{\theta}_0/g$), and the impact regime (represented by $\mathrm{Fr} = w_1/c_0$). Empirical data is obtained for the functional relationships denoted by

$$a/h = f_1(\alpha, \beta, \mathrm{Fr}), \tag{5.11}$$

$$c/c_0 = f_2(\alpha, \beta, \mathrm{Fr}), \tag{5.12}$$

where $\alpha = z_f/h$ and $\beta = Q_0\bar{\theta}_0/g$, and $c_0 = \sqrt{(\sigma g h/2)}$.

5.6 Definition of the Starting "Blob"

The initial condition in the simple model of a microburst discussed above is an isolated "blob" of cold air prescribed instantaneously at startup as a perturbation of the ambient atmosphere. This can also be thought of as a gravity driven cold air mass ("cold pool") which produces a two-dimensional axisymmetric "thermal" and results in generation of vorticity as the thermal descends. The idea here is to model the downdraft process (from thunderstorms) which can disturb stable layers in the atmosphere and produce wave motions. A cold pool of air defined in a similar fashion has been used by Anderson et al. (1986) in a simple model of the thunderstorm subcloud environment. Also, Drogemeier (1988) has used a similar functional form as a "plume" forcing mechanism for a distribution of rainwater in a model of a microburst. The initial mass of cold air is defined in terms of a temperature perturbation by the following functions:

$$q(x,z) = \sqrt{(\frac{x-x_0}{x_r})^2 + (\frac{z-z_0}{z_r})^2}, \tag{5.13}$$

$$\theta'(x,z) = -T_p \cos^2(\mathrm{Min}[q(x,z),1]\frac{\pi}{2}), \tag{5.14}$$

where T_p is the magnitude of the peak temperature perturbation. The function $\theta'(x,z)$ is displayed in Fig 5.2. The associated pressure perturbation field is initially assigned using the hydrostatic condition:

$$\frac{\partial \Pi'}{\partial z} = \frac{g\theta'}{C_p(\bar{\theta}(\bar{\theta}+\theta')}, \tag{5.15}$$

$$\Pi'(x,0) = 0, \tag{5.16}$$

where $\bar{\theta}$ is the ambient potential temperature.

The initial buoyancy deficit Q_0 of the blob defined above is calculated as:

$$\bar{Q}_0 = 4\frac{g}{\bar{\theta}_0}\int_{x_0}^{x_r}\int_{z_0}^{z_r}\theta'(x,z)\mathrm{dxdz}. \tag{5.17}$$

This can be evaluated as:

$$\bar{Q}_0 = -\frac{gx_r z_r}{\bar{\theta}_0}\frac{T_p}{2}(\pi - \frac{4}{\pi}). \tag{5.18}$$

The evaluation of $\bar{Q}_0$ given above assumes that Q_0 is uniform and therefore makes an approximation (across the 2D volume cross section) to (5.14). This means that (5.14), which is a spatially varying non-linear function in (x,z), is approximated as a uniform temperature distribution in terms of T_p. Values of $\bar{Q}_0$ are evaluated using (5.18) for analysis only and comparison of results. The use of $\bar{Q}_0$ alone will not completely define the characteristics of a starting blob

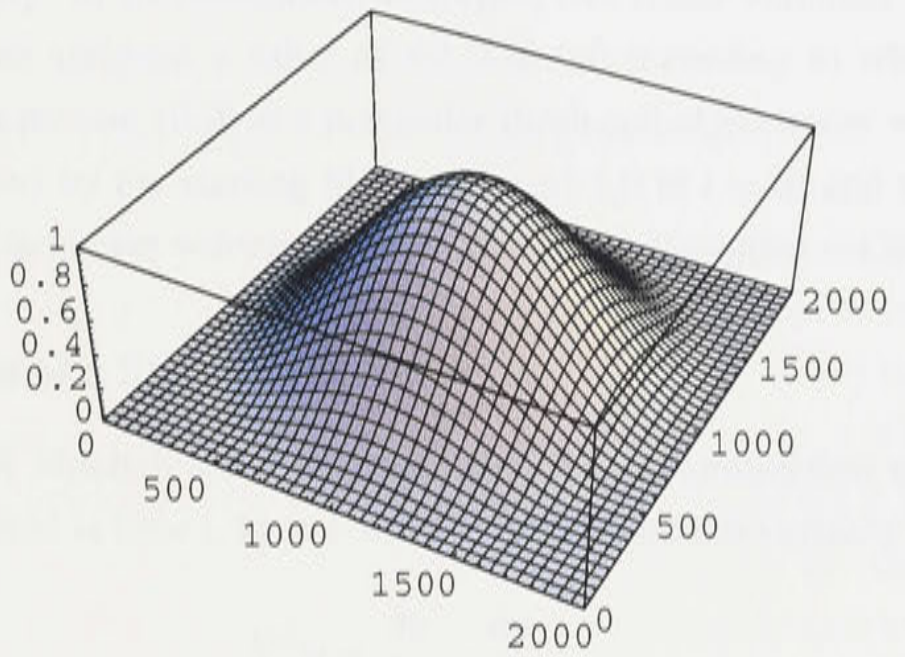

Figure 5.2: Mathematica Plot of Blob field $[x_r = z_r = 1000.0]$

due to this assumption of uniform temperature.

Although the definition of a starting blob presented here makes any direct analysis complicated, it represents a more physically realistic atmospheric disturbance than a blob of uniform temperature and has been found to provide a perturbation that is computationally stable across the range of different mesh resolutions that have been used. It is believed that real downdrafts behave in a similar fashion to a descending axisymmetric thermal albeit with horizontal shear playing a major role. Some experiments will therefore also be carried out in which the falling thermal descends in an ambient shear flow.

5.7 Experimental Tools

5.7.1 Use of Passive Tracers

In the experiments that follow it is useful for flow visualization to include additional tracer variables in addition to the main governing equations. The passive tracer concentration is updated according to advective and diffusive processes only and can be compared to the use of physical tracers such as dyes to visualize fluid flow in laboratory experiments. The equation used to update a tracer variable ξ is:

$$\frac{\partial \xi}{\partial t} + u\frac{\partial \xi}{\partial x} + w\frac{\partial \xi}{\partial z} + K_\xi^x \frac{\partial^2 \xi}{\partial x^2} + K_\xi^z \frac{\partial^2 \xi}{\partial z^2} = 0. \tag{5.19}$$

This equation is independent of the governing equations presented in chapter 3. The first part of this equation deals with the advective processes and is governed by the u and w velocity fields, and the second part implements Fickian diffusion with diffusion coefficients K_ξ^x and K_ξ^z as discussed previously. In all simulations to follow, two tracer variables have been used and each has initially been assigned a value of ± 1.0 or 0.0 according to whether tracer fluid is present (± 1.0) or not present (0.0) at a particular mesh cell. One tracer will be used to mark fluid initially contained by the starting blob (assigned 1.0 at $t = 0$) and the other tracer will mark the interface of the lower waveguide layer of depth h (assigned -1.0 at $t = 0$).

5.7.2 Calculation of a Streamfunction

Using the approach of Mitchell and Hovermale (1977) a streamfunction ψ will be calculated, for a particular flow field at time t, by solving the streamfunction-vorticity equation

$$\nabla^2 \psi = \frac{\partial w}{\partial x} - \frac{\partial u}{\partial z}, \tag{5.20}$$

as a boundary value problem for ψ with u and w assigned from the computed velocity fields and ψ assigned appropriate boundary values according to the overall computed flow field. The streamfunction calculation has a boundary condition which imposes an upstream condition based on the estimated wavespeed c_w of the disturbance so that

$$\psi(x, z) = \int_0^z c_w dz' \qquad (x \to -\infty). \tag{5.21}$$

A similar condition is applied downstream of the disturbance. The elliptic equation (5.20) is solved as a boundary value problem using the numerical technique of successive over relaxation (SOR). It should be noted that ψ calculated here is only the rotational part of a flow field that is actually made up of both rotational and divergent components. The divergent component for the atmospheric flows examined here is primarily linked to the sound waves present in the model and such waves are considered to be of limited physical relevance. Therefore, ψ is expected to provide good flow visualization.

In practice the use of (5.20) to calculate relative streamlines and provide a measure of wave amplitude has been found to over-estimate the actual value of a/h for the wave generation experiments in this chapter. This is attributed to a dependence on mesh resolution for the numerical solution of the boundary value problem (5.20), so that for high values of Δx and Δz there will generally be an overestimation of the vorticity associated with the closed circulation cell (and therefore an over-estimation of the size of the cell). The use of different horizontal and vertical grid resolution with the SOR method seems to contribute to this problem. Low grid resolution is expected to cause a type of low pass filtering on the estimate of streamlines associated with a wave. Because of the possible errors in the solution of (5.20) wave amplitudes

in this chapter will be calculated using the vertical displacement of the tracer field marking the interface of the lower waveguide layer. The relative streamlines provided by the solution of (5.20) will be provided in this chapter as a visualization aid only but will be used to calculate wave amplitudes in later chapters where higher grid resolution is used.

5.8 Numerical Experiments (no ambient shear)

Numerical experiments were performed using the mesoscale model and associated boundary conditions described in Chapters 3 and 4. An initial set of control experiments were run with a homogeneous ambient environment so that measurements could be made of the downflow speed of a range of falling thermals originating from starting blobs of different volumes and temperatures. This measurement was made at the height corresponding to the depth of a lower waveguide layer to be used in the remaining experiments (but in the absence of such a layer for the control homogeneous environment). These initial control experiments are grouped as set one. A second set of experiments (set 2) were then used to examine conditions under which a thermal can impact a lower stable layer and produce highly non-linear waves. These experiments all used the same fixed value of σ which defines the variation in potential temperature over the depth of the waveguide layer. The final set of experiments (set 3) examined conditions which result in highly non-linear wave generation for different values of σ.

5.8.1 Set 1: Homogeneous atmosphere (control set with $\sigma = 0; N = 0$)

A set of control simulations were performed with a homogeneous neutral background so that the Brunt-Väisälä frequency N for the whole domain is zero (ie $\sigma = 0$). These simulations are performed on a numerical grid with $\Delta x = 200$ grid points, $\Delta z = 100$ grid points and $K^x = 60m^2/s, K^z = 15m^2/s$. A requirement of simulations that result in wave formation will be a domain of sufficient horizontal extent. This is because in order to allow a generated wave to achieve a quasi-steady state, the numerical domain needs to encompass a wave formation region near the impact zone (produced by the falling blob) and a relatively undisturbed region containing a stable waveguide layer. Due to computational limitations this requires reasonably high values of Δx and Δz. These control experiments used the same grid resolution for consistency. An initial "blob" of buoyancy deficit $\bar{Q}_0$ was used to generate a thermal which falls through height z_f before a measurement was taken of w_1, the downflow speed of the thermal front. The initial volume and peak temperature perturbation of the starting blob were varied to give a range of w_1.

The estimate of downflow speed provided by the formula (5.2) has certain constraints based on the scale of the initial blob and the distance it falls as a thermal. For (5.2) to apply the thermal should have accelerated to a certain speed over a certain scale vertical distance. This scale distance should be of the order of $V_0^{1/2}$ (where V_0 is effectively area in these 2D simulations),

so that the thermal should fall through a distance of the order of a diameter (of the initial blob area) before (5.2) provides a good estimate of the downflow speed as entrainment etc occurs. Because the height a thermal will fall through is only of order a diameter and the temperature perturbation within the blob is actually non-linear, use of formulae (5.2) (which is based on uniform Q_0) will be avoided and the downflow speed w_1 will be estimated directly from numerical data. All the simulations below represent a thermal that has fallen through a short vertical distance z_f, with minimal vortex rollup, before impacting a ground based stable layer. The downflow speed w_1 is calculated as the speed of the thermal front, the vertical position of which can be recorded by observing the evolution of the tracer variable representing the fluid initially contained by the blob.

The tables 5.1, 5.2 and 5.3 show normalized buoyancy deficit $\bar{Q}_0$ versus w_1 for different values of z_f. Here the non-dimensional normalized estimate $\bar{Q}_n$ is defined as

$$\bar{Q}_n = \bar{Q}_0 \bar{\theta}_0 / (V_{00} g), \tag{5.22}$$

where V_{00} is a reference cross sectional area of $1000\pi\ m^2$ and $\bar{\theta}_0 = 287.0$K. The value of w_1 is estimated using the tracer field to keep track of the progress of the thermal front. This is done by using a flag within the computer algorithm that records the value of the vertical velocity at $z = h$ when the value of the tracer field there first increases past a threshold value (as the front passes this point). A larger than ideal value of Δz has been used in order to retain consistency over all wave generation simulations.

Tables 5.1, 5.2 and 5.3 present a range of w_1 a starting blob of variable volume (defined using the normalized volume $V_n = V_0/V_{00}$) and temperature distribution (denoted by the peak value T_0 K), for three different values of the initial height of release given by $H_0 = 3.5, 4.0, 4.5$ km. The values of w_1 displayed in the tables show that $\bar{Q}_n$ alone is not adequate to represent the properties of the starting blob. Therefore the three parameters $[\bar{Q}_n, V_n, T_0]$ will be included in all subsequent results.

A last consideration of these control experiments is the effect of the various numerical boundary conditions on the flow dynamics. The top and RHS boundary conditions are radiative boundary conditions which allow gravity wave energy to leave the domain without reflection and allow disturbances to be freely advected from the domain. These boundary conditions are discussed in detail in the previous chapter. In terms of the flow dynamics the bottom and LHS boundary conditions need further discussion. The bottom boundary condition is an implementation of a rigid free-slip condition. Simpson (1972) and Simpson and Britter (1979) have examined the effects of a rigid no-slip lower boundary on the dynamics of a gravity current head. Simpson (1972) concludes that the lower boundary is fundamental to the nature of the substructure (ie mixing processes) associated with the current head and that a no-slip condition at the lower boundary will result in convective instability as the head propagates over a thin layer of less dense fluid. Lui and Moncrieff (1996) find that the use of a free-slip (rather

Q_n	V_n	T_0 (K)	w_1 (m/s)
2.23	3.0	2.5	3.93
4.46	3.0	5.0	5.55
6.68	1.5	15.0	7.36
8.91	3.0	10.0	7.98
8.91	1.5	20.0	9.24
13.37	3.0	15.0	9.87
17.83	3.0	20.0	11.59
17.83	4.0	15.0	10.20
22.30	5.0	15.0	10.00
23.78	4.0	20.0	12.00
29.73	5.0	20.0	11.63

Table 5.1: Values of Q_n and w_1 for $H_0 = 4.0$ km

Q_n	V_n	T_0 (K)	w_1 (m/s)
6.68	1.5	15.0	8.34
13.37	3.0	15.0	9.82
17.83	4.0	15.0	10.80
22.30	5.0	15.0	10.60

Table 5.2: Values of Q_n and w_1 for $H_0 = 4.5$ km (constant $T_0 = 15$ K)

than the no-slip) condition in their numerical model of an advancing gravity current produces some different results from the laboratory experiments of Simpson and Britter, with a head wind tending to raise the height of the density current head and a tail wind tending to flatten it (which is different from the result in the laboratory experiments). A symmetry boundary condition (as described in the last chapter) is imposed on the LHS of the domain for all experiments described below. The symmetry of the flow field will break down at some point after the impact of a blob with the waveguide layer as nonlinear interactions increase. It is therefore expected that there will be a region of spurious nonlinear interactions near the LHS boundary in the vicinity of the impact zone. This is clearly observed in surface pressure measurements in the experiments below. It is believed that these spurious interactions do not significantly affect the solution of interest since they are limited to a zone near the LHS boundary whilst the wave disturbance propagates to the right away from the impact zone within a short time period. The use of a LHS symmetry condition allows a much larger horizontal domain length to be studied than would otherwise be possible under the computational limitations of these experiments.

5.8.2 Set 2: Impact Regime

As the falling downdraft collapses into the lower stratified layer it experiences a sharp increase in the degree of stratification which causes rapid deceleration. This process, for minimal vortex rollup, has been studied in detail in the laboratory by Noh et al (1992), Young and Lane (1989)

Q_n	V_n	T_0 (K)	w_1 (m/s)
6.68	1.5	15.0	8.39
13.37	3.0	15.0	9.87
17.83	4.0	15.0	7.88
22.30	5.0	15.0	7.55

Table 5.3: Values of Q_n and w_1 for $H_0 = 3.5$ km (constant $T_0 = 15$ K)

and others. Some of the downdraft air will begin spreading horizontally at the top of the stratified layer. The downdraft air is generally colder than that in the boundary layer, hence we can expect convective as well as shear instabilities. As mentioned above, the different types of possible impact can be described as non-penetrating, diverging or non-diverging. In the non-penetrating impact the downdraft does not reach the ground but loses its energy to horizontal spreading before it has penetrated far. A non-diverging impact penetrates to the ground but does does not then continue to spread horizontally but is confined to a limited impact region. In contrast to this a diverging impact continues to spread horizontally into a sustained outflow. The experiments presented in this chapter will concentrate on diverging outflows that can generate highly nonlinear waves. Scorer (1978) provides an analytic method for predicting the type of outflow generated in the impact. This method takes into account the density difference and the velocity at impact. The same general idea has been used here and the prediction of the impact regime as either diverging or non-diverging will be defined entirely by the use of $\mathrm{Fr} = w_1/c_0$.

A set of experiments are presented in this section to classify the different impact regimes. These experiments use a [199x99] point mesh with $(\Delta z = 100\mathrm{m}, \Delta x = 100\mathrm{m})$ so that the domain is 20km by 10km. The Fickian diffusion coefficients are set as $K^x = 15\mathrm{m}^2/s, K^z = 15\mathrm{m}^2/s$. The horizontal domain length is just large enough to see whether the impact produces a potential wave forming diverging outflow. The lower stratified layer has been defined as part of the ambient environment using a tanh function, as described previously, with σ used as a parameter representing the degree of temperature variation over the depth of the layer. A set of values of Fr are obtained for a range of impact regimes resulting from a starting blob with variable parameters $[V_n, T_0, w_1]$. This process is repeated for both $\sigma = 0.026$ and $\sigma = 0.040$. A set of experiments with higher resolution $(\Delta z = 50\mathrm{m}, \Delta x = 50\mathrm{m})$ are re-run to examine the processes involved within the impact zone for the different cases.

The three different regimes can be summarized as follows. In the first case, the thermal only penetrates a limited distance into the lower layer before its energy is dissipated due to horizontal spreading. This is shown in Fig 5.3 where Fig 5.3(a) (at $t = 900$ secs) shows the thermal penetrating a limited distance and the beginning of horizontal spreading and Fig 5.3(b) (at $t = 1290$ secs) displays the impact after the majority of the thermals energy has been transfered into horizontal motion.

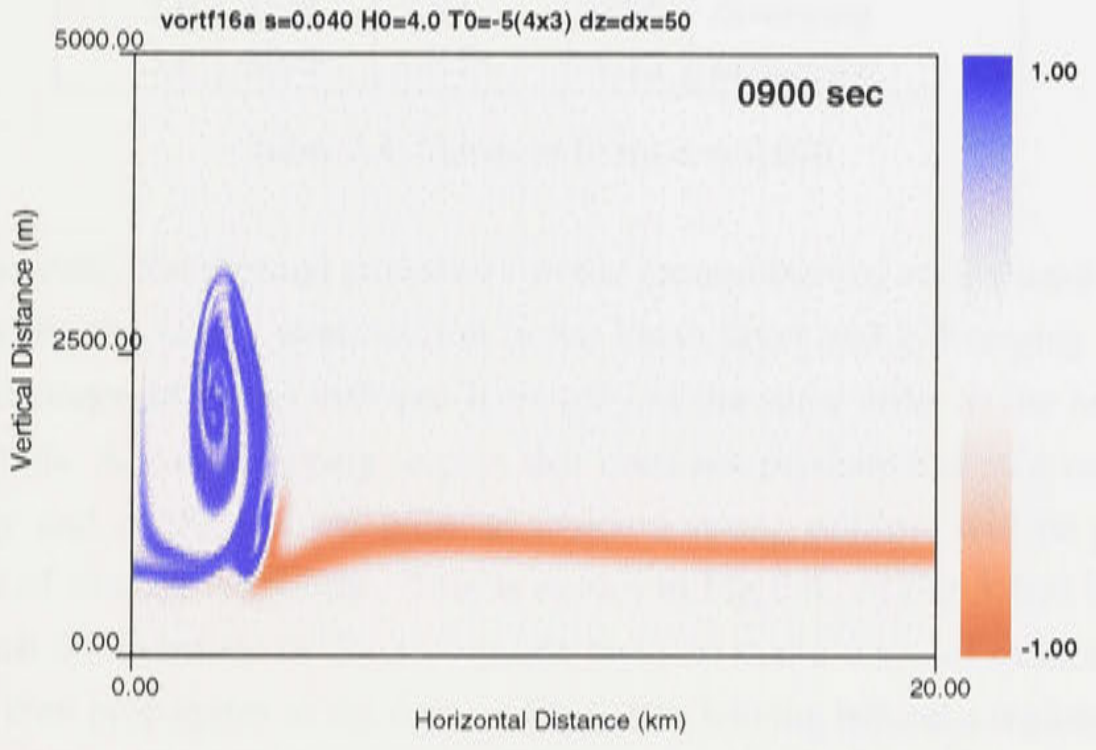

(a) Non-penetrating case (at 900 secs)

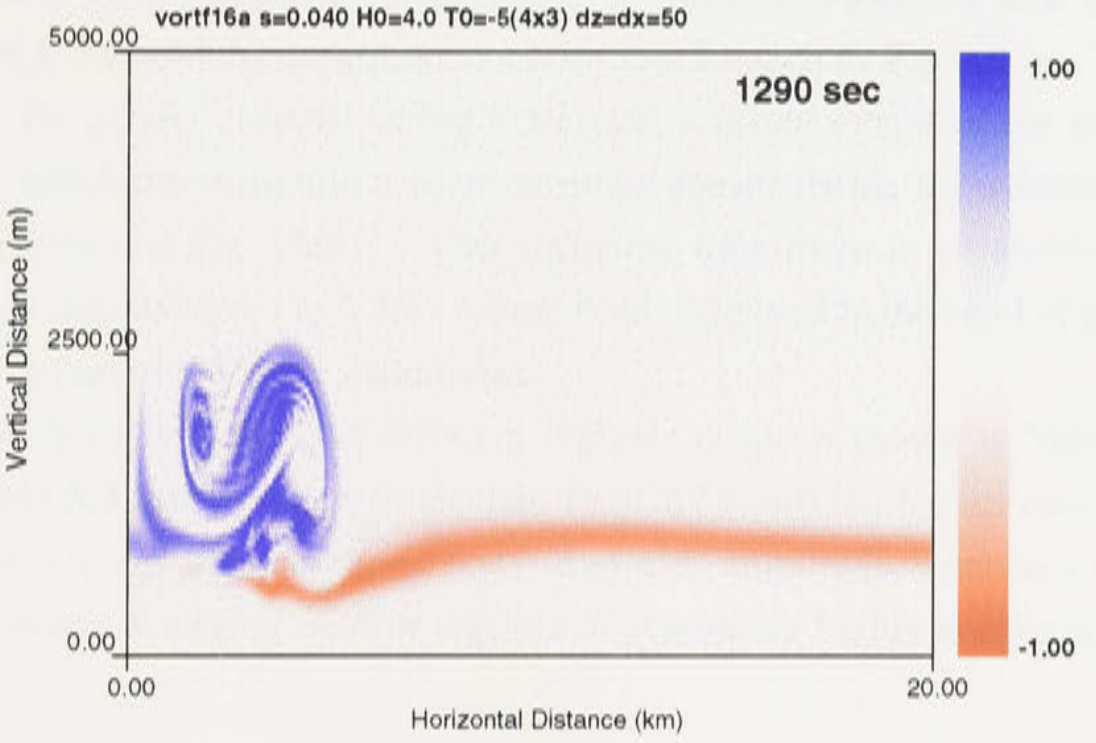

(b) Non-penetrating case (at 1290 secs)

Figure 5.3: Tracer fields for non-penetrating case. The blue tracer represents fluid initially contained by the starting blob; the red tracer denotes the interface of the lower layer. Note in (a) there is a limited penetration depth and the beginning of horizontal spreading. (b) The energy of impact is transfered into horizontal spreading

V_0/V_{00}	T_0 (K)	w_1 (m/s)	Fr	regime
3.0	2.5	3.93	0.38	non-penetrating
3.0	5.0	6.67	0.64	non-diverging
3.0	10.0	7.98	0.77	almost diverging
3.0	15.0	9.87	0.95	diverging
3.0	20.0	11.59	1.12	diverging

Table 5.4: Values of Fr for $\sigma = 0.026$

In the second case, the thermal penetrates to the ground but the vortex motion of the thermal is dissipated by the strong stratification in the lower layer and a diverging outflow is not produced. The distance of vortex collapse is roughly of the same order as the horizontal scale of the starting blob. A non-diverging impact that does not produce a strong outflow, but has sufficient energy and is close to the point at which a strong outflow will be produced, can generate a wave of modest amplitude. This is shown in Fig 5.4. In Fig 5.4(a) the impact can be seen to perturb the interface of the waveguide layer so that a wave of modest amplitude is generated. This then propagates to the right in Fig 5.4(b) leaving behind a region of vortex collapse in the vicinity of the impact zone. The third and final case results in a diverging outflow at the ground. A case showing the development of a highly nonlinear wave from the outflow is shown in Fig 5.5. Here the initial enhancement of vorticity associated with the impact and the generation of a horizontally propagating vortex can be seen in Fig 5.5(b). This results in a strong outflow (ie gravity current) in Fig 5.5(c) and a displacement of the interface of the waveguide layer which develops into a wave envelope encapsulating the detached head of the gravity current (shown in Fig 5.5(d)). After sufficient time there is a transition to a highly nonlinear wave, as displayed in Fig 5.5(e), where fluid contained in the head of gravity current is now advected as part of the wave disturbance.

The range of Fr for which these different regimes occur is shown in Table 5.4. It can be seen from Table 5.4 that a value greater than Fr ≈ 0.7 is needed for the case $\sigma = 0.026$ to produce an impact capable of generating a wave of modest amplitude, whereas a value Fr ≈ 0.9 is required for a strong diverging outflow capable of generating highly non-linear waves.

The diverging outflow

For our requirements the diverging impact is of most interest due to the high probability of wave generation, particularly for the formation of highly nonlinear waves (amplitude greater than order of waveguide depth) which form closed circulation cells that transport mass. However the following experiments will also study several impacts that generate a wave of modest

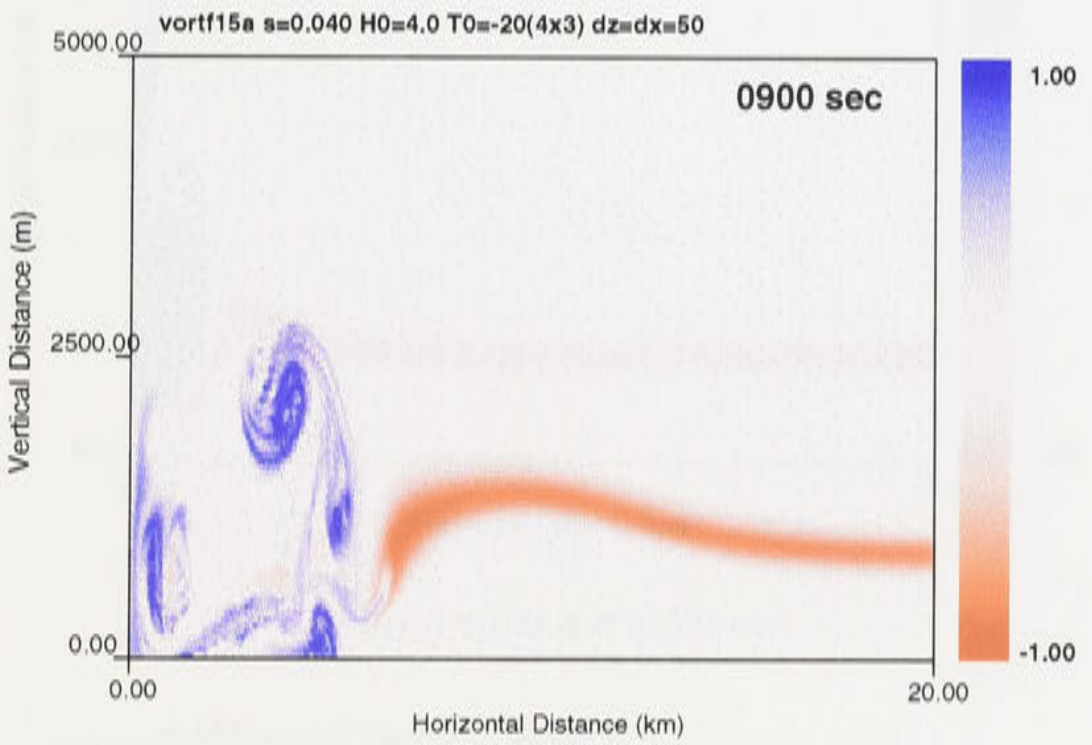

(a) Borderline diverging case (at 900 secs)

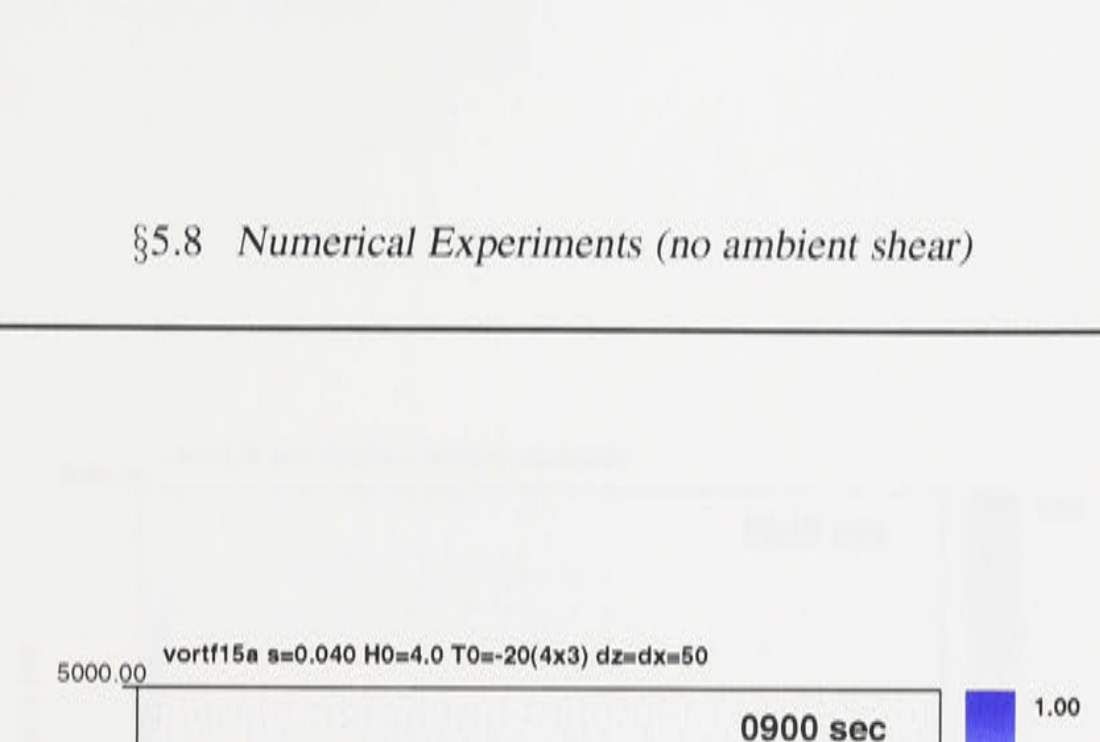

(b) Borderline diverging case (at 1290 secs)

Figure 5.4: Tracer fields for borderline diverging case. The blue tracer represents fluid initially contained by the starting blob; the red tracer denotes the interface of the lower layer. Note in (a) there is sufficient energy in the impact to generate a wave of modest amplitude; in (b) the region of vortex collapse in the wake of the wave

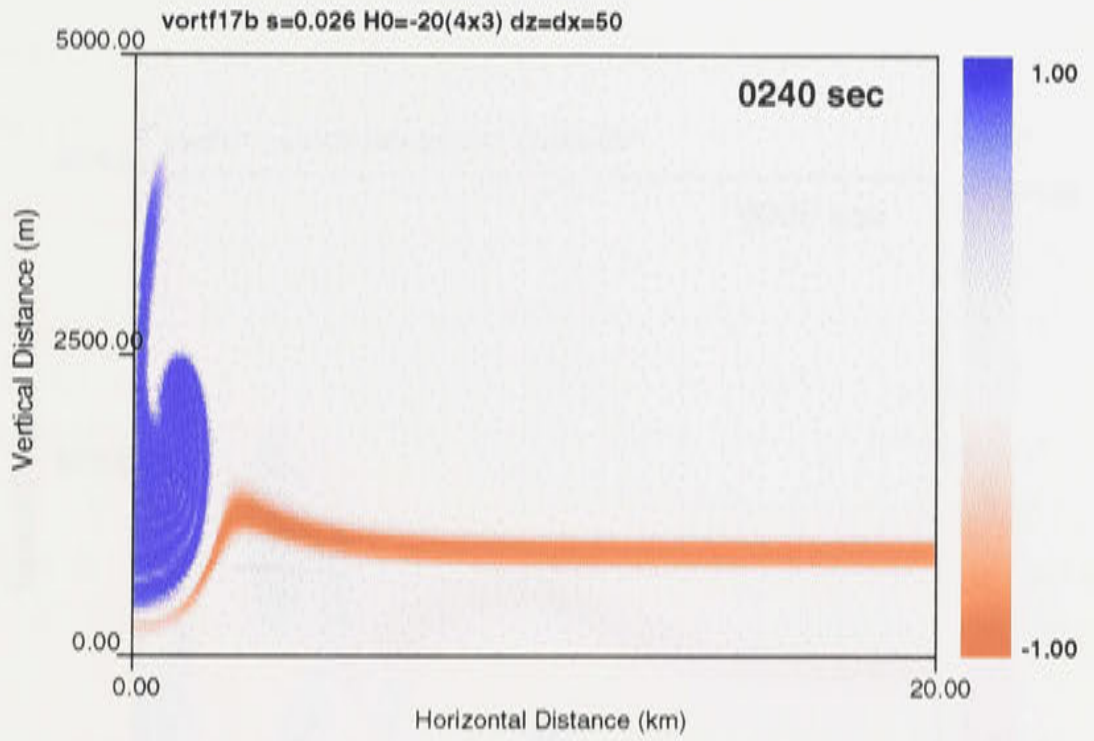

(a) The diverging case at 240 secs

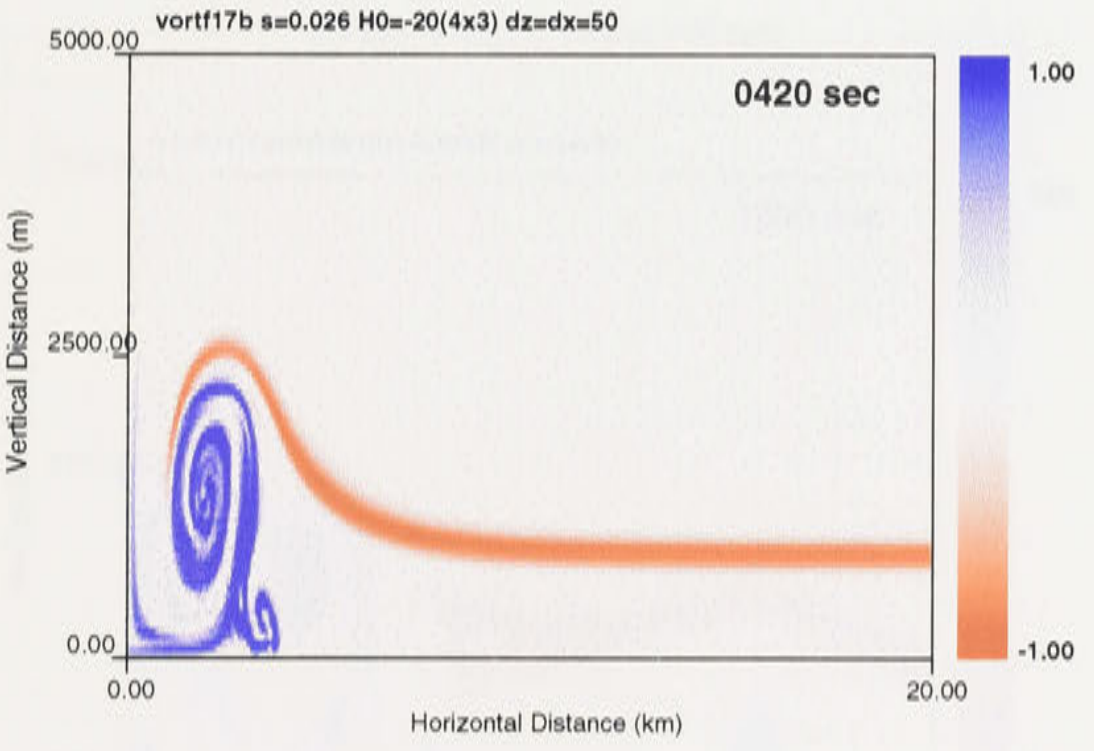

(b) The diverging case at 420 secs

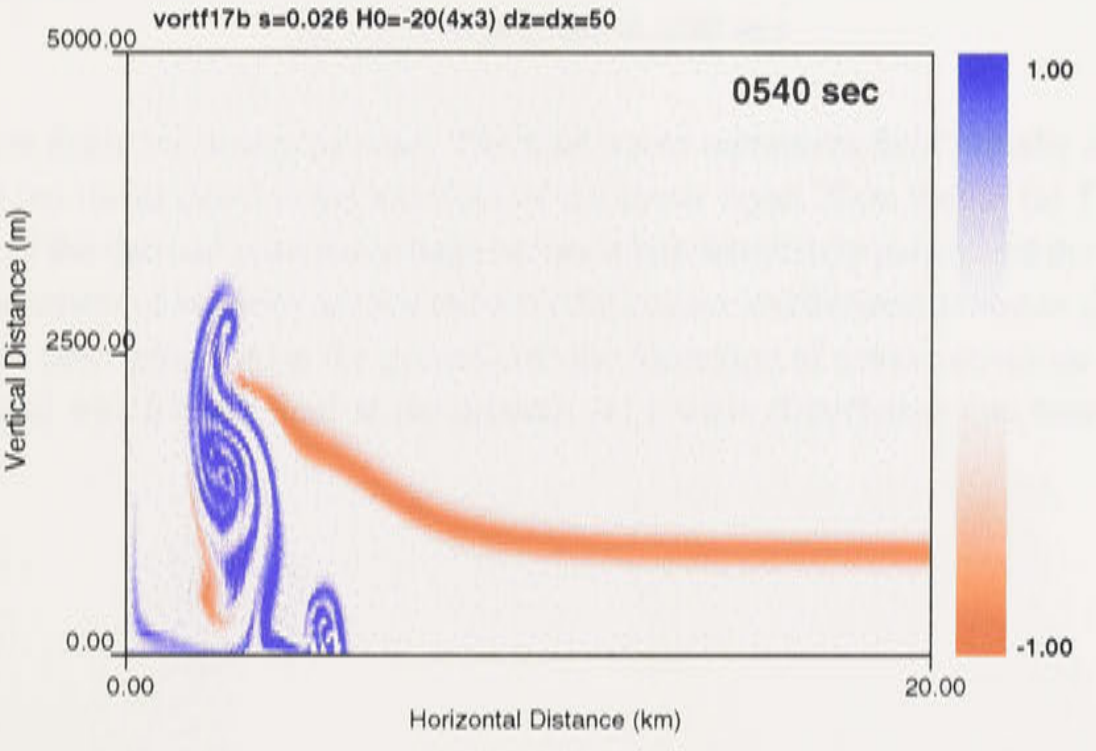

(c) The diverging case at 540 secs

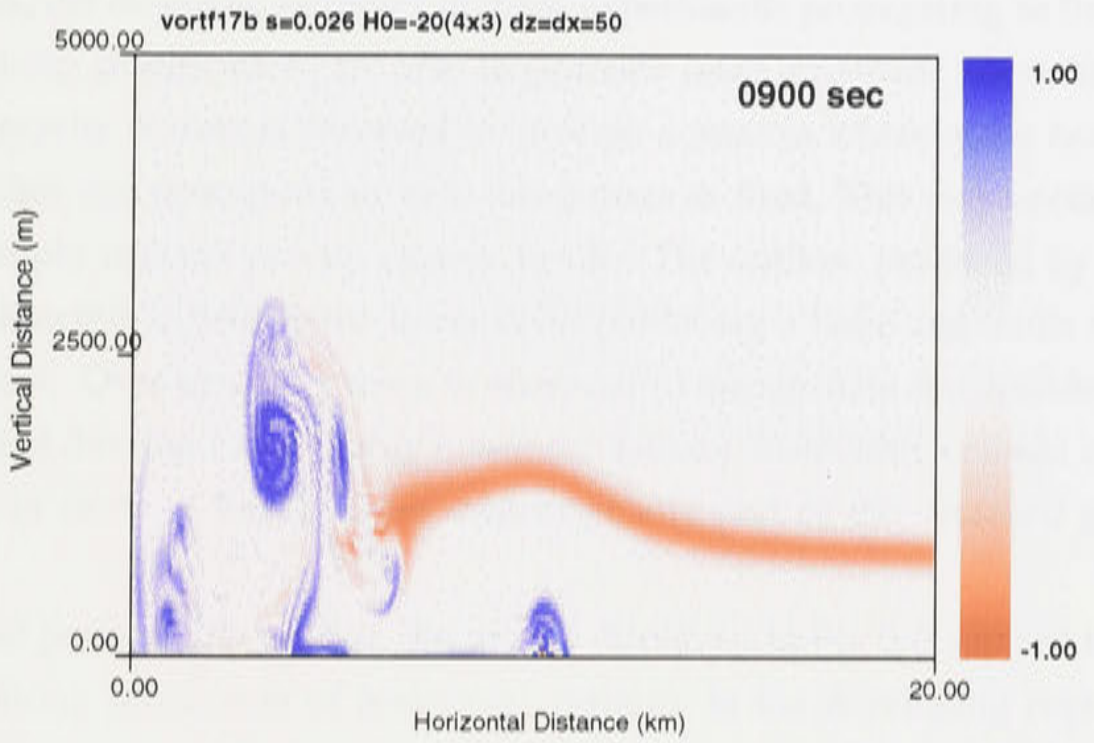

(d) The diverging case at 900 secs

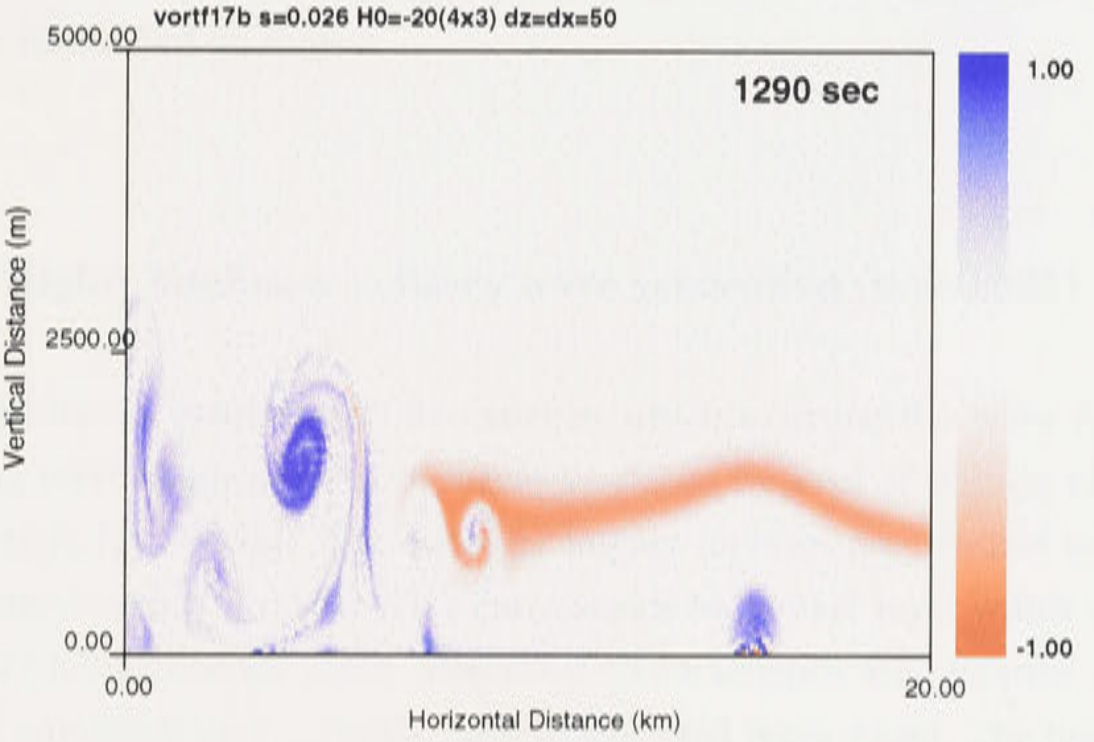

(e) The diverging case at 1290 secs

Figure 5.5: Tracer fields for diverging case. The blue tracer represents fluid initially contained by the starting blob; the red tracer denotes the interface of the lower layer. Note that in (a) The figure shows the initial impact of the thermal at an early stage before it has completely penetrated the stable layer; (b) There is an enhancement of vorticity associated with the impact and horizontal vortex generation; (c) A gravity current has been generated at the ground; (d) the formation of a wave envelope over a detached gravity current head which leaks fluid at the ground; (e) a wave disturbance that transports fluid as a first order effect

amplitude. The diverging outflow takes the form of a gravity current and has a well defined structure consisting of a head and trailing flow. As described by Simpson (1981) for laboratory experiments, the diverging outflows in these experiments propagating in the lower region of stable continuous stratification, are able to generate large amplitude waves in the stratified layer. Also the gravity current is observed to undergo a process whereby the head of the gravity current detaches and propagates as an isolated mass of fluid. This may occur several times resulting in multiple isolated gravity current heads. The outflow produced by the impact of the thermal is observed to perturb the lower layer producing a large amplitude wave ahead of the gravity current. Over time this wave is observed to encapsulate the detached head of the gravity current and develop into a highly nonlinear solitary wave with a closed circulation cell (which consists of some of the fluid that was originally part of the detached gravity current head).

At the impact point on the ground, the results displayed in Fig 5.5 support the conclusion that there is a strong production of horizontal vorticity in the developing region, where the vertical velocity is being reduced to zero and the radial velocity is just beginning to increase as distance increases from the center of the downdraft. We would expect a vortex stretching mechanism to be at work and any strong vortex zone already at the edge of the downdraft will have its vorticity intensified on impact.

5.8.3 Set 3: Highly nonlinear solitary wave generation ($\sigma = 0.026$)

A set of experiments are presented in this section which examine the wave formation process and resulting wave characteristics of waves produced by a set of starting blobs classified using the parameters $[\bar{Q}_n, V_n, T_0]$. The different impact regimes are denoted using Fr for an ambient environment with $\sigma = 0.026$. This corresponds to a lower layer which is stably stratified and an upper homogeneous layer. The wave characteristics are recorded using a/h the non-dimensional amplitude and c_w/c_0 the non-dimensional wave speed. The linear long wave speed for the waveguide layer is given by

$$c_0 = \sqrt{\sigma g h/2} \tag{5.23}$$

so that for $\sigma = 0.026$, $c_0 = 10.4$m/s. These experiments use a [499x99] point mesh with $(\Delta z = 100\text{m}, \Delta x = 200\text{m})$ so that the domain is 100km by 10km. The Fickian diffusion coefficients are set as $K^x = 60\text{m}^2/s, K^z = 15\text{m}^2/s$. The horizontal domain length chosen provides an adequate distance for clear wave formation over most of the experimental parameter range. Initially a set of experiments were run for a range of starting blobs with fixed temperature distribution (denoted using T_0), constant H_0, and variable volume V_n. This process was repeated

to produce a second set of results for different value of T_0. A third set of experiments was run using a different value of H_0.

Properties of solitary wave solutions

The properties of a resulting solitary wave disturbance are recorded using non-dimensional amplitude and wave speed. As mentioned above the estimate of wave amplitude a/h is made by measuring the vertical displacement of the tracer marking the top of the lower layer relative to the depth h of the layer. The estimate of wavespeed c_w is made using the horizontal position of the disturbance at a series of time samples. These time samples are chosen (as far as possible given the horizontal domain length) for values of time beyond a point that corresponds to the leading disturbance obtaining a single stable wave form. The horizontal position of the disturbance is most easily obtained by using the perturbation pressure field at the ground where a wave disturbance is clearly identified by a characteristic hump. All the following experiments are analyzed using the amplitude a/h obtained from the tracer field and the surface pressure trace at $(z = 0)$ over a range of simulation time.

By examining the time evolution of each experiment, it can be seen that the impact of the blob with the stable layer creates a diverging outflow of limited duration. Initially this resembles a gravity current with a well formed head. The head of the gravity current can be seen to detach and as it propagates through the lower layer it generates a wave envelope that, after sufficient time, encapsulates the fluid that made up the gravity current head and propagates as a stable wave formation with a region of recirculating fluid. Using the pressure traces to measure the horizontal position of the disturbance, the propagation speed of the disturbance can be shown to vary during this wave formation process. The plots of surface perturbation pressure for a fully developed wave are similar to those produced for theoretical solutions to the DJL equation by Brown (1995) and Brown and Christie (1998). Looking at the time evolution of the surface perturbation pressure it can been seen that there is initially a strong negative perturbation as a result of the vortex cell of the gravity current head and that this develops into a surface perturbation signal that is similar to those associated with solitary waves.

First set of experiments

The first set of experiments uses a starting blob with $T_0 = 20.0$ K, $H_0 = 4.0$ km and a range of volumes $V_n = 1.5, 3.0, 4.0, 5.0$ producing a range of Froude numbers given by Fr $= 0.89$, 1.11, 1.15, 1.12. The depth of the waveguide layer is $h = 850$m. The relative streamlines and

surface pressure traces at $t = 72$ min are displayed in Figs 5.6(a), 5.6(b), 5.6(c) and 5.6(d). Here Fr $= 0.89$ results in a wave of modest amplitude. Highly non-linear wave formation occurs within the horizontal dimensions of the domain for all other values of Fr except in the experiment with $V_n = 4.0$ where it is clear from the pressure trace that the disturbance is still propagating as a gravity current head at $t = 72$min. The reason for this is probably related to the transfer of momentum at impact. The calculated speed is greater than that expected from a wave of similar amplitude. This case has been examined in detail by re-running the experiment using a domain with a horizontal length of 160km. These results are summarized in Table (5.5). The parameter w_n is used to record the number of waves produced. A $(*)$ in the table denotes that the wave formation process is still incomplete after 100km (the standard horizontal domain length used in these simulations).

Detailed examination of $V_n = 4.0$ case

It was found that given sufficient horizontal distance the disturbance for the case with $V_n = 4.0$ evolves into a wave. Initially the head of the gravity current (which is generated in the impact) has a height which is greater than the depth of the waveguide layer. This can be seen in Fig 5.7(a) using the tracer which corresponds to fluid initially contained in the thermal before the impact. It is clear that up to $t = 72$ min there has been little loss of tracer from the gravity current head through leakage of fluid at the ground. The speed of this gravity current head is faster than that of a wave with amplitude corresponding to a comparable displacement of the interface.

Compared to a plot of the tracer field at the same time for the experiment with $V_n = 5.0$, shown in Fig 5.7(b), it can be seen that the $V_n = 5.0$ case results in a wave which advects only a very small amount of tracer mostly visible through leakage of fluid in the wake of the wave. A gravity current can be seen at approximately 35 km. This gravity current is what remains of the original strong outflow, produced after the initial impact, which was the source from which gravity current heads detached (in a repeated process of head formation and detachment) and propagated ahead during the evolution of the two visible wave disturbances. The speed of this gravity current is much less than that of the waves. The experiment with $V_n = 4.0$ can be compared to the work of Haase and Smith (1989). At $t = 72$ mins the disturbance can be considered to be a gravity current with depth exceeding that of the waveguide layer. Its speed would appear to satisfy the case described by Haase and Smith where the gravity current propagates faster than the critical speed needed for waves to be generated on the stable layer. Using the extended domain the experiment with $V_n = 4.0$ can be studied for time beyond $t = 72$ min. The evolution of surface perturbation pressure for $t > 72$ min is shown in Fig 5.8. The perturbation

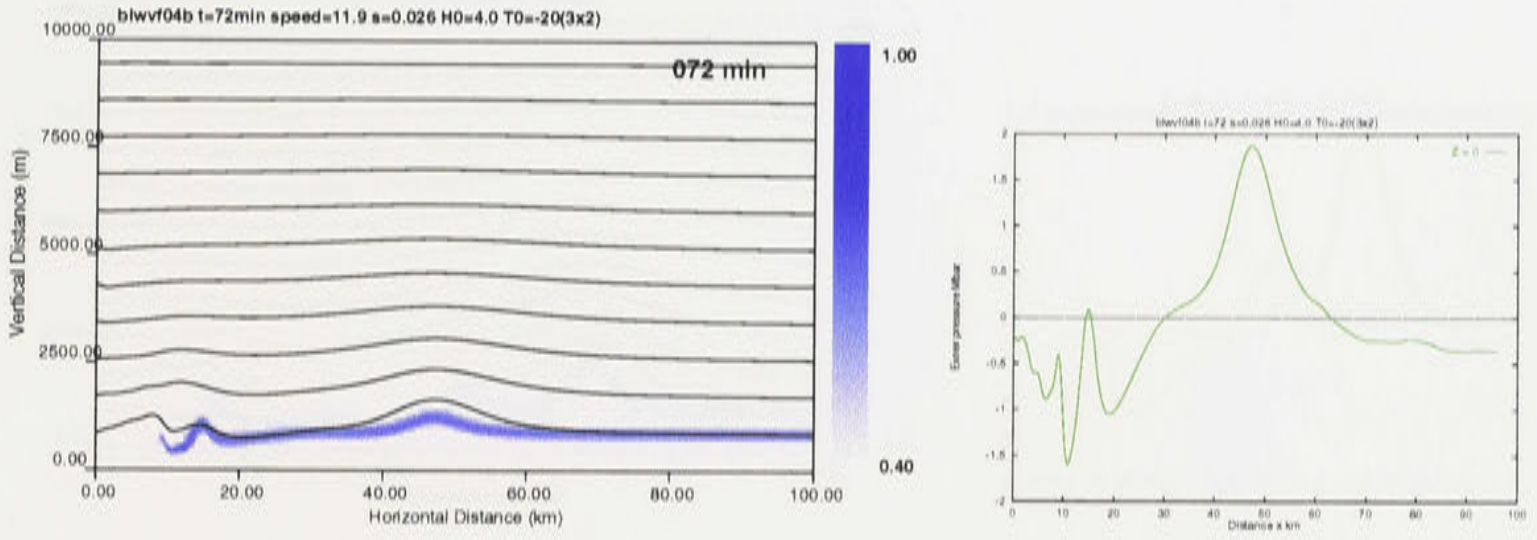

(a) Experiment 1 with $\sigma = 0.026$, $H_0 = 4.0$ km and $T_0 = -20$ K. The starting blob has normalised volume $V_n = 1.5$

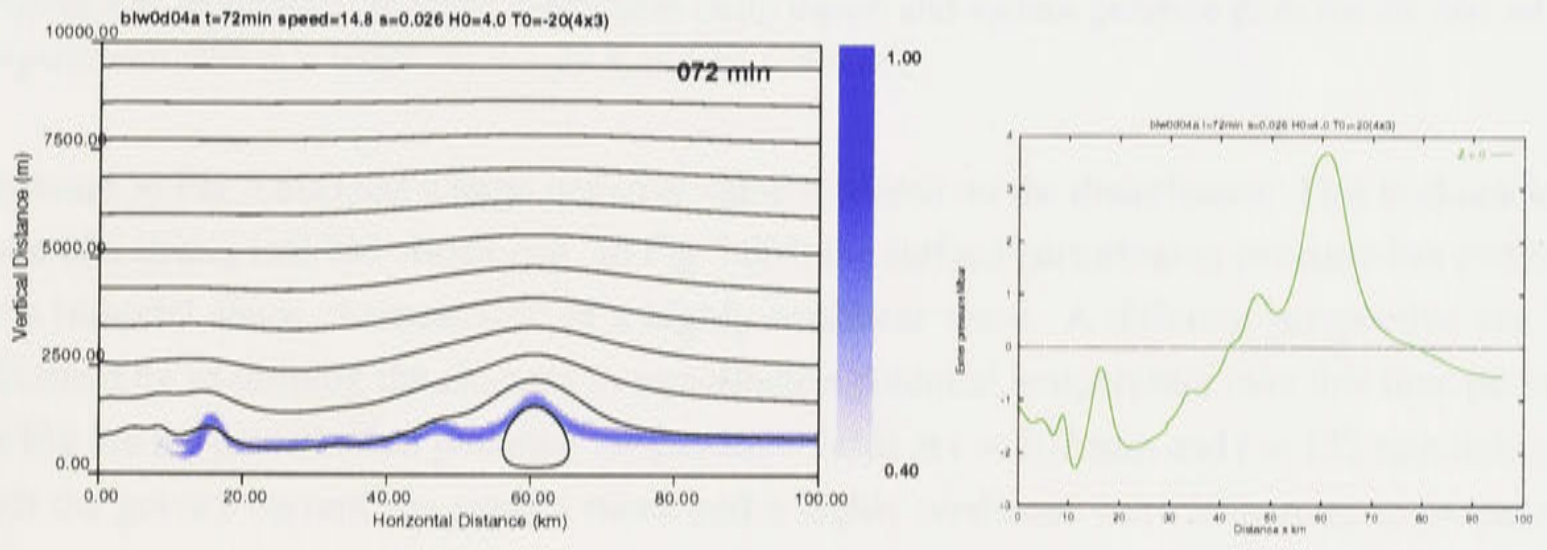

(b) Experiment 2 with $\sigma = 0.026$, $H_0 = 4.0$ km and $T_0 = -20$ K. The starting blob has normalised volume $V_n = 3.0$

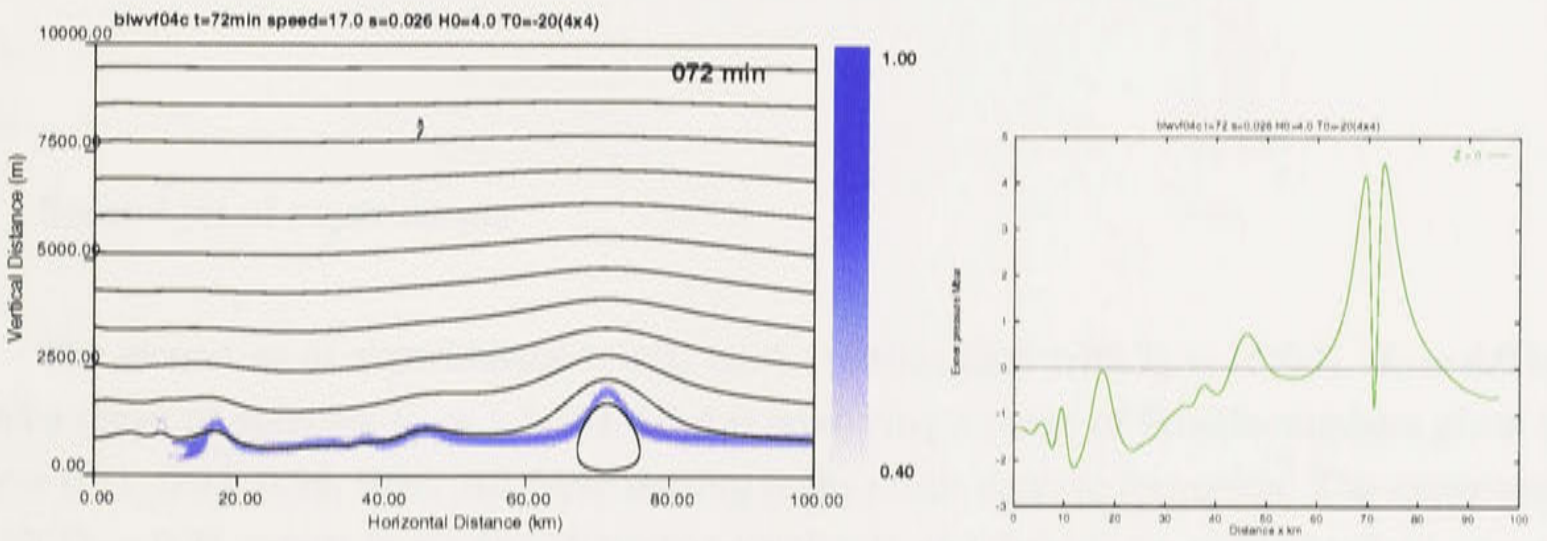

(c) Experiment 3 with $\sigma = 0.026$, $H_0 = 4.0$ km and $T_0 = -20$ K. The starting blob has normalised volume $V_n = 4.0$

Figure 5.6: Relative streamlines (with tracer) and surface pressure plots for the first set of experiments with $\sigma = 0.026$ and $H_0 = 4.0$ km. Note that in (d) the surface pressure trace indicates that the disturbance has not yet developed into a wave.

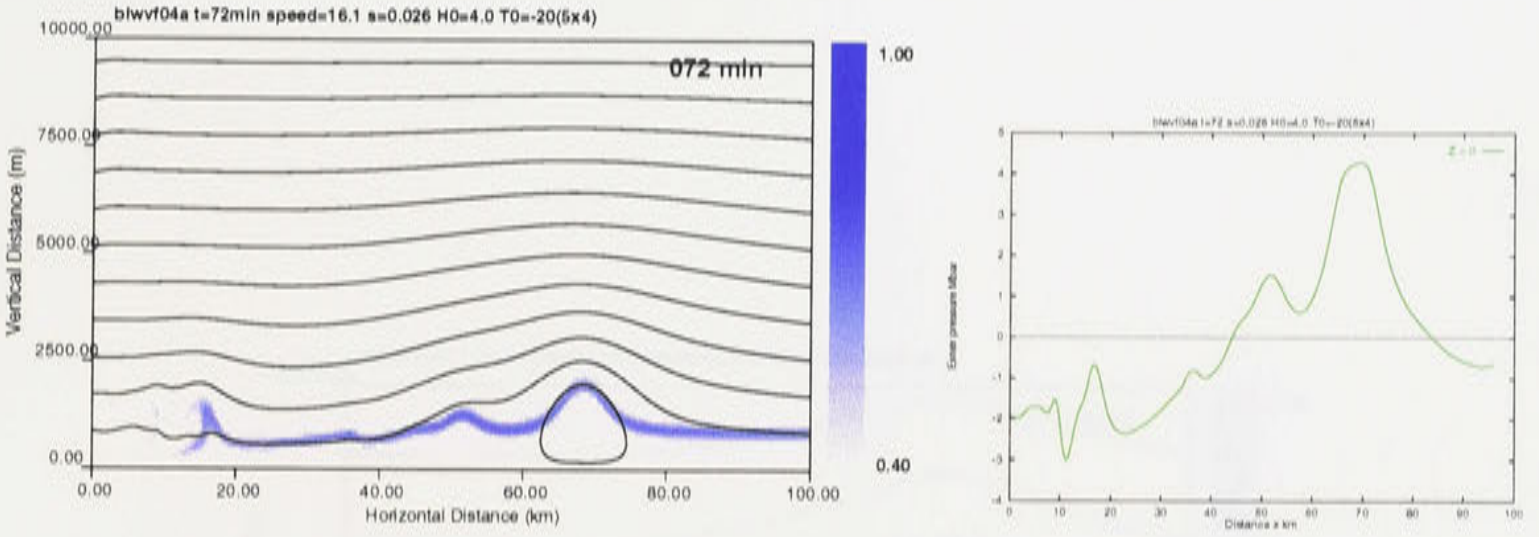

(d) Experiment 4 with $\sigma = 0.026$, $H_0 = 4.0$ km and $T_0 = -20$ K. The starting blob has normalised volume $V_n = 5.0$

Figure 5.6: (continued) Relative streamlines (with tracer) and surface pressure plots for the first set of experiments with $\sigma = 0.026$, $T_0 = -20$ K and $H_0 = 4.0$ km.

pressure in Fig 5.8(a) has a large negative value centered on the disturbance. This is characteristic of a strong isolated vortex cell. In Fig 5.8(d) the surface perturbation pressure has evolved to a bimodal shape characteristic of a highly nonlinear wave. A different perspective can be obtained by examining the changes in perturbation potential temperature over this time period. In Fig 5.9 the perturbation potential temperature fields at $t = 102$ min and $t = 132$ min indicate that the gravity current has slowed down and a highly nonlinear wave is starting to propagate away from its parent gravity current. This is similar to experiments described by Haase and Smith (1989) which show that a detached gravity current head of sufficient size propagating in a stably stratified waveguide layer will evolve into a highly nonlinear wave over time.

Second set of experiments

The second set of experimental results used a starting blob with $T_0 = 15.0$ K, $H_0 = 4.0$ km and a range of volumes $V_n = 1.5, 3.0, 4.0, 5.0$ producing a range of Froude numbers given by Fr = 0.71, 0.95, 0.98, 0.96. All these starting blobs result in wave formation. The experiment with Fr = 0.71 results in a wave of modest amplitude and there is no strong outflow present. The other values of Fr all result in the formation of highly non-linear waves that develop as the wave envelope of a detached gravity current head. The resulting wave properties for the waves produced are given in Table 5.5.

Many of the experiments performed in this chapter result in multiple wave formation. It can be seen in the experiments with $V_n = 3.0$ and $V_n = 5.0$ that there are multiple waves. For

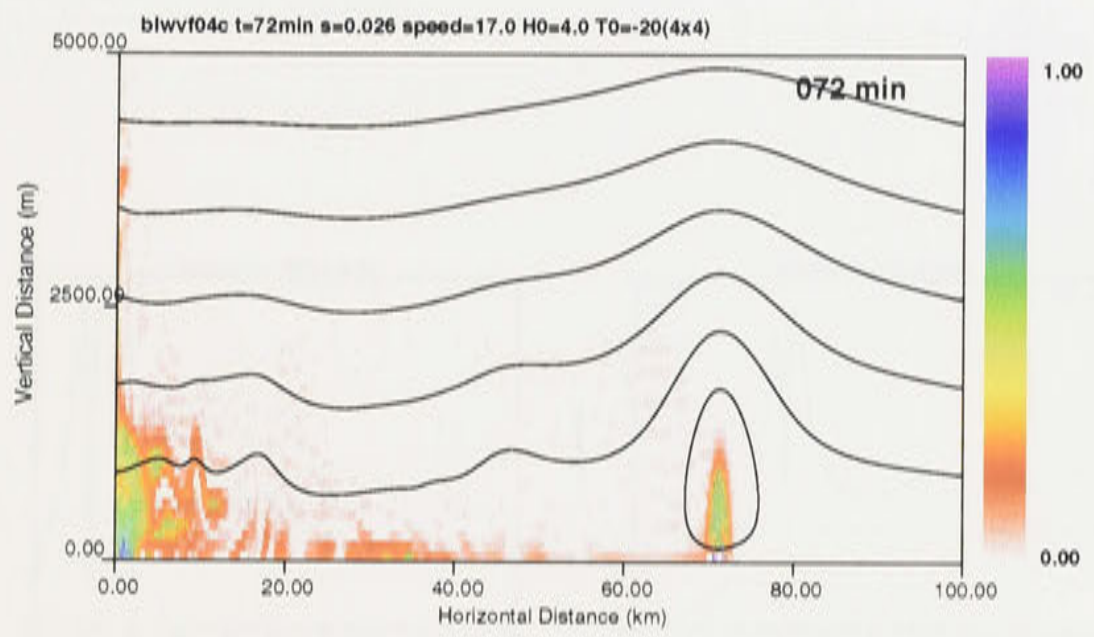

(a)

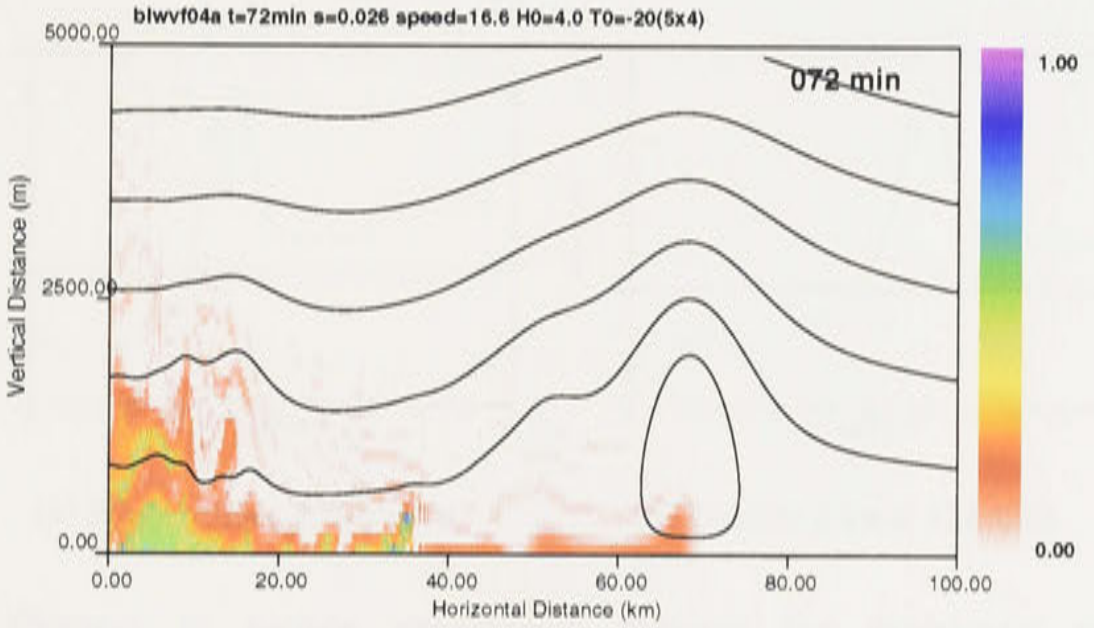

(b)

Figure 5.7: Relative streamlines and tracer field for experiment with $\sigma = 0.026$, $H_0 = 4.0$ km and (a) $V_n = 4.0$; (b) $V_n = 5.0$. The contour scheme is chosen to aid visualization of the tracer and variations only represent the effect of diffusion.

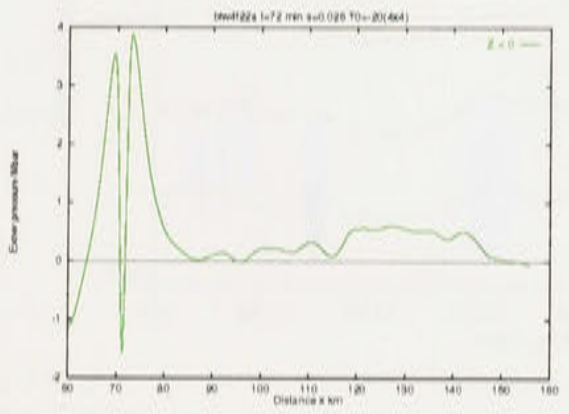

(a) Pressure trace at 72 mins

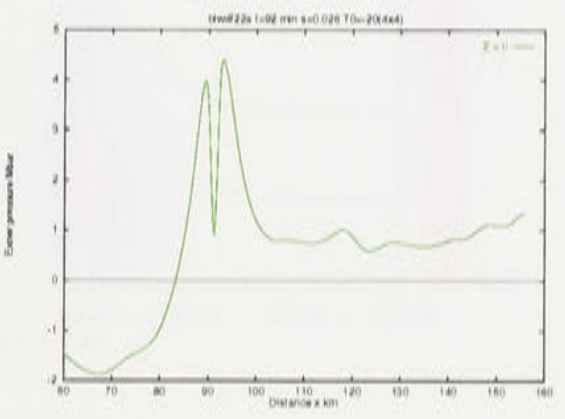

(b) Pressure trace at 92 mins

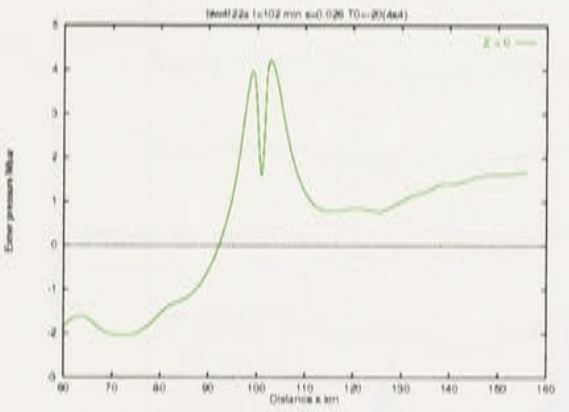

(c) Pressure trace at 102 mins

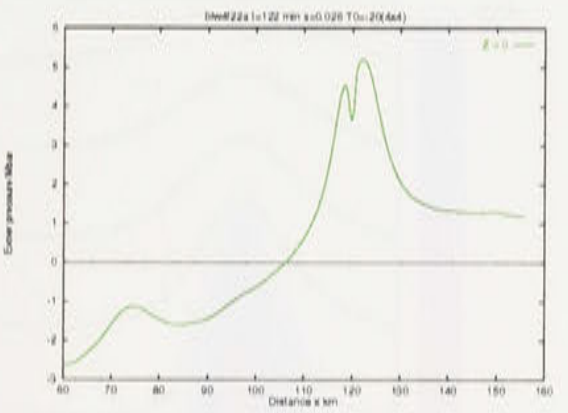

(d) Pressure trace at 122 mins

Figure 5.8: Changes in surface perturbation pressure for experiment with parameters $[\sigma = 0.026, H_0 = 4.0\,\text{km}, V_n = 4.0]$.

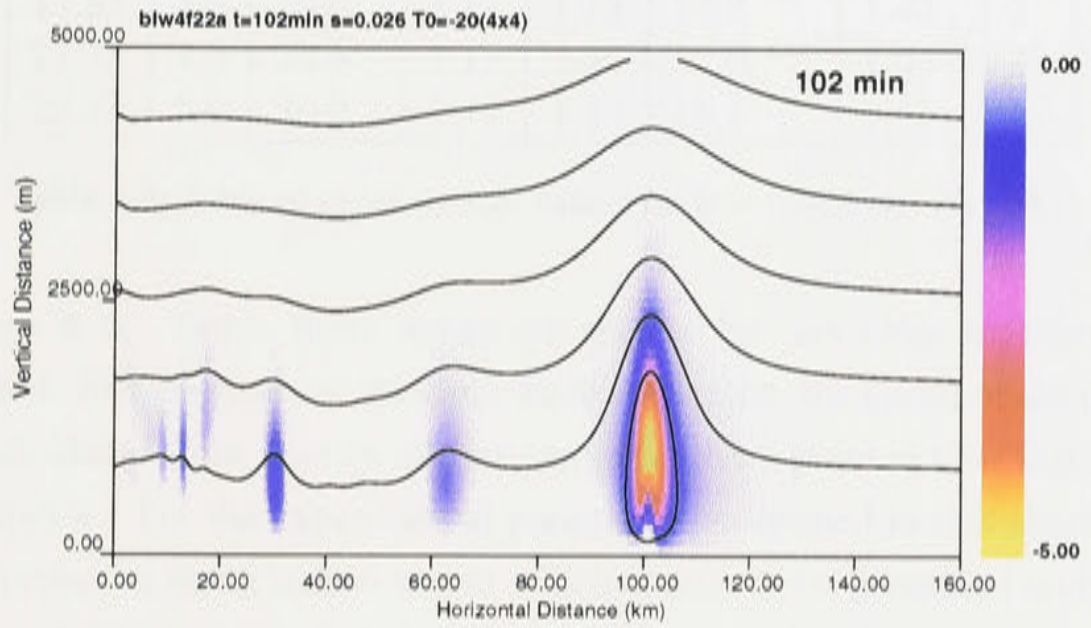

(a) disturbance at 102 mins

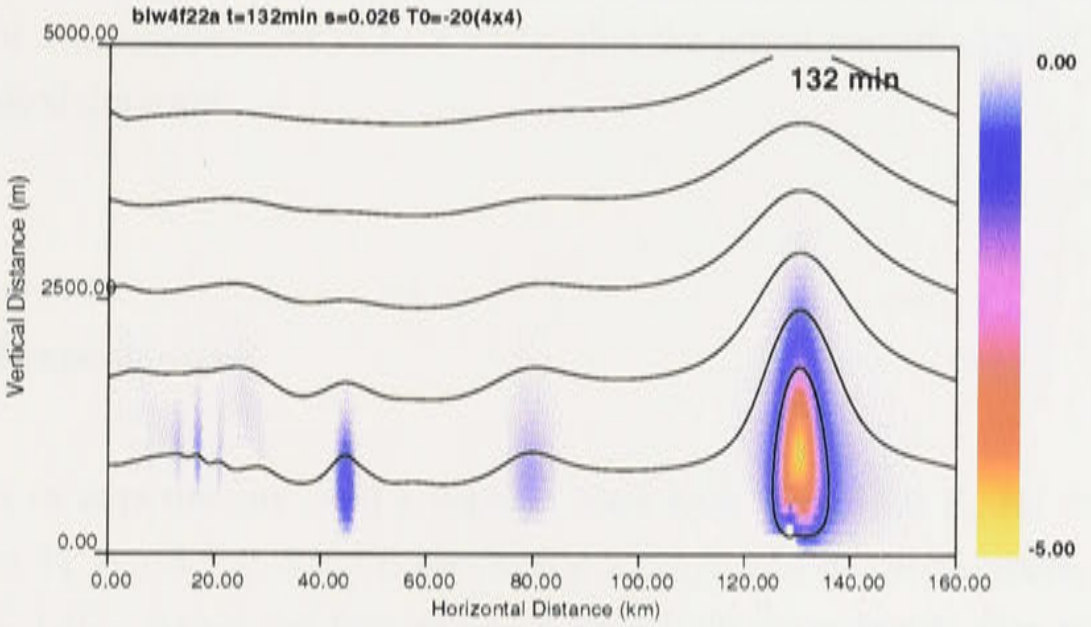

(b) disturbance at 132 mins

Figure 5.9: Relative streamlines and perturbation potential temperature with $\sigma = 0.026$, $H_0 = 4.0$ km for (a) $t = 102$ mins; (b) $t = 132$ mins. The gravity current head is visible as a white blob because of the displacement of perturbation temperature in the potential temperature field of the forming wave disturbance.

Q_n	V_n	T_0 (K)	Fr	a/h	c_w (m/s)	c_w/c_0	n_w
6.68	1.5	15.0	0.71	0.46	11.3	1.09	1
13.37	3.0	15.0	0.95	0.83	13.5	1.30	1
17.83	4.0	15.0	0.98	1.23	15.4	1.48	2
22.30	5.0	15.0	0.96	1.24	15.5	1.49	2*
8.91	1.5	20.0	0.89	0.55	11.9	1.14	1
17.83	3.0	20.0	1.11	1.13	14.8	1.42	2
23.78	4.0	20.0	1.15	1.40	17.0*	1.63	2*
29.73	5.0	20.0	1.12	1.43	16.1	1.55	2

Table 5.5: Table of experimental values for $\sigma = 0.026$ and $H_0 = 4.0$

the $V_n = 3.0$ case at $t = 72$min these waves are seen to be very close together and have not properly separated. In such cases of multiple wave formation, the speed of the dominant wave disturbance is calculated from a series of time samples after a point in time that corresponds to clear wave separation. For the experimental parameters examined in this chapter all cases of multiple wave formation result in two waves which appear to be generated under similar conditions (ie localised forcing of limited duration) to the two isolated waves observed by Doviak and Christie (1991) who examined a case of nonlinear wave formation by a thunderstorm generated downdraft. In the observations of Doviak and Christie (1991) the thunderstorm moved rapidly across the waveguide layer in such a way that the initial perturbation of the waveguide layer was of limited duration.

Third set of experiments

The third set of experiments used a starting blob with $T_0 = 15.0$ K, $H_0 = 4.5$ km and a range of volumes $V_n = 1.5, 3.0, 4.0, 5.0$ producing a range of Froude numbers given by Fr = 0.80, 0.94, 1.04, 1.02. Again the first value of Fr = 0.80 corresponds to a wave of modest amplitude being generated. The other values of Fr produce single highly non-linear waves, except for the case with $V_n = 5.0$ where there is evidence of a combination of wave modes at $t = 72$min and the wave formation process at this time is still incomplete. The relative streamlines and surface pressure traces at $t = 72$ min are displayed in Figs 5.10(a), 5.10(b), 5.10(c) and 5.10(d). Wave formation occurs within the horizontal dimensions of the domain for all cases. Compared to the second set of experiments all corresponding initial blob volumes produce waves of similar properties, indicating that change of this order in the value of H_0 has little effect on the wave properties and that the value of Fr combined with the parameters describing the blob characteristics $[\bar{Q}_n, V_n, T_0]$ govern the type of wave produced. The resulting wave properties are given in Table (5.6).

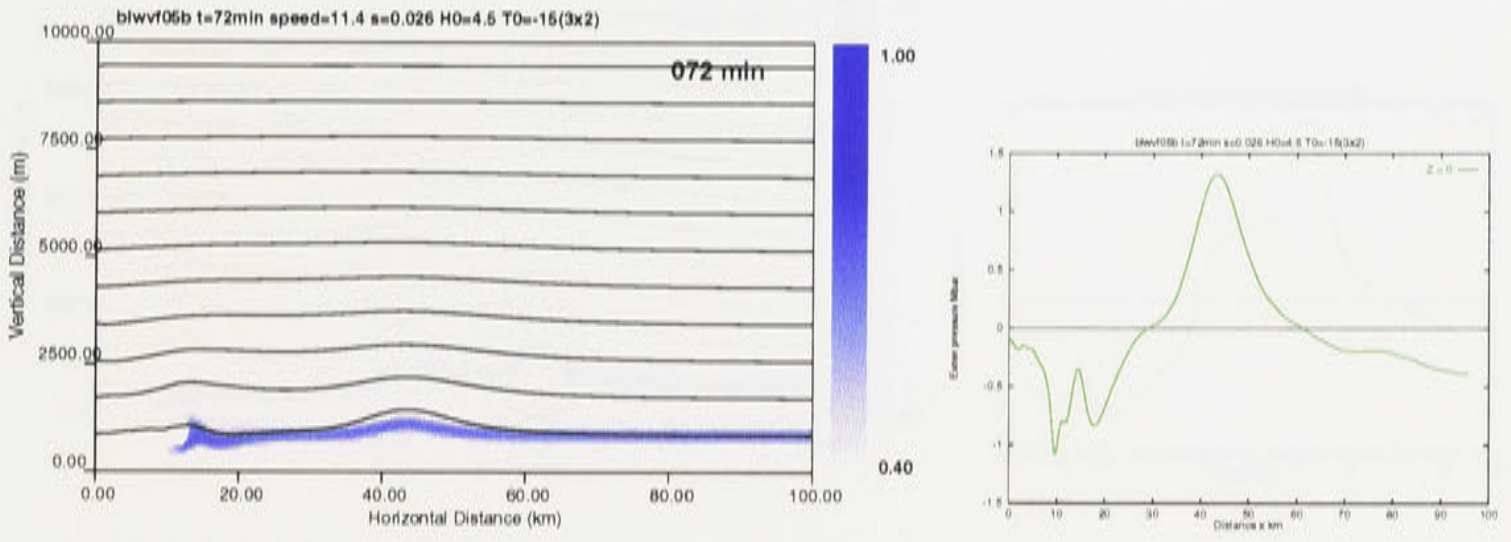

(a) Experiment 1 with $\sigma = 0.026$, $H_0 = 4.5$ km and $T_0 = -15$ K. The starting blob has normalised volume $V_n = 1.5$

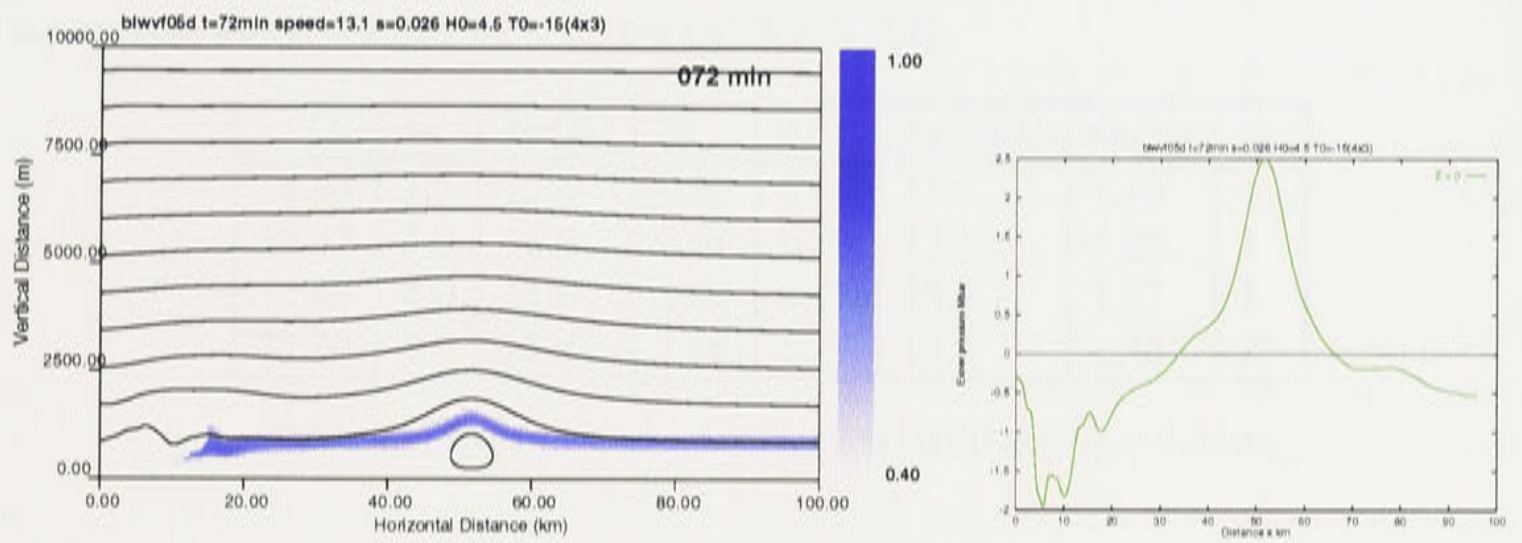

(b) Experiment 2 with $\sigma = 0.026$, $H_0 = 4.5$ km and $T_0 = -15$ K. The starting blob has normalised volume $V_n = 3.0$

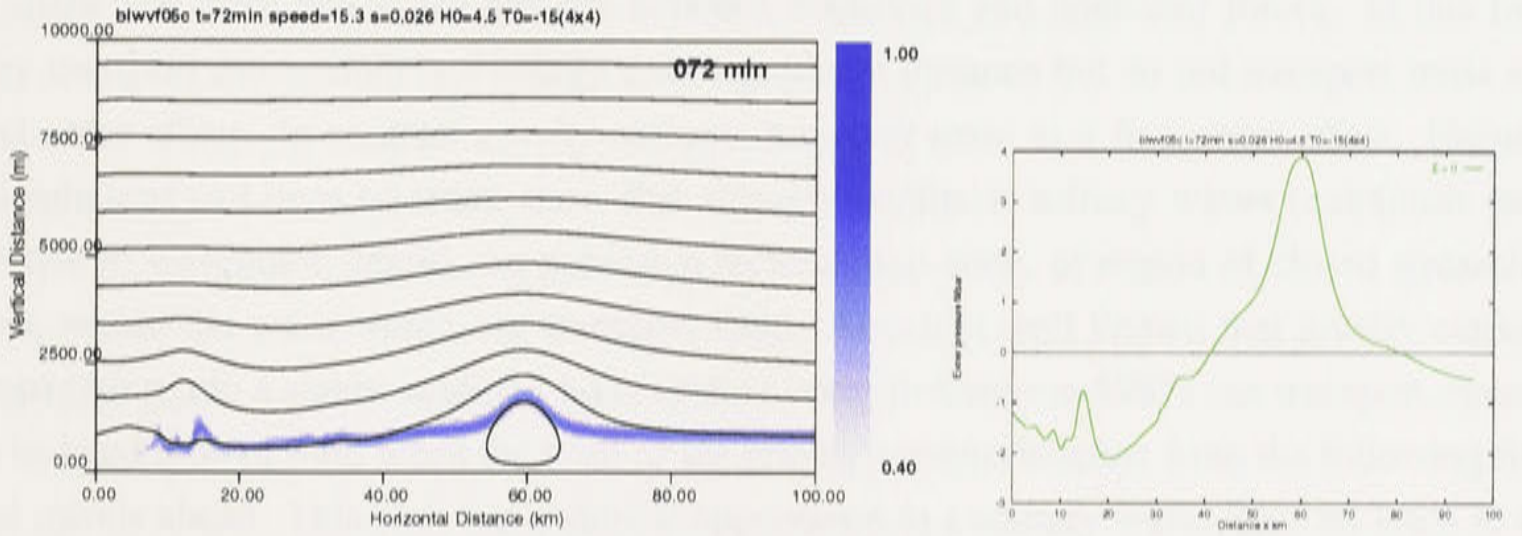

(c) Experiment 3 with $\sigma = 0.026$, $H_0 = 4.5$ km and $T_0 = -15$ K. The starting blob has normalised volume $V_n = 4.0$

Figure 5.10: Relative streamlines (with tracer) and surface pressure plots for the third set of experiments with $\sigma = 0.026$, $H_0 = 4.5$ km and $T_0 = -15$ K.

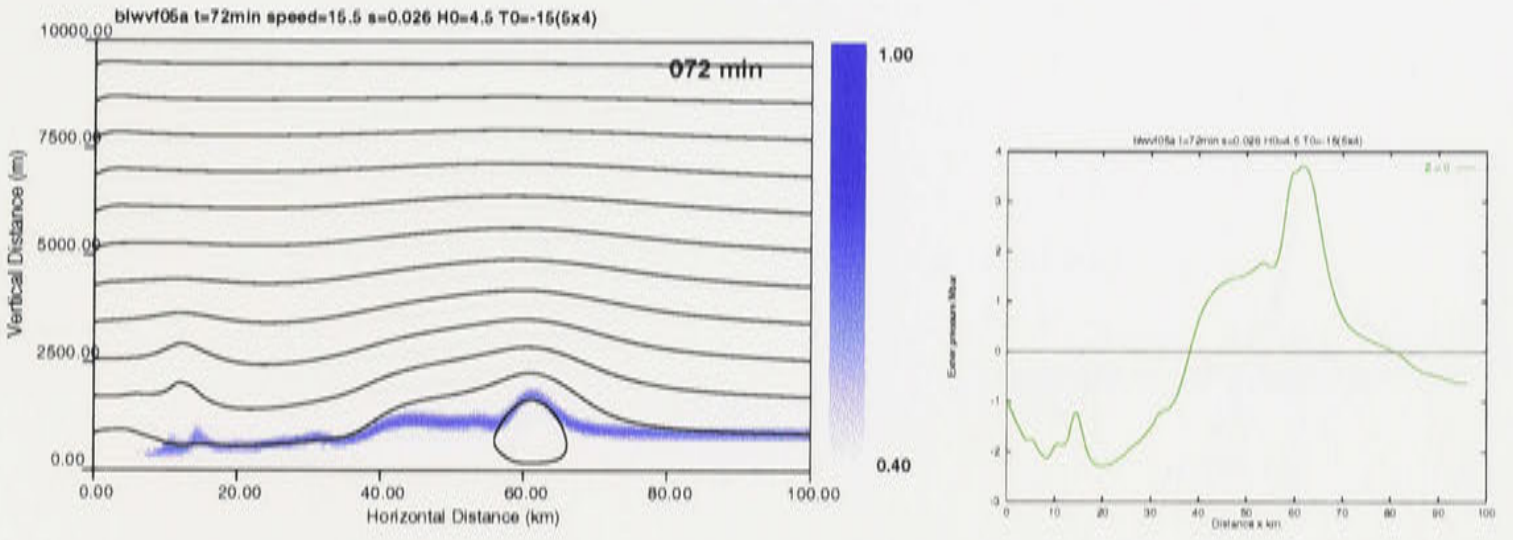

(d) experiment 4 of the set with $\sigma = 0.026$, $H_0 = 4.5$ km and $T_0 = -15$ K. The starting blob has volume $V_n = 5.0$

Figure 5.10: (continued) Relative streamlines (with tracer) and surface pressure plots for the third set of experiments with $\sigma = 0.026$, $H_0 = 4.5$ km and $T_0 = -15$ K.

Q_n	V_n	T_0 (K)	Fr	a/h	c_w (m/s)	c_w/c_0	n_w
6.68	1.5	15.0	0.80	0.48	11.4	1.10	1
13.37	3.0	15.0	0.94	0.79	13.1	1.26	1
17.83	4.0	15.0	1.04	1.17	15.3	1.47	1
22.30	5.0	15.0	1.02	1.17	14.9	1.43	2*

Table 5.6: Experimental values for $\sigma = 0.026$ and $H_0 = 4.5$ km

It is now important to consider the details of the wave formation process. First we need to make a distinction between gravity current and solitary wave dominated flow. Here we follow the reasoning of Manasseh et al. (1998). Pure solitary waves are waves that travel unchanged in shape and form due to the balance between dispersive and nonlinear forces. In this form they transport momentum and energy over significant distance but do not transport mass as a first order effect. In contrast gravity currents transport mass as a first order effect. Numerical solutions to Longs equation show that strongly nonlinear solitary waves (amplitude large relative to waveguide depth) can possess a recirculation zone, or region of closed streamline flow, within the wave which can transport fluid. Also it is well known that gravity currents propagating into a stably stratified layer (called bores in Simpson 1987) can transport mass as an isolated blob of fluid when the head of the gravity current detaches from the following flow and travels ahead. This blob has a similar appearance to a solitary wave. This all leads to the conclusion that there exists a hybrid that describes a solitary wave that encapsulates a mass of cold outflow air (a detached isolated head of a gravity current) and transports it as a first order effect. This could also be described as a transition state during an evolution process toward a stable highly nonlinear solitary wave.

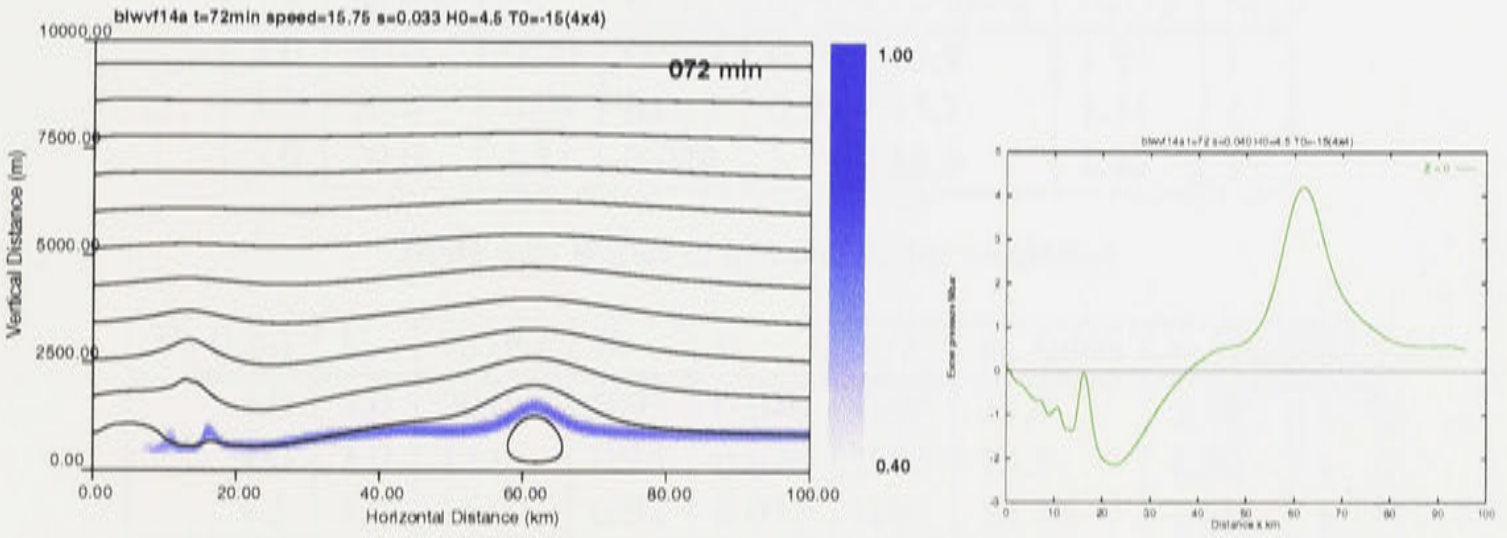

Figure 5.11: Relative streamlines and surface pressure ($\sigma = 0.040$)

5.8.4 Set 4: solitary wave generation (variable σ)

Using the same numerical domain presented in the last section the effect of varying σ was examined. Firstly the properties of waves produced using a starting blob with the same characteristics were examined for $\sigma = 0.026, 0.033, 0.040$. Then wave generation for values of Fr close in magnitude was studied for the three cases $\sigma = 0.026, 0.033, 0.040$.

Three experiments were performed for the impact regime that results in wave generation using a starting blob with the same parameters $[V_n = 3.0, T_0 = 15.0K]$ and same value of $H_0 =$ 4.0km. A different value of σ was used in each case. These are $\sigma = 0.026, 0.033, 0.040$. For each experiment the results are again displayed in terms of the streamfunction ϕ and the perturbation exner pressure at the ground Π'_0 at a value of time ($t = 72$ min) which allows a sufficient period for the wave formation process to occur and a stable waveform to be produced.

For the first experiment the main parameters were $\sigma = 0.026$ and Fr $= 1.11$. The wave formation process seems to be completed by $t = 72$min and using a set of data points which record wave position for $t \geq 72$min, the wave speed was estimated as $c = 14.8$m/s so that the ratio c/c_0 is approximately 1.42. Using the displacement of the tracer field at $t = 82$min, a non-dimensional wave amplitude was calculated as $a/h \approx 1.13$.

The second experiment has $\sigma = 0.033$ and Fr $= 0.99$. For this case the linear long wave speed is given by $c_0 = 11.72$m/s. There is clear wave formation by $t = 52$min and a wave speed estimate was calculated as $c = 15.3$m/s, so that $c/c_0 = 1.31$. Using the tracer field at $t = 72$min, a non-dimensional wave amplitude was calculated as $a/h \approx 0.9$.

Fig 5.11 shows two plots from the third experiment with $\sigma = 0.040$ and Fr $= 0.90$. For this case the linear long wave speed is given by $c_0 = 12.9$m/s. There is clear wave formation by $t = 52$min and the wave speed was estimated as $c = 15.9$m/s, so that $c/c_0 = 1.23$. Using the tracer field at $t = 72$min, a wave amplitude was estimated as $a/h \approx 0.7$.

A summary table for values of the parameters representing the relative degree of ambient stratification (over the waveguide depth) σ, the Froude number Fr, and the wave speed c_w, for

V_n	T_0 (K)	Fr	σ	a/h	c_w (m/s)	c_w/c_0	n_w
3.0	20.0	0.90	0.040	0.70	15.9	1.23	1
3.0	20.0	0.99	0.033	0.90	15.3	1.31	1
3.0	20.0	1.11	0.026	1.13	14.8	1.42	1

Table 5.7: Values of a/h and c_w for variable σ

H_0 (km)	V_n	T_0 (K)	Fr	σ	a/h	c_w (m/s)	c_w/c_0	n_w
4.0	4.0	20.0	0.93	0.040	0.95	17.9	1.39	1
4.0	3.0	15.0	0.95	0.026	0.83	13.5	1.30	1
4.5	4.0	15.0	0.92	0.033	0.92	15.75	1.35	1

Table 5.8: Values of a/h and c_w/c_0 for variable σ with similar values of Fr

the three experiments is given in 5.7.

The final set of experiments looks at variable σ for similar values of Fr. The results are displayed in Table 5.8. An isolated highly nonlinear solitary wave with closed circulation was produced for all three experiments. It can be seen that waves of similar amplitude are produced for the experiments with ($\sigma = 0.033$; Fr $= 0.92$; $V_n = 4.0$) and ($\sigma = 0.040$; Fr $= 0.93$; $V_n = 4.0$), as expected given the independence of the Froude number on the degree of stratification for waveguides with the same effective depth h, and that the experiment with ($\sigma = 0.026$; Fr $= 0.95$; $V_n = 3.0$) produces a wave of slightly smaller amplitude than the other two experiments. This suggests that the resulting amplitude for the highly nonlinear waves produced in these experiments is dependent, to some degree, on the properties of the starting blob of cold air (such as the blob volume represented by V_n).

All the experiments presented here using different values of σ result in only a single isolated wave. When the values of Fr which correspond to these results are compared to values of Fr and w_n from the experiments using $\sigma = 0.026$ it would seem that there is a relation between the magnitude of Fr, representing a measure of the energy associated with an impact, and the number of waves produced. Larger values of Fr seem to result in multiple waves (in these experiments up to two). This can be related back to the properties of the initial thermal in terms of the buoyancy deficit and initial volume of the starting blob.

5.8.5 Analysis of wave properties

The properties of the waves generated in the above experiments were examined in the context of highly non-linear wave theory. A plot of the non-dimensional amplitudes a/h versus the non-dimensional speeds c/c_0 for all wave producing experiments is shown in Fig 5.12. A solid line is plotted from numerical solutions to the corresponding theoretical equation, known as the DJL equation (see the next chapter for details), for the same ambient environment. It can be seen that the experimental values are very close to the predicted values. There is a

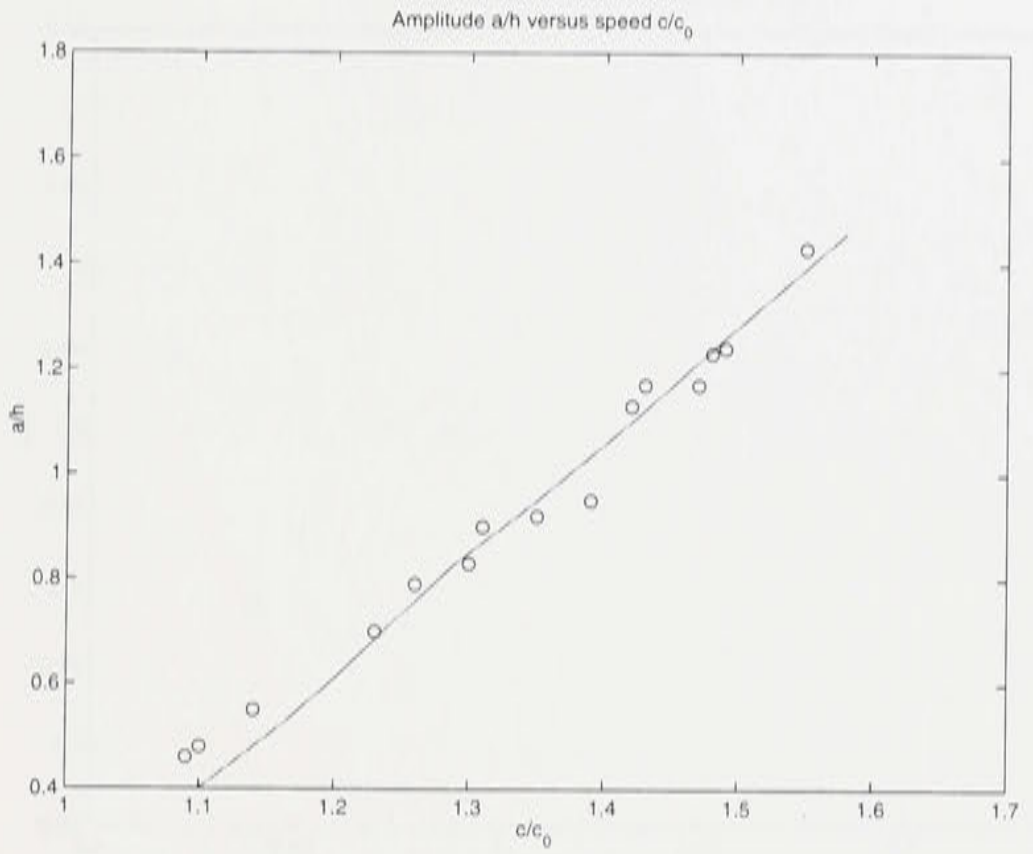

Figure 5.12: Non-dimensional amplitude a/h versus c/c_0 the non-dimensional wave speed. Data points have been taken from all wave generating experiments. The solid line connects a set of data points $[a/h, c/c_0]$ which correspond to values provided by solutions to the DJL equation (see next chapter) for the same ambient environment.

small degree of divergence from the predicted values for small amplitude. This divergence can probably be attributed to the uncertainty associated in estimating smaller amplitudes from the tracer field. It should also be noted that the highly nonlinear waves produced in the above experiments seem to possess a region of closed circulation for values of a/h which are smaller than the value of a/h predicted for the onset of closed circulation from the corresponding DJL solutions. A plot of Fr versus a/h is shown in Fig 5.13 for waves generated from the same starting volume $V_n = 3.0$. There seems to be a linear relationship between Fr and wave amplitude for a constant value of V_n. However, these results, in terms of the dependence on starting volume, are inconclusive due to the uncertainty associated with the estimates of w_1 on which Fr depends.

In the analysis of highly non-linear waves, the tracer variable representing fluid which was initially contained in the starting blob is particularly useful. The tracer allows a clear visualization of any gravity current at the ground and the behaviour of the fluid contained in the gravity current head. After a large amplitude wave has fully developed and the detached gravity current head has developed into a closed circulation cell, fluid is observed to leak from this cell in a thin layer at the ground. Maxworthy (1980), in his laboratory work, showed that recirculating fluid trapped in the interior of a highly nonlinear solitary wave was deposited at the surface behind the wave disturbance. There is also evidence to suggest that this leaked

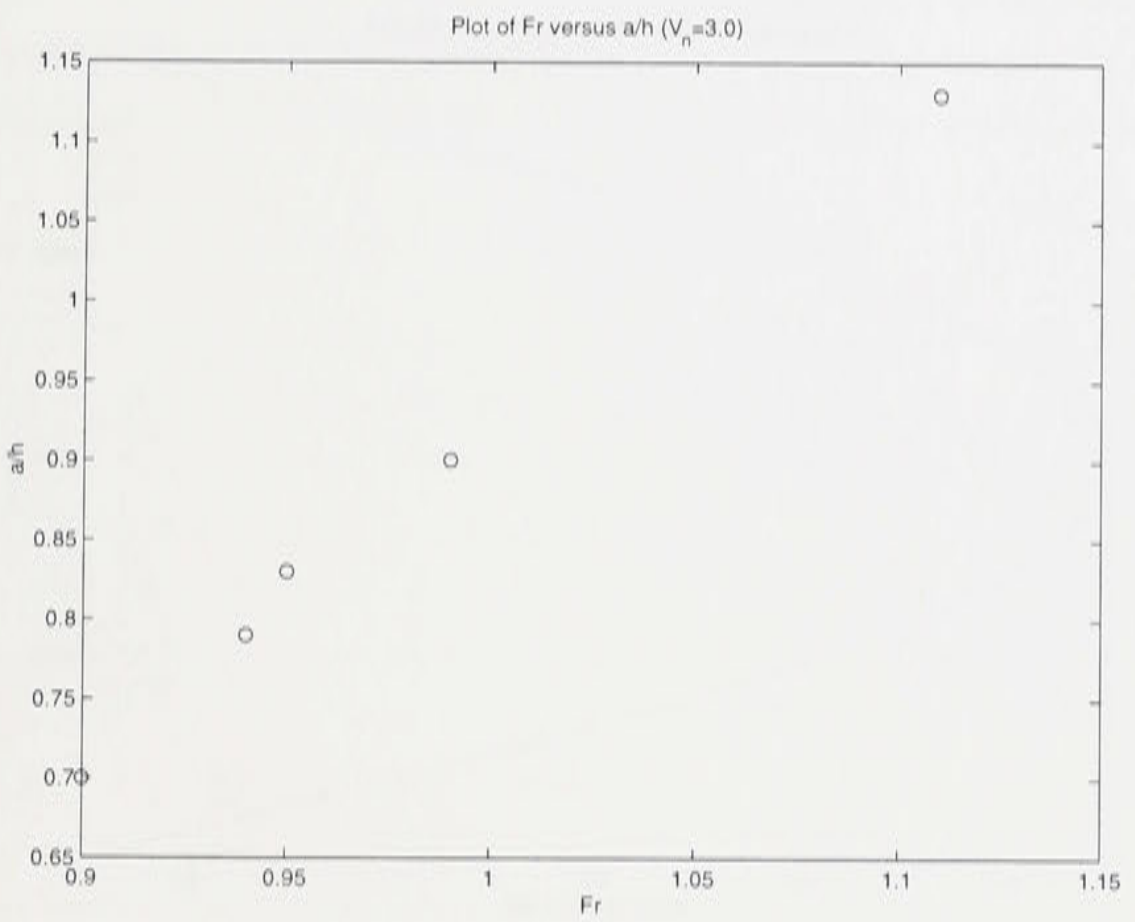

Figure 5.13: Non-dimensional amplitude a/h versus Fr the Froude number. Data points have been taken from experiments with the same starting volume $V_n = 3.0$.

fluid in the numerical experiments represents warmer air from higher levels which has been subjected to mixing processes and deposited in the wake of the wave. An analysis of the internal structure of a highly nonlinear wave from the above experiments using the complete potential temperature field shows that the closed circulation region (after sufficient time) seems to consist of fluid with the same temperature as that lying at ground level.

5.9 Inclusion of wind shear above waveguide layer

Generally realistic waveguide conditions in the lower atmosphere do not have homogeneous conditions above the waveguide layer. Instead there is usually some degree of ambient windshear present above the waveguide. This windshear can have an important effect on the nature of a descending microburst and its impact with the waveguide layer. The most obvious change in the descent of a thermal such as those generated in the above experiments is that the evolution of the descending thermal is no longer axisymmetric. A few experiments will now be presented to examine some non-symmetric impacts where a windshear layer exists above the waveguide. This provides a more realistic representation of conditions generally encountered by a descending microburst in the lower atmosphere.

All these experiments, with wind shear above the waveguide, use the same basic model parameters. The model domain uses a [799x99] mesh representing an atmosphere of 80km extent

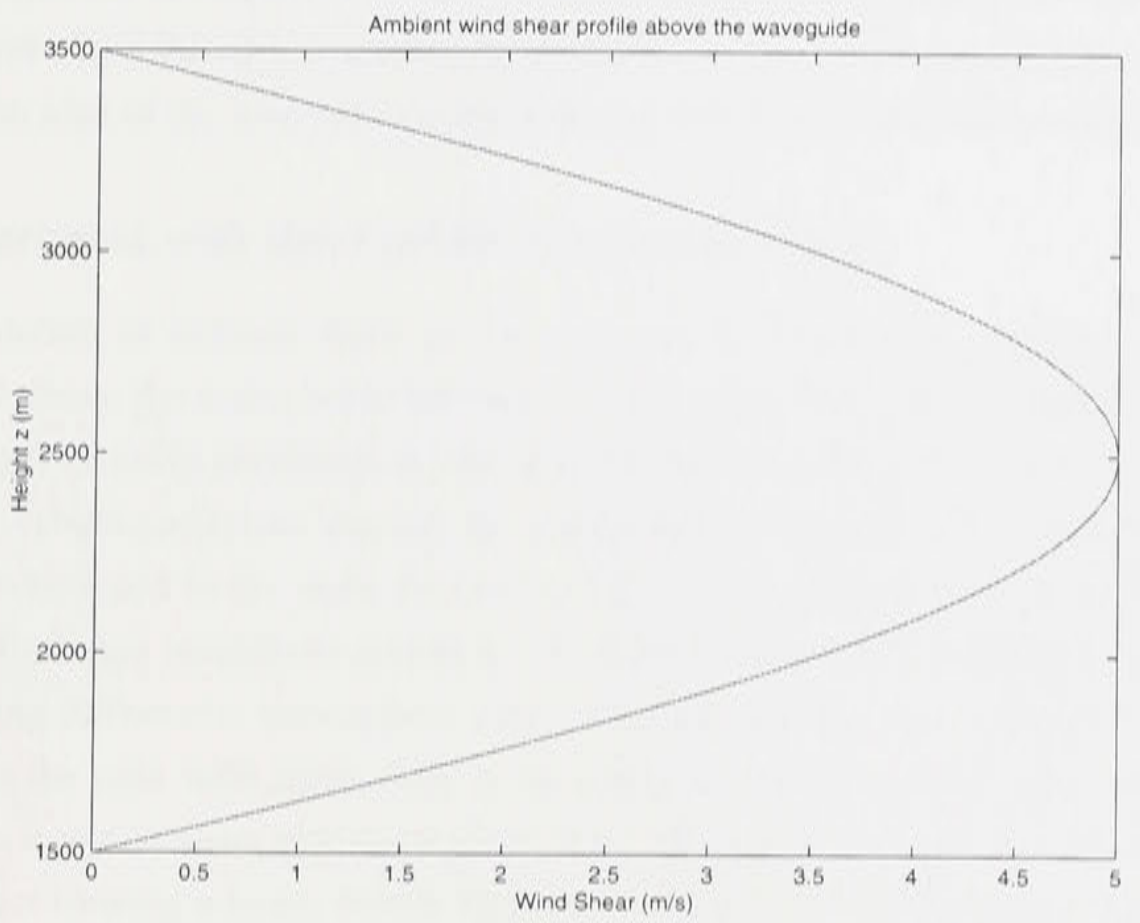

Figure 5.14: Plot of a wind shear profile imposed above the wave guide layer and specified using a cos function so that the maximum wind shear is 5 m/s.

in the horizontal and 10km extent in the vertical. Because these experiments are investigating a non-symmetric phenomena, radiation boundary conditions have been applied on both right and left lateral boundaries. The initial cold blob of air is located at height of $z = 4.5$ km and is centered at a horizontal distance of $x = 30$km (so that it is not too close to the left lateral boundary). The cold blob is specified using equation (5.14) with horizontal semi-axis $x_r = 4$km, vertical semi-axis $z_r = 4$km, and a maximum temperature perturbation of -15 K. The stable layer is defined using the same tanh function as the experiments above with $\sigma = 0.026$ and effective depth $h = 850$ m. The horizontal and vertical diffusion coefficients are $K^x = K^z = 25\text{m}^2/s$. For the simulations here an ambient shear profile, specified using a cos function, is included above the waveguide layer between 1.5 km and 3.5 km. This shear profile is shown in Fig 5.14.

5.9.1 Control experiment (no shear)

In order to describe the effect of the interaction of a microburst with a stable layer when wind shear is present we first need a control experiment without shear in the ambient environment. This case is directly comparable to the other experiments which were performed using a symmetric domain. The descent of the thermal is axisymmetric and for the chosen blob parameters the impact penetrates completely to the ground and results in an outflow (as described in experiments above). The tracer fields a short time after impact are shown in Fig 5.16(a). As before,

the red tracer (placed at height $z = h$) denotes the interface of the waveguide layer and the blue tracer represents fluid initially contained by the blob. A plot of the perturbation potential field, which gives an idea of the thermal dynamics during descent and impact, is shown in Fig 5.15.

5.9.2 Experiment with shear profile (maximum 5 m/s)

For this simulation an ambient shear profile using a cos function (as shown in Fig 5.14) has been included above the stable layer between 1.5 km and 3.5 km. The dynamics of the falling thermal, visualized using perturbation potential temperature in Fig 5.17, are clearly no longer axisymmetric. The thermal now impacts the stable layer at an angle. There is now significantly more energy transfered to the right than to the left and, as expected, this results in a solitary wave of slightly larger amplitude as seen in Fig 5.16(b). The tracer fields in Fig 5.16(b) show some interesting differences between the case with shear and the case without. The blue tracer shows that for the case with shear there is no generation of an outflow containing blob fluid at the ground. It would seem that the impact of the thermal at an angle has resulted in energy from the impact causing a large, mostly impulsive, disturbance of the waveguide layer on the right side of the impact zone. There is only a very small amount of blue fluid that has spread along the ground on the right and the vorticity which was generated by the descending thermal rapidly dissipates in the vicinity of the impact zone. This is in contrast to the case without shear where there is a strong symmetric outflow at the ground due to a transformation of some of the energy associated with the symmetric vortices of the thermal in addition to a impulsive disturbance of the waveguide layer which encapsulates the outflow. It is expected that as the shear is increased this will produce even greater energy transfer to the right.

5.9.3 Experiment with shear profile (maximum 10 m/s)

It is expected that a further increase in the degree of windshear will result in a greater transfer of energy to the right in the impact. To test this hypothesis, the amount of windshear above the waveguide layer (between 1.5 km and 3.5 km) was increased from a maximum value of 5 m/s to a maximum value of 10 m/s. The tracer field (at the same time $t = 32$ min as the other experiments) after the impact is shown in Fig 5.16(c). It can be seen that the impact in this case results in a slightly larger impulsive disturbance of the waveguide layer on the right of the impact than the previous cases. Also there is a further decrease in the impulsive disturbance generated on the left on the impact zone. It would appear from this experiment that a substantial increase in the magnitude of the windshear does not cause a large increase in the impulsive disturbance of the waveguide layer (on the side of the asymmetric impact that corresponds to the direction of the windshear). This seems to indicate that important factors for the dissipation of the vorticity associated with the thermal are the disturbance of axisymmetry as it passes through the shear layer and the angle at which the thermal impacts the waveguide

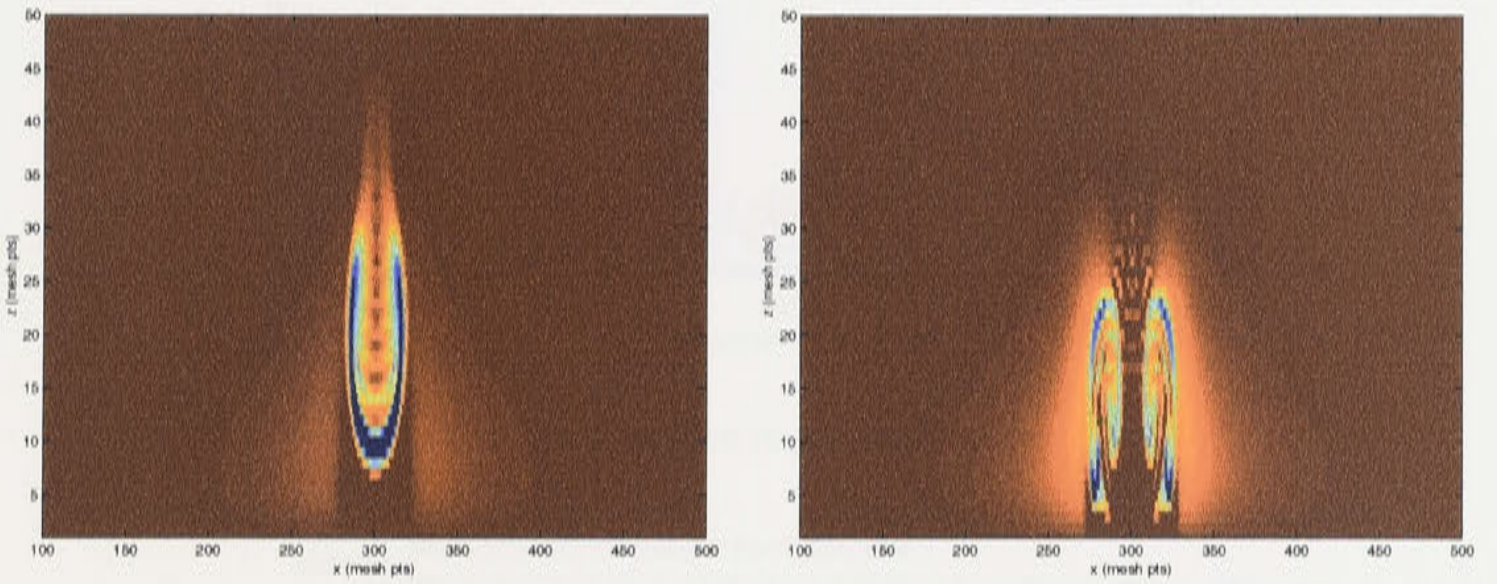

(a) 4 min

(b) 6 min

(c) 10 min

(d) 20 min

Figure 5.15: Evolution of perturbation potential temperature (using contouring $[-10,0]$ K) for the impact of a blob of -15K maximum temperature perturbation when no shear is present above the waveguide layer.

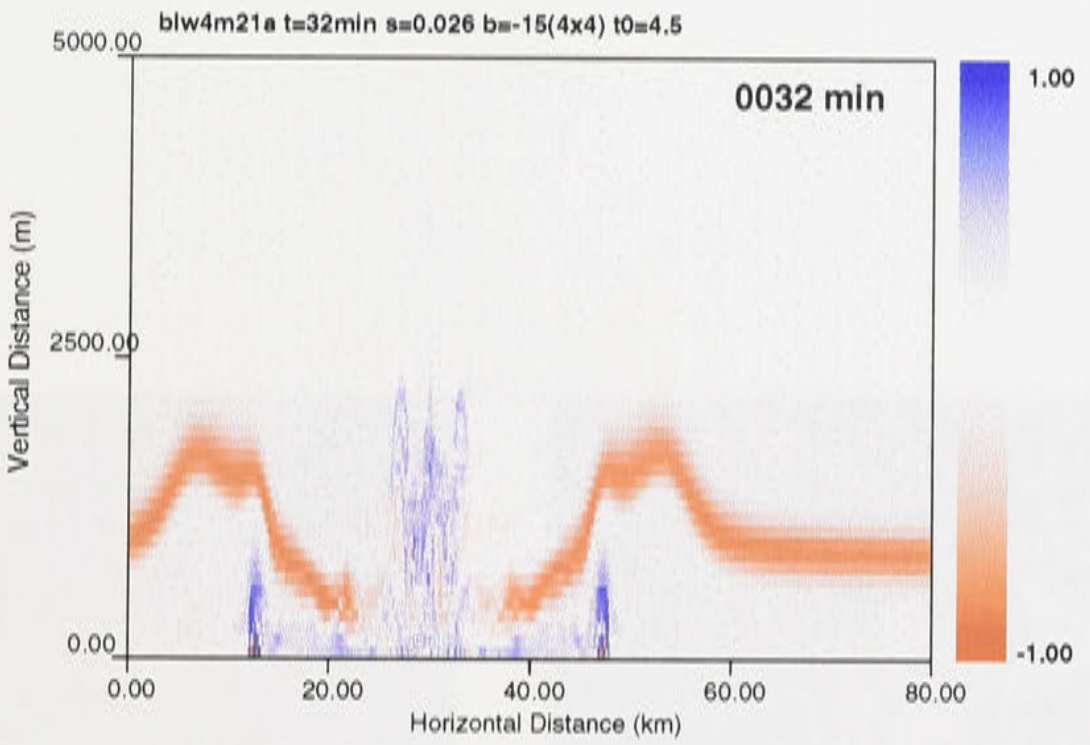

(a) microburst impact with no shear

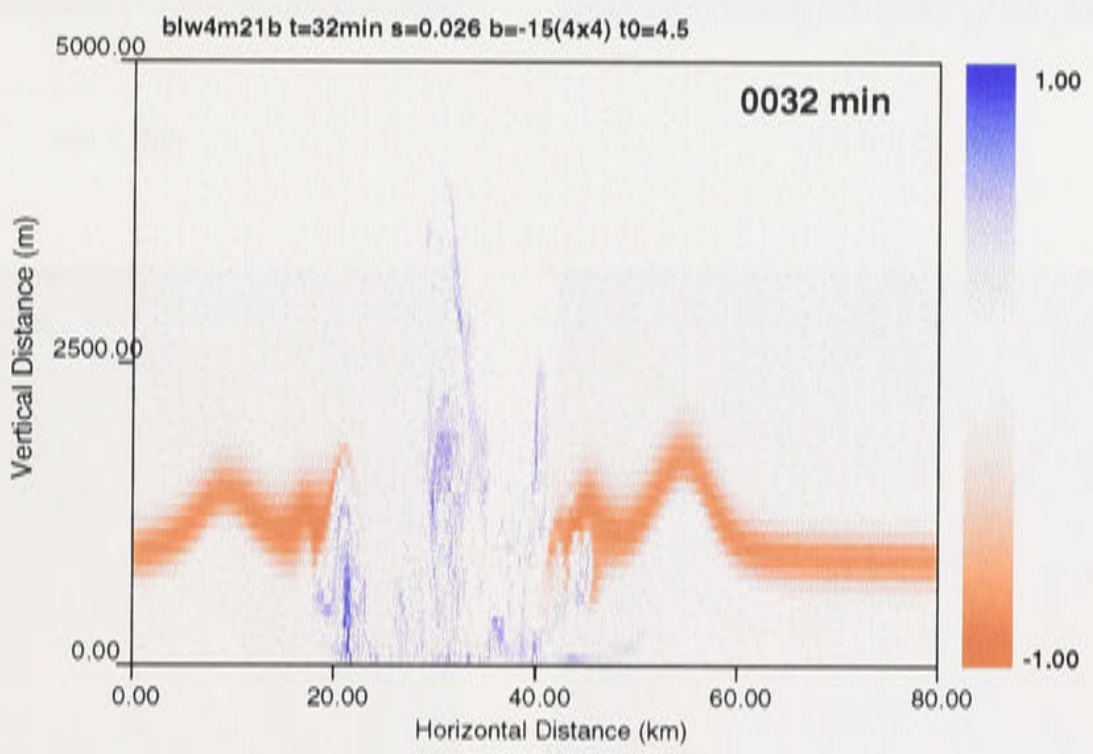

(b) microburst impact with maximum shear 5 m/s

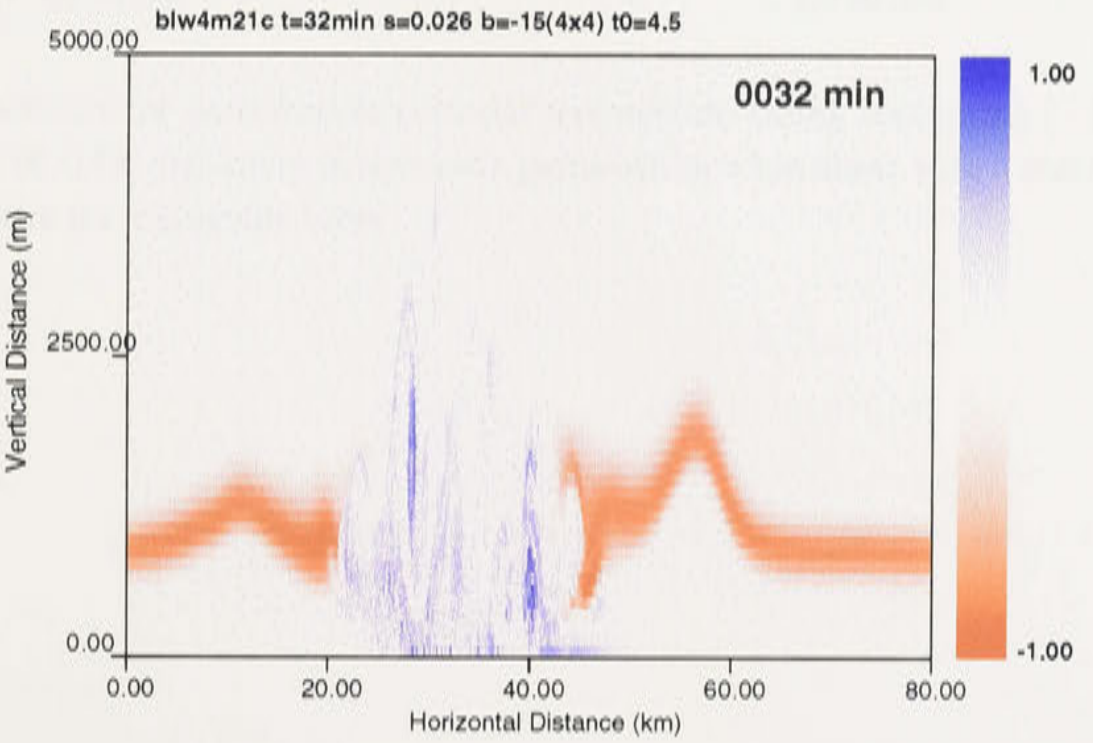

(c) microburst impact with maximum shear 10 m/s

Figure 5.16: Tracer fields cases with and without environmental shear

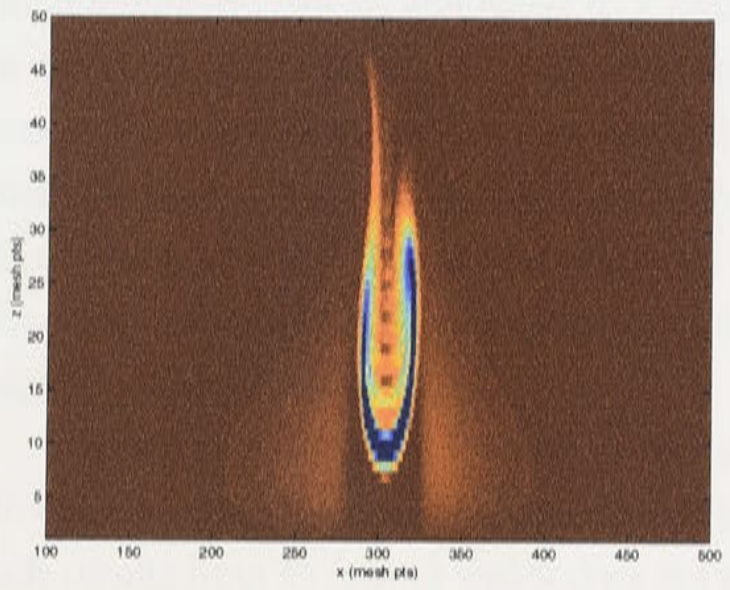

(a) 4 min

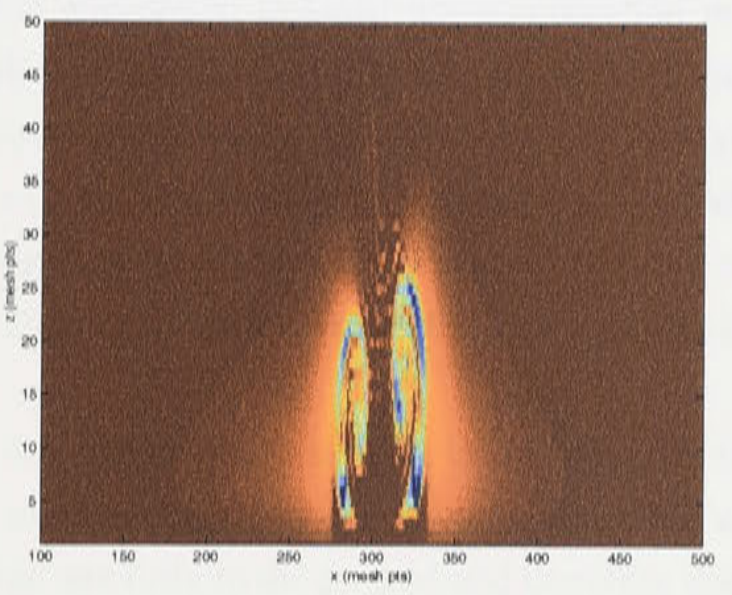

(b) 6 min

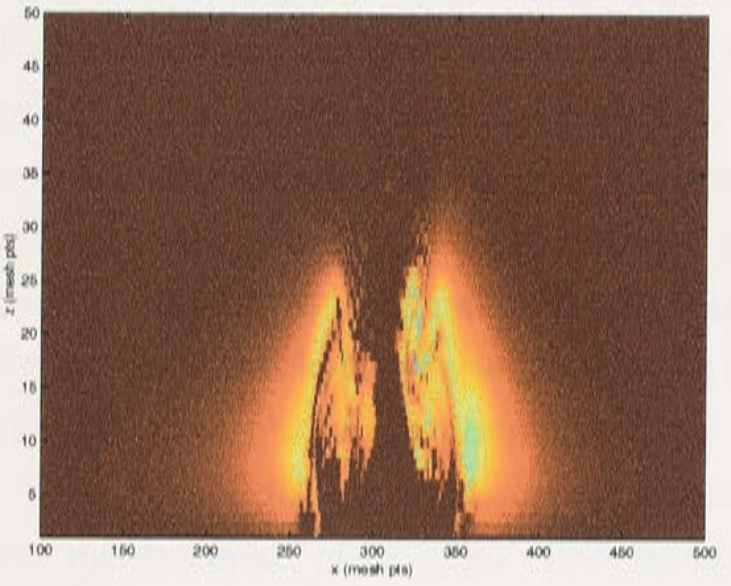

(c) 10 min

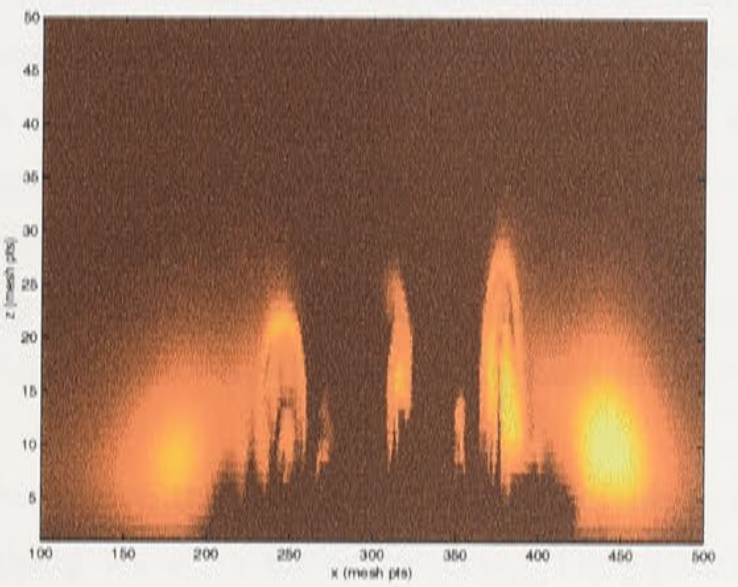

(d) 20 min

Figure 5.17: Evolution of perturbation potential temperature (using contouring $[-10,0]$ K) for the impact of a blob of -15K maximum temperature perturbation when shear with a maximum value of 5 m/s is present above the waveguide layer.

layer.

5.10 Summary of results

The work in this chapter shows that a region of buoyancy deficit of limited spatial extent can generate an isolated large amplitude solitary wave after impacting a ground based stable layer. Such a scenario can be compared to a possible microburst induced wave generation process in the lower atmosphere. In numerical studies of large amplitude solitary wave formation processes, it is desirable to have an isolated waveform to study. However many of the popular methods used to generate solitary wave motions, such as models of undular bores, produce a disturbance which evolves into a family of amplitude ordered solitary waves. For this reason the wave generation process explored in this chapter is useful for studies of the properties of highly nonlinear waves.

Furthermore, the experimental results of this chapter indicate that in the wave formation process resulting from the impact of a falling axisymmetric thermal, a wave of modest amplitude results from an impact which does not penetrate fully to the ground and therefore does not produce a strong outflow at the ground. These waves of modest amplitude seem to be created by the impulsive disturbance of the waveguide. The initial microburst vortices dissipate rapidly and do not propagate away from the point of impact. In contrast, a highly nonlinear wave with closed circulation seems to result from a ground penetrating impact which initially creates a strong outflow at the ground in addition to an impulsive disturbance of the waveguide which encapsulates the outflow head. Here the outflow head seems to result from the transformation of some of the energy associated with the descending microburst vortex pair and has a wave envelope due to the perturbation of the waveguide layer. Through a process of head separation the wave envelope encapsulating some of the outflow fluid seems to develop into a highly nonlinear wave after a transition period.

It is shown that the inclusion of windshear above the waveguide layer can substantially alter the dynamics of an impact and the resulting wave formation process. The disturbance of axisymmetry as the descending thermal passes through a shear layer and its subsequent impact at an angle to the waveguide layer effect the transfer of energy associated with the vorticity generated by the descending thermal so that most of this energy goes into a impulsive disturbance of the waveguide layer.

Although the initialization of a blob of cold air and subsequent generation of a falling thermal used in the simulations presented here represent a very simple model of a complicated phenomenon such as a microburst, it is feasible that large amplitude solitary waves can be produced by similar processes in the atmosphere. The observations of Doviak and Christie (1991) of waves generated by a thunderstorm downdraft would seem to support this conclusion. It would seem that multiple wave formation, such as the case observed here of a larger amplitude

wave followed by one of much smaller amplitude, is the result of sufficient energy in the impact (this can be related to the volume and buoyancy deficit of the initial starting blob of cold fluid) which perturbs the waveguide layer.

Chapter 6

Highly nonlinear starting wave solutions

6.1 Introduction

The aim of this chapter is to show that a range of large amplitude internal solitary waves with closed circulation can be formed in a controlled manner to act as starting wave solutions in a study of radiative decay. This is achieved by using solutions to an incompressible equation which are mapped to our compressible mesoscale numerical model. In the previous chapter a mechanism was examined that produces highly non-linear internal solitary waves. This mechanism is thought to provide a simple model of processes that can lead to highly non-linear wave motion in the lower atmosphere. Here some of the theory developed for the treatment of highly non-linear waves in stratified fluids is introduced. The theoretical solutions presented here will serve two purposes. Firstly, they will provide a comparison of theoretical steady waveform solutions to the waveforms observed in the results of the last chapter. Secondly, these theoretical steady solitary waveforms represent a well defined set of solutions that can act as "ideal" starting wave solutions for the study of radiative decay in the next chapter. By ideal we mean a solution set that allows freedom in the selection of wave parameters and provides single waveforms free of interference from other disturbances. The results of the last chapter provided only a limited range of wave amplitudes and were subject to certain limitations in the selection of grid resolution so that a suitable horizontal domain length was available. A significant time period was also required for the waves generated in the last chapter to obtain a stable wave form. In the study of wave radiation it will be more advantageous to have a higher grid resolution as well as the ability to study waves of arbitrary amplitude. If the upper medium above the waveguide is weakly stratified then a falling thermal will generate a internal wave field during its descent which will make it difficult to study the effect of wave radiation for an isolated waveform without other disturbances in the ambient media. These are all good reasons to use a more ideal starting solution.

This chapter looks at how theoretical time-independent inviscid incompressible solutions

of a boundary value PDE problem can be mapped across to the time dependent compressible mesoscale model. The processes by which wave energy can be lost are quite complex and no complete theory exists for the time dependent description of the radiative decay of highly non-linear waves in a stratified medium. We have decided to study this problem by using time independent steady wave solutions of a theoretical equation, which are mapped to and then allowed to evolve in the time dependent model. For this approach to be successful suitable theoretical solutions and a stable mapping technique are required. These are presented below.

To date, there exist two distinct approaches to the theoretical description of highly non-linear wave propagation in a stratified medium. One of these approaches addresses a class of solutions by solving for highly non-linear interfacial solitary waves which satisfy complicated boundary conditions governing the interface between two incompressible fluids with different but constant densities. This type of approach has been the subject of research by Pullin and Grimshaw (1988) and the reader is referred to their paper for further details. A different approach, which is favored for the type of work here, has been to study the problem as a boundary value problem in terms of a streamfunction. A non-linear partial differential equation (in terms of a streamfunction ϕ), known as Longs equation or the Dubreil-Jacotin-Long (DJL) equation, provides a description of highly non-linear waves in continuously stratified fluid and is generally subject to a set of assumptions that reduce the complexity of the mathematical problem. Even with these assumptions, the DJL equation has proved to be a difficult equation to solve. Solutions to date have adopted a fairly simple set of boundary conditions but this is not considered a severe restriction in the context of the present work. It is therefore advantageous to use a ready-made program, which has been developed by Brown (1995) as part of a comprehensive study of the DJL equation with simple boundary conditions, to solve for solutions here.

A method is presented below which allows solutions of the DJL equation, to be mapped to the compressible non-hydrostatic mesoscale model of Chapter 3. These solutions to the DJL eigenvalue problem are calculated as eigenvalue, eigenfunction pairs $[\Lambda, \phi]$ along a chosen solution branch. A mapping technique was developed to transfer these eigenfunctions to the mesoscale model with an radiative upper boundary condition and a lower waveguide layer. The solitary wave properties of the solution in the mesoscale model are then analyzed after a short adjustment period. The ambient background consists of a stable layer at the ground acting as the waveguide with neutral conditions above. Under these conditions the change of wave morphology of large amplitude waves with closed circulation is examined. Fluid is observed to leak from the closed circulation cell and the resulting effect on the wave amplitude is examined as the wave evolves over time. The waves produced in this chapter will be used as starting wave solutions in the study of radiative decay in chapter 7 when the region above the waveguide layer is weakly stratified and supports internal waves.

6.2 Highly nonlinear solitary waves in incompressible media

The DJL equation is an nonlinear elliptic partial differential equation that describes the motion of stationary finite-amplitude wave motions in an incompressible and inviscid stably stratified fluid. Stably stratified density profiles are able to be assigned quite generally. This equation was independently derived by both Dubreil-Jacotin (1937) and Long (1953). Under an assumption of quasi-steady inviscid flow such that $t \to \infty$ and $(\nu, \kappa) \to (0,0)$ where ν and κ are coefficients of viscosity and diffusion (Tung et al. (1982) explain that the order that these limits are applied can result in different solutions especially in the case of large amplitude waves with closed circulation), it is possible to reduce governing equations of motion and continuity for a streamfunction ψ to the general form of the DJL equation (see for example Tung et al., 1982) given by:

$$\nabla^2\psi + \frac{1}{\rho}\frac{d\rho}{d\psi}\left[\frac{(\nabla\psi)^2}{2} + gz\right] = H(\psi), \tag{6.1}$$

where $\rho = \rho(\psi)$ and $H(\psi)$ is a function determined by upstream conditions. Following the derivation of Tung et al. (1982), a steady waveform is assumed to exist in a coordinate system moving at the steady phase speed c so that upstream ($x \to \infty$) there is a steady current at speed c. Then by defining the limits:

$$\psi \to cz \qquad \text{as} \qquad x \to -\infty \tag{6.2}$$

$$\rho \to \rho_0(z) \qquad \text{as} \qquad x \to -\infty \tag{6.3}$$

$H(\psi)$ may be specified as

$$H(\psi) = \frac{1}{\rho_0}\frac{d\rho_0}{d\psi}\{\frac{c^2}{2} + g\frac{\psi}{c}\}. \tag{6.4}$$

If the main variables are now non-dimensionalised, using h as an effective depth over which there is substantial variation of density, so that we now have a set of variables given by[1]

$$z^* = z/h, \qquad x^* = x/h, \qquad \psi^* = \psi/ch, \tag{6.5}$$

and, if the ambient density profile is assumed to satisfy the functional form,

$$\rho = \rho_0(1 - \sigma F(\psi)), \tag{6.6}$$

[1] All variables are considered non-dimensionalised from this point and the star notation is dropped for equations that follow

where σ can be considered as representing the relative density change across the region bounded by h or as a Boussinesq parameter such that $\sigma \to 0$ is a statement of the Boussinesq approximation. It is now possible to rewrite the DJL equation as a eigenvalue problem in terms of the perturbation streamfunction $\phi = \psi - z$,

$$\nabla^2\phi + \frac{F'(\phi+z)}{1-\sigma F(\phi+z)}\left[\Lambda\phi - \frac{\sigma}{2}(\phi_x^2 + \phi_z^2 + 2\phi_z)\right] = 0 \tag{6.7}$$

with the eigenvalue Λ given by

$$\Lambda = \sigma g h / c^2. \tag{6.8}$$

Λ can also be thought of as representing an inverse internal Froude number. An eigenvalue Λ_0 can be defined which corresponds to the linear wave limit, where the speed is $c = c_0$, by the relation

$$\Lambda = \Lambda_0 c_0^2 / c^2. \tag{6.9}$$

In the Boussinesq approximation σ in (6.7) can be ignored except where it enters calculations through Λ. Under the Boussinesq approximation (6.7) reduces to the simpler form

$$\nabla^2\phi + \Lambda F'(\phi+z)\phi = 0. \tag{6.10}$$

The boundary conditions on ϕ for internal solitary waves solutions to the eigenvalue problem in a finite vertical domain $\mathcal{D} = \{0 < z < H_2\}$ are given by

$$\begin{aligned} \phi(0) &= 0, \\ \phi(H_2) &= 0, \\ \lim_{x\to\pm\infty} \phi &= 0. \end{aligned} \tag{6.11}$$

These are a simple set of boundary conditions. More complicated boundary conditions significantly increase the difficulty in obtaining solutions and generally will still represent an approximation which may or may not accurately represent the real physical processes. For wave solutions in a ground based waveguide layer with a very deep neutral layer above (so that H_2 is large relative to the depth of the wave guide layer and approximates an infinitely deep fluid layer above) the boundary conditions given by (6.12) should provide accurate solutions across the range of wave amplitudes. Brown (1995) shows that there will be a discontinuity at a particular value of wave amplitude for cases where the value of H_2 is small so that it represents a fluid of finite depth.

6.2.1 Numerical solutions for incompressible theory

Fully non-linear solitary wave solutions have been obtained numerically by Davis and Acrivos (1967), Tung et al. (1982), Turkington et al. (1991), Brown (1995) and Brown and Christie (1998). Tung et al. (1982) examine numerical solutions to the DJL equation in the Boussinesq approximation using a tanh ambient density profile concentrating primarily on solitary wave solutions corresponding to a domain with non-dimensional depth 4. Turkington et al. (1991) present a technique based on a variational principle for the solution of the more complicated non-Boussinesq form of the DJL equation and examine a limited set of solitary wave solutions including large amplitude solutions with closed circulation. Brown (1995) has developed an algorithm (based on a modified successive over-relaxation method) for the solution of either Boussinesq or non-Boussinesq forms of the DJL equation and solves for a wide range of solitary wave solutions using different values of the total domain depth (including very large values capable of representing the deep fluid regime). Brown (1995) also examines the inclusion of certain wind shear profiles and the effect on solitary wave solutions. Brown and Christie (1998) examine fully nonlinear solitary wave solutions to the Boussinesq form of the DJL equation for continuously stratified fluids. They extend the results of Tung et al. (1982) to higher wave amplitude and a wider range of total fluid depths, and also present calculations that show a clear discontinuity in the amplitude-eigenvalue curves for waves in finite-depth fluids. In this chapter the DJL equation is solved numerically for internal solitary wave solutions using an algorithm developed by Brown (1995) to solve the non-Boussinesq eigenvalue problem posed by (6.7). There are a continuous range of eigenvalues Λ for which there exist nonlinear eigenfunction solutions to this problem. Λ is a function of the solution amplitude and can be multivalued. The algorithm of Brown (1995) like that of Tung et al. (1982) is able to "follow" a solution branch once a neighboring solution has been found. Brown (1995) shows that for any value of Λ there are three possible solutions ϕ:

- a trivial solution $\phi = 0$,
- the steady state solution ϕ_0 of interest
- a solution of larger amplitude (corresponding to the upper branch solutions described by Tung et al. (1982))

A standard SOR relaxation scheme applied to (6.7) for any value of the relaxation parameter results in convergence to either the trivial or upper branch solution. Brown (1995) uses a modified SOR technique to find steady state solutions ϕ_0 by requiring values of ϕ which solve the time dependent problem (stated here in its Boussinesq form for simplicity)

$$\frac{\partial \phi}{\partial t} - (\nabla^2 + \Lambda F'(z))\phi = 0, \tag{6.12}$$

with ϕ values defined in terms of an amplitude $A(x,z)$, to relax towards the steady state value. In the relaxation scheme this means consecutive estimates of $A(x,z)$ are made by monitoring the convergence

$$\lim_{t\to\infty}\phi(x,z,t) = \lim_{t\to\infty}[\exp\{t(\nabla^2 + \Lambda F'(z))\}A(x,z)] \tag{6.13}$$

and assigning the next estimate $\Lambda^{(n+1)}$ according to whether the current estimate $\Lambda^{(n)}$ is converging to the desired value $\Lambda^{(0)}$. The convergence of the limit (6.13) in terms of $\Lambda^{(n)}$ is

$$\lim_{t\to\infty}\phi(x,z,t) = \begin{cases} 0 & \text{if } \Lambda^{(n)} < \Lambda^{(0)} \\ \phi_0 & \text{if } \Lambda^{(n)} = \Lambda^{(0)} \\ -\infty & \text{if } \Lambda^{(n)} > \Lambda^{(0)}. \end{cases}$$

6.2.2 Ambient density profiles

The density profile used in the solution of the DJL equation has a functional dependence given by (6.6). A tanh ambient density distribution (ie $F(\psi) = \tanh(\psi)$) has been chosen for the solutions calculated here. This density profile and the corresponding profile of $N^2(z)$, the square of the Brunt-Väisälä frequency, are shown in Fig 6.1. In mapping an incompressible steady state DJL solution to the time dependent compressible model, it is assumed that the ambient Brunt-Väisälä frequency profile remains the same. This means that there will be a condition relating the buoyancy forces expressed in terms of the ambient density $\bar{\rho}$ and the buoyancy forces expressed in terms of the ambient potential temperature $\bar{\theta}$ such that

$$g\frac{d\ln(\bar{\theta})}{dz} = -g\frac{d\ln(\bar{\rho})}{dz}. \tag{6.14}$$

This means that an equivalent form of (6.6) in terms of ambient potential temperature is:

$$\bar{\theta}/\theta_0 = (1 + \sigma F(\psi)). \tag{6.15}$$

Based on the temperature profiles introduced in Chapter 3 that will be used to define the two fluid system for the study of radiative decay, values of σ are chosen to provide temperature profiles that match closely the temperature variation corresponding to values of N_1 in the lower layer. For the DJL starting wave solutions generated in this chapter two values of σ have been used. These are $\sigma = 0.026$ and $\sigma = 0.040$.

6.2.3 Calculation of wave properties

In the study of highly nonlinear waves, it is important to specify how the amplitude and wavelength will be calculated. In order to be able to easily make comparisons between theory and experiment the following definitions have been chosen. Wave amplitude will be defined

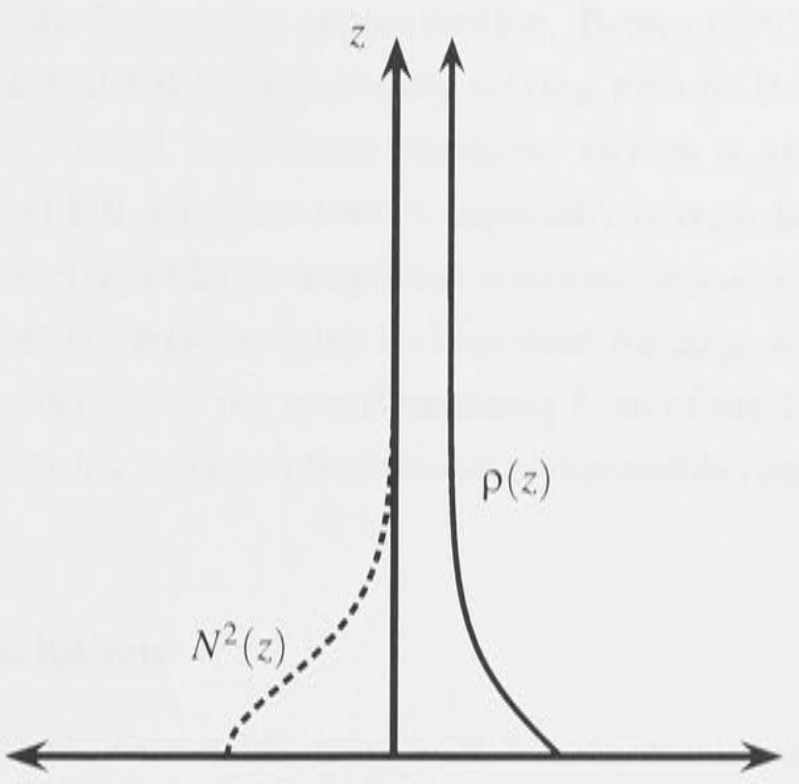

Figure 6.1: *Plot of density and N^2 profiles*

as equivalent to the maximum vertical displacement of a streamline η_{max}. Many theoretical studies (eg Tung el al, 1982) use $(-\phi)_{max}$, the maximum value of the negative perturbation streamfunction ($\phi = \psi - z$) as a measure of wave amplitude. For the case of deep fluids, both η_{max} and $(-\phi)_{max}$, will yield the same value as long as the location of $(-\phi)_{max}$ is not within the region of closed circulation. The wavelength of the waves will be represented by $\lambda_{1/2}$ which defines the full width of the wave at half maximum amplitude. For simplicity the same approach as Brown (1995) will be used and the streamline which has a nondimensional upstream height of 1.0 will be used to calculate $\lambda_{1/2}$ using the full wave width at half maximum perturbation of the streamline. The streamlines are calculated using a SOR routine that solves a streamfunction-vorticity equation as described in the last chapter. It has been found that care must be taken in the solution of this problem using a SOR technique when there are different mesh resolutions used in the horizontal and vertical directions. All DJL solutions presented here are solved using a [200x100] mesh that corresponds to $\Delta x = 100$ m and $\Delta z = 50$ m in a domain using physical units. A linear interpolation for all field variables in x is used when solving for the streamfunction to eliminate any problems arising from differences in horizontal and vertical mesh resolution.

6.2.4 Implications of the Boussinesq approximation

Long (1964) examines the role of the Boussinesq approximation in the theory of internal waves and in particular internal solitary waves. Long investigates certain analytic steady solitary wave solutions to a form of the DJL equation and shows that these solutions can have dependence on

small terms neglected in the Boussinesq approximation. Brown (1995) has found that steady solitary wave solutions calculated by numerically solving the non-Boussinesq DJL equation can have dependence on a small Boussinesq parameter (which is given as σ in the derivation of the non-Boussinesq DJL equation above), especially in regards to the nature of closed streamline flow which can exist for larger amplitude solutions. Because the inclusion of inertial terms involving small density variations may be important for large amplitude solitary waves with closed circulation, solutions to the non-Boussinesq form of the DJL equation have been used for the mapping of starting wave solutions to our compressible non-hydrostatic mesoscale model.

6.2.5 Tanh profile solutions

A ground based atmospheric waveguide layer with homogeneous conditions above can be represented using a tanh ambient density profile defined by

$$\bar{\rho}(z)/\rho_0 = 1 - \sigma\tanh(z/h). \tag{6.16}$$

Using this definition of ambient density, solutions were found to the non-Boussinesq form of the DJL equation for two non-dimensional domains. These were $[x_{\max} = 40.0, H_2 = 20.0]$ and $[x_{\max} = 47.0, H_2 = 11.76]$, where all units have been non-dimensionalised using $h = 850$m. For these domain definitions $x_{\max}$ defines the non-dimensional horizontal extent of a domain symmetric about the origin (due to the symmetry of the eigenfunctions) and H_2 defines a non-dimensional measure of the vertical extent (or total domain depth) for the domain with $\phi(H_2) = 0$. The value of H_2 is therefore directly related to the top boundary condition of the eigenvalue problem defined by (6.12). The value of H_2 will be used to differentiate between these two domains in the discussion of solutions. In both cases a [200x100] point mesh was used with linear grid scaling in both coordinate directions (this choice of grid scaling was found to be most stable in the mapping process)[2]. Two domains are used in order to identify any differences in solutions to the DJL equation for different values of H_2 which corresponds to the height of the upper rigid type boundary condition.

Using the algorithm of Brown (1995) to find solutions which lie on the branch for steady state solutions, a set of eigenvalue, eigenfunction pairs have been found for a tanh ambient density profile with $\sigma = 0.026$ and $\sigma = 0.040$ using both solution domains. An eigenvalue increment of $d\Lambda = 0.1$ has been used. Although a smaller value would provide a larger data set of eigenfunctions, this choice of $d\Lambda$ provides a reasonable range of possible starting wave solutions whilst reducing considerably the time of solution. Fig 6.2 shows the amplitude a/h versus eigenvalue Λ plot for DJL solutions using a density profile with $\sigma = 0.026$ and a domain

[2] An attempt was made to use nonlinear grid scaling but this led to instabilities in the mapping process

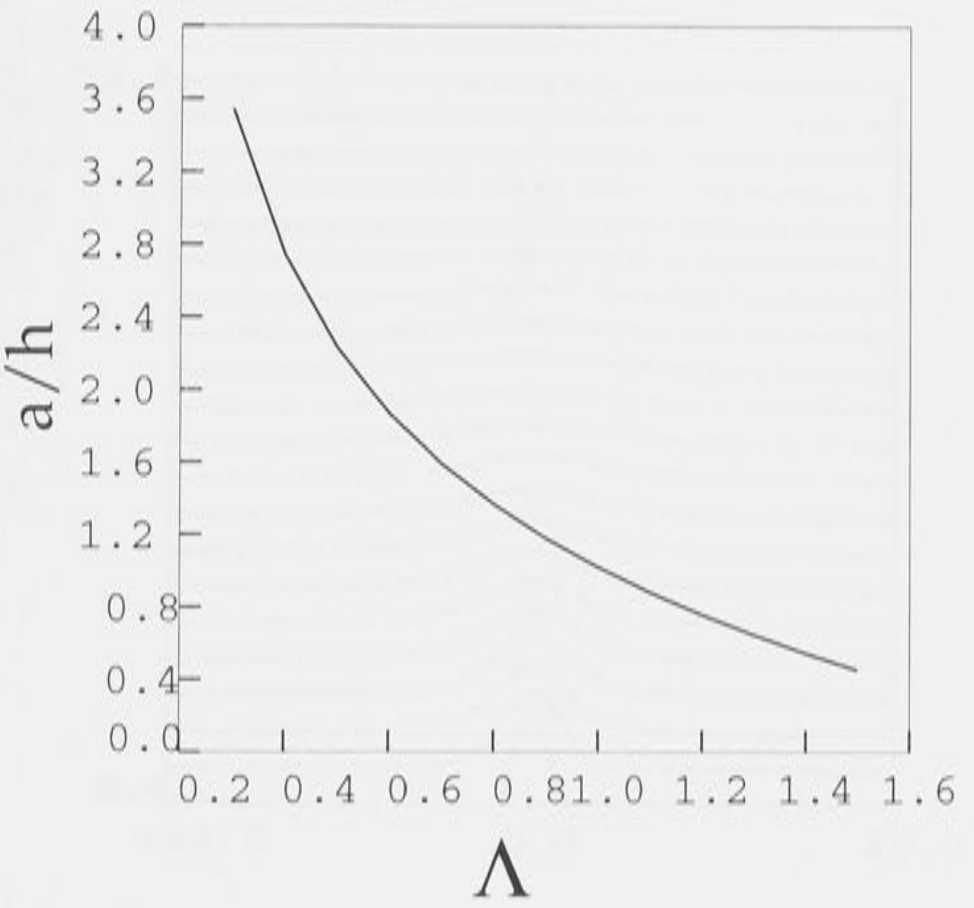

Figure 6.2: The non-dimensional wave amplitude a/h versus the eigenvalue Λ (corresponding to a particular solution of the DJL equation) plot for an ambient density tanh profile with $\sigma = 0.026$ and a total domain depth $H_2 = 20$

depth of $H_2 = 20$. It can be seen that smaller eigenvalues result in wave solutions of larger amplitude. A typical streamfunction plot for this choice of σ and H_2 is shown ($\Lambda = 0.5$) in Fig 6.3 for a solution with closed streamlines (a complete set of streamfunctions for the case with $\sigma = 0.026$ and $H_2 = 11.76$ is provided in Appendix B). The amplitude is calculated as the maximum vertical displacement of a streamline for a particular eigenfunction.

The non-dimensional amplitude a/h versus non-dimensional wave speed c/c_0 graph for the DJL solutions with $\sigma = 0.026$ and $H_2 = 20$ is shown in Fig 6.4. This is a linear relationship and is calculated directly using the incompressible theory. The linear long wave speed for the tanh ambient density distribution is given by

$$c_0 = \sqrt{(\sigma g h/2)}, \tag{6.17}$$

and the wave speed for a solitary wave solution with eigenvalue Λ is calculated directly using (6.8) as

$$c = \sqrt{(\sigma g h)/\Lambda}. \tag{6.18}$$

A solution set of eigenfunctions was also calculated for the same value of sigma for the domain with total non-dimensional depth $H_2 = 11.76$. The non-dimensional amplitude versus

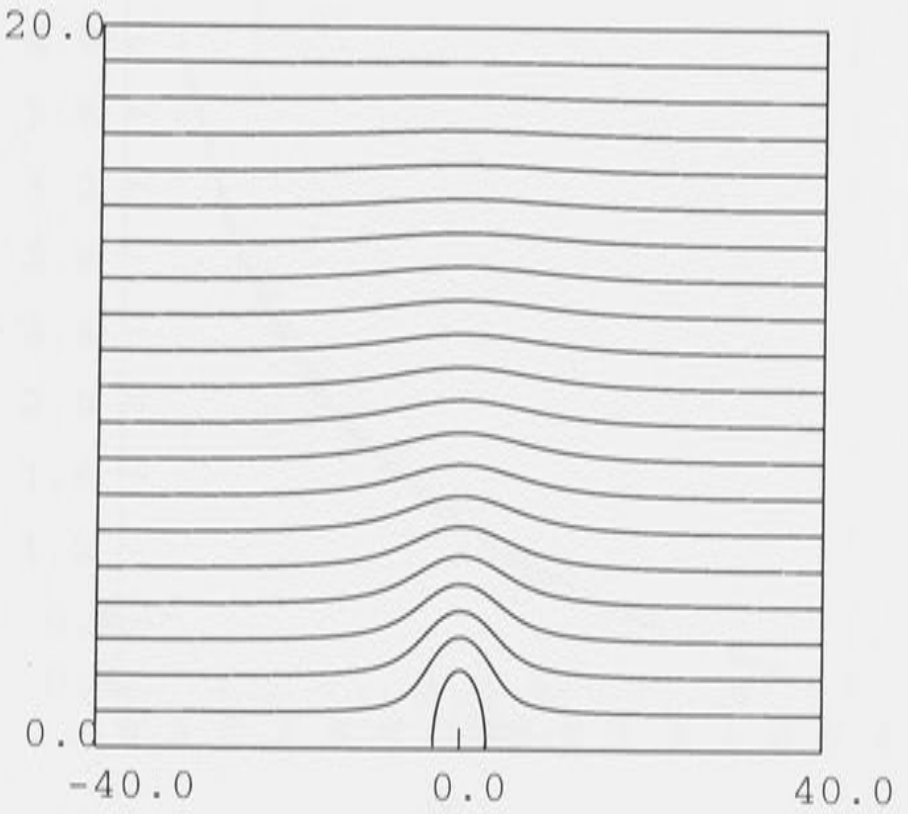

Figure 6.3: The Streamfunction for a solution to the DJL equation with eigenvalue $\Lambda = 0.5$, ambient density tanh profile with $\sigma = 0.026$, and total domain depth $H_2 = 20.0$

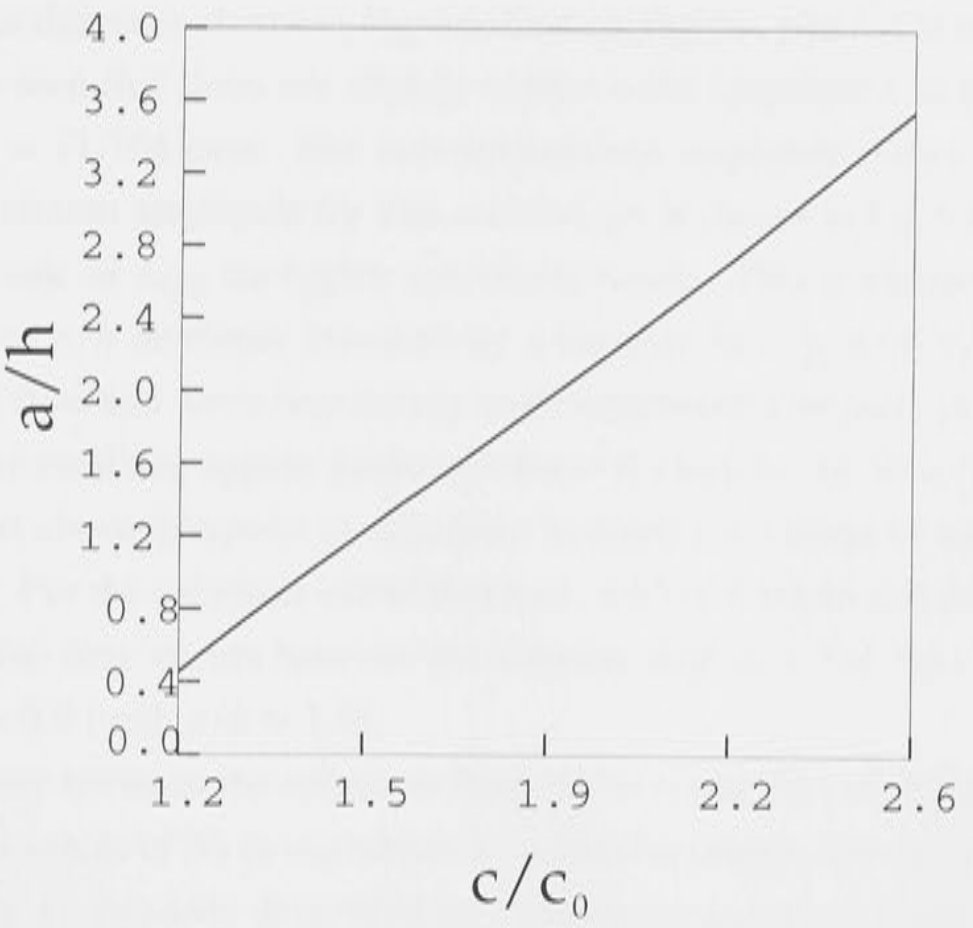

Figure 6.4: The non-dimensional wave amplitude a/h versus the non-dimensional wave speed c/c_0 plot for $\sigma = 0.026$ and $H_2 = 20$

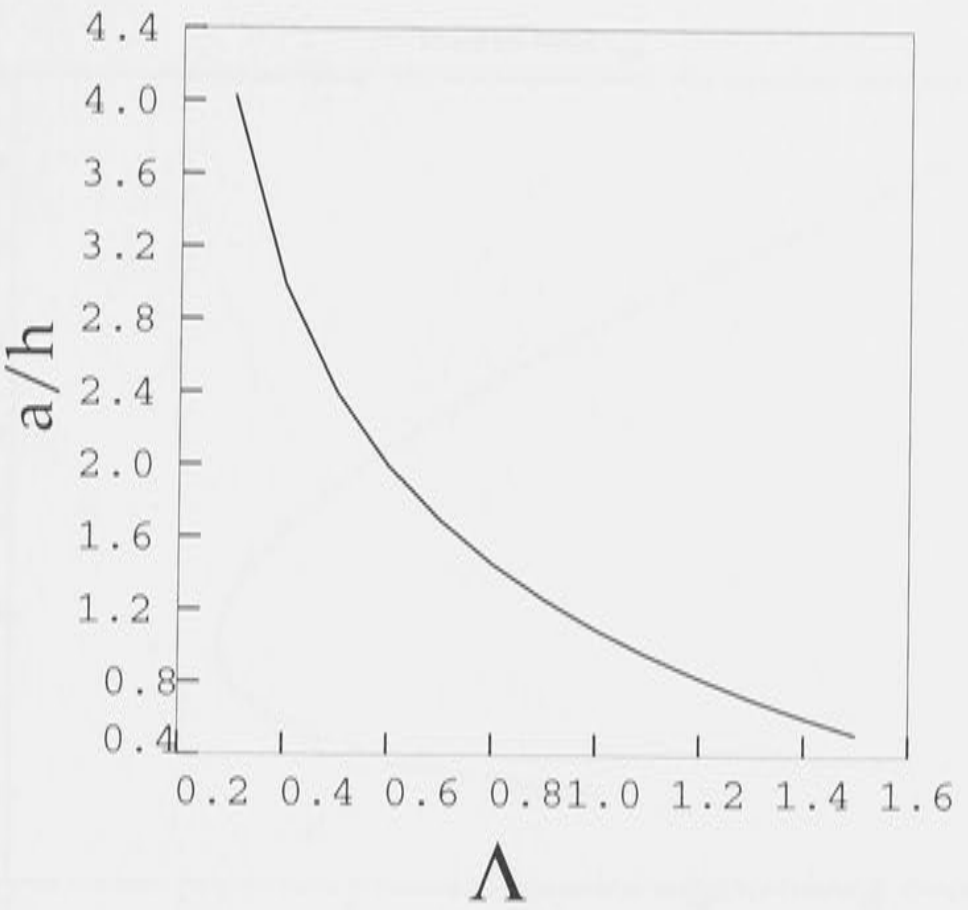

Figure 6.5: Non-dimensional wave amplitude a/h versus eigenvalue Λ (each corresponding to a solution of the DJL equation) plot for an ambient tanh density profile with $\sigma = 0.026$ and a total domain depth $H_2 = 11.76$

eigenvalue plot for this set is shown in Fig 6.5. Comparing this plot to the one for the $H_2 = 20.0$ domain it can be seen that there are slightly higher wave amplitudes in the lower eigenvalue range for the $H_2 = 11.764$ case. The non-dimensional amplitude versus $\lambda_{1/2}$ the full wavelength at half maximum amplitude for this solution set is shown in Fig 6.6. This curve shows the typical behaviour of $\lambda_{1/2}$ for highly non-linear waves. This is characterized by an initial decrease in $\lambda_{1/2}$ as a/h increases followed by a increase in $\lambda_{1/2}$ with a/h after the onset of closed streamline flow and wave broadening as the amplitude continues to increase. The point at which closed streamlines appear in the solutions is close to the wavelength minimum but occurs for a/h just above this point as discussed in detail for a range of general DJL solutions by Brown (1995). For the solutions calculated here, with $\sigma = 0.026$ and $H_2 = 11.76$, the onset of closed streamline flow occurs between the solution with $\Lambda = 1.0$ (with $a/h \approx 1.0$) and the solution with $\Lambda = 0.9$ (with $a/h \approx 1.2$).

The discrepancy between the solutions from the two domains with $H_2 = 11.76$ and $H_2 = 20.0$ is due to both values of H_2 being relatively small (for computational reasons) for a domain depth representing an infinitely deep fluid and introduces a slight dependence in solutions on the domain depth. Brown (1995) solved the DJL equation, using a nonlinear mesh scaling that concentrated points in the lower part of the domain, for a range of H_2 values and found that the amplitude of solutions is dependent on H_2 for small values of H_2. Brown found that

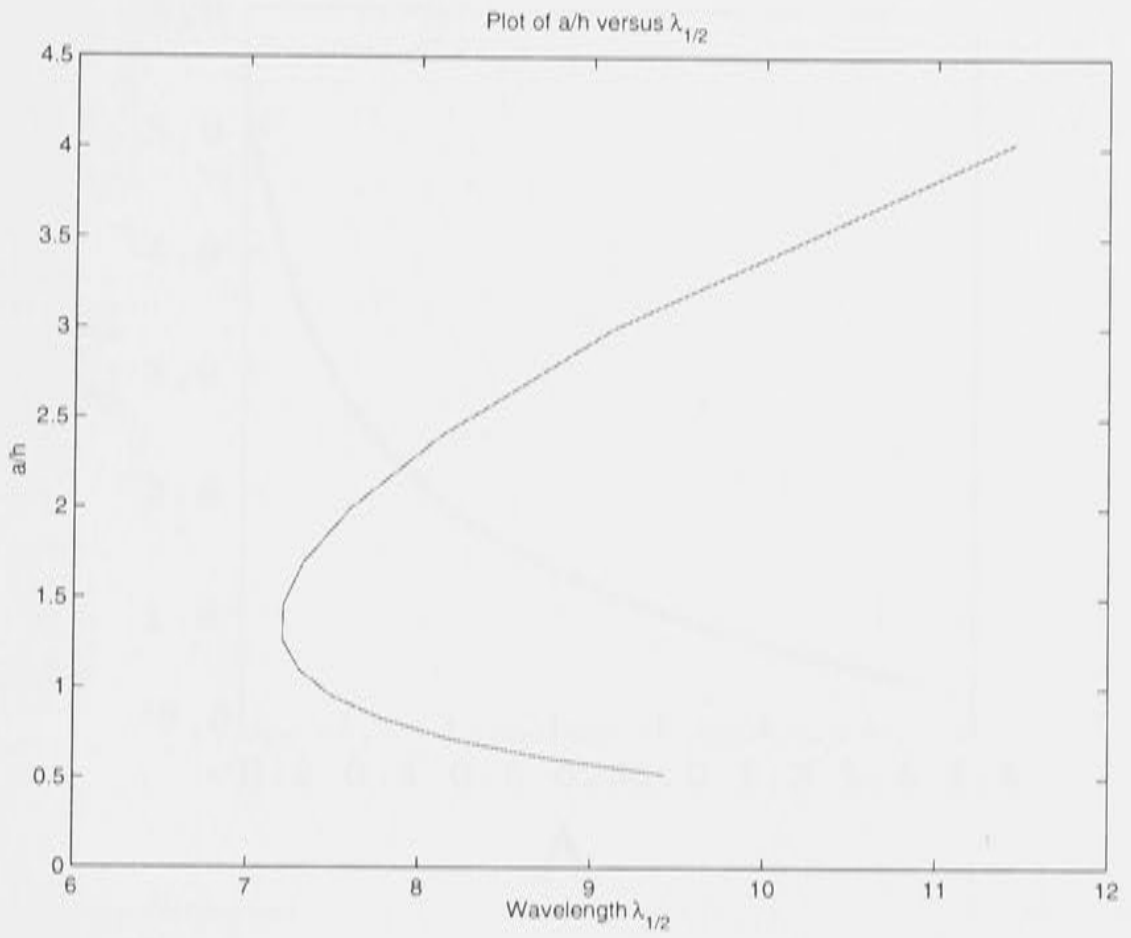

Figure 6.6: Non-dimensional amplitude versus $\lambda_{1/2}$ the full wavelength at half maximum amplitude for $\sigma = 0.026, H_2 = 11.76$ DJL solution set

this dependence becomes asymptotically smaller as H_2 becomes sufficiently large corresponding to H_2 approaching the limit of an infinitely deep fluid regime. For smaller values of H_2 (corresponding to finite depth fluids) he found there to be a maximum amplitude in possible solutions. A sufficiently large value of H_2 (Brown uses $H_2 = 30,200$ as examples) results in amplitude-wavelength curves that match closely up to very large amplitude solutions (nondimensional value 10). As starting wave solutions the solutions generated here are sufficiently accurate given that the maximum amplitudes studied are not greater than a non-dimensional value of 2 and are expected to undergo a transient "adjustment" period when mapped into the compressible model. This can be considered a relaxation process to a stable waveform supported by the compressible model. The degree of "adjustment" was found to be very small in practice if the different solution domains have mesh parameters which match as closely as possible.

Solutions were also calculated for the DJL equation using a tanh ambient density profile with $\sigma = 0.040$. Fig 6.7 shows the non-dimensional amplitude a/h versus eigenvalue Λ for the DJL solutions with an ambient tanh density profile with $\sigma = 0.040$ and a total domain depth $H_2 = 20$. A plot of the streamfunction of a solution ($\Lambda = 0.5$) with closed streamlines for $\sigma = 0.040$ is shown in Fig 6.8. The amplitudes are comparable across the range of eigenvalues for the different sigma values but the wave speeds (calculated using (6.18)) differ due to the

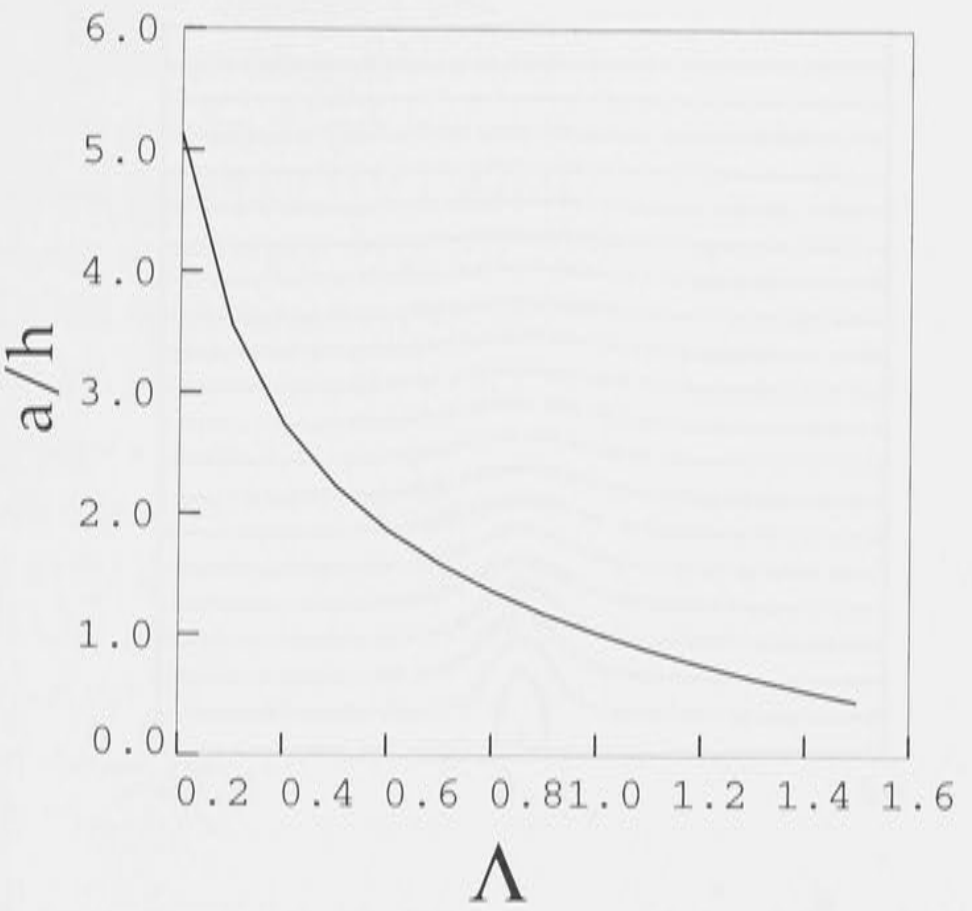

Figure 6.7: Non-dimensional wave amplitude a/h versus solution eigenvalue Λ plot for $\sigma = 0.040$ and $H_2 = 20$

different levels of stratification in the waveguide layer. For both values of σ the wave speed increases linearly with non-dimensional wave amplitude.

6.2.6 Two layer solutions

In addition to finding solitary wave solutions to the DJL equation for a tanh density profile, solutions have been found for a two layered density case where the upper layer is weakly stratified. Here σ is removed from the formulation of the DJL equation and a two layer domain is incorporated into the eigenvalue problem. Each layer represents a constant value of Brunt-Väisälä frequency defined by

$$N_i^2 = -\frac{g}{\rho}\frac{d\rho}{dz} \qquad (i = 1,2), \tag{6.19}$$

where N_1 corresponds to a lower stratified layer and N_2 to an upper layer of relatively weaker stratification. This configuration represents an ambient environment that can support internal wave motions in the upper region.

The eigenvalue Λ is redefined as

$$\Lambda = \frac{gh}{c^2}, \tag{6.20}$$

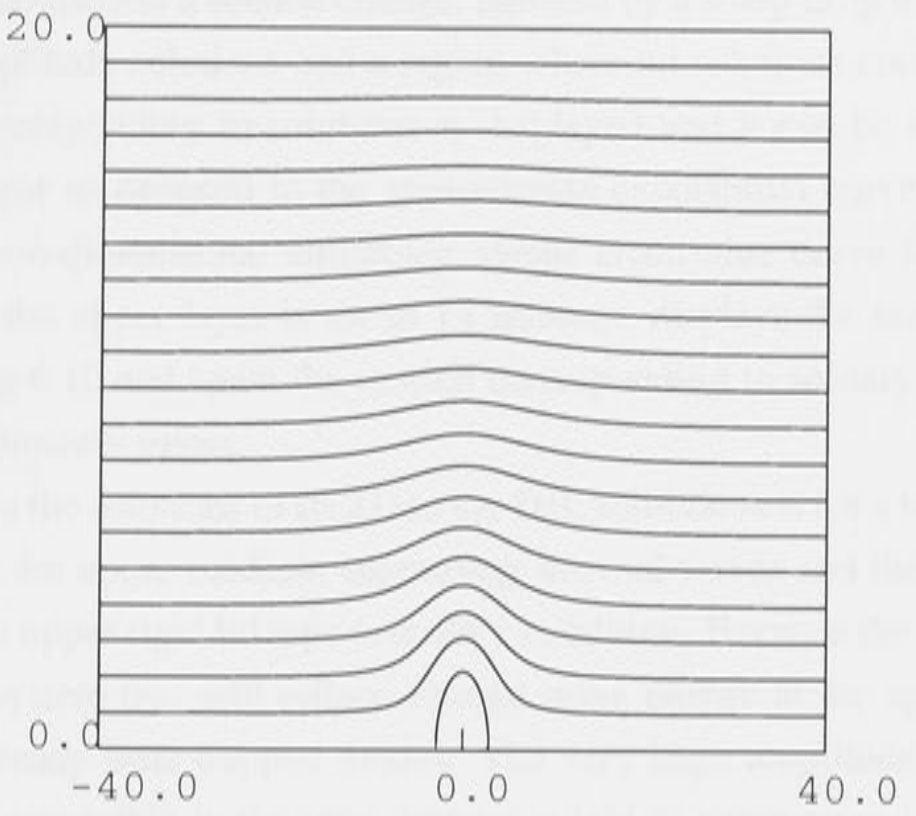

Figure 6.8: Streamfunction for the DJL solution with $\Lambda = 0.5, \sigma = 0.040, H_2 = 20.0$

where h is the scale depth of the lower layer, and K_i (i=1,2) is defined as a non-dimensional variable replacing the N_i, where z now represents a vertical coordinate which has been non-dimensionalised with respect to h,

$$K_i = -\frac{1}{\rho}\frac{d\rho}{dz} = \frac{h}{g}N_i^2. \tag{6.21}$$

A requirement of a smooth transition between layers introduces the approximation

$$K \approx K_1 + \frac{(K_2 - K_1)}{2}(1 + \tanh[\xi(z-d)]), \tag{6.22}$$

where ξ is a constant representing the degree of smoothing and $d = 1$ for non-dimensional height z. The DJL equation can be now be re-written in terms of the streamfunction ψ, using K, as

$$\nabla^2\psi - K[\Lambda(z-\psi) + (\psi_x^2 + \psi_z^2 - 1)] = 0. \tag{6.23}$$

This new form of the DJL equation, represented by (6.23) is now solved for eigenvalue, eigenfunction pairs along the solution branch for steady state solutions. Two different cases (in terms of $[N_1, N_2]$ values) are presented here. For both of these cases the lower layer has a period of 6 minutes. The value of the period in the upper layer is varied between solution sets. Fig 6.9 shows the non-dimensional amplitudes versus eigenvalue for the solution eigenfunctions when the upper layer has a period of 12 minutes. The first clear difference from the tanh profile

solutions above, is that there is a sudden change, denoted by a sharp drop in the curve, between a region of large amplitude solutions and a region where no solutions could be found. In Fig 6.9(b) the region corresponding to solutions is displayed and it can be seen that this curve is approximately linear as opposed to the approximate exponential curves found in the tanh solution sets. The non-dimensional amplitude versus eigenvalue curve for the second case, where the period in the upper layer is set to 14 minutes, displays the same behaviour. This curve is shown in Fig 6.10 and again the section corresponding to solitary wave solutions can be seen to be approximately linear.

The differences in the solutions of (6.23) to the DJL solution sets for a tanh ambient density profile are related to the upper medium supporting internal waves and the formulation of the DJL equation with an upper rigid lid type boundary condition. Because the solutions are steady state solutions of a system that will reflect internal wave energy at the upper boundary, they probably represent steady state trapped modes. The very large amplitude solutions and their scale size which is comparable to the total domain height in some cases (see Fig 6.11 for the streamfunction for $\Lambda = 200$) strongly support this conclusion (Note: a set of streamfunctions for the two layer density profile solutions is included in Appendix B). Wave trapping and the existence of trapped modes have been observed in the atmosphere and are described by several authors (eg. Crook, 1988; Skyllingstad, 1991). Crook (1988) describes how an inversion layer at a certain height above a lower stable layer can reflect wave energy and if the layer between is weakly stratified this can lead to an enhancement of wave amplitudes for waves propagating in the lower stable layer. In the case of the DJL equation solved with a rigid type upper boundary condition, reflection of wave energy is certain at height $z = H_2$. This will provide the opportunity for a degree of constructive interference between upward and downward propagating vertical wave modes. It is most likely that the two layer solutions presented here represent such steady state solutions of trapped modes for the model atmosphere defined by (6.22).

The two layer solutions described here are not used as starting solutions because of a number of important limitations. Limitations of two layer solutions of the DJL equation are firstly that they are steady state solutions whereas wave radiation depends strongly on time evolution. Secondly the DJL equation (as presented in this chapter) is solved with a rigid lid upper boundary condition (at $z = H_2$). This has important implications for wave radiation. The use of such a boundary condition introduces the possibility of solutions that represent wave trapping when the region below the upper boundary is weakly stratified (ie the two layer case). It has been suggested by some researchers that the use of a rigid lid upper boundary condition can be compared to the energy reflecting properties of an internal wave critical layer (see eg. Rottman and Einaudi, 1993). To avoid the possibility of reflected wave modes in the DJL solutions a more complicated upper boundary condition would need to be implemented. This would substantially increase the difficulty in solving for solutions. Lastly it should be noted

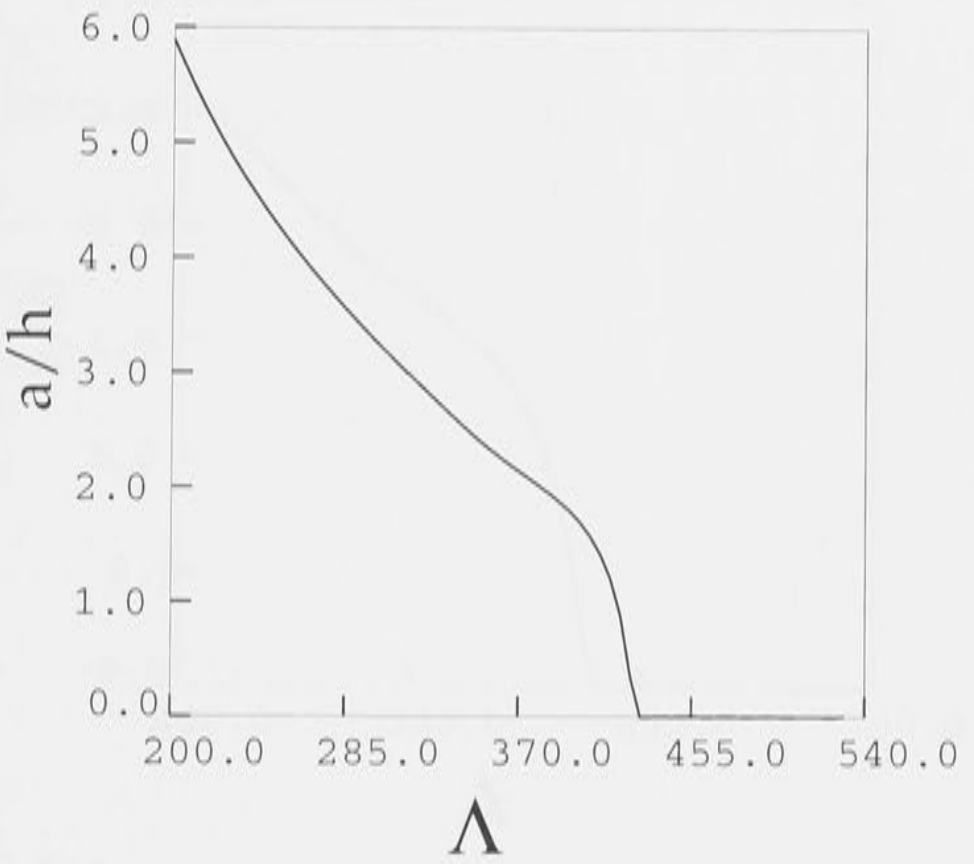

(a)

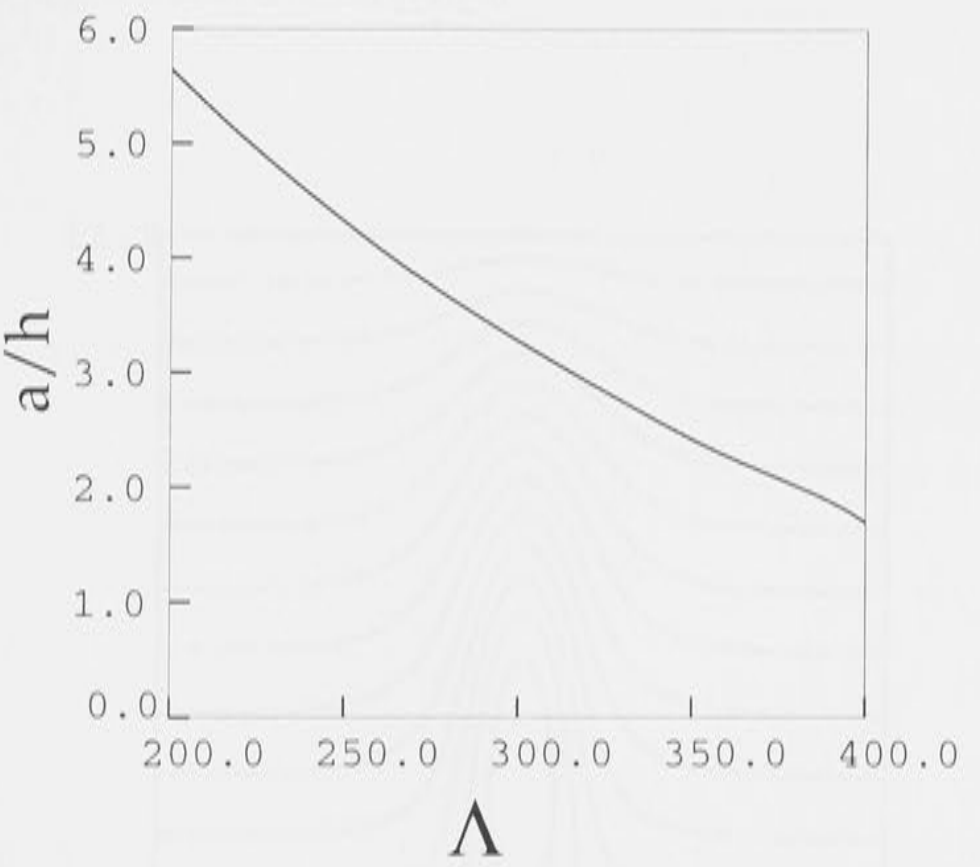

(b)

Figure 6.9: (a) The non-dimensional wave amplitude a/h versus solution eigenvalue Λ plot for a two layer domain with $N_1 = 2\pi/(6.60)$ and $N_2 = 2\pi/(12.60)$; (b) a closeup of the same plot for the range $200 < \Lambda < 400$.

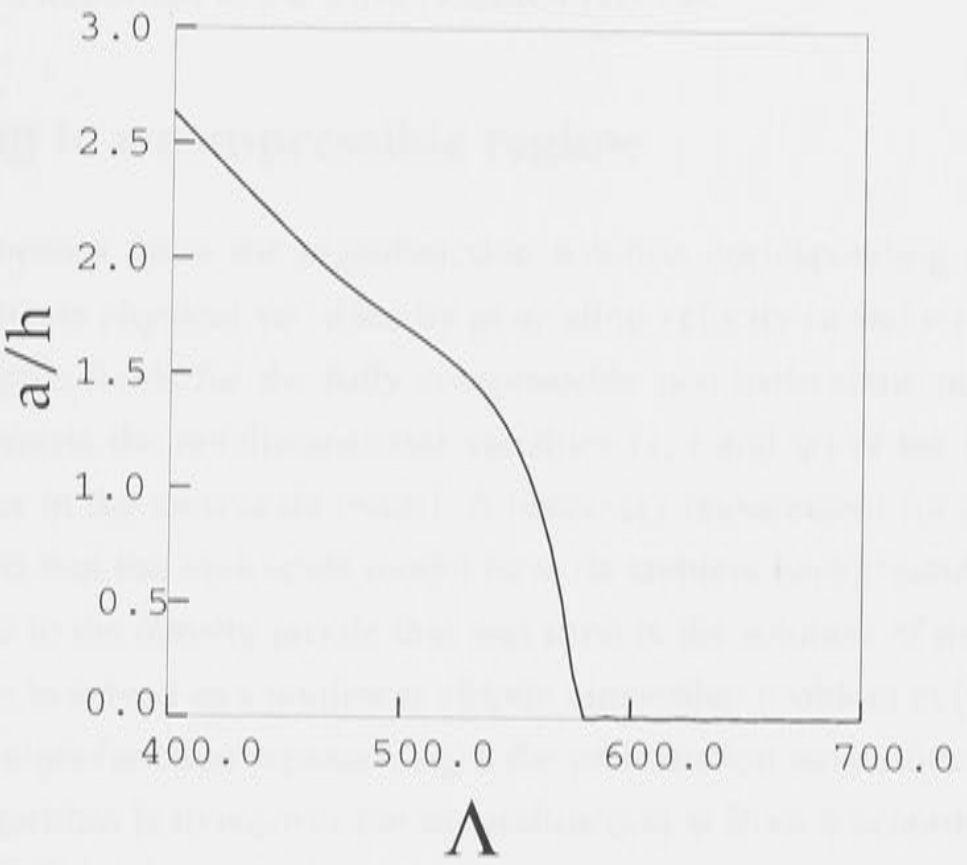

Figure 6.10: Non-dimensional wave amplitude a/h versus solution eigenvalue Λ plot for a two layer domain with $N_1 = 2\pi/(6.60)$ and $N_2 = 2\pi/(14.60)$

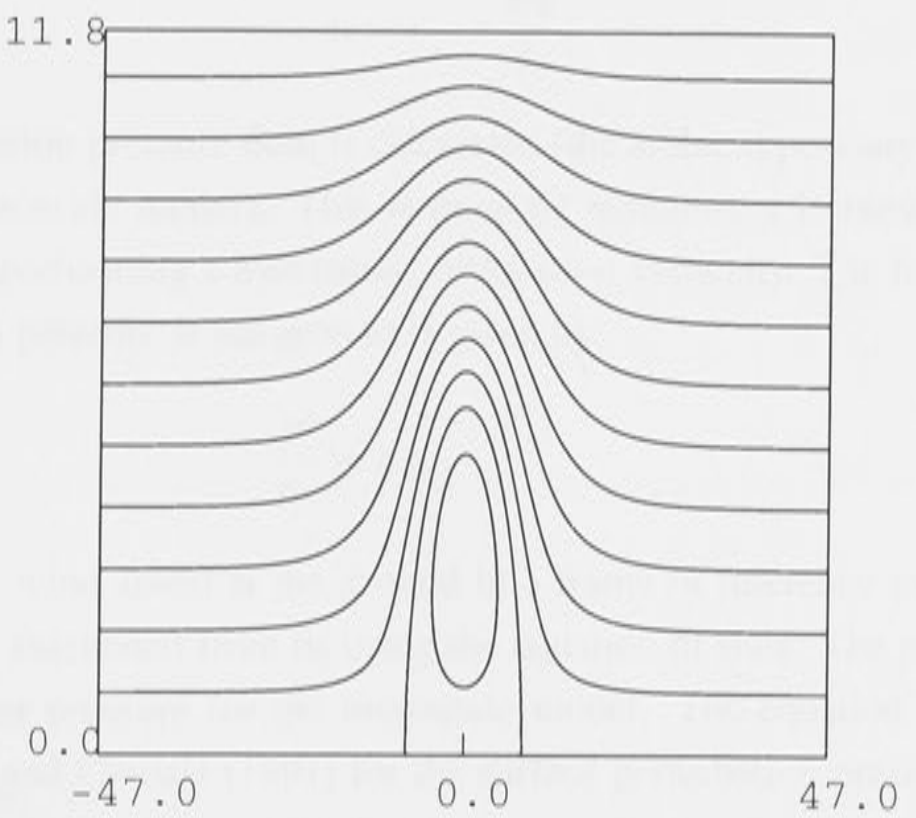

Figure 6.11: Streamfunction for DJL solution with eigenvalue $\Lambda = 200$ for a two layer domain with buoyancy period 6 min in the lower layer and period 12 min in the upper layer

that all DJL solutions do not include viscous forces (ie it is an inviscid equation) and it is likely that such forces are important to the wave radiation process.

6.3 Mapping to a compressible regime

The mapping algorithm takes the eigenfunction solution corresponding to a specified DJL eigenvalue and extracts physical variables by generating velocity (u and w) and thermodynamical (t and p) variable fields for the fully compressible non-hydrostatic numerical mesoscale model. It also converts the nondimensional variables (x, z and ψ) of the DJL solution to dimensional variables in the mesoscale model. A necessary requirement for successful mapping of a DJL solution is that the mesoscale model have its ambient background assigned to values that are compatible to the density profile that was used in the solution of the DJL equation.

Longs equation is solved as a nonlinear elliptic eigenvalue problem in (ϕ, Λ) where each Λ corresponds to an eigenfunction representing ϕ the perturbation streamfunction. The first step in the mapping algorithm is to recover the streamfunction ψ from ϕ according to:

$$\psi = \phi + z. \tag{6.24}$$

Then the velocity fields[3] u and w are obtained using the standard relations:

$$u = \frac{\partial \psi}{\partial z}, \tag{6.25}$$

$$w = -\frac{\partial \psi}{\partial x}. \tag{6.26}$$

Next the perturbation pressure field is calculated (the ambient pressure being a hydrostatic base state in the mesoscale model). This is done by assuming a Bernoulli type equation at the ground and then performing a hydrostatic integration vertically. The Bernoulli equation in terms of perturbation pressure at the ground is given by:

$$\frac{p'}{\rho_0} = u'[c - \frac{u'}{2}], \tag{6.27}$$

where the horizontal wind speed at the ground in a frame of reference moving at speed c is given by u' and ρ_0 is calculated from θ_0 using the equation of state. The pressure p must also be converted to Exner pressure for the mesoscale model. The equation (6.27) is similar to that used by Doviak and Christie (1991) for the surface perturbation pressure associated with stationary atmospheric waves except that there is no contribution from an ambient wind profile. The hydrostatic integration of the Exner pressure value (Π'_0 at $z = 0$) resulting from (6.27) is

[3] Making sure that non-dimensional quantities are converted to dimensional quantities

performed using the relation

$$\frac{\partial \Pi'}{\partial z} = \frac{g\theta'}{C_p \bar{\theta}(\bar{\theta}+\theta')}, \tag{6.28}$$

$$\Pi'(x,0) = \Pi'_0. \tag{6.29}$$

In addition to the assignment of pertubation Exner pressure, a method must be chosen for the initialization of the perturbation potential temperature field. Using the relative displacement of streamlines represented by ψ. If z_0 represents the upstream elevation of a particular streamline, then the relative displacement at (x,z) is defined by

$$\delta(x,z) = z - z_0. \tag{6.30}$$

Values of $\delta(x,z)$ are used as scaling factors on the ambient potential temperature profile $\bar{\theta}(z)$. The occurrence of closed streamline flow must be treated separately. It was decided here to initially set values of perturbation potential temperature at height z inside the closed circulation cell to the difference between the ambient temperature at the ground and the ambient background temperature at the height z:

$$\theta'(z) = \bar{\theta}_0 - \bar{\theta}(z). \tag{6.31}$$

This effectively means that the potential temperature of the fluid within the closed circulation cell is equal to the ambient temperature at the ground. Field observations (eg Clarke et al, 1981) have recorded similar temperature profiles within a closed circulation cell. Brown (1995) used a similar initialization of temperature inside regions of closed streamline flow for the mapping of DJL solutions to a compressible model with a rigid lid upper boundary condition. Values of potential temperature within closed circulation cells are beyond the limits of the information contained in DJL wave solutions. The method of approximation chosen here seems to provide a temperature field for the wave which is similar to that observed for waves with closed circulation generated in the last chapter.

There are several stability issues related to the mapping of the DJL solutions to the compressible mesoscale model. One of the most important is the influence of viscous effects through the Fickian diffusion coefficients K^x and K^z. As noted previously by Brown (1995) viscous effects are not necessary to maintain stability for the mapping of wave solutions that do not possess closed circulation but that small viscous terms are crucial for stable mappings of wave solutions with closed circulation. It has been further observed in the present study that the magnitude of the viscous terms (ie K^x and K^z) are slightly dependent, for fixed grid resolution, on the amplitude of the wave possessing closed circulation (and therefore to the size of the cell), with very large amplitude waves requiring larger values of K^x and K^z in order to remain stable during the "adjustment" period, during which intense internal mixing com-

mences within the wave. There would appear to be an upper limit in wave amplitude, for a chosen grid resolution, beyond which the mapped solution will become unstable regardless of the magnitude of small scale viscous dissipation represented by the choice of K^x and K^z. This is discussed further below.

As mentioned above the ambient profiles of $\bar{\theta}$ and $\bar{\Pi}$ are also crucial to a mapped solution being stable in the mesoscale model. This is especially true with respect to the perturbation pressure field Π'. Because the speed of sound is effectively infinite in an incompressible domain such as that for which the DJL equation is solved, it is expected that the mapping of solutions from an incompressible domain to a compressible one will pose problems. It was found in the mapping method chosen that the Π' field was sensitive, owing to its time dependent interaction with the radiative upper boundary condition, to the background profiles of $\bar{\theta}$ and $\bar{\Pi}$ present at $t = 0$. To avoid instability in the Π' field it was necessary to suppress (at least initially) any upward radiation of internal waves until the DJL solution had "adjusted" to the mesoscale model. This meant that any upper region of the ambient domain defined by $\bar{\theta}$ and $\bar{\Pi}$ must be initially neutral.

6.3.1 Analysis of mapped solutions

A major advantage of using mapped solutions such as those presented in this chapter is that they offer a single stable solitary wave disturbance without significant interference from any other processes. Other methods that have been used to generate solitary waves in numerical models usually involve the generation of a family of wave crests in the formation process, such as that produced in the transition from an undular bore to a family of amplitude ordered solitary waves, and often have undesirable forcing processes which can interact with the wave field. The mapped solutions used here are easily positioned in the center of the domain and a moving coordinate system can be used which is set at the speed of the initial mapped wave (at $t = 0$). The speed of the initial mapped solution is calculated using (6.18). A uniform opposing background wind is then applied to the model, so that effectively the wave is traveling in a coordinate system which itself is traveling at speed c. This setup is convenient for an analysis of radiative decay as the wave remains inside the horizontal bounds of the domain for a substantial period of time.

It can be seen from Fig 6.12 that solution mappings for the same eigenvalue ($\Lambda = 0.7$) for the different DJL solution domains ($H_2 = 11.76, 20.0$) are stable waveforms over time in the compressible model with slightly different amplitudes (due to differences in the solution sets). The rate of amplitude decay is very slow for an environment with neutral upper layer. The majority of the amplitude decay occurs over a short "adjustment" period and then the wave amplitudes remain almost constant with a very slow linear decay rate due to viscous losses associated with the closed circulation cell (and in the absence of frictional drag at the ground since the model represents the earths surface using a free slip lower boundary condition). It

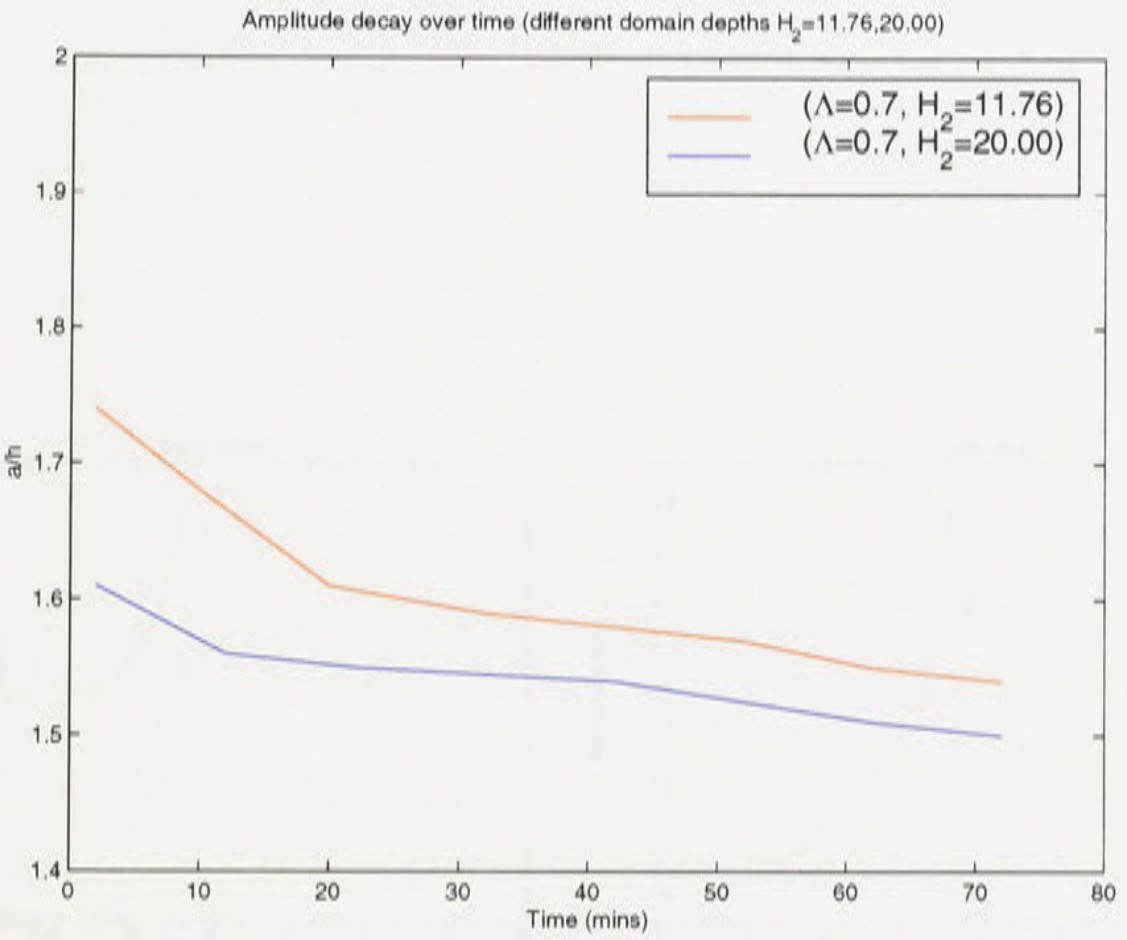

Figure 6.12: Amplitude decay of mapped solutions with eigenvalue $\Lambda = 0.7$ from DJL solution sets for a tanh ambient density profile with $\sigma = 0.026$ and different values of the solution domain depth H_2 which have relaxed to a stable wave solution in the compressible model with a matching ambient environment

can be seen in Fig 6.12 that the mapped solution for eigenvalue $\Lambda = 0.7$ has an amplitude which rapidly approaches the slow linear decay due to viscous dissipation. The time scale of the "adjustment" period can be seen to be in the order of 20 mins in the graph and a value of $t = 22$ mins has been selected as the minimum requirement to allow a mapped solution to relax to a stable waveform in the compressible model. The surface perturbation Exner pressure field is a useful measure of the degree of wave stability. This can be seen in Fig 6.13 which shows the changes in surface perturbation pressure which occur at a selection of time values within the initial 22 mins of wave evolution in the compressible model. During this "adjustment" period internal mixing has commenced within the closed circulation cell. This initialization of mixing leads to an initially increased rate of energy loss which seems to cause a more rapid decrease in wave amplitude and a small increase in the wavelength (ie increased wave broadening). The wave seems to have reached a stable state with closed circulation continuing within the wave by approximately $t = 20$ min. A typical plot of the perturbation Exner pressure at the ground after this short adjustment period is shown in Fig 6.14 and displays the characteristic bimodal shape of surface pressure that has been recorded for highly nonlinear solitary waves in the lower atmosphere.

Due to the vertical extent (10km) of the compressible model corresponding exactly to

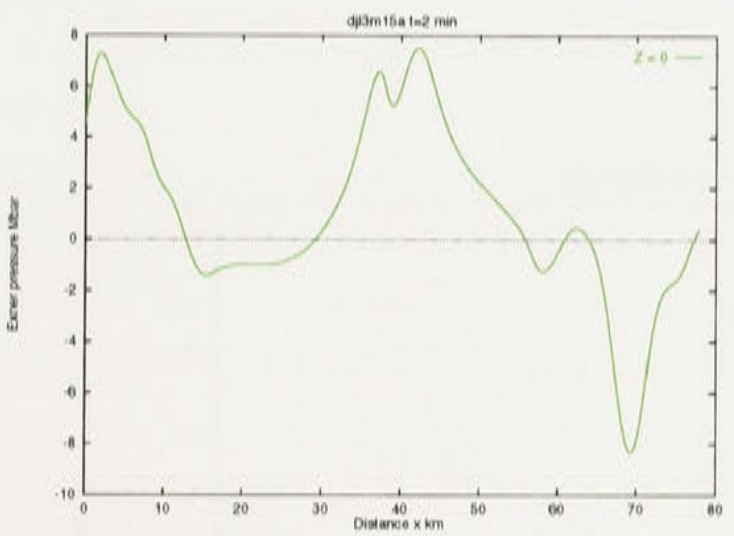

(a) 2 mins

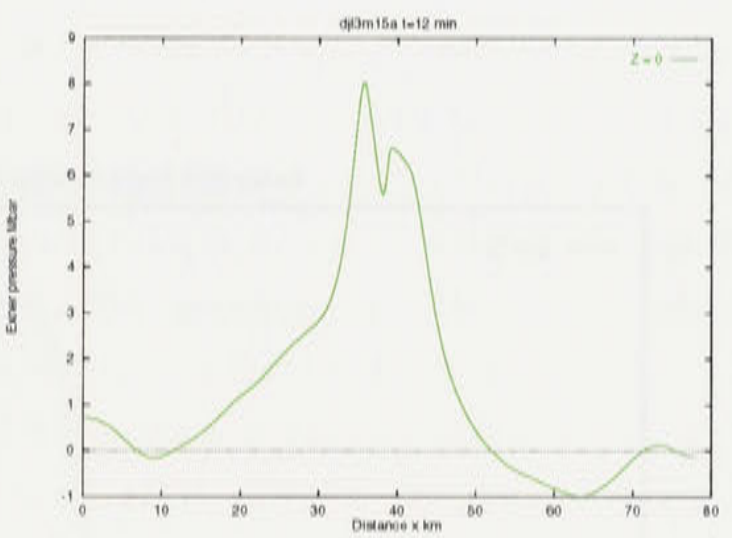

(b) 12 mins

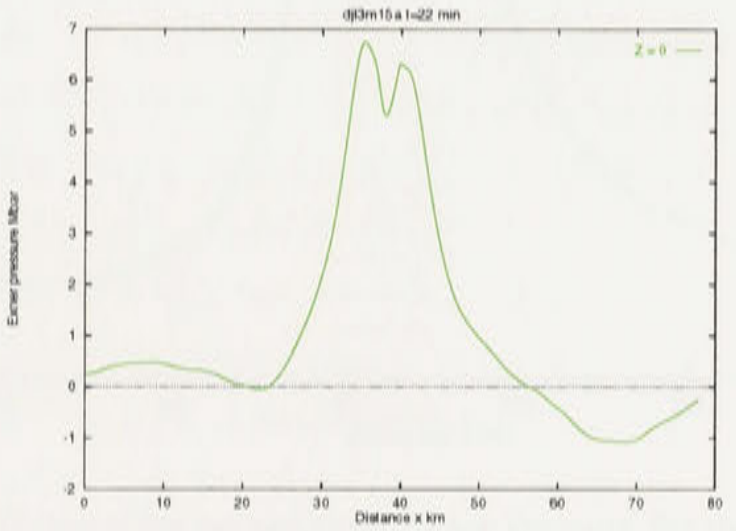

(c) 22 mins

Figure 6.13: Changes in surface perturbation Exner pressure during the first 22 mins of wave evolution in the compressible model.

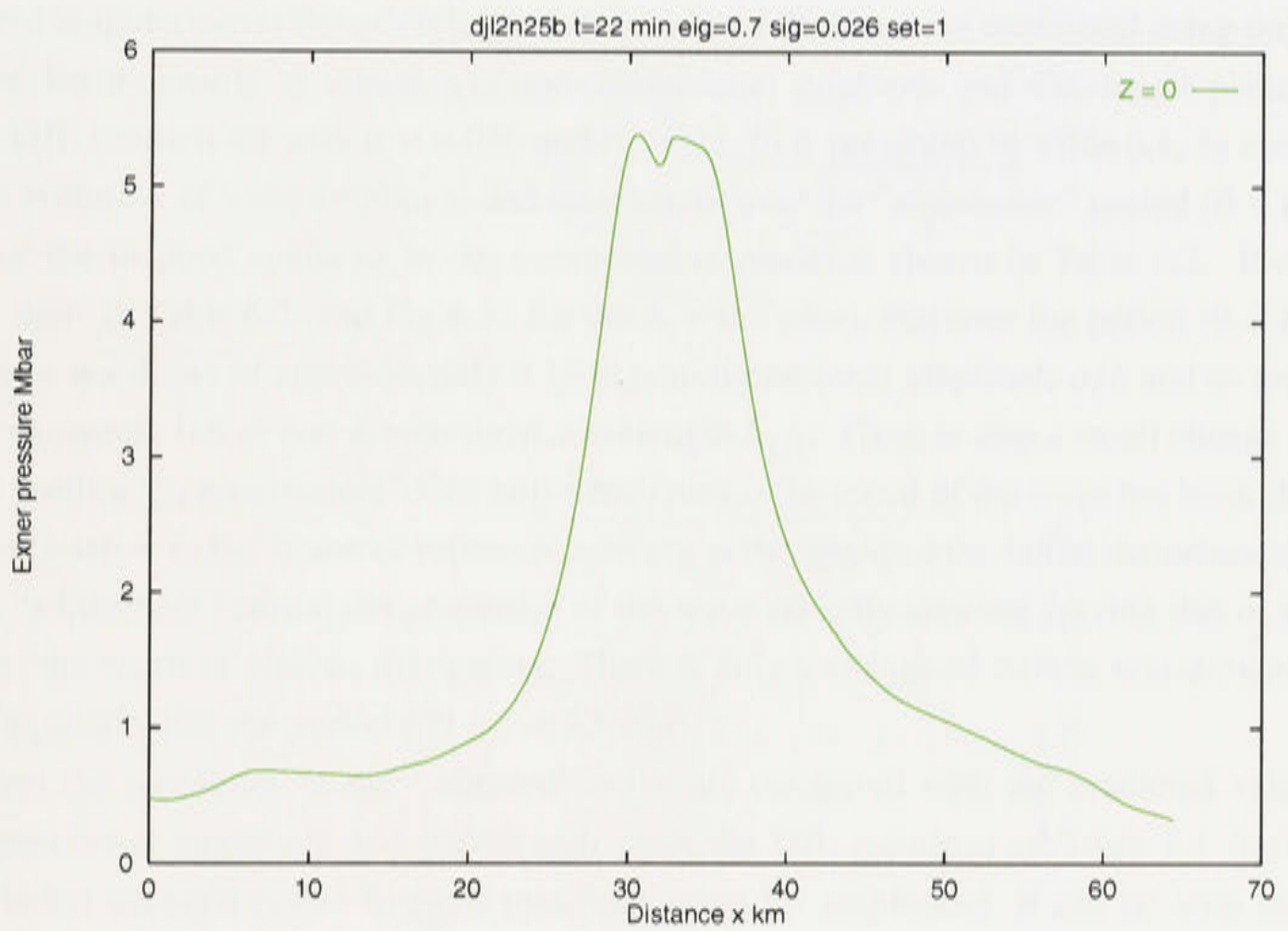

Figure 6.14: Surface ($z = 0$) trace for perturbation Exner Pressure for mapped solution at time = 22 minutes. The characteristic bi-modal shape has been observed in atmospheric measurements.

the non-dimensional $H_2 = 11.76$, it has been decided to use mapped solutions from the DJL solution set with $H_2 = 11.76$ as starting wave solutions in the next chapter. This provides a greater effective vertical grid resolution during mapping of solutions compared to the use of the solution set with $H_2 = 20$. Typical streamfunction plots of a solution with ($\sigma = 0.026, H_2 = 11.76, \Lambda = 0.7$) are shown in Fig 6.15. The concentration field for the tracer fluid used to mark the interface between the lower and upper layers has been included in the streamfunction plots for comparison. It can be seen that some tracer (initialized at $t = 0$ min as a straight line through the mapped wave solution) has been caught up by mixing processes within the wave.

A comparison is now made between the properties of the mapped solution from the eigenvalue $\Lambda_{t=0} = 0.7$ and $\Lambda_{t=0} = 0.6$ cases, as they evolve in the compressible model and the predicted amplitude-wavelength relationship from the DJL solutions calculated using the same ambient density profile. A selection of non-dimensional amplitude and wavelength parameters for the DJL solution set with $\sigma = 0.026$ and $H_2 = 11.76$ is presented in Table 6.1. In comparison the evolution of wave amplitude and wavelength over the "adjustment" period ($0 < t < 20$ min) for the mapped solutions in the compressible model is shown in Table 6.2. It can be clearly seen, in Table 6.2 (and Fig 6.12 for the $\Lambda = 0.7$ case), that over the period ($0 < t < 20$ min) there is a decay of approximately 0.15 in non-dimensional amplitude a/h and an increase of approximately 0.6 in non-dimensional wavelength $\lambda_{1/2}$. There is also a small change in the wave's position (approximately -1.15 km) which means the speed of the wave has been slightly reduced (relative to the frame of reference moving at the speed of the initial disturbance). After this "adjustment" period the properties of the wave are only slowing varying due to a slow decay as the result of viscous dissipation. There is only a change of 0.06 in non-dimensional wave amplitude over the period ($20 < t < 72$ min).

When the properties of the "adjusted" wave are compared with the predicted values of non-dimensional amplitude and wavelength from the DJL solutions of Table 6.1 (using an interpolation between points to get a matching value for amplitude), it can be seen that the wavelength in the compressible model is greater than that predicted from inviscid theory (DJL). A constant difference seems to result for a range of different mapped solutions (ie values of $\Lambda_{t=0}$). It is proposed, based on this observed difference in wavelength of a mapped solution which has relaxed to a quasi-steady state in the compressible model (ie after the "adjustment" period), that for the purpose of making comparisons later with DJL solutions an adjustment of 0.6 be made to the DJL values.

A typical evolution of a closed circulation cell (for $\Lambda = 0.7$) in the early stages after mapping to the compressible model is shown in Fig 6.16. In Figs 6.16(a), 6.16(b) and 6.16(c) it is clear that there is strong mixing occurring within the closed circulation cells as the mapped solution "adjusts" to the compressible model. In Fig 6.16(d) the wave has reached a quasi-steady state and the closed circulation cell can be seen to leak fluid in a thin trail at ground level in the wake of the wave. The relative size of the closed circulation cell in a larger amplitude solution

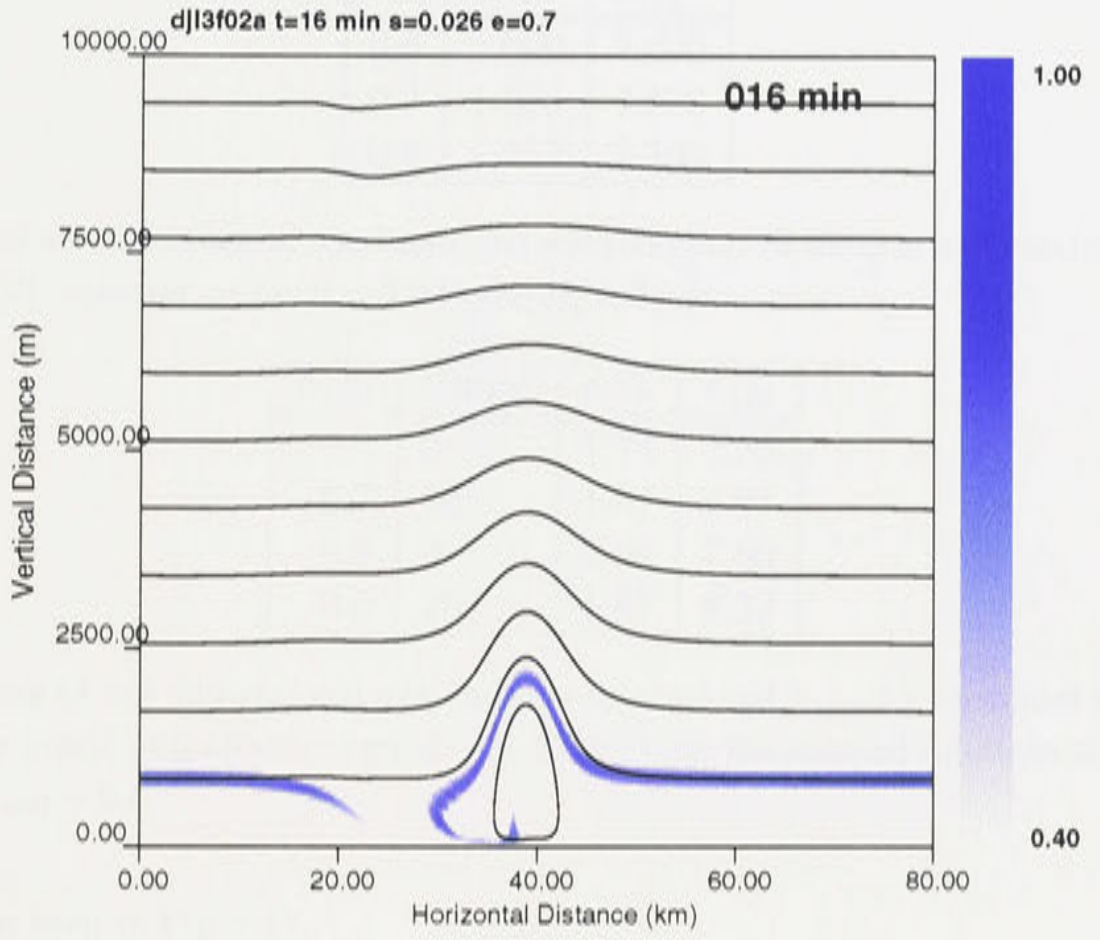

(a)

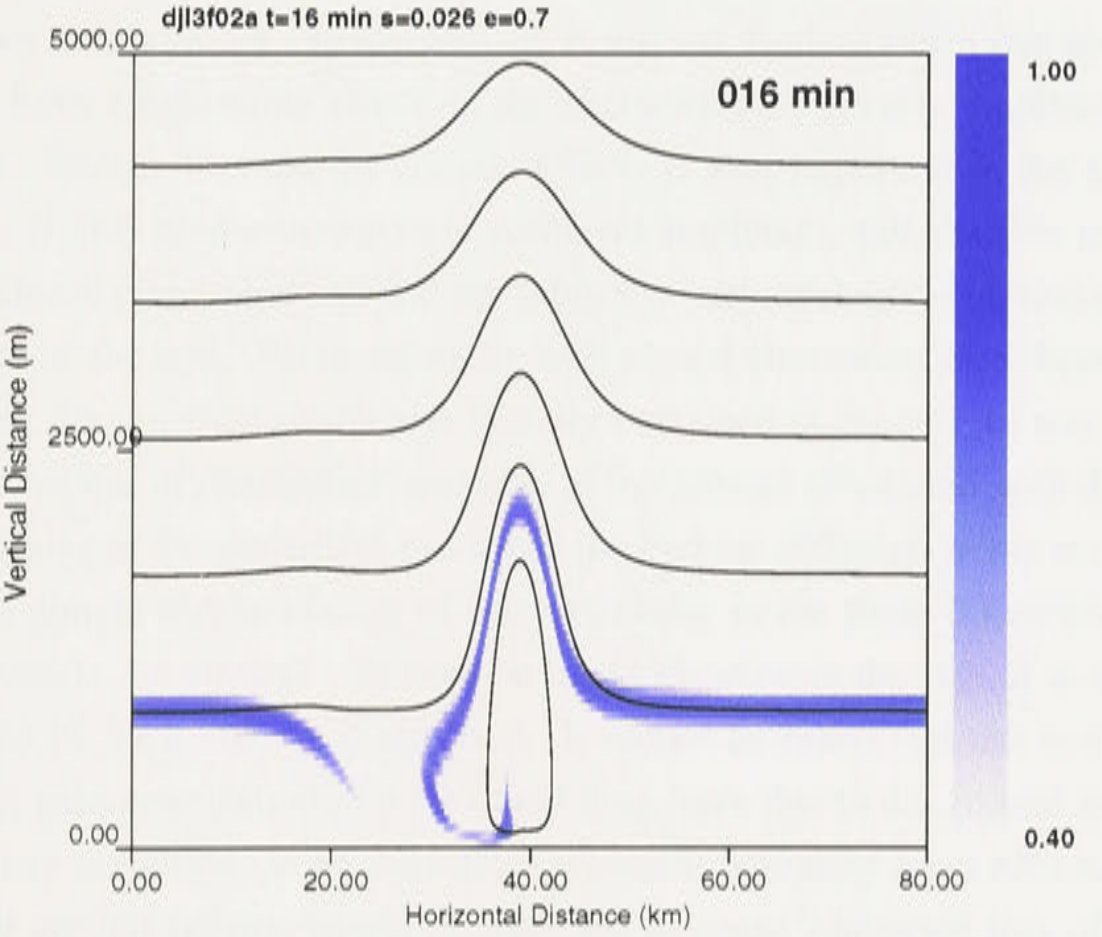

(b)

Figure 6.15: (a) Streamfunction (calculated using SOR routine) for mapped solution with $\sigma = 0.026$ where starting wave solution is $\Lambda = 0.7, \sigma = 0.026, H_2 = 11.76$. The tracer used to mark the interface of the lower waveguide layer has been included. Some of the tracer (initialized at $t = 0$ min as a straight line through the mapped wave solution) has been caught up by mixing processes within the wave; (b) closeup of the same streamfunction where the vertical coordinate range is now $0 < z < 5.0$ km.

Λ	a/h	$\lambda_{1/2}$
0.6	2.000	7.600
0.7	1.695	7.328
0.8	1.457	7.209

Table 6.1: A set of non-dimensional amplitude and wavelength (full width at half maximum amplitude) values from the DJL solution set for $\sigma = 0.026$ and $H_2 = 11.76$.

$\Lambda_{t=0}$	t(min)	a/h	$\lambda_{1/2}$
0.7	0	1.74	7.35
0.7	20	1.61	7.95
0.6	0	2.04	7.60
0.6	20	1.87	8.22

Table 6.2: Estimate of non-dimensional a/h and non-dimensional $\lambda_{1/2}$, for the initial mapping ($t = 0$ min) and after the initial "adjustment" period ($t = 20$ min), for the mapped solutions corresponding to $\Lambda_{t=0} = 0.7$ and $\Lambda_{t=0} = 0.6$.

($\Lambda = 0.6$) can be seen in Fig 6.17.

6.3.2 Energy loss due to viscous effects

It has been shown in laboratory experiments by Koop and Butler (1981) that energy loss due to viscosity can have a noticeable effect on the characteristics (mostly amplitude) of weakly nonlinear waves. Energy loss due to viscous effects is also important in the case of highly nonlinear waves. Highly nonlinear waves of sufficient amplitude, with suitable ambient conditions, possess a closed circulation cell and are subject to varying degrees of viscous dissipation based on the size of the cell. Wave solutions with closed circulation have been observed to leak a thin trailing flow of fluid which was initially contained in the cell (as was shown in Fig 6.16) due to the transfer of momentum and heat to the ground associated with dissipation occuring at small scales in the numerical model (ie the Fickian diffusion terms used for subgrid dissipation and a simple representation of eddy viscosity in the finite difference form of the governing equations). An attempt will now be made to estimate the rate of amplitude decay due to energy lost by such viscous dissipation. It should be noted that our numerical model makes no explicit parameterization of a frictional drag force due to the ground and uses a free slip lower boundary condition (ie no attempt to represent boundary layer effects). Such a parameterization of ground friction would be expected to cause additional loss of energy from the wave. The limits of the mapping technique in terms of an upper limit on the amplitude of waves which can be successfully mapped is also discussed below. This limit seems to be directly related to the ability of the compressible model and mapping technique to represent the increasing viscous dissipation associated with the increasing wave amplitude (and size of the closed region of recirculating flow) of DJL solutions.

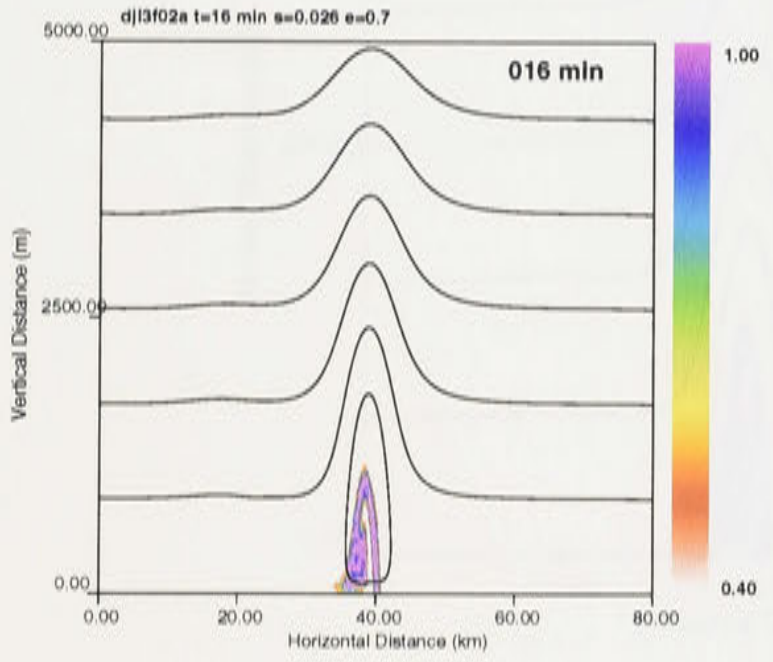

(a) Tracer at 16 mins

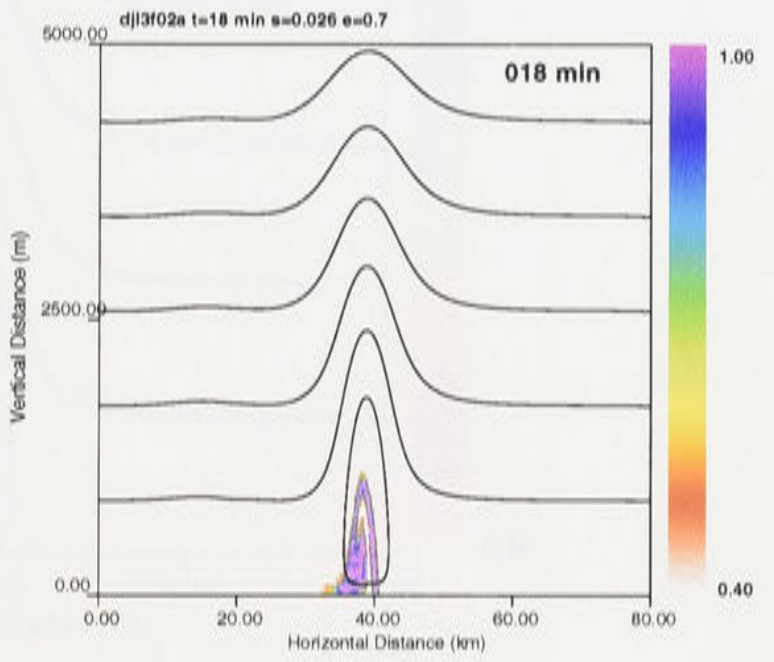

(b) Tracer at 18 mins

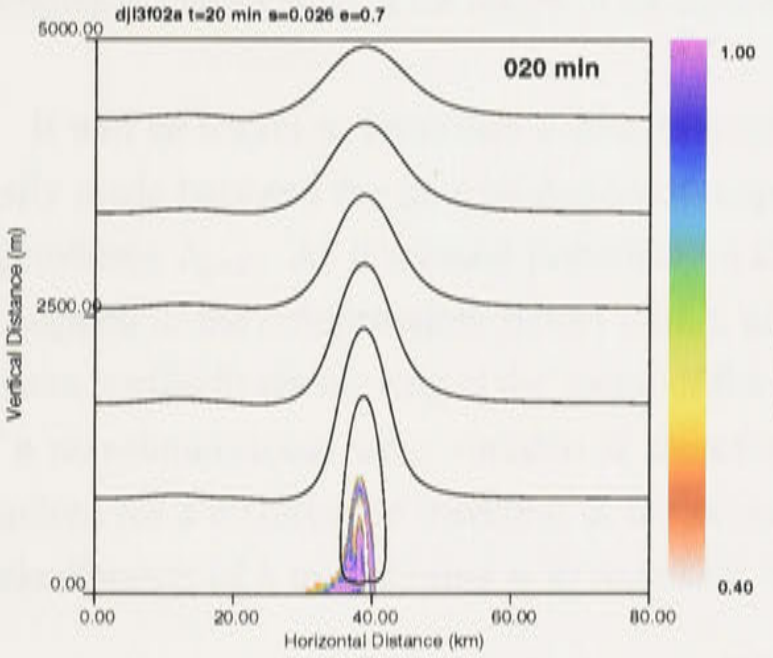

(c) Tracer at 20 mins

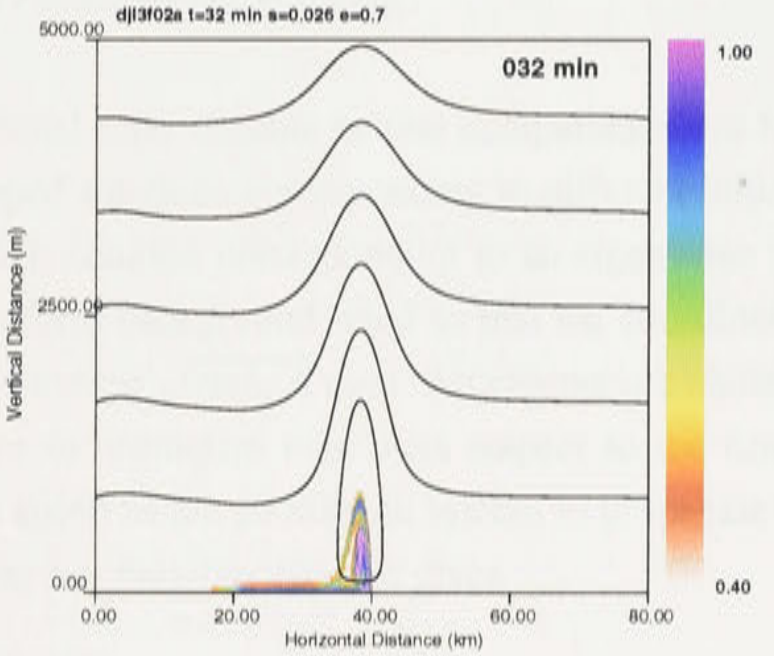

(d) Tracer at 32 mins

Figure 6.16: Evolution of closed circulation cell as a mapped solution "adjusts" to the compressible model. The contour scheme represents a tracer variable placed inside the circulation cell at startup with calculated pseudo-streamlines superimposed. Note that in (a) tracer is being advected along by the wave enclosed in the circulation cell; (b) and (c) there is visible circulation within the cell; (d) It is apparent that tracer is leaking out of the circulation cell at the ground leaving a thin trail in the wake of the wave.

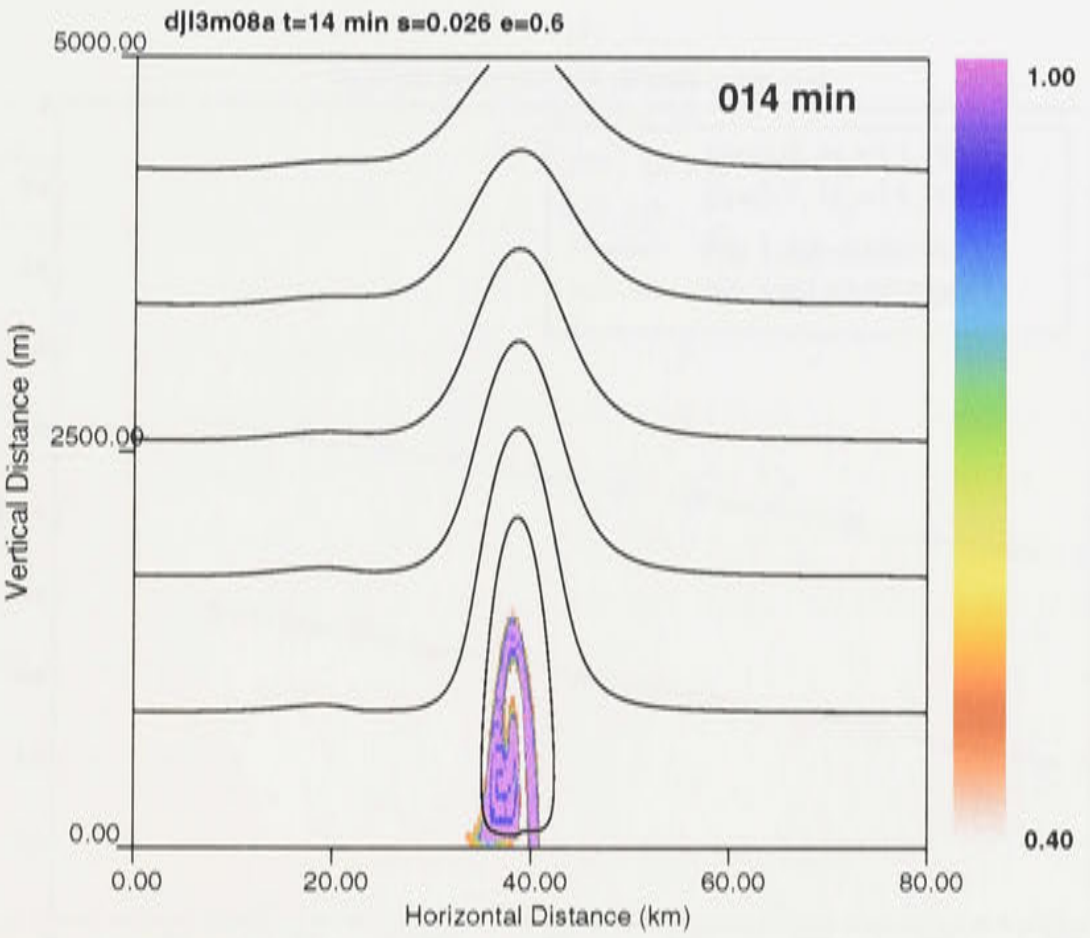

Figure 6.17: Streamfunction (Closeup) for mapped solution with $\sigma = 0.026$ where starting wave solution is $\Lambda = 0.6, \sigma = 0.026, H_2 = 11.76$. The streamlines are superimposed on the Tracer field corresponding to tracer placed in the region of the closed circulation cell at startup.

It will be useful to introduce a non-dimensional time variable so that comparisons can be easily made between the time evolution of mapped solutions corresponding to different initial eigenvalues $\Lambda_{t=0}$. As discussed previously a DJL solution corresponding to an eigenvalue Λ is mapped to the compressible model with a uniform background wind so that the coordinate system is effectively moving at the speed of the wave (ie $\sqrt{\sigma g h/\Lambda}$ m/s). An appropriate choice of a non-dimensional time variable is therefore to normalize time with respect to the time required for a disturbance traveling at the same speed as the coordinate system to propagate a scale distance of h m. Defining t_0 to represent the normalizing variable gives

$$t_0 = h\sqrt{\Lambda/(\sigma g h)}. \tag{6.32}$$

The change in wave amplitude, for two mapped solutions which posses closed circulation (with $[\Lambda_{t=0} = 0.7, (a/h)_{t=0} = 1.74]$ and $[\Lambda_{t=0} = 0.8, (a/h)_{t=0} = 1.52]$) is plotted versus t/t_0 in Fig 6.18. After the initial "adjustment" period ($t/t_0 < 27$) there is a clear linear decay in wave amplitude in both cases. A linear line segment has been fitted to the data points corresponding to each case (where data points where sampled at 10 min intervals). The case with $\Lambda_{t=0} = 0.7$ yielded a linear decay constant of $\kappa = 0.0012$ and the case with $\Lambda_{t=0} = 0.8$ yielded $\kappa = 0.0014$. The error associated with the estimates of wave amplitude (measured manually from output plots of streamlines) will be affected by the chosen vertical resolution of the model. When $z = 50$m and $h = 850$m, the error of a/h is about ± 0.0588 which means that the linear best

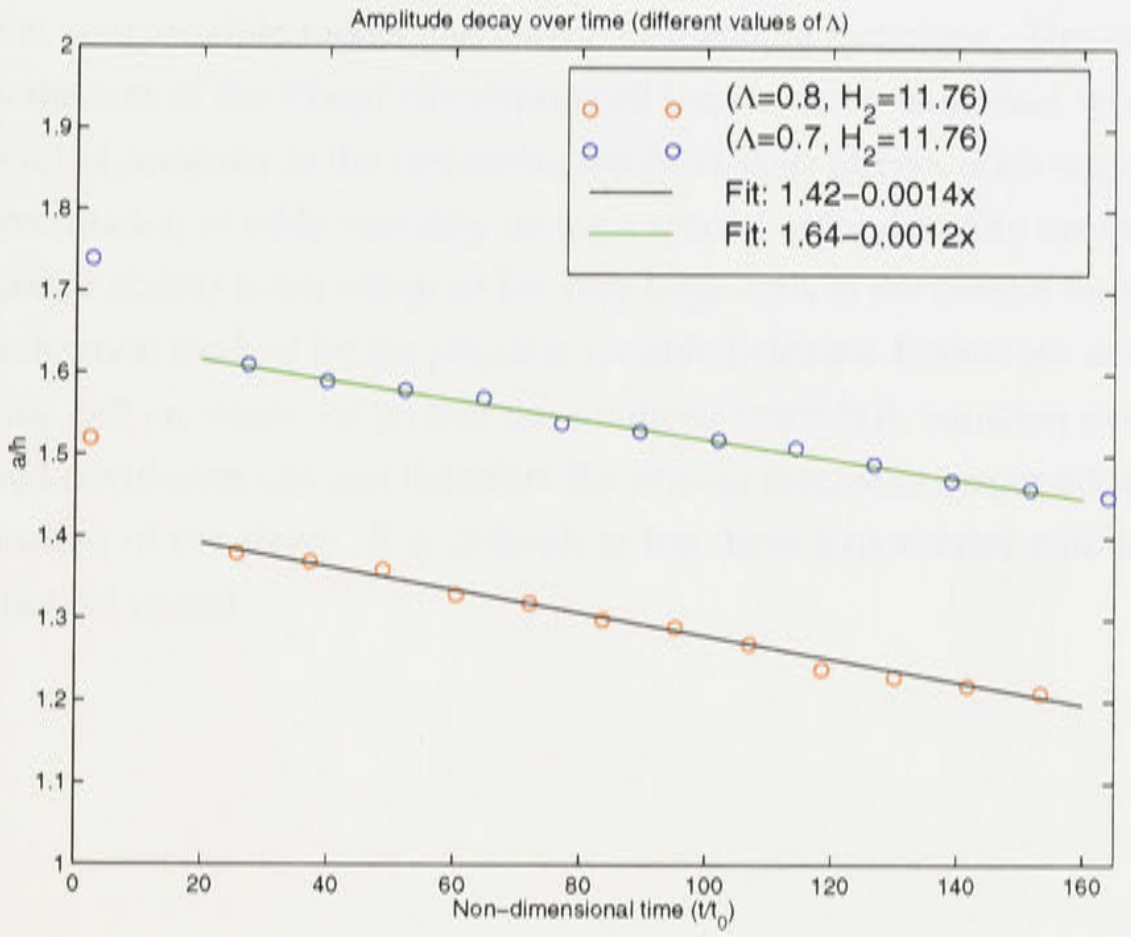

Figure 6.18: Amplitude decay of mapped solutions corresponding to initial eigenvalues $\Lambda_{t=0} = 0.7$ and $\Lambda_{t=0} = 0.8$. The linear decay due to viscous dissipation (associated with the closed circulation within the wave) has been fitted using a straight line segment in each case.

fit estimates (Fig 6.18) of κ have an approximate error, using 12 data points and $\Delta(t/t_0) \approx 10$ between samples, of about ± 0.0005. The linear decay constant, associated with loss of energy due to dissipation at the ground, can therefore be given as $\kappa = 0.001 \pm 0.0005$ based on this data.

In the compressible model, the parameters K^x and K^z represent the magnitude of small viscous forces. The mapping algorithm described above has been found to be extremely stable in the mapping of any DJL wave solution of modest amplitude without closed circulation regardless of how small K^x and K^z are. When the DJL solution possesses a region of closed circulation, viscous dissipation becomes important for the representation of internal mixing within the closed circulation cell. The larger the closed circulation cell the greater the magnitude of the internal mixing. Using numerical grid resolution of $\Delta z = 50$ m and $\Delta x = 100$ m (these values are of the same relative magnitude as the different horizontal and vertical grid resolution used in the solution of the DJL equation), it has been found that solutions of either DJL problem ($H_2 = 11.76$ or $H_2 = 20.0$) can be mapped to a stable waveform in the compressible model for the range of eigenvalues $(0.1 \leq \Lambda \leq 0.6)$ using $K^x = 60\text{m}^2/s, K^z = 15\text{m}^2/s$. Larger amplitude solutions can be mapped if K^x and K^z are increased slightly. The solution for $\Lambda = 0.5$ seemed to remain stable using $K^x = 100\text{m}^2/s, K^z = 20\text{m}^2/s$. However this seemed

to represent the upper limit of amplitude that was able to be mapped as a stable waveform using the current compressible model and choice of mapping technique. This would seem to indicate that as the size of the closed circulation cell increases the numerical model requires a much higher level of accuracy in the representation of viscous effects. This may mean that (a) the simple representation of eddy viscosity (using a second order damping operator to remove energy at the lowest scales) is not adequate for very large cells in the current model; or (b) that the chosen initialization method for the physical variable fields has limitations as the size of the closed circulation cell increases; or (c) that the solutions to the DJL equation overestimate the size of the closed circulation cell and therefore the mixing processes assocated with the wave; or (d) a combination of the above. It is difficult to test these hypothesies within the limits of the current numerical model.

Chapter 7

Radiative Energy Loss from Waves

7.1 Introduction

A long internal solitary wave propagating on an atmospheric waveguide layer can be considered as a wave packet. The energy associated with the packet then corresponds to a spectrum of wavenumbers with much of the energy concentrated in the long wave limit $k \to 0$. The solitary wave form is effectively the envelope of the wave packet and in a stratified medium the displacement of fluid due to the wave can induce mean motions which then result in an interaction between the wave packet and the induced motions. When suitable conditions exist in the ambient environment, a loss of energy can occur from the wave packet to the mean motions and therefore produce damping of the solitary wave. Depending how this loss of energy affects the wavenumber spectrum of the solitary wave, the balance between nonlinear forces which transfer energy to low wavenumbers and dispersive forces which tend to transfer energy to higher wavenumbers, may be disturbed so as to cause the solitary wave to be subject to dispersive effects. Dispersion generally causes a single wave disturbance (made up of different component wavenumbers) to evolve into a family of amplitude ordered waves.

The aim of this chapter is to examine radiative decay of solitary waves for the fully nonlinear case where waves of sufficiently large amplitude can possess a region of closed streamline flow and the relationship between amplitude and wavelength differs significantly from that of weakly nonlinear theory. This will be achieved by using mapped starting solutions, as described in the previous chapter, to examine the effects on wave morphology of varying the degree of stratification in the medium above the waveguide layer. Firstly, however, it will be useful to place in context previous work on the radiative decay of long internal solitary waves in the weakly nonlinear long wave limit (which was described in detail in Chapter 2). The limitations associated with the different approximations upon which the weakly nonlinear theory depends confirm the importance of a study of the radiative decay of fully nonlinear solitary waves with as few approximations as possible. In this chapter we present such a study using a fully nonlinear numerical model with appropriate radiative boundary conditions and ambient stratification.

The level of stratification in the ambient environment above the waveguide layer has been chosen to reflect realistic values based on data from observations of the conditions present during highly nonlinear solitary wave events in the lower atmosphere. Typical data from such observations was presented in Chapter One. It is often difficult to make comparisons between theoretical studies and observations of atmospheric solitary wave events since theoretical treatments do not generally include many of the measured quantities such as temperature and pressure of observational data. There is therefore a key advantage in the use of of realistic ambient conditions and a model with provides both momentum and thermodynamical variables so that useful comparisons can be made between the model and field data. One useful measure of wave properties that is examined below is the perturbation Exner pressure at the surface.

7.2 Discussion of relevant weakly nonlinear theory

For a wave packet to propagate as a coherent entity in a waveguide layer, which is part of a medium that supports energy loss from the waveguide, it must satisfy a ducting condition based on the properties of the medium. As outlined in Chapter 2, Maslowe and Redekopp (1980) have shown that the requirement for finite amplitude long internal waves to be ducted along a thermoclinic waveguide layer in a shear free flow, is for the wave amplitude to satisfy the condition

$$a/h > O(N_\infty/N_0) \tag{7.1}$$

where h represents the vertical scale of a thermocline with Brunt-Väisälä frequency N_0 and the ambient fluid surrounding the thermocline is weakly stratified with Brunt-Väisälä frequency N_∞. Waves with amplitudes that fail to satisfy (7.1) are dispersed throughout the entire fluid column. Condition (7.1) is a requirement for existence of ducted modes and only affects the time dependent behaviour of allowable wave modes in that a ducted wave with decaying amplitude may fail to satisfy (7.1) at some finite time and become dispersed.

There has also been theoretical work by Maslowe and Redekopp (1980) and Grimshaw (1981a), discussed in detail in Chapter 2, on the shear free radiative decay of a free solitary wave in the weakly nonlinear limit. Also, Mitsudera and Grimshaw (1991) have studied the effect of radiative decay on resonantly generated internal gravity waves and Grimshaw et al. (1998) have examined the weakly nonlinear damping of a solitary wave in rotational systems. Maslowe and Redekopp (1980) present an generalized form of the BDO equation describing the evolution of a wave packet $A(x,t)$ that incorporates the effect of wave damping as a result of the wave losing energy to mean motions in a shear free stratified environment. This equation

is governed by the following conservation identities:

$$\frac{\partial}{\partial\tau} < A > = \frac{\partial}{\partial\tau}\int_{-\infty}^{\infty} A(\xi,\tau)d\xi = 0, \tag{7.2}$$

$$\frac{\partial}{\partial\tau} < A^2 > = \frac{-2|\delta|}{\pi}\int_0^{\hat{\alpha}} k(\hat{\alpha}^2 - k^2)^{\frac{1}{2}} |\mathcal{F}(k,\tau)|^2 dk, \tag{7.3}$$

where $\mathcal{F}(k,\tau)$ represents the Fourier transform of $A(\xi,\tau)$. The first corresponds to volume conservation and the second gives an energy decay law. The RHS of the second conservation identity can be considered to represent a term $F(A,\hat{\alpha})$ resulting from loss of energy to a deep fluid weakly stratified upper medium due to excitation of internal gravity waves. The ability of the upper medium to support internal gravity waves is governed by a cutoff wavenumber

$$\hat{\alpha} = \frac{N_\infty}{|U_\infty - c|}, \tag{7.4}$$

where N_∞ is the constant Brunt-Väisälä frequency in the upper region, U_∞ is the constant background wind and c is the phase speed of the wave. The cutoff wavenumber $\hat{\alpha}$ defines a Helmholtz equation for a vertical modal function which represents the effect of the internal wave field supported by the upper media and $\hat{\alpha}$ is assumed small, in the derivation of equation (7.3), corresponding to weak stratification.

Doviak, Chen and Christie (1991) examine appropriate ducting conditions under more general conditions in the weakly non-linear limit, based on the Scorer parameter, when wind shear is present in the ambient environment. The same approach is outlined here and we start by examining the internal wave field which is supported by a weakly stratified medium lying above the waveguide layer. In chapter 2, an eigenfunction equation was introduced for the vertical modal function $\phi(z)$ describing the steady forcing of a stratified Boussinesq fluid and given by

$$\phi'' + (l^2(z) - k^2)\phi = 0, \tag{7.5}$$

where

$$l^2(z) = \frac{N^2}{(U-c)^2} - \frac{U''}{U-c}, \tag{7.6}$$

is the Scorer parameter (Scorer, 1949) calculated using the ambient Brunt-Väisälä frequency $N(z)$ and ambient wind profile $U(z)$. This equation describes the ability of a region with $N(z)$ and $U(z)$ to support propagation of internal wave modes. Upward transfer of wave energy is possible only if $l^2 > k^2$ (comparable to a condition $\hat{\alpha}^2 > 0$ in the work by Maslowe and Redekopp). A ducted horizontally propagating disturbance with spectral components satisfying $k < l$ will lose wave energy due to modes being excited that will propagate vertically as well

as horizontally. The Scorer number will always be positive if there is insignificant curvature in the ambient wind profile $U(z)$. Christie (1989) suggests a extension of the results of Maslowe and Redekopp (1980) and Grimshaw (1981a) to include variations in the upper wind profile by making the substitution $\hat{\alpha}^2 = l^2$ in the governing Helmholtz equation for the supported internal wave field. The evolution of a wave packet will then still be described by identities (7.2) and (7.3) provided the Scorer parameter is small and constant.

Measurements of the structure of the lower atmosphere during observed solitary wave events often have weak stratification present above a lower waveguide layer (such as a ground based stable layer). Such a weakly stratified region is able to support internal wave motions which for steady forcing are described by equation (7.5) above. Observed solitary waves often propagate for substantial distances without significant decay even when the stratification above the waveguide is relatively strong. It is therefore of substantial interest to study conditions in the ambient environment which make this possible. A solitary wave when thought of in terms of the envelope of a wave packet can then be subjected to Fourier decomposition into a wavenumber spectrum representing the spectral energy of component wave modes. An important question is that if the bulk of the solitary waves energy is located in a certain wavenumber range, then what significance does this have for loss of wave energy due to upward radiation of internal waves? In the weakly non-linear limit this question can be addressed based on an assumption that each spectral component with wavenumber k can be considered to satisfy equation (7.5) independently. Doviak, Chen and Christie (1991) give a condition for a solitary wave to propagate without significant damping based on component wavenumbers being limited to a range $k > l$ (so that the condition for vertical excitation of wave modes in equation (7.5) is not satisfied).

When fully nonlinear waves include a closed circulation cell viscous forces become increasingly important due to dissipation of wave energy associated with leaking of fluid from the region of closed circulation. A further extension of the weakly nonlinear BDO equation that is therefore worth mentioning is the addition of a diffusive term with a Burgers eddy diffusivity coefficient μ to represent turbulent frictional dissipation. This type of equation does not provide a good representation of highly nonlinear waves but does show what effect the inclusion of viscous forces can have on wave evolution. The BDO-Burgers equation has been studied by many researches including Christie (1989) who showed, based on a numerical time integration of the BDO-Burgers equation as an initial value problem using an arbitrary starting disturbance, that the inclusion of viscous effects can result in the effects of dispersion being suppressed (as μ is increased). A complete evolution equation for a weakly nonlinear long wave packet in a deep fluid regime subject to frictional dissipation and radiative damping is therefore provided by a generalized BDO equation including viscous and radiative decay forcing terms (combining the BDO-Burgers equation and the forcing term due to radiative damping derived

by Maslowe and Redekopp (1980) and Grimshaw (1981a)). This equation has the form

$$A_\tau + \gamma A A_x + \delta(\mathcal{H}(A))_{xx} = \mu A_{xx} + \delta F(A, \hat{\alpha}), \tag{7.7}$$

where γ and δ represent coefficients of nonlinearity and dispersion dependent on the ambient environment and (x, τ) are appropriate stretched coordinates of space and time. The domain of validity of many of the approximations used to derive equation (7.7) make such an equation inappropriate for a study of highly nonlinear wave decay in stratified fluids. These limitations are discussed before the presentation of results from a study of the radiative decay of fully nonlinear waves using our mesoscale model and the fully nonlinear starting solutions of the last chapter.

7.2.1 Limitations of weakly nonlinear theory

The above theory has been derived under several approximations. First there is a weakly nonlinear approximation. In the weakly nonlinear case there is an assumption that component wave modes with wavenumber k independently satisfy equations such as (7.5). The spectrum of a ducted solitary wave is assumed slowly varying so that it can be considered as the superposition of wave modes with different values of k. In a fully nonlinear system different spectral components do not generally evolve independently. Modes with different wave numbers and different frequencies interact with each other in nonlinear processes that can significantly change the wavenumber spectrum. A slowly varying wave profile is likely to be relatively well approximated by spectral components which evolve independently but this is not a good approximation for a more rapidly evolving wave profile.

An important limitation of the generalized forms of the BDO equation is that they are derived under the assumption of a slowly varying time variable. This means that any interaction between the wave packet and the mean flow is assumed to take place on a slow time scale which allows the wave packet to adjust gradually to changes in the mean flow as it propagates in the waveguide layer. Many observations of the ambient waveguide conditions present during solitary wave events in the lower atmosphere include an upper medium above the waveguide which has a level of stratification sufficient to cause rapid loss of energy that does not satisfy this assumption of a slowly varying wave form.

Highly non-linear waves have a wavelength-amplitude relationship that is not described by weakly non-linear theory. Given the dependence of the above weakly nonlinear description on a particular scaling relationship between amplitude and wavelength it is likely that highly non-linear waves under radiative decay will not be well described by equations such as (7.7).

The evolution equations for a wave packet $A(x,t)$ derived under weakly nonlinear theory often have a set of associated conservation identities. For instance, the conservation identity (7.2) derived by Maslowe and Redekopp (1980) depends on conservation of the volume of a

wave packet (ie the volume of the wave packet remains constant). This is satisfied for ideal weakly nonlinear waves (ie of permanent form), but for fully nonlinear waves, even when other possible mechanisms of energy loss are ignored, the presence of a closed circulation cell results in broadening of the volume of the wave packet (as represented by an integration in x over the wave packet where the height of the wave packet is taken as the perturbation of the non-dimensional 1.0 streamline). The onset and disappearance of closed circulation therefore represent a change in wave morphology which means that identity (7.2) is not strictly conserved during decay. Loss of energy due to viscous forces are also important in the consideration of highly nonlinear waves with a closed circulation cell. Viscous losses also result in the volume of a wave packet failing to be conserved.

The parameter $\hat{\alpha}$, defined above as a cutoff wavenumber governing the internal wave field supported by a stratified upper medium, is assumed small corresponding to weak stratification. In the derivation of a generalized form of the BDO equation which includes radiative energy loss, Maslowe and Redekopp (1980) assume $\hat{\alpha}$ is small when making an approximation in terms of the Hilbert transform so that the error in their approximate evolution equation in terms of amplitude is $O(\hat{\alpha})$. This means that increasing $\hat{\alpha}$ increases the error of an equation such as (7.7).

The limitations discussed above all support the study of the radiative decay of fully nonlinear solitary waves with as few approximations as possible.

7.3 Model setup: Two Fluid case

Ambient conditions that support the ducting of highly nonlinear solitary waves in the lower atmosphere can often be thought of in terms of a two fluid system, where the lower fluid represents the waveguide and the upper fluid the ambient media above the waveguide layer. As discussed in chapter 3, it will be useful in a study of radiative decay to adopt a two fluid system where the Brunt-Väisälä frequency will have constant value N_1 in the lower layer and N_2 in the upper layer. This allows the potential temperature profile to be written as:

$$\frac{\theta}{\theta_0} = \begin{cases} \exp[(N_1^2/g)z] & \text{if } (z < h) \\ \exp[(N_2^2/g)(z - h + \frac{N_1^2}{N_2^2}h)] & \text{if } (z > h) \end{cases} \tag{7.8}$$

where h defines the depth of the lower layer. Such a two layer profile will be used for ambient temperature initialization to give a lower waveguide layer and a weakly stratified upper layer.

One problem with adopting the above temperature profile is that the interface between layers (at $z = h$) represents a non-smooth transition. We are mapping across solutions from the

DJL equation which was solved using an ambient profile given by

$$\frac{\theta}{\theta_0} = 1 + \sigma \tanh(z/h) \tag{7.9}$$

where σ represents the degree of variation in temperature over depth h and is assumed small ($\sigma \ll 1$) and $\sigma \to 0$ is a statement of the Boussinesq approximation. Since we wish to minimize any instability in a mapped wave soliton due to the choice of ambient temperature profile, we need a modified version of (7.8) which involves a smooth transition between layers and which approaches the profile defined by (7.9) in the limit as $N_2 \to 0$. This problem has been solved by using the following smooth version of (7.8) defined by

$$\frac{\theta}{\theta_0} \approx \sigma \tanh(z/h) + \mathrm{Max}[1, \exp((z-h)N_2^2/g)], \tag{7.10}$$

where σ is assumed small and is evaluated as

$$\sigma = hN_1^2/g. \tag{7.11}$$

This means that $\sigma = 0.026$ with $h = 850$ m will correspond to a buoyancy period ($2\pi/N_1$) of approximately 6 min.

Another important issue in the use of the starting wave solutions introduced in Chapter 6, is that all mapped solutions initially must have a neutral upper layer so that they can remain stable during a short "adjustment" period. To study the radiative decay of waves, this initially neutral upper layer must be re-configured as a weakly stratified region with Brunt-Väisälä frequency N_2 so that (7.10) defines the vertical variation in temperature across the height of the domain. Several methods were examined to reconfigure the ambient environment after the adjustment of a mapped solution to the compressible model. The first of these involved imposing an instantaneous change in the ambient variables at a specified time t (with t greater than the adjustment period of the wave) so that the upper layer was assigned a constant value N_2 of the Brunt-Väisälä frequency. However, this approach was found to cause the solitary wave to become unstable and undergo a wave splitting process where a smaller amplitude wave splits from the original wave and rapidly falls behind (analogous to a reflected wave from the point at which the instantaneous change in media occurs). The original wave in such a process undergoes a reduction in amplitude due to energy lost to the smaller amplitude wave and this energy loss from the original wave is difficult to estimate accurately. This method of initialization of the upper media was therefore deemed undesirable in a study of radiative decay of waves where it is important to have accurate measurements of the change in wave properties.

Other approaches were examined using a transient time period for the adjustment of the ambient media. The most stable of these approaches was found to be the implementation of a

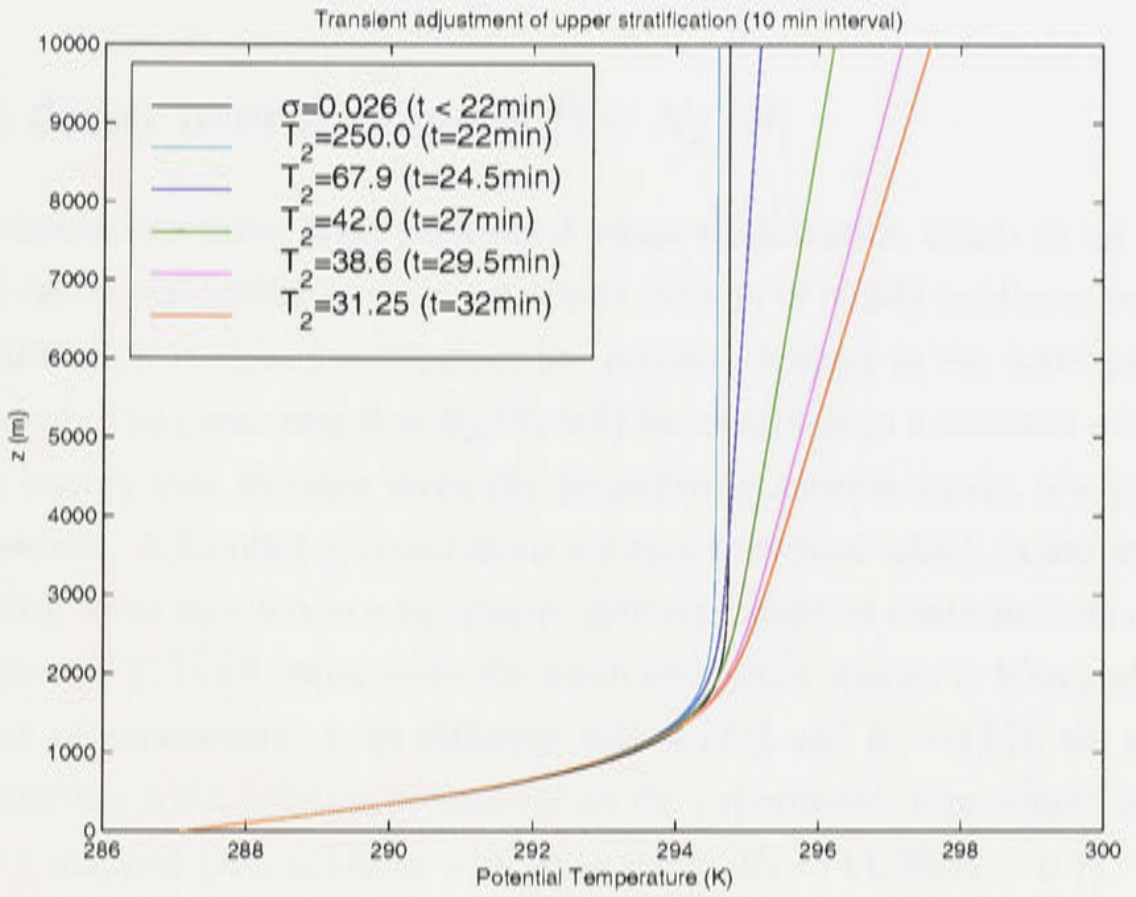

Figure 7.1: Potential temperature curves for selected times during a 10 min transient adjustment initialization of the upper stratified layer. $T_2 = 2\pi/(N_2 60)$min represents the buoyancy period of the upper layer.

short term continuous slow variation of the value of N_2 in the upper region. This was defined using the period $T_2 = 2\pi/N_2$ so that T_2 is changed from an initial value of T_0 to a value of T_f over a time period of t_p. The smooth variation in T_2 was implemented using a sine function so that

$$T_2 = T_0/[1 + (\frac{T_0}{T_f} - 1)\sin(\frac{\pi}{2}\frac{(t-t_0)}{t_p})] \tag{7.12}$$

where t_0 is the starting time (ie 22 min) after the mapped wave solution has adjusted to the compressible model. The value of T_0 corresponds to a sufficiently large enough buoyancy period so as to approximate a homogeneous ambient environment (which is required initially for the mapped solutions). A typical magnitude is $T_0 = 250$ min. A transient time period of $t_p = 10$ mins was found to give the most stable results whilst being small enough to cause minimal changes in the wave amplitude, for a range of final values of T_2 and has been used in all simulations which follow.

Although use of a slow adjustment of N_2 imposes an unrealistic variation on the stratification present in the upper layer it has been found not to affect the stability of a wave propagating in the waveguide layer and is stable over small variations in the choice of transient time period. The stratification of the upper layer for a series of time slices during this transient adjustment

period are shown for a case producing a final configuration of $N_2/N_1 = 0.19$ in Fig 7.1.

7.4 Wave decay over a range of $\beta = N_2/N_1$

A number of simulations have been performed when stratification exists in an upper region above a ground based waveguide layer that supports ducting of highly nonlinear solitary waves. The upper stratification is varied to examine the relative changes in the wave properties of a ducted disturbance. The parameter $\beta = N_2/N_1$ will be identified as a measure of the degree to which radiative energy loss, through vertically propagating internal waves, is supported by the ambient environment. A number of simulations are now presented which examine the radiative decay of a starting wave solution in a number of different ambient environments characterized by different values of β. In all simulations the mesh resolution was $\Delta z = 50$m and $\Delta x = 100$m. Results for a set of experiments with different values of β and $\sigma = 0.026$ are shown in Fig 7.2. The same starting wave solution is used for all the experiments represented in Fig 7.2 and corresponds to a mapped DJL solution with $[\sigma = 0.026, H_2 = 11.76, \Lambda = 0.7]$. This starting solution is mapped across to the numerical model using the technique presented in the last chapter. A constant background wind is applied to the whole domain so that the coordinate system is effectively moving at the speed of the wave disturbance (given by $\sqrt{\sigma g h/\Lambda}$). In these experiments the transient adjustment of the upper stratification occurs between 22 min and 32 min. The effect of this transient adjustment on wave amplitude can be seen in Fig 7.2 and is not very large (average of less than 0.2 in terms of non-dimensional amplitude).

The radiative decay of a starting wave of slightly larger amplitude ($\Lambda_{t=0} = 0.6$ with $\sigma = 0.026$) is also examined for a number of different values of β. The resulting wave decay curves are shown in Fig 7.3 where the non-dimensional time variable t/t_0 (where $t_0 = h\sqrt{\Lambda/(\sigma g h)}$) which was introduced in the last chapter has been used to represent the time axis. When the decay curves for $\Lambda_{t=0} = 0.6$ case are compared directly with the $\Lambda_{t=0} = 0.7$ case, using the non-dimensional time variable t/t_0 and the same value of β (ie $\beta = 0.27$), it can be seen in Fig 7.4 that the rate of amplitude decay is approximately the same for each case.

The effect of internal wave modes generated in the upper layer can be seen in the stream-function displayed in Fig 7.5 for $\beta = 0.27$. The internal wave field in the upper layer above the waveguide is visible as sloping streamlines. These sloping streamlines bear a similarity to those observed for mountain lee waves when there is fixed non-variable topography but are not completely smooth and laminar suggesting a non steady-state behaviour as would be expected from a changing wave shape. A case with stronger stratification in the upper layer ($\beta = 0.42$) is shown in Fig 7.6 and it can be seen that for $\beta = 0.42$ the degree of wave damping, compared with the case $\beta = 0.27$, has been substantially increased over a similar time period.

In the wave decay curves presented in Fig 7.2 and Fig 7.3 it is clear that for the smaller values of β the decay is almost linear and that as β increases the decay starts to become slightly

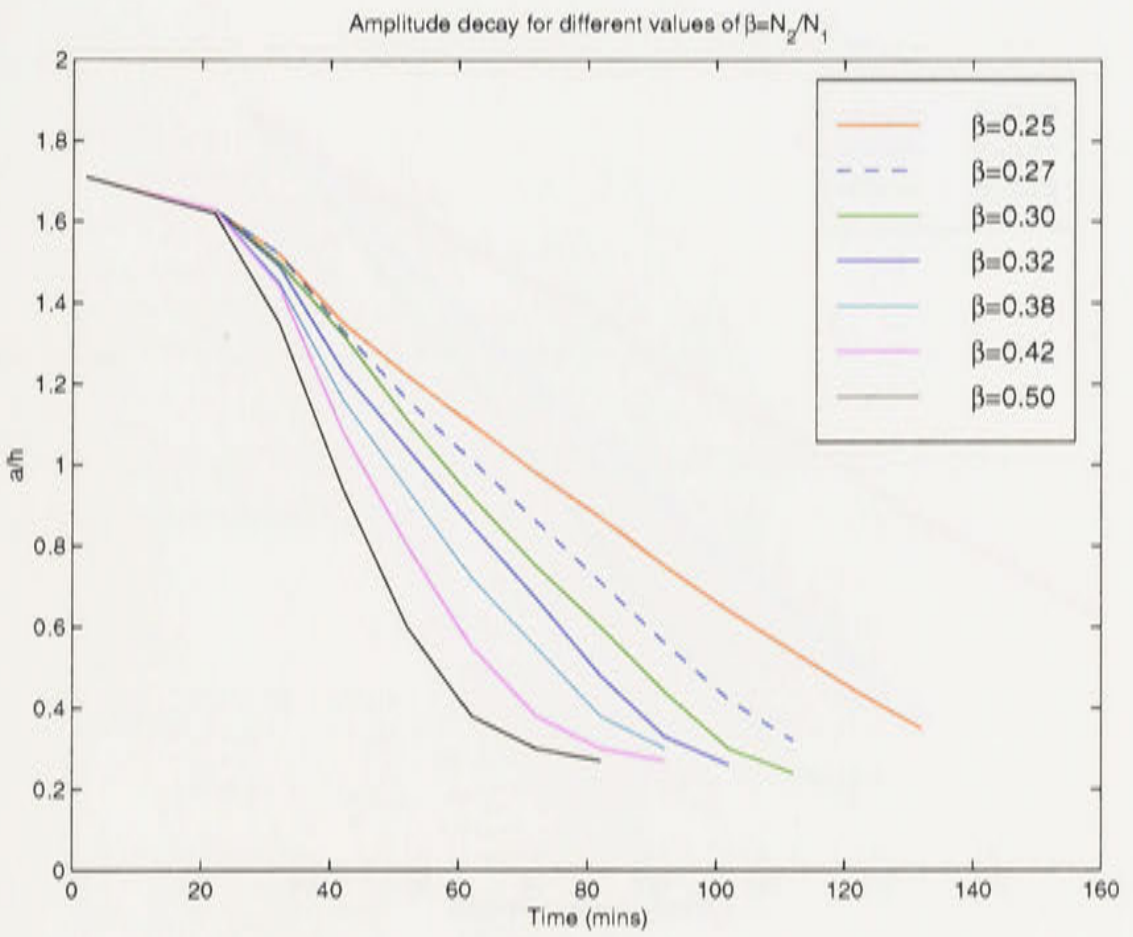

Figure 7.2: Amplitude decay for different values of the parameter $\beta = N_2/N_1$ when N_1 remains fixed and N_2 is varied. All starting waves solutions for these cases had $\Lambda_{t=0} = 0.7$. The data is sampled at 10 min intervals from a starting value of $t_0 = 2$ min.

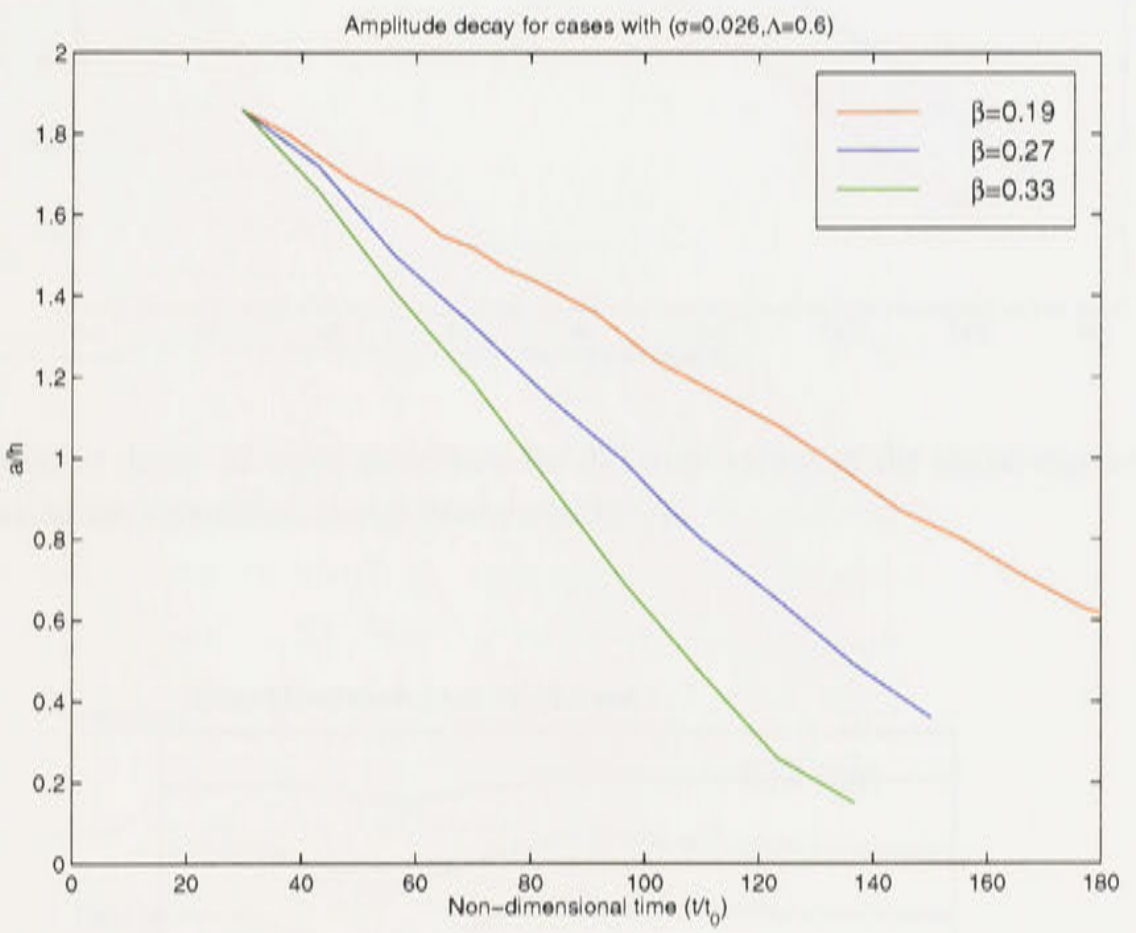

Figure 7.3: Amplitude decay for different values of the parameter $\beta = N_2/N_1$ for a starting wave solution with $\Lambda_{t=0} = 0.6$. The data is sampled at 10 min intervals and plotted against the non-dimensional time variable t/t_0.

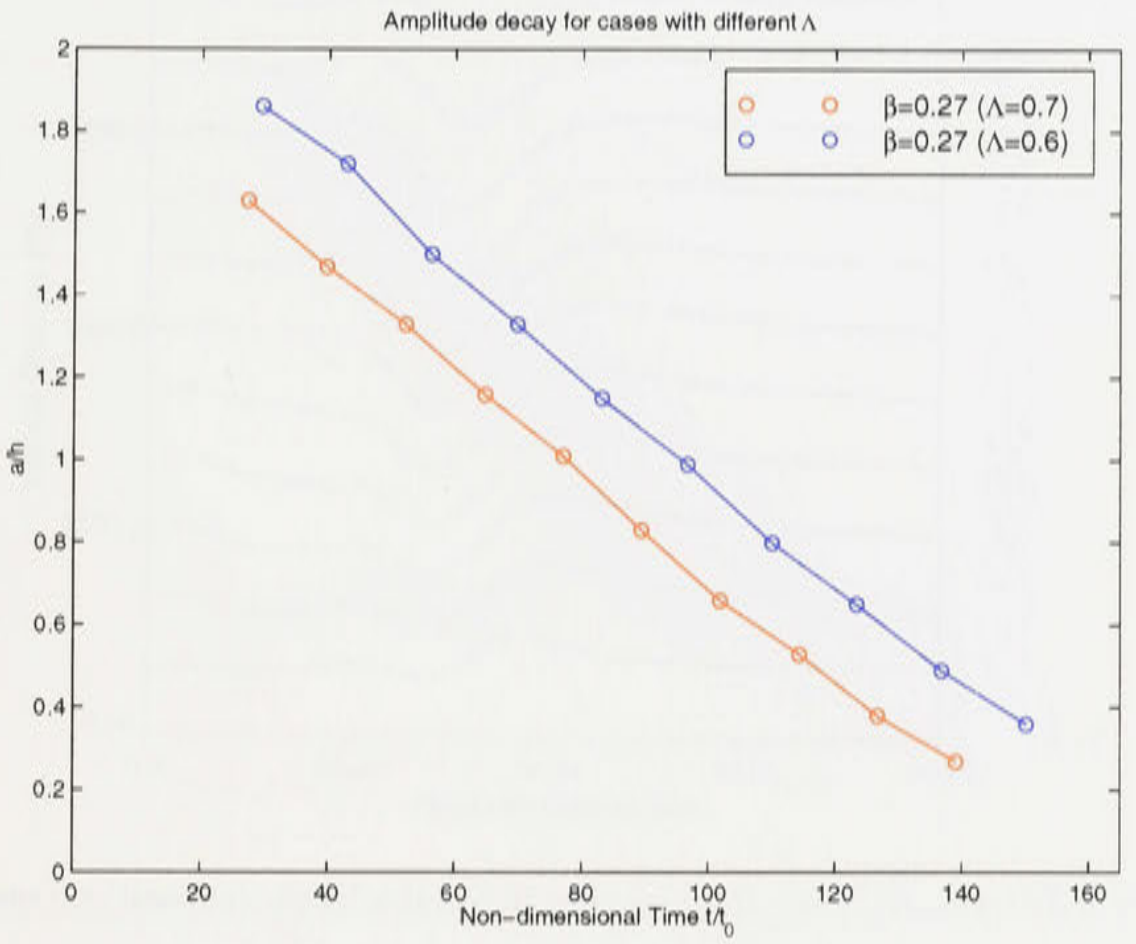

Figure 7.4: Radiative decay of wave amplitude for different values of the initial eigenvalue $\Lambda_{t=0}$. The data is plotted using the non-dimensional time variable t/t_0.

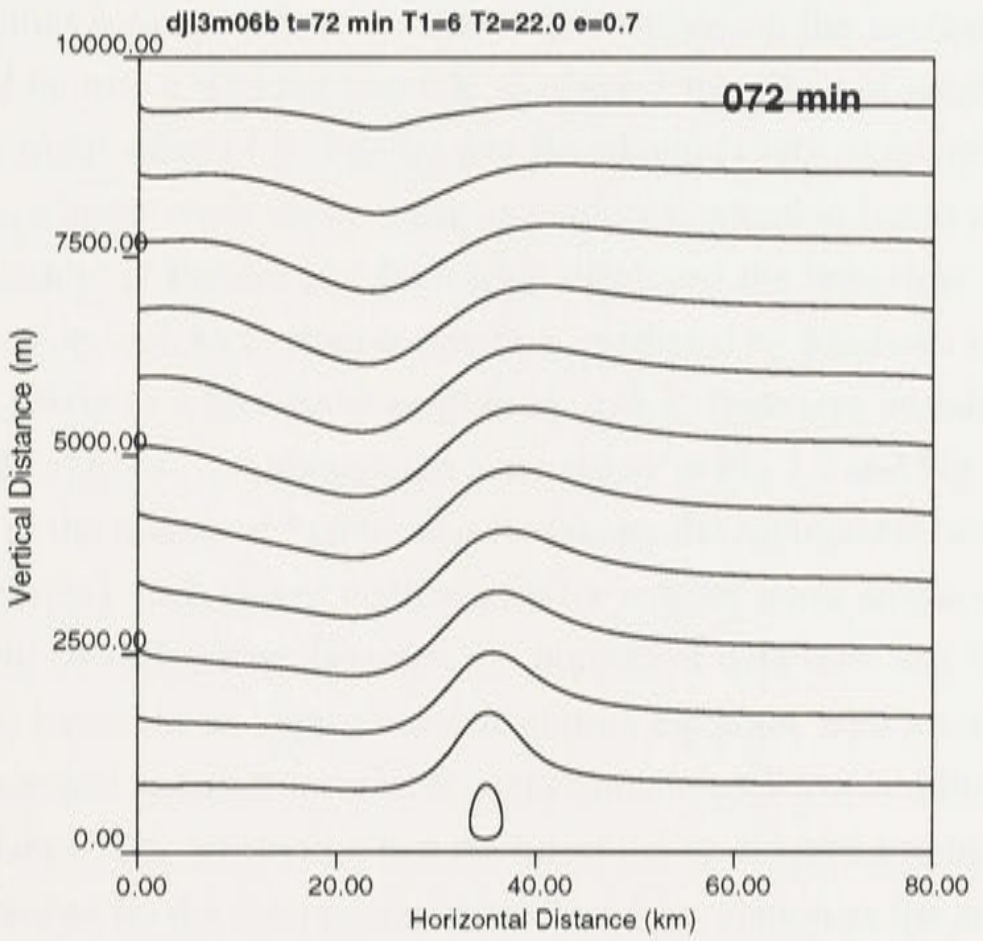

Figure 7.5: Streamfunction (calculated using SOR routine) for $\beta = 0.27$, $\Lambda_{t=0} = 0.7$, $\sigma = 0.026$ at time $t = 72$min.

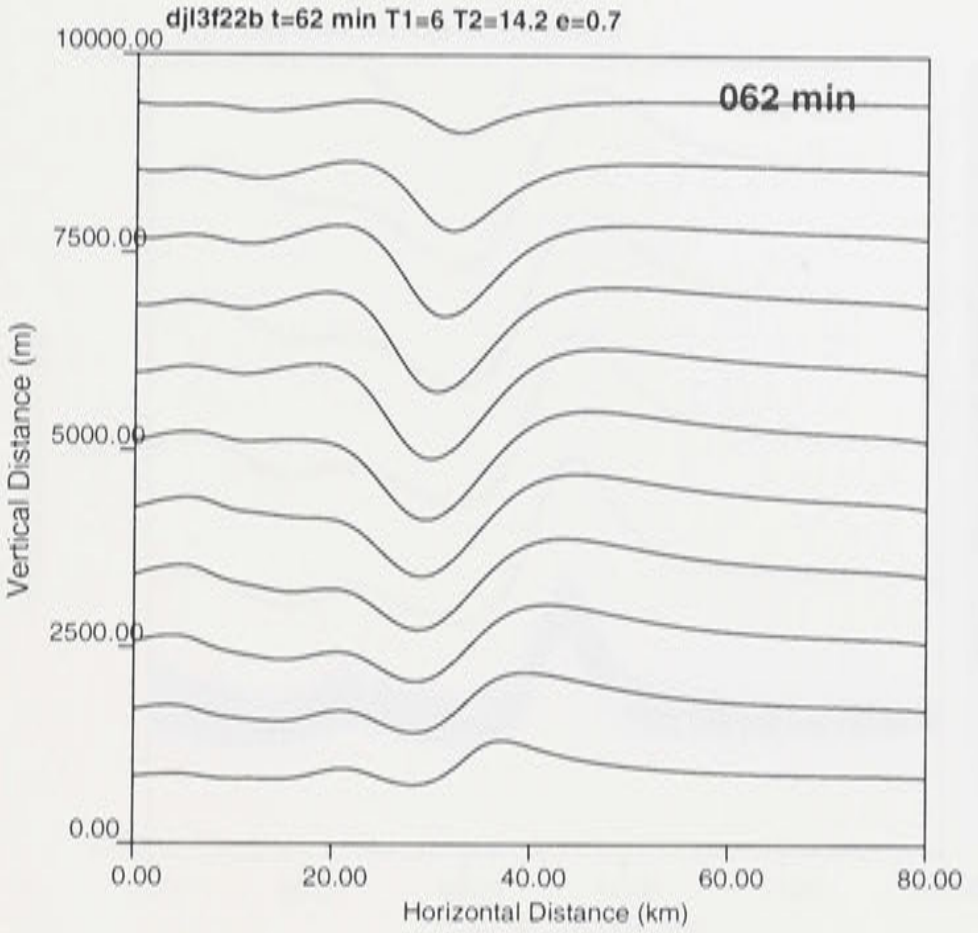

Figure 7.6: Streamfunction (calculated using SOR routine) for $\beta = 0.42$, $\Lambda_{t=0} = 0.7$, $\sigma = 0.026$ at time $t = 62$min.

more nonlinear as the decaying wave amplitude results in smaller values of a/h. The asymptotic behaviour as β increases seems to approach a tanh curve bounded at one end by the starting wave amplitude and at the other by the cutoff amplitude at which the wave disperses throughout the fluid column. However due to limitations on the maximum length of time a simulation could be run, it was not possible to observe the effect of amplitude decay at small amplitude and a small value of β. Pereira and Redekopp (1980) examined a special adiabatic case of weakly nonlinear wave decay using an evolution equation based on the identities (7.2) and (7.3). The results of Pereira and Redekopp displayed the behaviour of weakly nonlinear wave decay, based on such an evolution equation, predicted by Maslowe and Redekopp (1980) and Grimshaw (1980,81) where wave amplitude ($a/h < 1$) decays initially as $a/h \propto t$ and for smaller amplitude $a/h \propto t^{-1}$. Although the wave decay in Fig 7.2 and Fig 7.3 has some quantitative similarity to the results of Pereira and Redekopp the asymptotic behaviour of amplitude decay does not display such strong nonlinearity for smaller wave amplitude. It is not surprising that there will be differences between the numerical data here and the weakly nonlinear results which are based on an approximate evolution equation with a set of simplifying constraints. The numerical results here start at highly nonlinear wave amplitudes where the wave has closed circulation. It is interesting that the linear decay of wave amplitude does not seem to be strongly influenced by the disappearance of closed circulation as the amplitude decreases.

Large values of β seem to cause a rapid process by which the initial wave has been observed to develop, during amplitude decay, into a leading wave and a set of trailing wave undulations

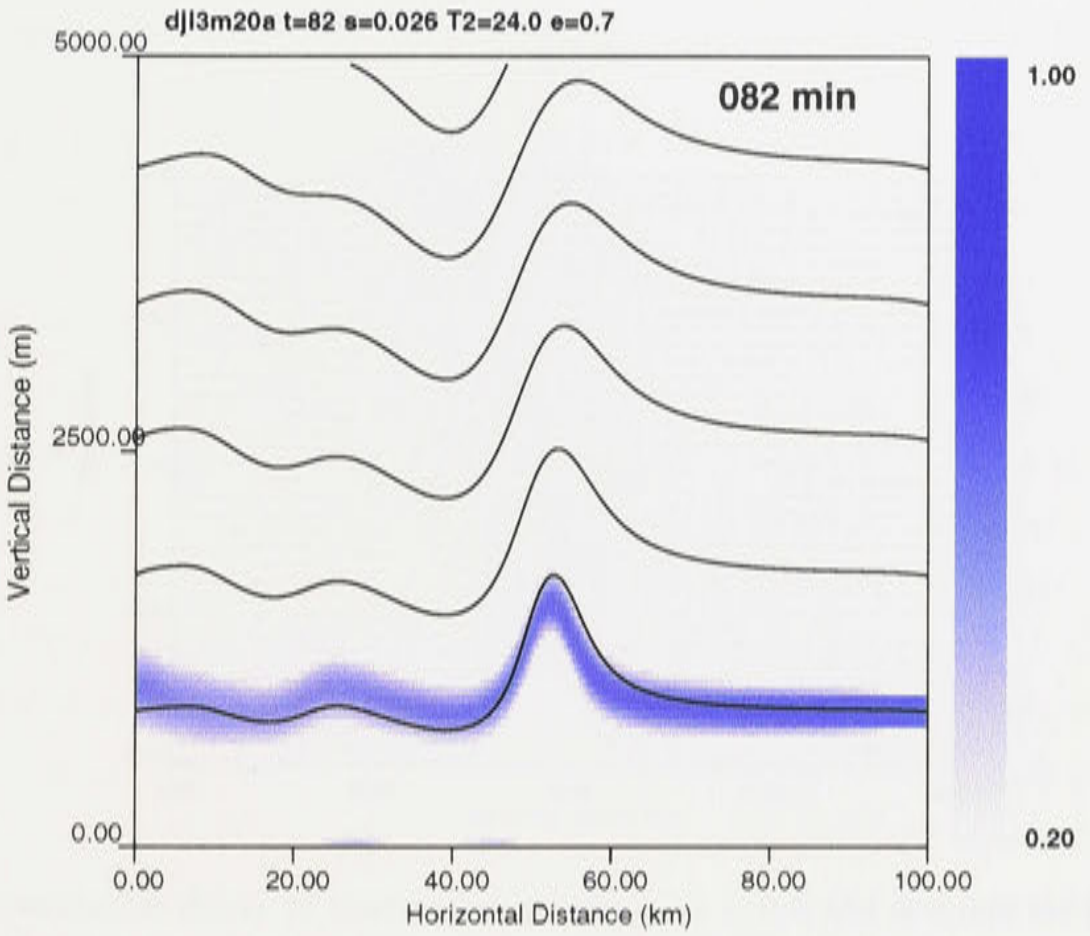

Figure 7.7: Streamfunction (calculated using SOR routine) + tracer for $\beta = 0.25$, $\Lambda_{t=0} = 0.7$, $\sigma = 0.026$ at time $t = 82$min.

which seem to result due to the effects of wave dispersion. This can be seen in the plot of the streamlines in Fig. 7.6 for a case with $\beta = 0.42$ (ie by examining the non-dimensional 1.0 streamline) and in the time evolution of the 1.0 streamline shown in Fig 7.9 for a case where $\beta = 0.6$. The proximity of the solitary wave to the LHS boundary makes it difficult to examine this dispersive effect. Visualization using the calculated streamlines has limitations due to the upstream boundary conditions used for the solution of the streamfunction equation. Therefore an additional experiment was performed using a larger numerical grid of [999x199] with $\Delta x = 100$ m and $\Delta z = 50$ m (ie a 100km by 10km domain) and with the wave center initially positioned ($t = 0$) at 60 km. The streamfunction at a time just after closed circulation disappears is shown in Fig 7.7. A secondary wave of smaller amplitude is clearly visible behind the larger amplitude leading wave disturbance. But in this case (with smaller β) the dispersive effect does not seem as strong.

A useful visualization of the change in wave amplitude over time for varying degrees of radiative damping is achieved by plotting the streamline corresponding to a non-dimensional depth of 1 (ie relative to h) over time. This is shown in Fig 7.8 for a wave originating from a starting solution for $\Lambda = 0.6$ in an environment characterized by $\beta = 0.27$. A case for the same initial wave but in an environment producing much greater wave damping ($\beta = 0.60$) is shown in Fig 7.9. It is interesting in this case that the dispersive effects are not particularly strong and are more apparent after the wave has undergone a substantial decay of wave amplitude.

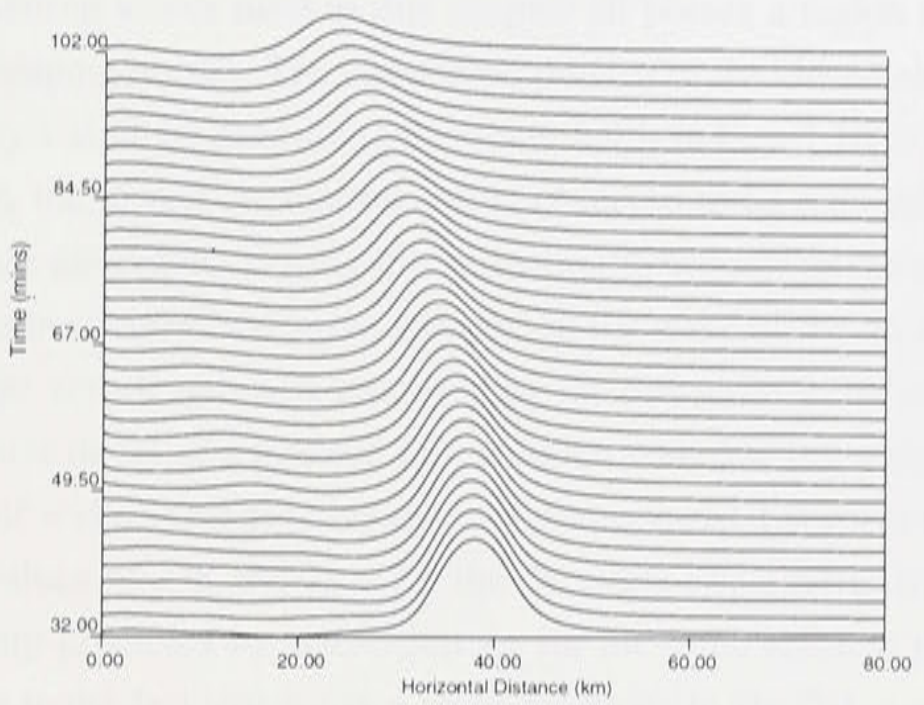

Figure 7.8: Time evolution decay of starting wave with $\Lambda_{t=0} = 0.6$ and ambient environment corresponding to $\beta = 0.27$. The wave is seen moving backwards since the coordinate system moves at the speed of the initial disturbance and decay of wave amplitude results in a reduction of wave speed.

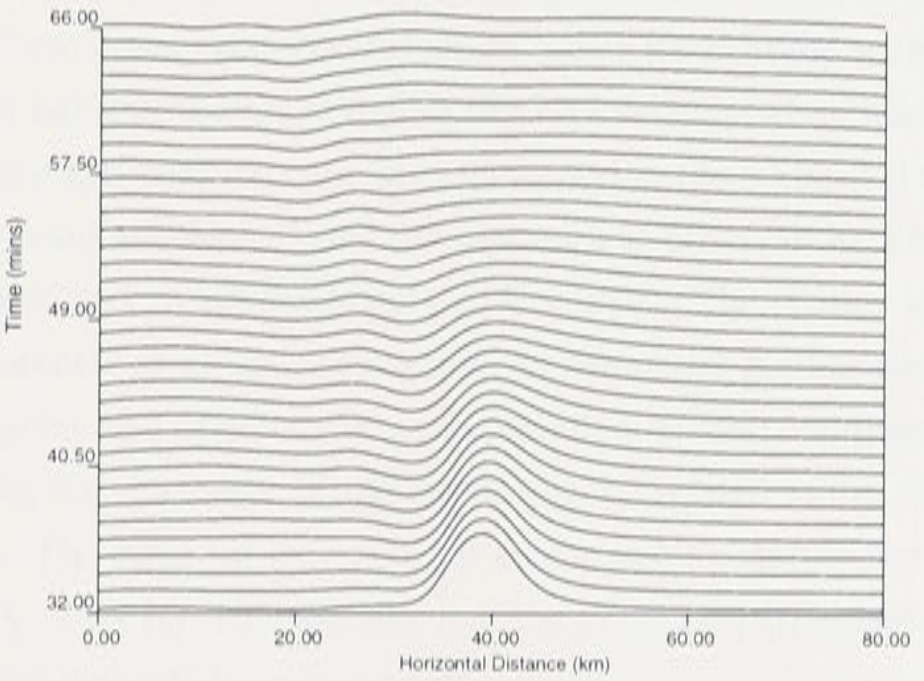

Figure 7.9: Time evolution decay of starting wave with $\Lambda_{t=0} = 0.6$ and ambient environment corresponding to $\beta = 0.6$. Here a large value of β (strong damping) seems to cause a rapid decay of wave amplitude and as the amplitude of the initial wave becomes small, a transfer of some wave energy into a smaller amplitude wave in the wake of the wave as the result of dispersive effects.

7.5 Wave morphology under radiative decay

Highly nonlinear starting waves used in this chapter all posses a region of closed streamline flow before wave damping occurs. The circulation present in the closed circulation cell during wave decay is clearly visible by examining the tracer fields in Figs 7.10(a) and 7.10(b). During the decay of a wave, the closed circulation cell is observed to be reduced in size until closed circulation disappears altogether. During this reduction in the size of the cell fluid is observed to leak out at the ground (visualized using a tracer) in the wake of the decaying wave.

The change in the wavelength $\lambda_{1/2}$ representing the full wave width at half maximum amplitude during radiative decay of a mapped DJL solution with $\Lambda = 0.7$ is shown in Fig 7.11 (the estimate of wave half width is made using the non-dimensional 1.0 streamline). It can be seen that the measured values of a/h and $\lambda_{1/2}$ for the decaying wave differ from the wavelength-amplitude relationship predicted by DJL solutions for the same ambient profile. This is not a surprising result due to the fact that solitary wave solutions to the DJL equation have a strong dependence on the ambient density profile used in the solution of the appropriate boundary value problem for the governing PDE (Tung et al., 1982). Therefore any changes made to the density structure of the ambient environment, as required here to produce an upper stratified region with constant Brunt-Väisälä frequency N_2, are expected to change the wavelength amplitude relationship of solutions to the DJL problem. It can be seen in Fig 7.11 that, below the minimum wavelength turning point in the curve, the ambient environment characterized by equation (7.10) seems to support solitary waves with slightly larger wavelengths than those predicted from DJL solutions based on a tanh density profile which represents a waveguide with neutral conditions above (even with the correction factor for solution mapping as discussed in the last chapter). It is interesting to note that in Fig 7.11 substantial increases in wavelength, as predicted by the theoretical solutions and also measured in the numerical results, do not occur until a/h is near the point at which closed circulation was observed to dissappear from within a decaying wave (measured as approximately $a/h = 0.85$). The change in wave morphology, during the dissappearence of closed circulation, is discussed further below. The minimum wavelength turning point also seems to be a sharper effect for the computed wave decay cases. It is hypothesized that the sharpness of the curve may be related to the adaption of a wave to the change in media. The effect of increasing β seems to be a shift in the amplitude at which this minimum occurs. This further indicates that the wave properties are dependent on small changes in the ambient waveguide environment.

In table 7.1 the time and wave amplitude at the point at which closed circulation disappears for the decay of waves in the compressible model is displayed. The point at which closed circulation disappears is estimated using the plots of streamfunction. Since these are calculated from a streamline vorticity equation they should give the clearest indication of when vorticity within the wave disappears. The value of a/h at which closed circulation disappears is

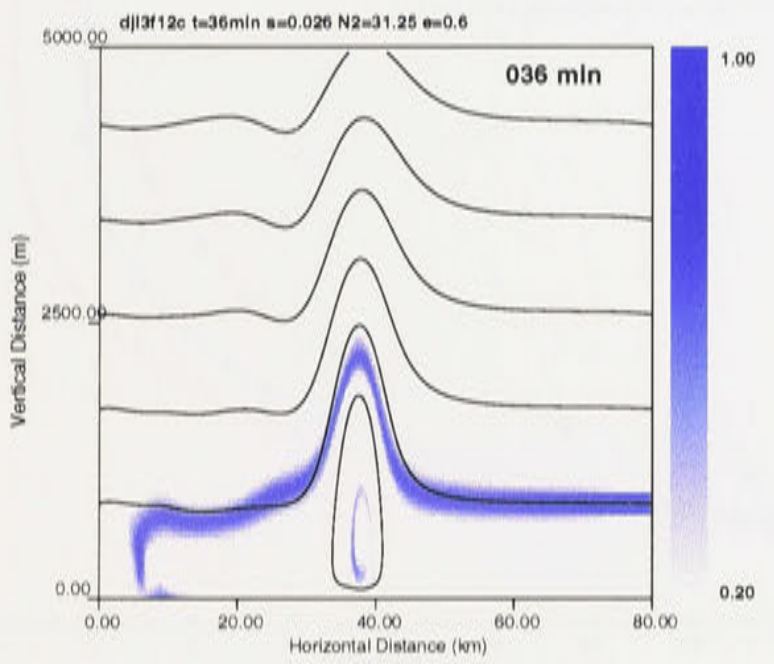

(a)

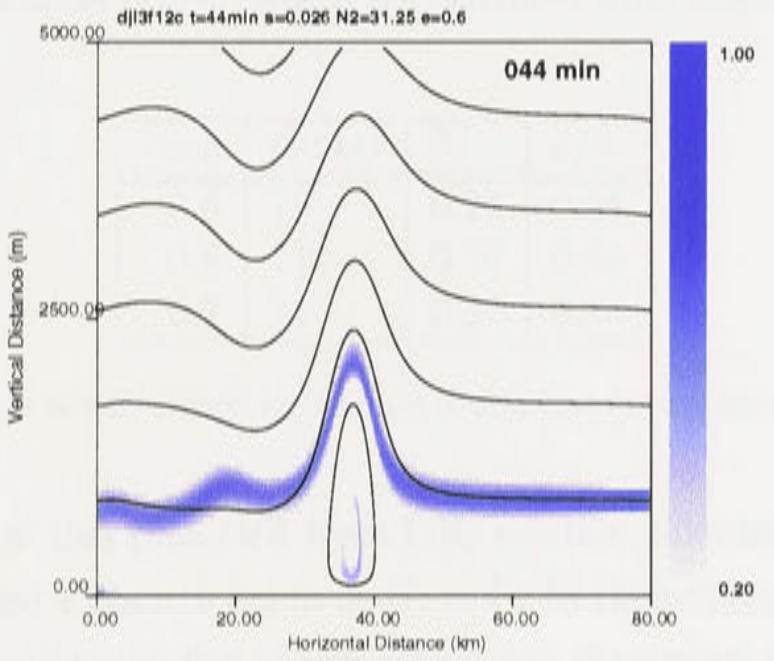

(b)

Figure 7.10: Two plots of the streamlines and tracer (initialized at $t = 0$ as a straight line at the interface between the waveguide and upper medium) for the case with $\Lambda_{t=0} = 0.6$, $\sigma = 0.026$, $\beta = 0.19$. It can be seen that some tracer has been caught up in the closed circulation cell and shows the circulating flow over time.

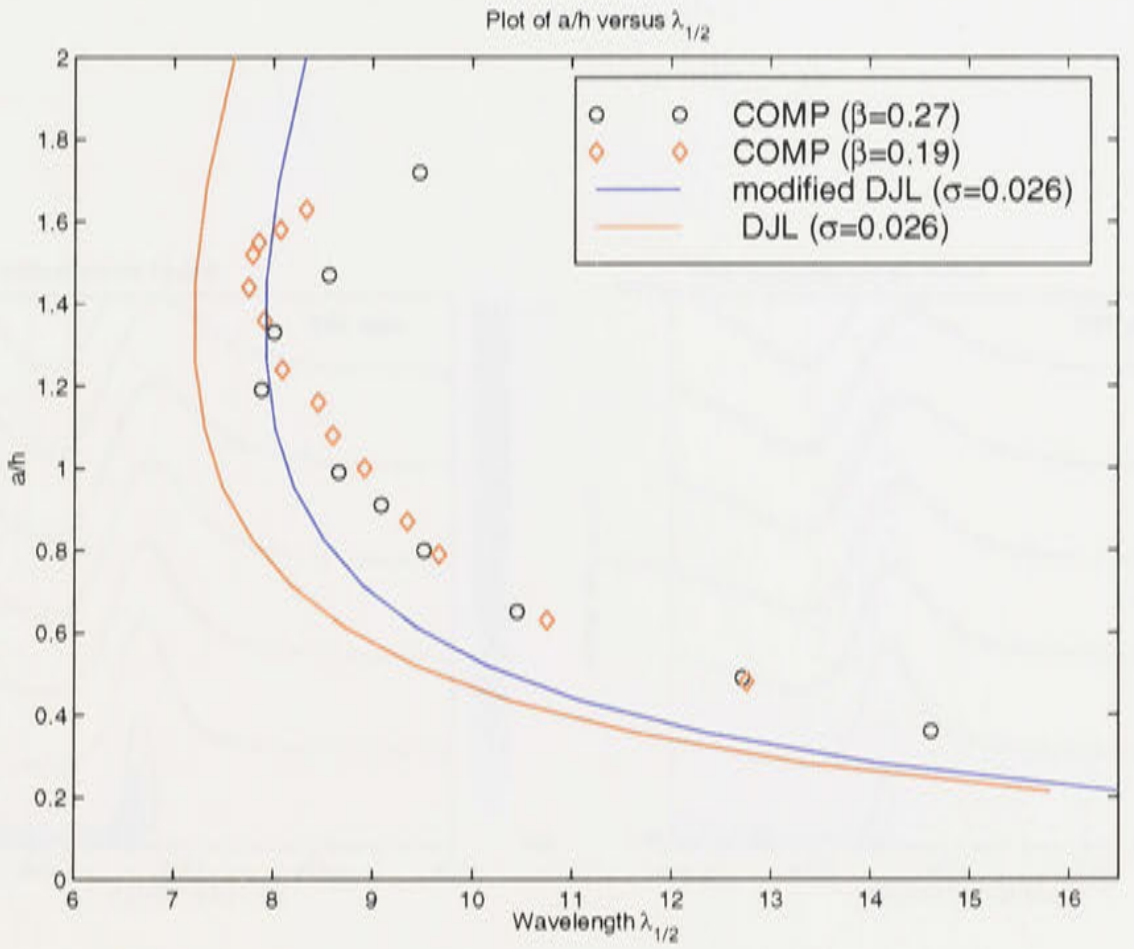

Figure 7.11: Non-dimensional wave amplitude versus the full width at half maximum amplitude wavelength $\lambda_{1/2}$ for the radiative decay of two mapped DJL solutions with $\Lambda_{t=0} = 0.6$ and $\beta = 0.27, 0.19$.

$\Lambda_{t=0}$	t(min)	β	a/h
0.6	79	0.27	0.85
0.6	112	0.19	0.84
0.7	71	0.27	0.84

Table 7.1: Estimate of a/h at which closed circulation disappears (using the calculated streamfunction)

observed to be lower than that predicted from DJL solution calculated using a tanh density profile with $\sigma = 0.026$ and a domain depth of $H_2 = 11.76$ (non-dimensional units). The DJL solutions (see last chapter) predict that closed circulation disappears from solitary wave solutions with amplitude between $a/h = 1.2$ and $a/h = 1.0$. It is interesting that the microburst wave generation experiments of Chapter 5 also produce highly nonlinear solitary waves with closed circulation for lower values of a/h than that predicted by the DJL equation. This suggests that wave properties are sensitive to physical quantities not included within the domain of validity of the DJL equation.

The time evolution of the tracer initially placed in the region of closed streamline flow is shown in Fig 7.12 for a set of times which span the point at which closed circulation disappears. It can be seen that when closed streamline flow vanishes the fluid that was leaking in a trailing flow at the ground starts to fall behind the wave.

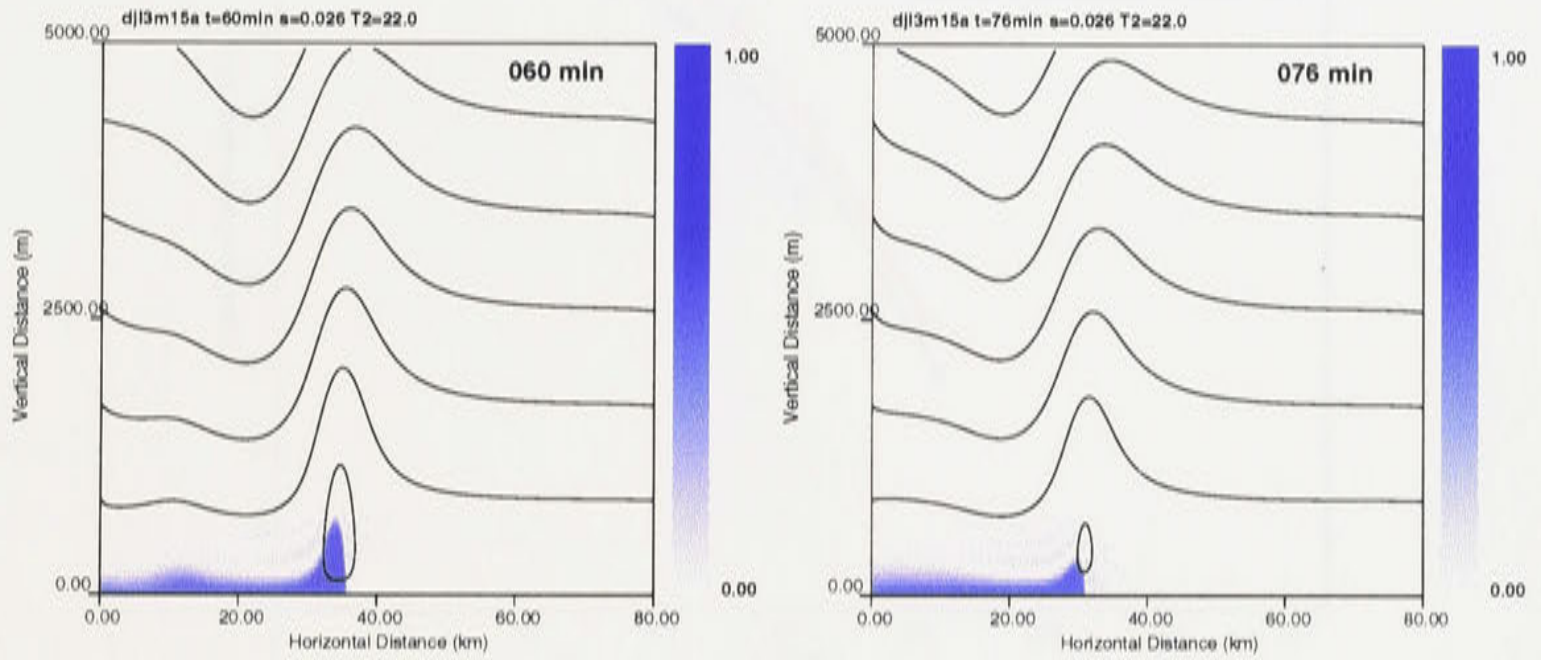

Figure 7.12: Wave morphology under decay ($\beta = 0.27$). (a) $a/h = 1.22$ fluid has been leaking in a thin flow at the ground from the closed circulation cell which is diminishing in size; (b) $a/h = 0.91$; (c) $a/h = 0.85$; (d) $a/h =$ closed circulation cell has disappeared and tracer which was being carried by wave left in wake at ground level.

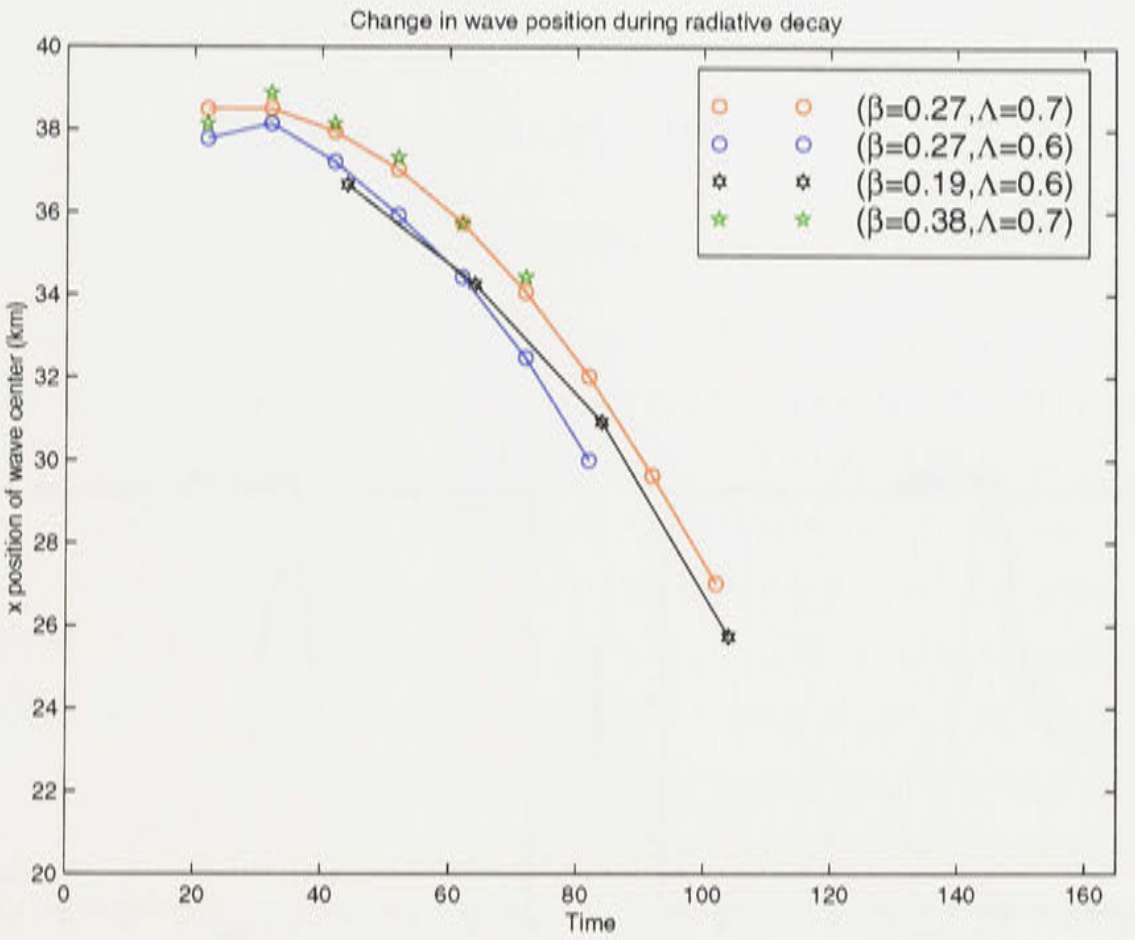

Figure 7.13: Plot of data points representing the change in wave position during radiative decay for several of the experiments.

It can be seen in plots such as Fig 7.8 that the wave speed decreases as the wave propagates under radiative decay. By recording the x position of the wave center during radiative decay for a number of experiments set of data points shown in Fig 7.13 was constructed. It can be seen from this data that the change in wave position is approximately quadratic indicating that the change in wave speed is approximately linear with the linear decay in wave amplitude.

In the experiments presented above an interesting result is that the highly nonlinear solitary wave remains a stable isolated waveform for relatively high values of β suggesting that the balance between dispersive and nonlinear forces, which maintains the solitary wave shape, is sustained for a substantial range of β corresponding to decay of wave amplitude that falls outside any assumption of slow variation in the wave profile. It has been found that the perturbation Exner pressure at the surface can give an indication of the degree of wave stability. The experiment that was discussed above using an extended domain (100km by 10km) has been studied over the period when closed circulation disappears from the wave using the surface perturbation Exner pressure. The changes in surface perturbation pressure are shown in Fig 7.14 and suggest that the presence of closed circulation can suppress the effects of wave dispersion. At $t = 42$mins, shown in Fig 7.14(a), there are no substantial pressure fluctuations in the wake of the wave but just before the disappearance of closed circulation (ie Fig 7.14(b)) there is a substantial increase in the pressure fluctuations behind the wave which seem to represent the

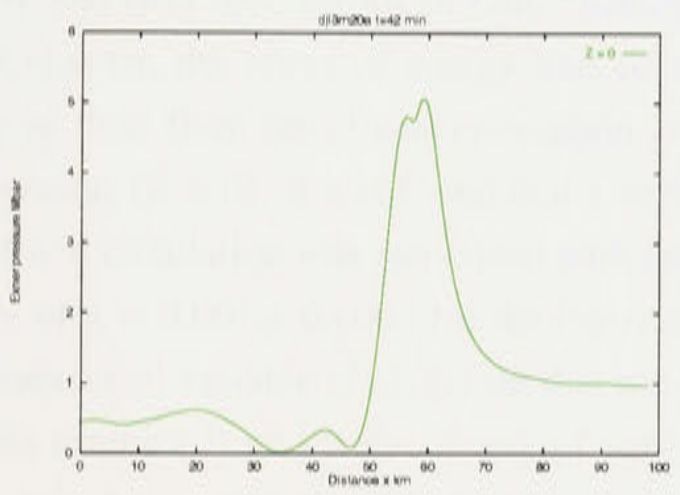

(a) 42 mins

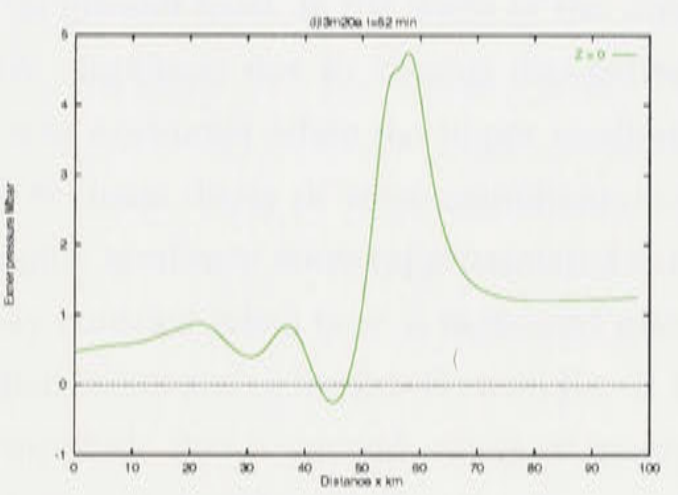

(b) 52 mins

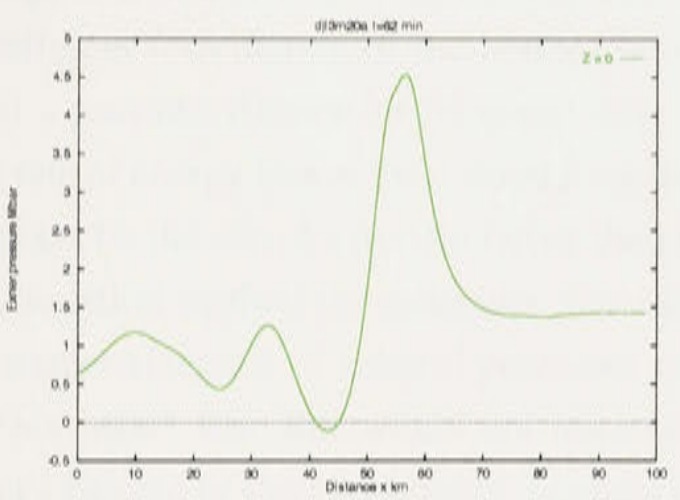

(c) 62 mins

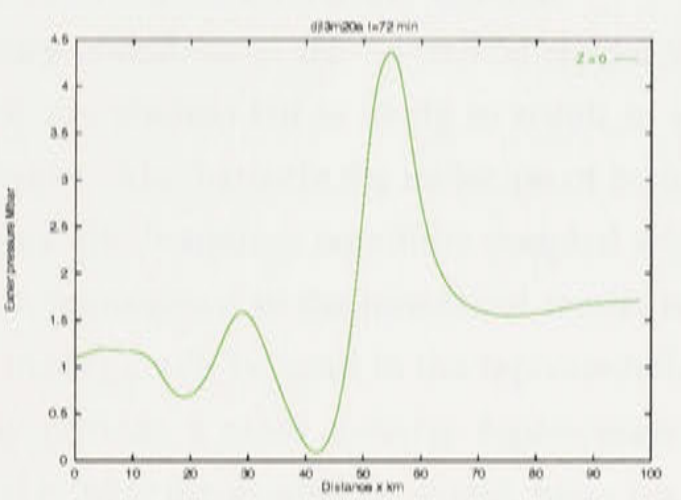

(d) 72 mins

Figure 7.14: Changes in surface perturbation Exner pressure for an experiment with $\beta = 0.25$ over a time period that includes the disappearance of closed circulation from the wave. Closed circulation is characterized by a bimodal shape in the peak of the surface perturbation pressure signature.

effects of wave dispersion.

7.6 Different mechanisms of energy loss

7.6.1 Viscous losses due to a closed circulation cell

As shown using the results of numerical experiments solitary waves of sufficient amplitude in an atmospheric waveguide will possess a region of closed circulating fluid which travels with the wave and over time results in fluid "leaking" at ground level, in the wake of the wave. In the last chapter, the effect of energy loss on wave amplitude due to viscous dissipation and leaking of fluid from the closed circulation cell was examined when the upper medium was homogeneous ($\beta = 0$). It was found that a very slow linear decay of wave amplitude occurred when closed circulation was associated with the highly nonlinear wave (approximated using an estimate of $\kappa = 0.001 \pm 0.0005$ for the linear decay constant when time is measured using the non-dimensional variable t/t_0). Given that the experiments above for $\beta > 0$ (with $\beta > 0.19$ for the cases examined) all involve decay of wave amplitude that is several orders of magnitude greater than the measured decay rate for viscous losses, it would seem that for these cases the change in wave amplitude due to energy lost to the stratified upper medium dominates over any energy loss due to viscous forces and that the latter can be effectively ignored.

A different formulation of the bottom boundary condition in the numerical model which included a parameterization of frictional drag was not studied but is likely to result in an increased rate of energy loss at the ground from the wave. Alternatively the inclusion of boundary layer effects by the use of a no-slip rather than a free-slip boundary condition coupled with the direct simulation method (ie molecular viscosity is represented in the numerical model but no other parameterizations of subgrid processes are made) could be used in the representation of the surface layer. But, this would not necessarily provide a more accurate representation of the exact structure of the atmospheric boundary layer near the ground (it would, however, be a good representation of the friction layer in laboratory experiments) and has therefore not been implemented. It would be necessary to implement a different bottom boundary condition if a detailed study of frictional losses was to be undertaken in future work.

7.6.2 Effect of a "drag" force during amplitude decay

As discussed above Maslowe and Rekopp (1980) derive two identities associated with radiative decay due to an ambient environment which supports internal waves in the weakly nonlinear limit. These are given as equations 7.2 and 7.3. The first of these is a conservation identity requiring conservation of the volume of a wave packet. This is not strictly satisfied for the decay of highly nonlinear waves. The second defines a decay law in terms of an integral which is the same as that used in Baines (1996) to represent the effects of a drag force due to an

internal wave field generated by fixed topography in a stratified flow. It is proposed to examine here the relative effects of a force represented by

$$F_1(A,\hat{\alpha}) = \int_0^{\hat{\alpha}} k(\hat{\alpha}^2 - k^2)^{\frac{1}{2}} |\mathcal{F}(k,t)|^2 dk, \tag{7.13}$$

acting on a wave packet $A(x,t)$ with Fourier transform $\mathcal{F}(k,t)$ which is evaluated for a set of highly nonlinear wave parameters (ie amplitudes and wavelengths) taken from solutions to the DJL equation calculated in Chapter 6. This is analogous to testing the width and height dependence of the drag force represented by F_1 on an obstacle in the case of flow over fixed topography when the medium surrounding the object is stratified. The integral F_1 can also be considered as the x domain analog (by way of the convolution theorem) of the modulation of the signal representing the spectral energy of $A(x,t)$ by a function (in terms of wavenumber) representing the effect of loss of spectral energy due to internal wave modes excited in the stratified deep fluid upper medium governed by cutoff wavenumber $\hat{\alpha}$ (the deep fluid regime is incorporated by the assumption of a radiation condition whereby there are no modes which correspond to downward transfer of energy ie no reflection of wave energy in the upper media). In the formulation of F_1 there is an assumption of hydrostatic balance and steady state flow, and an obstacle height which is assumed small (ie weakly nonlinear amplitude a/h) so that $(a/h)\hat{\alpha} \ll 1$. If $A(x,t)$ is assumed to be only very slowly varying with time then F_1 should still make a valid approximation to wave drag. A rapidly varying wave packet $A(x,t)$ will produce non-steady state flow that cannot be described using a slow variation approximation. Even though many of the wave radiation cases presented above do not satisfy a slowly varying approximation and the wave amplitudes are initially outside those governed by weakly nonlinear theory, it will still be interesting to examine the effect of a term such as F_1.

First we assume that the solitary wave shape is approximated by

$$A(x,t) = [a(t)/h]\frac{\lambda_{1/2}(t)^2}{(x^2 + \lambda_{1/2}(t)^2)} \tag{7.14}$$

where $[a(t)/h]$ and $\lambda_{1/2}(t)$ define the waves amplitude and wavelength at time t. The term $|\mathcal{F}(k,t)|^2$ in the integral F_1 can be considered as a measure of the spectral energy associated with the wavenumber spectrum that defines the shape of $A(x,t)$. If $A(x,t)$ can be approximated using (7.14) then $|\mathcal{F}(k,t)|^2$ is given by

$$|\mathcal{F}(k,t)|^2 = \pi^2(a/h)^2\lambda_{1/2}^2 \exp[-2\lambda_{1/2}k] \tag{7.15}$$

When evaluating the integral F_1 we have to consider how the cutoff wavenumber $\hat{\alpha}$, defining the allowable internal wave modes produced in the stratified media and given by equation (7.4), should be evaluated. Equation (7.4) implies that α is dependent on the speed of the

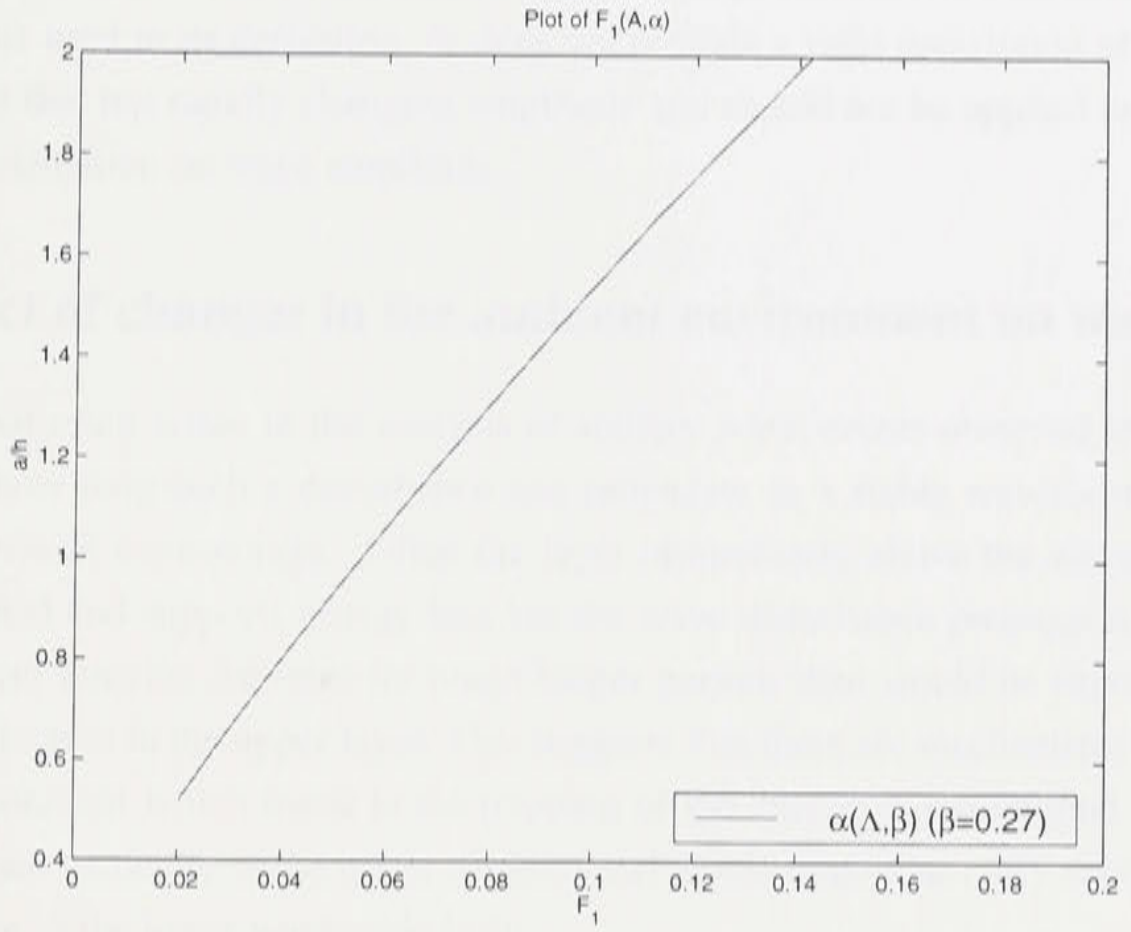

Figure 7.15: Plot of the integral $F_1(A, \hat{\alpha})$ for the case where $\hat{\alpha}(\Lambda)$ is assumed variable and amplitude-wavelength data is taken from a set of DJL solutions using $[\Lambda, a/h, \lambda_{1/2}]$.

disturbance. In the last chapter it was shown that highly nonlinear solitary wave solutions have associated speeds that are a linear function of wave amplitude. It was decided to test the behaviour of F_1 for a set of DJL solitary wave solutions. A set of data for $[a/h, \lambda_{1/2}, c]$ corresponding to a set of solutions with each solitary wave solution, for some eigenvalue Λ, having non-dimensional amplitude a/h, wavelength $\lambda_{1/2}$ (full width at half maximum amplitude), and speed $c = \sqrt{(\sigma g h)/\Lambda}$ was taken from DJL solutions calculated in chapter 6 for the ambient environment with $\sigma = 0.026$ (measure of density variation in waveguide layer) and $H_2 = 11.76$ (the total domain depth corresponding to 10km). For each solution in the set F_1 was evaluated with a value of $\hat{\alpha}$ estimated using

$$\hat{\alpha} = \beta\sqrt{\Lambda} \tag{7.16}$$

The results for $\beta = 0.27$ are shown in Fig (7.15). This seems to indicate that F_1 has a predominantly linear behaviour dependent on wave amplitude (which dominates over the effect of wavelength).

It would seem, therefore, that the magnitude of F_1 will be completely dominated by rapid changes in wave amplitude. The linear behaviour of F_1 with amplitude indicates a quadratic reduction in wave speed (if it is assumed the drag force is applied in a steady manner). The observed change in waves under radiative decay from the above experiments does not support

such a prediction. This would seem to confirm that, as expected based on the domain of validity of assumptions used in its derivation, F_1 does not provide a valid description of the "drag" on a wave packet that has rapidly changing amplitude and should not be applied outside a slowly varying approximation on wave amplitude.

7.7 Effect of changes in the ambient environment on wave decay

A question that often arises in the analysis of solitary wave events observed in the lower atmosphere is how long such a disturbance can propagate as a stable waveform given energy loss to the ambient environment. Often the layer immediately above the waveguide layer is weakly stratified and supports energy loss but the wave disturbance propagating in the lower waveguide layer remains coherent for much longer periods than would be expected given the level of stratification in the upper layer. This suggests that there are mechanisms at work in the ambient environment which result in the trapping of the energy of the internal gravity waves which propagate vertically in the upper medium and would otherwise carry energy away from the disturbance in the lower waveguide layer.

Crook (1988) has made a numerical study of different mechanisms which can result in trapping of low level internal gravity waves in a stratified environment. Crook notes that the observations of the Morning Glory by Clarke et al. (1981) report that the ratio β is typically $0.25 \sim 0.33$. According to the results presented above this corresponds to a rapid decay of wave amplitude and within a short time all the wave energy has been radiated away. Observations of the Morning Glory record such a disturbance propagating for substantial times over long distances. This leads to consideration of other mechanisms in the ambient environment that contribute to the longevity of such waves.

7.7.1 Effect of an inversion layer

One such mechanism proposed by Crook (1988) is the presence of an inversion layer at a higher level above the waveguide layer. Observations of some morning glory solitary wave events have recorded the presence of an upper inversion layer at a height of approximately 3-4 km. If an inversion layer is included in the ambient potential temperature profile so that the variation of ambient potential temperature is as shown in Fig 7.16, the rate of decay of wave amplitude for a highly nonlinear solitary wave seems to be reduced. This is shown in Fig 7.17 for an inversion layer centered at $z = 6.85$ km compared with an ambient environment without stratification for the same degree of stratification in the media immediately above the waveguide layer.

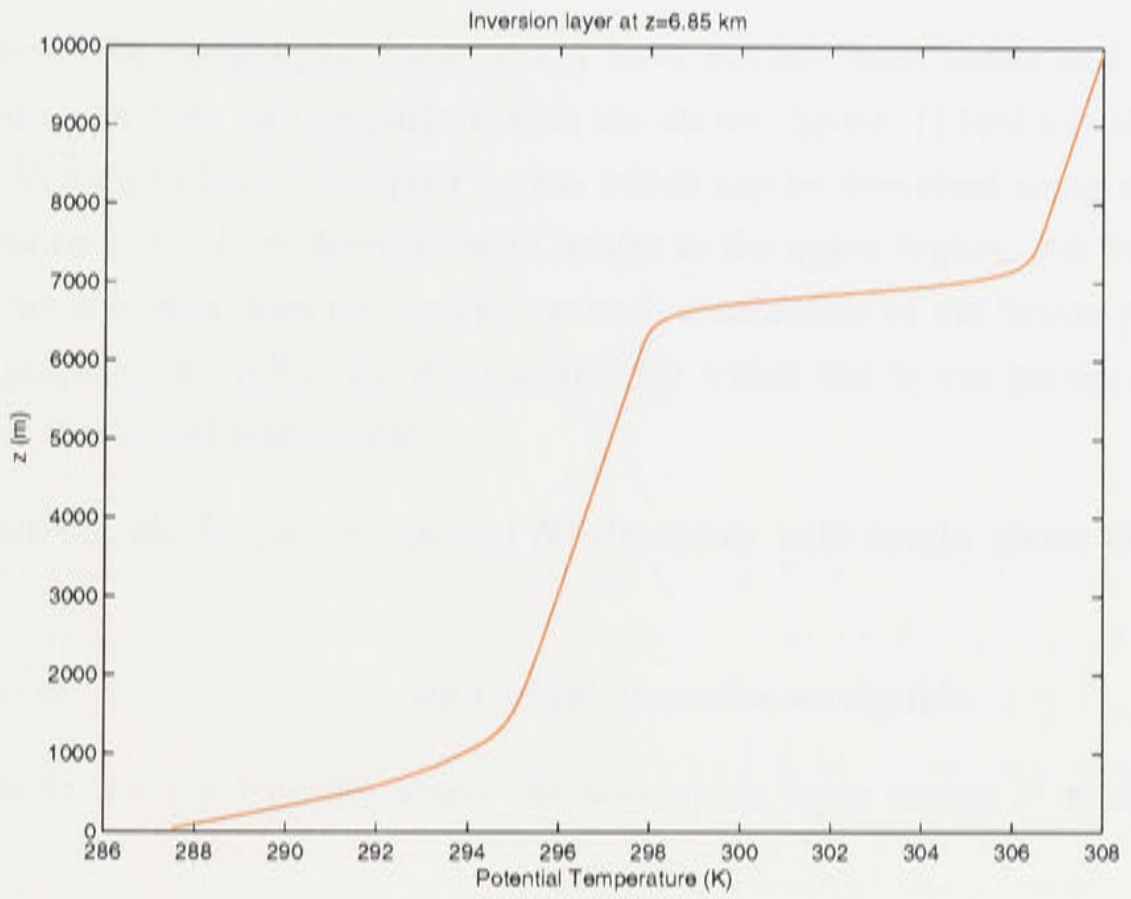

Figure 7.16: Potential temperature plot with an inversion of 8K change in temperature at a height of 6.85 km with weak stratification ($N = 2\pi/(22.60)$ below and above the inversion.

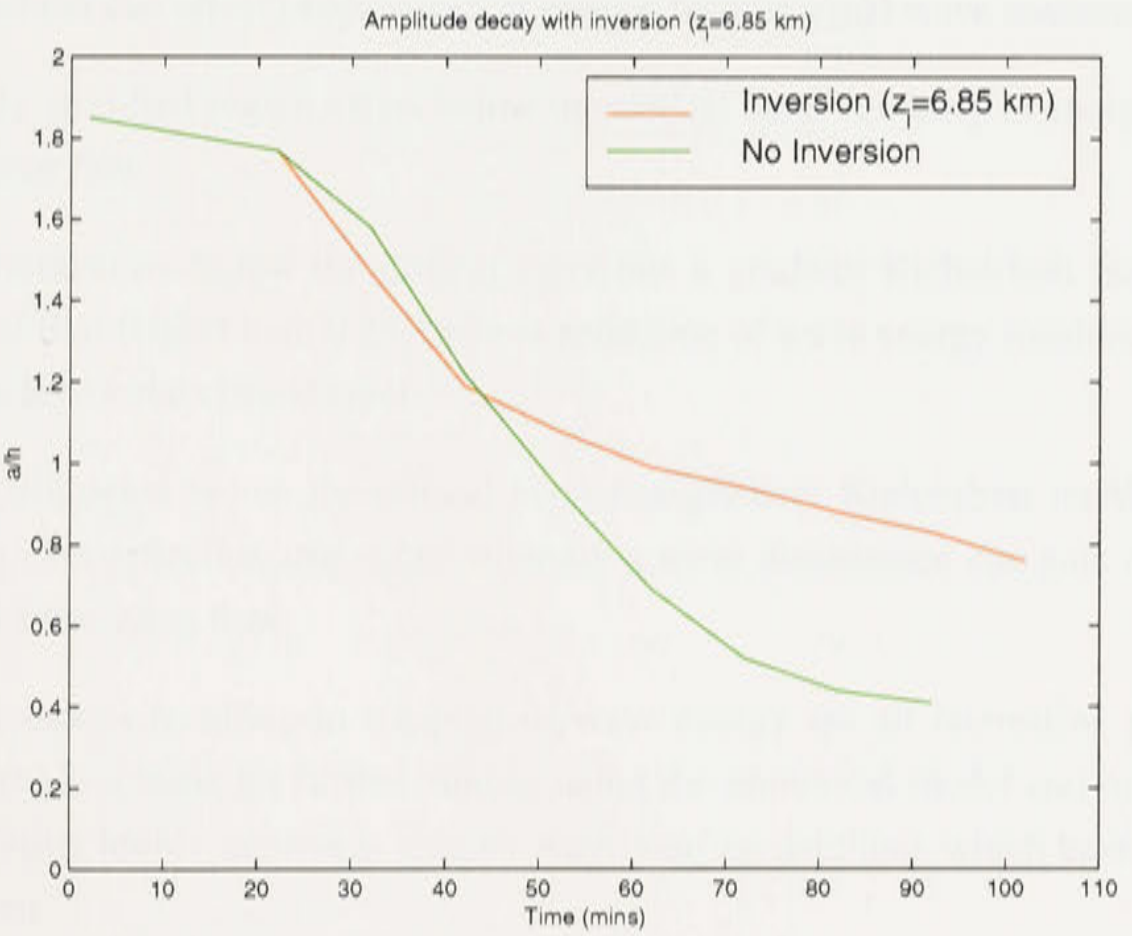

Figure 7.17: Amplitude decay for the case of an inversion layer of 8 K change in potential temperature centered at $z = 6.85$ km. The case with no inversion is included for comparison. Data is sampled at 10 min intervals.

7.7.2 Other mechanisms

Other mechanisms for trapping of wave energy have already been mentioned in Chapter 2 but are outlined again here for comparison with the above. Scorer (1949) has shown that for energy to remain trapped below an upper region which can be described using equation (7.5) a suitable condition is for l^2 to decrease with height in the upper region. An inversion layer which reflects wave energy does not depend on such a reduction of the Scorer parameter but Crook (1986) proposes the following mechanisms for which the Scorer parameter above the waveguide layer is reduced with height:

1. The Brunt-Väisälä frequency squared N^2 decreases with height above the waveguide layer.

2. The value of $(U-c)^2$ increases with height above the waveguide.

3. Curvature in the wind profile above the waveguide layer causes l^2 to decrease with height.

Finally, Skyllingstad (1991) has shown that the presence of critical layers, where $U = c$ (but the problem posed by equation (7.5) is still able to be solved near the singularity with certain imposed constraints), above the waveguide layer can have important implications for trapping of wave energy. Skyllingstad (1991) describes three different mechanisms associated with critical layers which can affect propagation of energy from internal wave motions:

1. A strongly stratified region exists below the critical layer resulting in energy absorption by the mean flow.

2. If the stratification below the critical layer has a gradient Richardson number, in the vicinity of (but larger) than 0.25, there is reflection of wave energy resulting in trapping of energy below the critical layer.

3. If the stratification below the critical layer has gradient Richardson number less than 0.25 then over-reflection can occur whereby a wave disturbance can gain energy at the expense of the mean flow.

These mechanisms resulting in trapping of wave energy are all interesting phenomenon which could provide a basis for further studies using the numerical model and mapping technique for generating highly nonlinear solitary wave starting solutions which have been developed in this thesis.

Conclusion

This thesis has examined, using numerical simulation, highly nonlinear internal solitary wave motions and associated internal gravity wave phenomena in an atmospheric context. This has lead to the development of several useful numerical techniques and has provided a set of results relating to the processes of wave formation and decay for highly nonlinear solitary waves on waveguide layers in the lower atmosphere. The radiative decay of highly nonlinear solitary waves in the atmosphere has not been previously studied and is particularly relevant to observations of atmospheric events which involve strongly nonlinear waves with a region of closed re-circulating flow.

In order to undertake such a study the development of appropriate numerical tools was necessary. A numerical model was constructed for these studies which implemented a set of fully nonlinear governing equations based on the Navier-Stokes equations, an equation for mass continuity, a relationship for thermodynamic conservation of heat and an equation of state. The governing equations were solved using a finite difference method with as few approximations as possible. This meant that instead of resorting to parameterizations whose physical validity could be questioned, a direct simulation method was adopted where a high grid resolution combined with a second order dissipation operator to remove energy at the smallest scales (and which also provided a form of simple eddy viscosity) were used to represent features of interest. A simple test involving a falling blob of cold air, which generated strong vortex motions as it descended, and its subsequent impact with a rigid free-slip bottom boundary was used to examine the ability of the model to resolve an appropriate level of fluid dynamics. The results of this test compared well with the behaviour of a vortex ring reported in laboratory experiments.

A study of highly nonlinear wave motions in environments which include an upper region of stratification above the waveguide layer (and therefore can support internal wave motions) requires suitable boundary conditions. Any numerical model that depends on a limited area domain (as was the case here) must prevent reflections of wave energy from the boundaries interacting with the solutions. This problem was addressed by the use of radiative boundary conditions on the lateral and upper boundaries. The upper boundary was particularly important as a potential source of wave energy reflection and the method chosen utilized a spectral

filtering condition to insure that wave motions at the upper boundary did not contain Fourier components which corresponded to downward transfer of energy (this method was based on the linear internal wave formulation of Bougeault (1982) and Klemp and Durran (1982)). A test using an oscillating dipole at the ground to generate an internal wave field showed that wave energy was successfully radiated out of the numerical domain and that the vertical flux of wave energy rapidly approached a constant steady state value within the time scale for vertical propagation through the domain of the slowest wave mode. This indicated that there was no build up of reflected wave energy. An upper boundary condition of this type has computational advantages (ie does not require a larger domain) over other methods used to suppress reflection of wave energy such as the use of extra "sponge" layers in the numerical domain.

Once an appropriate numerical model had been implemented and tested, a mechanism was examined that could result in the generation of highly nonlinear solitary waves in a ground based atmospheric waveguide layer. A set of experiments were conducted to simulate the impact of a downdraft of limited spatial extent with the waveguide layer. The downdraft was modeled using a simple representation based on a "cold pool" (or blob) of air which developed into a falling thermal. These experiments provided a simple model of a possible scenario for wave generation due to a low level microburst. It was found, given suitable waveguide conditions, that a limited area downdraft (often called a "downburst") of sufficient volume and potential temperature perturbation would produce a highly nonlinear wave disturbance with a region of recirculating fluid. When the medium above the waveguide was homogeneous there was only a very slow decay of wave energy due to viscous dissipation associated with the leaking of a thin trailing layer of fluid at the ground from the region of closed circulation. The leaking of fluid in the wake of highly nonlinear waves with closed circulation has been observed in laboratory experiments and in observations of waves in the lower atmosphere. The chosen method for wave generation represented a simple model of real physical processes and avoided the use of artificial source/sink functions that are often used as forcing mechanisms in numerical studies.

By varying a set of parameters governing the dynamics of the falling thermal a range of different wave-generating impacts were initiated. These included experiments resulting in the formation of a single waveform and others that resulted in multiple wave formation (with at most 2 waves). Waves of both modest amplitude and those falling into the highly nonlinear category (with closed circulation) were produced. The type and quantity of waves formed in these experiments seemed to be directly related to the energy associated with the impacting thermal. A comparison was made between the waves produced in the experiments and incompressible inviscid highly nonlinear wave theory (ie an appropriate boundary value PDE solved with the same ambient conditions and simplified boundary conditions). Values of a/h, representing non-dimensional wave amplitude, were plotted against c/c_0, representing non-dimensional wave speed, and compared well with theoretical predictions. However, some

of the waves in the numerical experiments possessed a region of closed circulation for smaller values of a/h than predicted by theory, indicating some difference in wave properties due to the ambient conditions in our model. There were also strong similarities between these numerical experiments and laboratory work such as that of Maxworthy (1980), Noh et al. (1992) and Manasseh et al. (1998). The dynamics of the observed highly nonlinear wave motions also compared well with observations of waves in the lower atmosphere such as the study of a thunderstorm initiated wave disturbance by Doviak et al. (1991).

A close examination was made of the formation process that occurred during the wave generation experiments. The results of the numerical experiments indicated that two different mechanisms of wave formation were observed. An impact that did not penetrate fully to the ground (and therefore did not result in a strong ground based diverging outflow) seemed to produce, by its impulsive disturbance of the waveguide, a wave of modest amplitude. Vorticity associated with the initial microburst was confined to the vicinity of the point of impact and dissipated rapidly due to vortex collapse. In contrast, an impact that penetrated to the ground initiated a strong horizontally propagating gravity current along the ground (of limited duration) due to the transformation of some of the energy associated with the descending microburst vortex pair. Such an impact also resulted in an impulsive disturbance of the waveguide layer which encapsulated the gravity current head. Through a process of head separation the wave envelope encapsulating the fluid associated with the gravity current head seemed to develop, after a transition period, into a highly nonlinear wave with a region of closed recirculating fluid. These results demonstrated the existence of a transient state after the formation of a short lived outflow in a ground-based waveguide layer that lead to a highly nonlinear waveform which contained trapped outflow air in a re-circulation cell.

Numerical experiments were also studied which simulated a microburst impact with a waveguide layer when a windshear layer existed above the waveguide. For this type of impact the presence of windshear can substantially alter the dynamics of the impact and the resulting wave formation process. The disturbance of the axisymmetric flow of the descending thermal as it passes through a shear layer was observed to cause an impact at an angle to the waveguide which altered the transfer of energy associated with the vorticity of the thermal. In these asymmetric impacts most of the energy was observed to go into an impulsive disturbance of the waveguide layer. An asymmetric impact due to the presence of a windshear layer was also observed to suppress the formation of an outflow at the ground.

These wave generation experiments demonstrated that potentially hazardous windshear events, associated with large amplitude solitary waves, can be generated by a short duration disturbance of suitable waveguide conditions in the lower atmosphere. Strong short-lived downdrafts (ie microburst type events), which fit this description of a possible wave generation mechanism, are often formed during thunderstorm activity. The type of wave generation mechanism, simulated in the experiments, is sufficiently general that it may provide a simple

representation for other types of atmospheric forcing mechanisms which can be modeled by the use of a falling thermal.

Having investigated a possible scenario for wave generation in the lower atmosphere, I decided to examine in detail the process by which wave energy can be lost from a propagating highly nonlinear wave disturbance due to a weakly stratified upper medium above the waveguide layer which can support internal wave motions. The experiments, resulting in wave generation by a microburst type impact, imposed certain limitations on our ability to accurately specify properties of the highly nonlinear waves which were produced and were not completely free of other disturbances in the numerical domain. In order to provide a more suitable initial isolated waveform for a study of radiative decay, I therefore decided to examine the use of theoretical wave solutions as starting waves in our numerical model. This required a stable method for the mapping of solutions.

A mapping technique was presented which mapped steady solitary wave solutions from an incompressible time independent boundary value problem (ie a PDE equation with fairly simple boundary conditions) to our compressible time dependent mesoscale numerical model (which also solved a boundary value problem based on fully nonlinear governing equations for fluid flow but with much more complicated boundary conditions). The mapped starting wave solutions were dependent on additional thermodynamical variables not included in the PDE solutions and these variables were therefore assigned initial values based on the hydrostatic Euler equations. Starting waves which possessed a region of closed circulation also required a suitable method for the initialization of the physical processes associated with the closed circulation cell. The potential temperature of fluid within the closed circulation cell was set equal to the ambient temperature at the ground (observations from field experiments and the temperature profile of waves generated in Chapter 5 seemed to support this choice). Several stability issues associated with the numerical solutions were linked with the initialization of strong mixing processes within the wave. The nature of our numerical model and the chosen mapping technique were found to result in an upper limit on the amplitude of highly nonlinear waves which could be mapped to a stable waveform. This appeared to be related to the representation of viscous effects in the numerical model. These results indicated that highly nonlinear boundary layer waves, with closed circulation, are strongly influenced by viscous effects. It was also shown that mixing was initiated in the interior of large amplitude waves if a potential temperature deficit existed.

Once a starting wave was successfully mapped to the compressible mesoscale model, it was found necessary to impose an "adjustment" period to allow the wave to relax to a quasi-stable waveform (ie stable apart from losses associated with physical processes represented in the model). The surface perturbation Exner pressure was found to give a good indication of the wave stability. The surface perturbation pressure possessed a bimodal character, similar to that observed for highly nonlinear waves in the lower atmosphere, which indicated that there was

closed circulation within the wave. In the mapping of solutions from an incompressible time independent boundary value problem, the use of certain time dependent boundary conditions in our numerical model were found to result in initial instability of the starting wave solution. The "adjustment" period was necessary to allow spurious fluctuations to die out without the interaction of such fluctuations with the time dependent boundary conditions. This was found to be particularly true for the upper boundary due to the use of a radiative boundary condition with time dependence on the perturbation pressure field. Instability occurred in this case if the upper medium above the waveguide layer was not initially homogeneous.

All starting wave solutions originated from numerical solutions to the Dubreil-Jacotin-Long (DJL) equation which provides a description of highly non-linear waves in an incompressible inviscid continuously stratified fluid. The DJL equation by itself, as shown by Brown (1995), does not provide an accurate description of highly nonlinear waves in compressible viscous flow. For this reason, the initialization of additional physical variables was required for the chosen mapping technique. DJL solutions were found, however, to be a useful basis for generating highly nonlinear starting waves. Steady solitary wave solutions to the DJL equation were calculated using an tanh ambient density profile to represent a waveguide with homogeneous conditions above. When mapped to the compressible model, using the mapping technique developed, waves with closed streamline flow were observed to leak fluid at the ground from a closed circulation cell. The rate of amplitude decay associated with this energy loss due to leaked fluid was estimated for a number of starting wave solutions. In addition to the solutions based on a tanh density profile, some interesting two layer solutions, using realistic values of constant Brunt-Väisälä frequency in each layer, were calculated from the DJL equation and seemed to match the description of steady state trapped wave solutions (due to the use of a rigid lid boundary condition for the solution of the DJL equation which resulted in reflection of wave energy).

A stable set of highly nonlinear starting wave solutions were now able to provide a starting point for the study of wave decay due to ambient stratification. The radiative decay of solitary waves due to stratification in the ambient media had been examined previously by a number of researchers (eg Maslowe and Redekopp, 1980; Grimshaw, 1980/81, 1981a,b; Pereira and Redekopp, 1980) within the framework of weakly nonlinear wave theory and under a number of assumptions including an important requirement of a slowly varying waveform. Many solitary wave events observed in the lower atmosphere, however, involve highly nonlinear solitary waves which are not well described by weakly nonlinear theory. Also, observations of the waveguide conditions during solitary wave events in the atmosphere often include an upper medium above the waveguide having a level of stratification sufficient to cause a degree of energy loss from the wave that does not satisfy the assumption of a slowly varying waveform. A study was therefore made of the radiative decay of fully nonlinear waves (with closed circulation) using the mapped starting wave solutions and our numerical model combined with

realistic ambient waveguide conditions. In order to maintain the stability of the mapped starting solutions it was found necessary to start with a neutral upper layer (ie no stratification) and to adjust the level of stratification (from zero to a finite amount) over a transient period. Starting waves were observed to remain stable during this transient period and suffer only a very small reduction in wave amplitude.

The decay of a set of highly nonlinear starting wave solutions was observed for a range of $\beta = N_2/N_1$ characterizing the degree of energy loss supported by ambient media with constant Brunt-Väisälä frequency N_2 above a waveguide layer with approximately constant Brunt-Väisälä frequency N_1. Highly nonlinear waves were observed to undergo an approximately linear decay in amplitude a/h down to amplitudes close to the cutoff amplitude (defining the minimum value of a/h for ducting of wave motions). At smaller amplitudes the decay became nonlinear. As the value of β was increased so did the rate of amplitude decay and dispersive effects were observed at small amplitudes. An interesting result was that highly nonlinear solitary waves remained coherent waveforms during decay under relatively large values of β and there were indications that the presence of closed circulation in the wave provided a degree of wave stability during radiative decay.

The properties of waves under radiative decay were found to be sensitive to small variations in the ambient stratification profile defining the waveguide conditions. Wave half-widths were found to be larger than predicted by fully nonlinear solitary wave solutions (ie solutions to the DJL equation based on a tanh density profile) and the amplitude-wavelength relationship near the wavelength minimum was found to be sensitive to the value of β. Closed circulation was also observed to remain present during radiative decay for smaller amplitudes a/h than predicted by fully nonlinear wave theory. Wave speed seemed to decrease in an approximately linear fashion during a linear decay of wave amplitude.

It has been suggested (eg Doviak et al., 1991), using a theoretical argument based on the spectral decomposition of a solitary wave packet, that the rate of amplitude decay for highly nonlinear solitary waves, as a result of the generation of an internal wave field in media above the waveguide, could be expected to be reduced near the wavelength minimum (given the wavelength amplitude relationship shown to exist for highly nonlinear waves). This further suggests that the disappearance of closed circulation, near this wavelength minimum, might represent a significant change in the rate of decay of wave amplitude. The results of our numerical study show no substantial variation in the radiative decay of highly nonlinear waves, from an approximately linear behaviour, over a time period which includes both a minimum in wavelength and the loss of re-circulating flow from within the wave. These results suggest that the predicted increase in the vertical loss of wave energy, after the minimum turning point in wavelength is passed, is insignificant compared to changes in the rate of energy loss resulting from reduction of wave amplitude (at least for the relatively rapid radiative decay studied). The numerical experiments also indicated that any effect on the rate of amplitude decay, due to the

disappearance of closed circulation, may be offset by other forms of energy loss from the wave such as wave dispersive effects within the waveguide layer.

Finally, a brief examination was also made of a mechanism by which wave energy was reflected from an upper inversion layer above the waveguide. This resulted in a slower decay of wave amplitude. This is one of many such mechanisms based on changes in the ambient profiles of $N(z)$, the Brunt-Väisälä frequency, and $U(z)$, the ambient wind shear, which can effect the transfer of wave energy in the ambient media and which could be examined in detail in future studies.

This research has provided further insight into the conditions which can lead to generation of highly nonlinear waves in atmospheric waveguide layers due to intense low level microbursts. Athough many of the physical processes associated with real microbursts, such as precipitation, have been omitted, the important dynamics of the wave generation process have been accurately simulated. In addition ambient conditions that can lead to rapid radiative decay of highly nonlinear waves propagating on atmospheric waveguide layers have been studied. An attempt was made to use a realistic ambient background based on measured temperature profiles from field data. The rapid decay of such waves under the simulated ambient conditions can be contrasted with observed cases of highly nonlinear wave propagation over substantial distances, without significant decay (and with a similar ambient environment), and therefore calls for a detailed study of other mechanisms which affect transfer of energy within the ambient medium. The numerical model developed in this thesis and the method for initializing highly nonlinear starting wave solutions provide useful tools for any such work.

Appendix A: a radiative decay problem

The following is a derivation of the initial value type problem used by Maslowe and Redekopp (1980) and Pereira and Redekopp (1980) for the study of a special adiabatic case of weakly nonlinear wave decay. The theory of radiative decay of weakly nonlinear waves is discussed in detail in Chapter 2.

Maslowe and Redekopp (1980) find a solitary wave solution to a special adiabatic case governed by volume conservation and an energy decay law in the form

$$A(\xi,\tau) = \frac{a\lambda^2}{(\xi - v\tau)^2 + \lambda^2}, \tag{A.1}$$

$$v = \frac{\gamma}{4}a, \qquad \lambda = |\frac{4\delta}{\gamma a}|, \tag{A.2}$$

with the properties,

$$< A > \;=\; \pi a\lambda = \quad 4|\frac{\delta}{\gamma}|, \tag{A.3}$$

$$< A^2 > \;=\; \frac{\pi}{2}a^2\lambda = \quad 2a|\frac{\delta}{\gamma}|. \tag{A.4}$$

This means that using the assumption of (2.39) the volume of the solitary wave is independent of its amplitude so that as the wave amplitude decreases the wavelength increases to preserve the volume.

The wave speed for the solution (A.1) is v in the ξ coordinate system, which is itself moving at the linear long wave speed c_0. This means that the speed in a stationary system is given by

$$c = c_0 + \varepsilon v. \tag{A.5}$$

If we now consider the solitary wave solution given by (A.1) in an unstretched coordinate system moving at speed c, then the Fourier transform $F(k,\tau)$, where k represents the wavenumber,

can be evaluated as

$$F(k,\tau) = \pi a \lambda \exp[-\lambda k], \tag{A.6}$$

Evaluating (2.40) using $F(k,\tau)$ with (A.3) and (A.4) (so that $\frac{\partial <A^2>}{\partial \tau} = 2|\delta/\gamma|\partial a/\partial \tau$), for the special adiabatic case above, gives a differential equation describing the radiative decay of a with respect to τ,

$$\frac{da}{d\tau} = -4\hat{\alpha}^3 \frac{|\delta|}{\pi} < A > f(2\hat{\alpha}\lambda), \tag{A.7}$$

$$\text{where} \qquad f(\beta) = \int_0^1 k'(1-k'^2)^{1/2} \exp(-\beta k') dk', \tag{A.8}$$

with $< A >= \pi a \lambda = 4|\delta/\gamma|$ and $v = |\delta|/\lambda = |\delta| a / < A >$. Rewriting this in terms of v only, the equation for amplitude decay becomes

$$\frac{dv}{d\tau} = -4\hat{\alpha}^3 \frac{\delta^2}{\pi} \int_0^1 k'(1-k'^2)^{1/2} \exp(-2\hat{\alpha}|\delta|k'/v) dk'. \tag{A.9}$$

Given $v(\tau = 0)$ and a value of δ this can then be solved as an initial value problem. The RHS of equation (A.9) will have the following asymptotic form as $v \to 0$

$$\lim_{v \to 0} f(2\hat{\alpha}\lambda) \approx O(v^2). \tag{A.10}$$

This means that given a wave profile that is initially steep (so that $a\lambda << 1$ is satisfied), there will be, for fixed α, an initial linear decay of amplitude (ie $a \propto \tau$) given by (A.9) until λ becomes large (and wave amplitude small) so that we are in the regime $v \to 0$ and the change in wave amplitude will be proportional to v^2. Substituting the result (A.10) into equation (A.7) this means that for small values of a we have

$$a \propto \tau^{-1}. \tag{A.11}$$

A limitation of the derivation presented above is that there must be a fixed relationship, for equation (A.7) it was constant, between the wave amplitude a, wavelength λ, and speed c in order to recast (2.40) as an initial value problem.

Appendix B: DJL eigenfunctions

B.1 tanh solutions

The following are a collection of eigenfunction solutions to the DJL equation when the ambient density profile is a tanh function and $\sigma = 0.026$ represents the relative variation in density over the effective depth of the waveguide layer $h = 850$m. The non-dimensional domain height is $H_2 = 11.7$ and the non-dimensional maximum horizontal domain length (which is symmetic about the wave center) is $x_{\max} = 47.0$. The eigenvalue Λ is defined by $\Lambda = \sigma gh/c^2$ where c is the wavespeed.

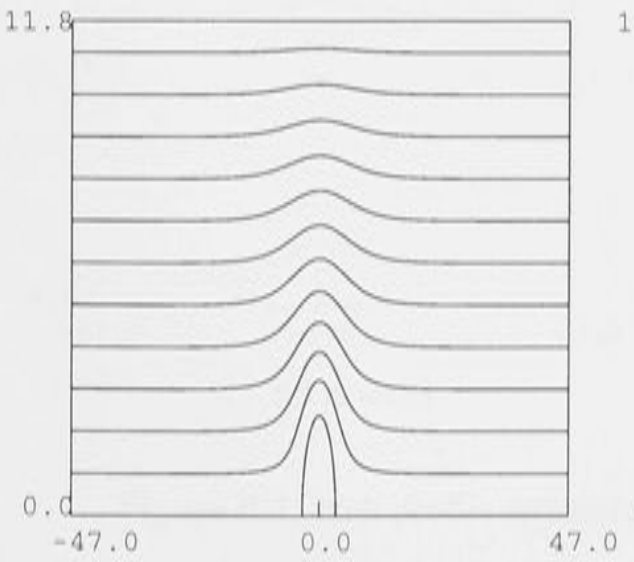

(a) $\Lambda = 0.3$

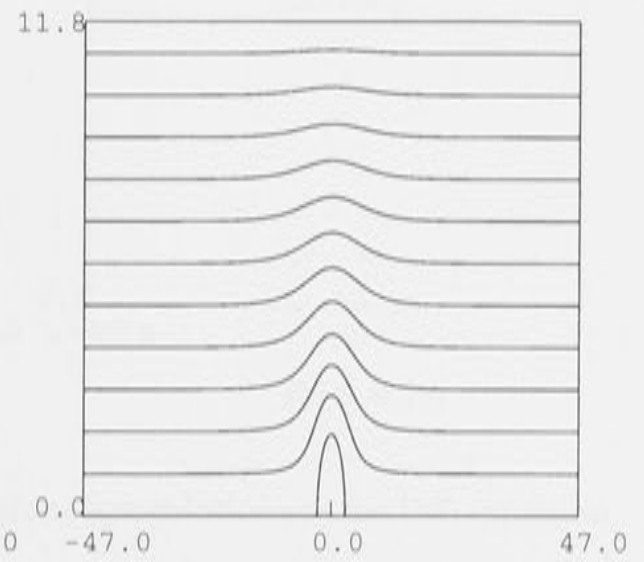

(b) $\Lambda = 0.4$

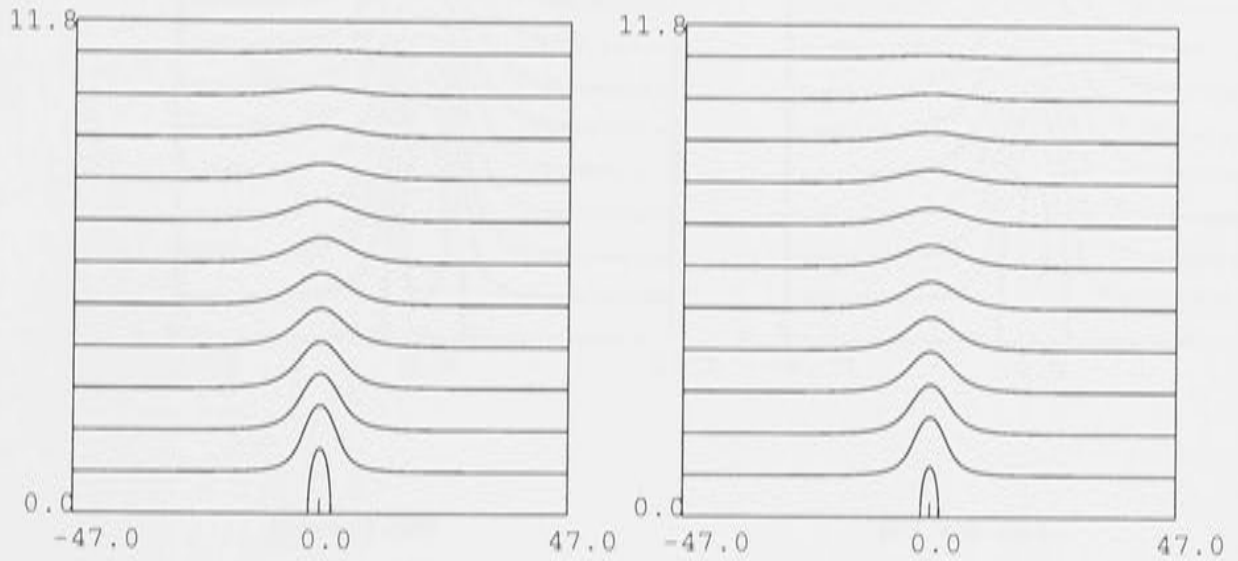

(c) $\Lambda = 0.5$ (d) $\Lambda = 0.6$

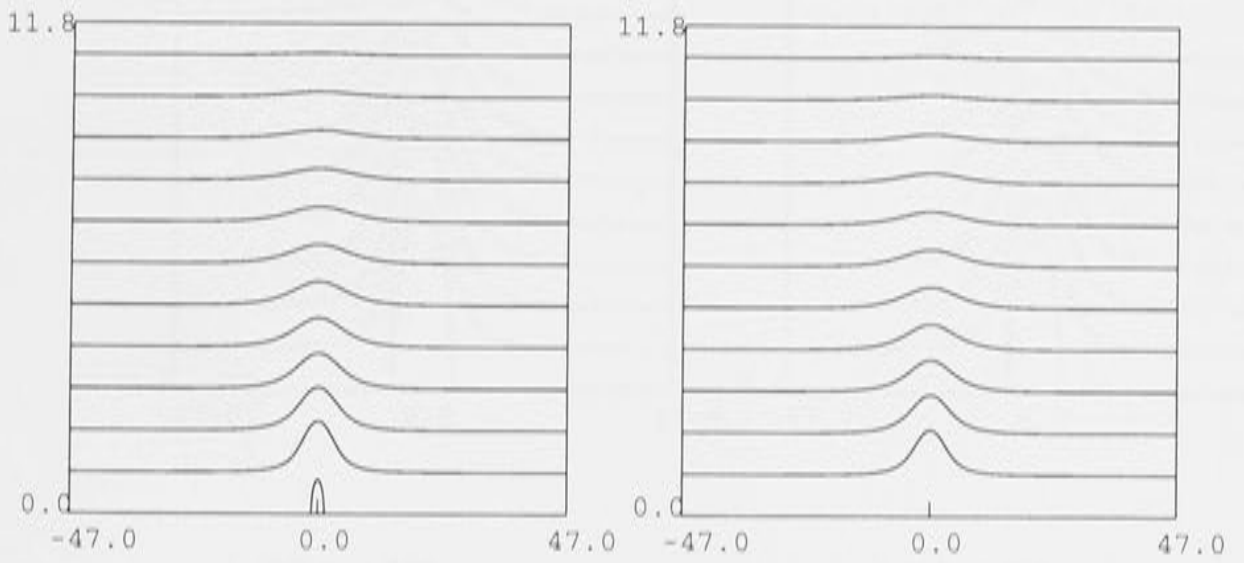

(e) $\Lambda = 0.7$ (f) $\Lambda = 0.8$

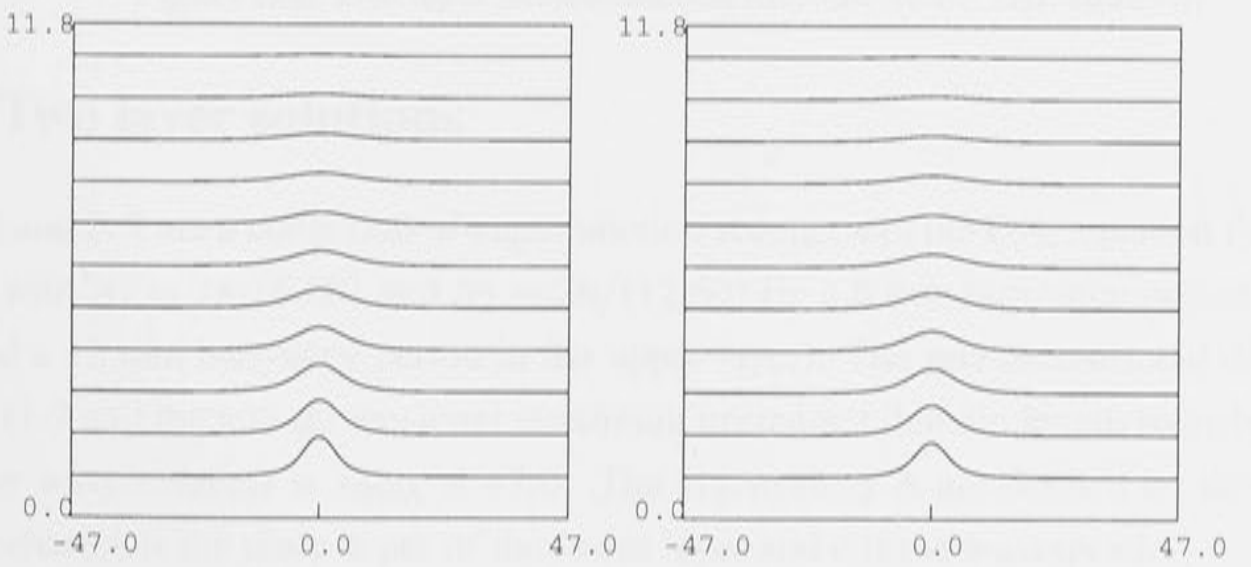

(g) $\Lambda = 0.9$ (h) $\Lambda = 1.0$

Figure B.1: tanh profile streamfunction solutions to the DJL equation

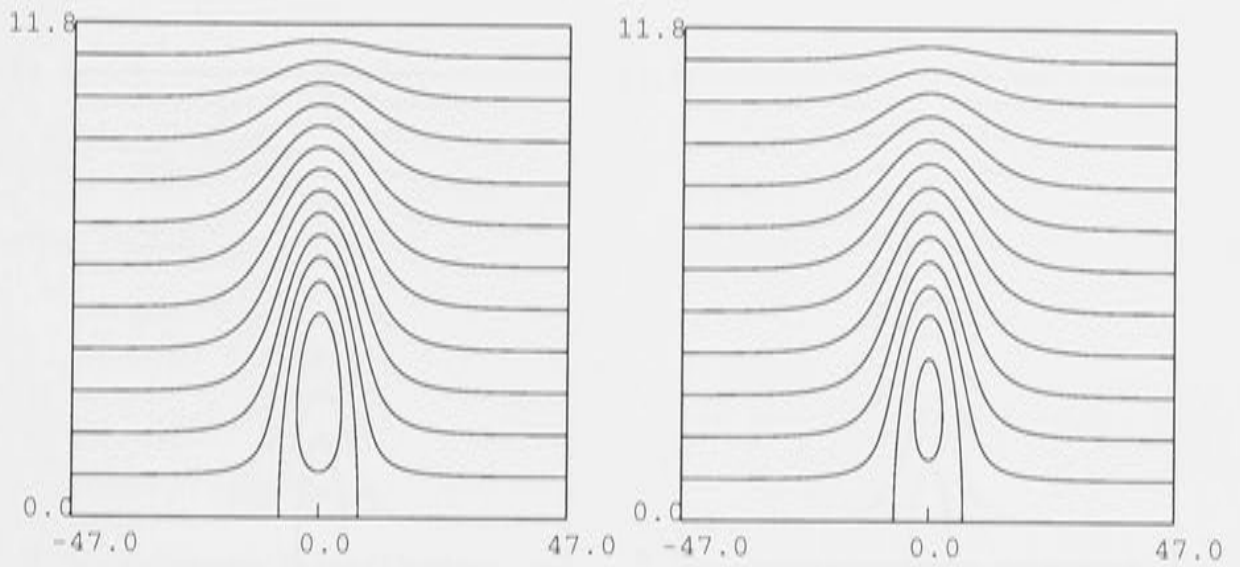

(a) $\Lambda = 200$ (b) $\Lambda = 225$

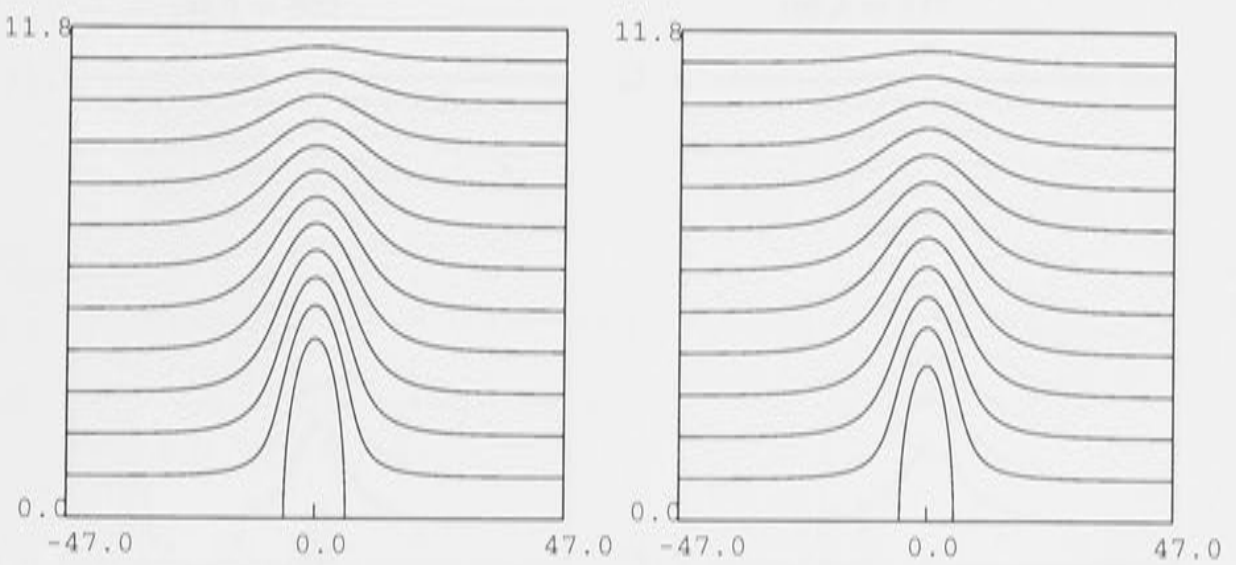

(c) $\Lambda = 250$ (d) $\Lambda = 275$

Figure B.2: Two layer streamfunction solutions to the DJL equation

B.2 Two layer solutions

Figs B.2 and B.3 are a collection of eigenfunction solutions to the DJL equation for a two layer domain with $N_1 = 2\pi/(6.60)$ and $N_2 = 2\pi/(12.60)$ (ie a 6 min buoyancy period in the lower layer and a 12 min buoyancy period in the upper layer). The non-dimensional domain height is $H_2 = 11.7$ and the non-dimensional maximum horizontal domain length (which is symmetic about the wave centers) is $x_{\max} = 47.0$. The eigenvalues Λ are defined by the relationship $\Lambda = \frac{gh}{c^2}$ where h is the scale depth of the lower layer and c is the wavespeed.

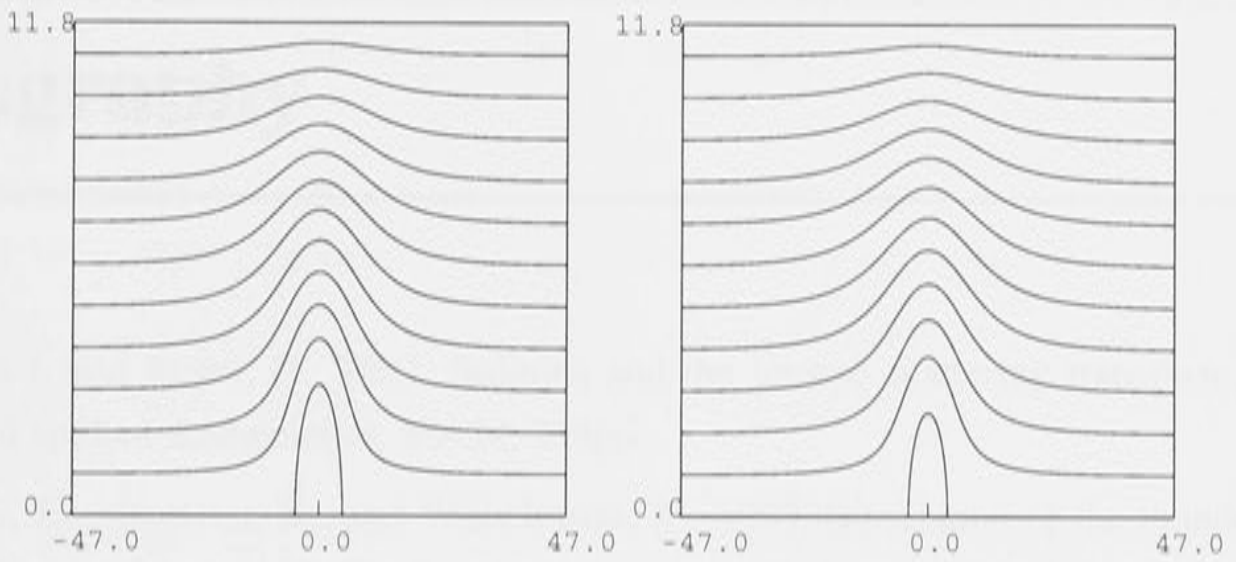

(a) $\Lambda = 300$ (b) $\Lambda = 325$

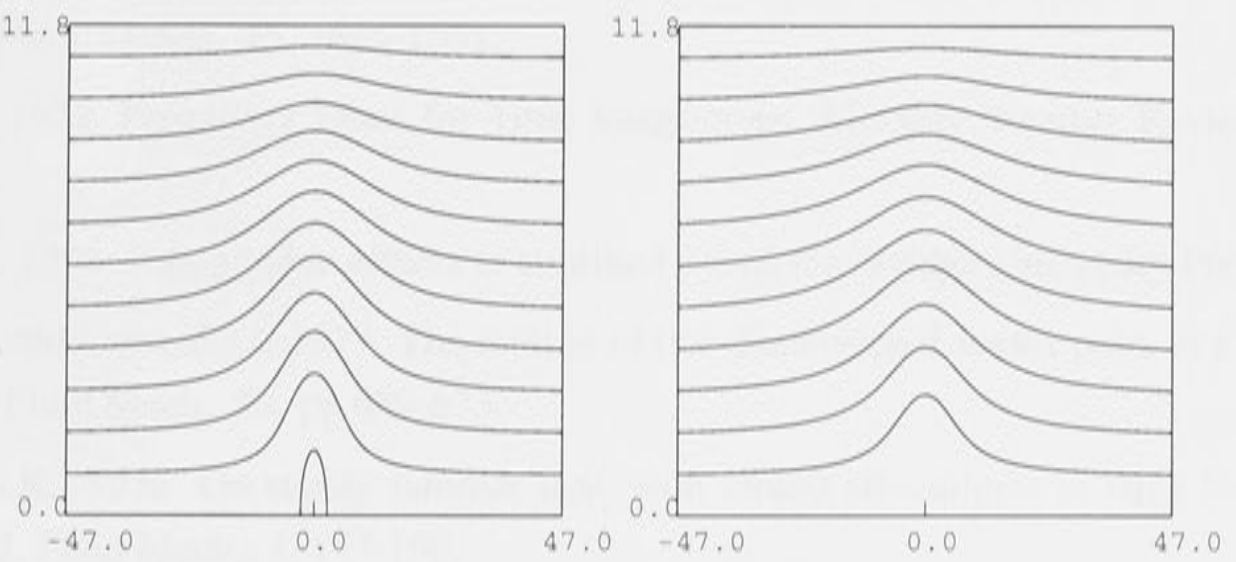

(c) $\Lambda = 350$ (d) $\Lambda = 375$

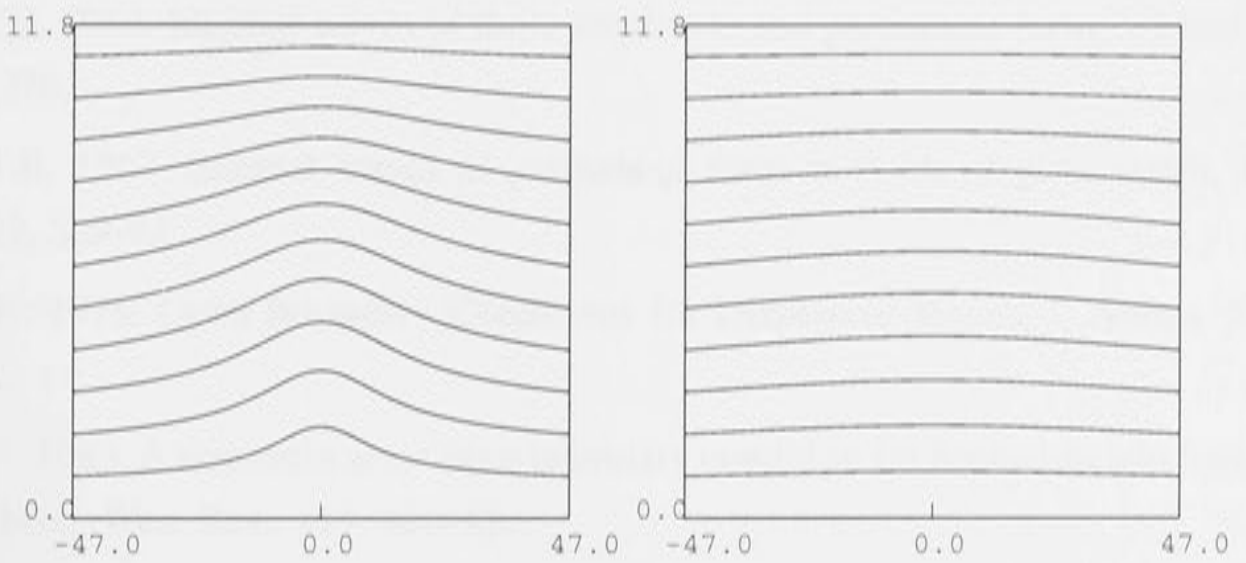

(e) $\Lambda = 400$ (f) $\Lambda = 425$

Figure B.3: Two layer streamfunction solutions to the DJL equation

Bibliography

Ablowitz, M.J. and Segur, H., 1981. Solitons and the inverse scattering transform, SIAM studies in applied mathematics, SIAM, 516pp.

Anderson, J., Droegemeier, K., and Wilhelmson, R., 1985. Simulation of the thunderstorm subcloud environment, 14th Conference on severe local storms, paper 5.1, AMS proceedings.

Apel, J.R., Holbrook, J.R., Liu, A.K., Tsai, J.J., 1985. The Sulu Sea Internal Soliton Experiment, J. Phys. Ocean., 15, 1625-1651.

Asselin, R., 1972. Frequency Filter for Time Integrations, Monthly Weather Review, 100, 487-490.

Baines, P.G., 1996. Topographic effects in stratified flows, Cambridge University Press.

Barker, S.J., and Crow, S.C., 1977. The motion of two-dimensional vortex pairs in a ground effect, J. Fluid Mech., 82, pp 659-673.

Batchelor, G.K., 1956. On steady laminar flow with closed streamlines at large Reynolds number, J. Fluid Mech., 1, 177-190.

Beland, M. and Warn, T., 1975. The Radiation Condition for Transient Rossby Waves, J. Atmos. Sci., 32, 1873-1880.

Benjamin, T.B. 1966. Internal waves of finite amplitude and permanent form, J. Fluid Mech., 25, 241-270.

Benjamin, T.B. 1967. Internal waves of permanent form in fluids of great depth, J. Fluid Mech., 29, 559-92.

Bennett, A.F., 1976. Open Boundary Conditions for Dispersive Waves, J. Atmos. Sci., 33, 176-182.

Bougeault, P., 1983. A non-reflective upper boundary condition for limited-height hydrostatic models, Mon. Wea. Rev., 111, 420-429.

Brown, D.J., Christie, D.R., 1998. Fully nonlinear solitary waves in continuously stratified incompressible Boussinesq fluids, Physics of Fluids, Vol. 10 No. 10, 2569-2586.

Brown, D.J., 1995. Nonlinear wave propagation in stratified shear flows, PhD thesis ANU.

Caracena, F., Ortiz, R., and Augustine, J., 1986. The crash of Delta Flight 191 at Dallas-Fort Worth international airport on 2 August 1985: Multiscale Analysis of weather conditions, NOAA technical report ERL 430-ESG 2.

Chen, C., Rottman, J.W., Koch, S.E., 1992. Numerical Simulations of Gravity Currents in Stratified Shear Flows, 5th Conference on Mesoscale Processes, Atlanta, Georgia.

Chen, C., 1991. A nested grid, nonhydrostatic, elastic model using a terrain-following coordinate transformation: the radiative-nesting boundary conditions, Mon. Wea. Rev., 119, 2852-2869.

Cheung, T.K. and Little, C.G., 1990. Meteorological Tower, Microbarograph Array, and Sodar Observations of Solitary-like Waves in the Nocturnal Boundary Layer, J. Atmos. Sci., 47, 2516-2536.

Clarke, R.H., Smith, R.K. and Reid, D.G., 1981. The Morning Glory of the Gulf of Carpentaria: An Atmospheric Undular Bore, Mon. Wea. Rev., Vol. 109, No. 8, 1726-1750.

Christie, D.R. 1989. Long nonlinear waves in the lower atmosphere., J. Atmos. Sci., 46, 1462-91.

Christie, D.R. 1992. The morning glory of the Gulf of Carpentaria: a paradigm for non-linear waves in the lower atmosphere, Aust. Met. Mag., 41, 21-60.

Christie, D.R., Muirhead, K.J., and Hales, A.L., 1978. On Solitary Waves in the Atmosphere, J. Atmos. Sci., 35, 805-825.

Christie, D.R., Muirhead K.J. and Hales A.L. 1979. Intrusive Density Flows in the Lower Troposphere: A Source of Atmospheric Solitons, J. Geophys Res, 84, 4959-4970.

Christie, D.R., and Muirhead, K.J., 1983a. Solitary Waves: A Hazard to Aircraft operating at Low Altitudes, Aust. Met. Mag., 31, 97-109.

Cotton, W.R. and Tripoli, G.J. 1978. Cumulus convection in shear flow - Three Dimensional Numerical Experiments, J. Atmos. Sci., 35, 1503-1521.

Crook, N.A. and Miller, M.J. 1985. A numerical and analytical study of atmospheric undular bores, Quart. J. R. Met. Soc., 111, 225-242.

Crook, N.A., 1986. The Effect of Ambient Stratification and Moisture on the Motion of Atmospheric Undular Bores, J. Atmos. Sci., 43, 171-181.

Crook, N.A., 1988. Trapping of Low-Level Internal Gravity Waves, J. Atmos. Sci., 45, 1533-1541.

Dahm, W., Scheil, C. and Tryggvason, G., 1989. Dynamics of vortex interaction with a density interface, J. Fluid Mech., 205, 1-43.

Davis, R.E. and Acrivos, A. 1967. Solitary internal waves in deep water, J. Fluid Mech., 29, 593-607.

Doviak, R.J., Chen, S.S. and Christie D.R., 1991. A thunderstorm- generated solitary wave observation compared with theory for nonlinear waves in a sheared atmosphere., J. Atmos. Sci., 48, 87-111.

Doviak, R.J., and Christie, D.R., 1991. Buoyancy Wave Hazards to Aviation, 4th International Conference on Aviation Weather Systems, Paris, France, 247-252.

Drazin, P.G., and Johnson, R.S., 1989. Solitons: An introduction, Cambridge University Press, London, 266pp.

Droegemeier, K.K. and Wilhelmson, R.B. 1987. Numerical simulation of thunderstorm outflow dynamics. Part I: Outflow Sensitivity Experiments and Turbulence Dynamics, J. Atmos. Sci, 44, 1180-1210.

Droegemeier, K.K. 1988. Simulation of microburst vorticity dynamics, 15th conference on severe local storms, AMS proceedings J107-J110.

Dubreil-Jacotin, M.K., 1937. Sur les théorèmes d'existence relatifs aux ondes permamentes pérodiques à deux dimensions dans les liquides hétérogènes, J. Math. Pures Appl., 16, 43-67.

Durran D.R. and Yang, Ming-Jen., Slinn, D.N., Brown, R.G., 1993. Toward More Accurate Wave-Permeable Boundary Conditions, Mon. Wea. Rev., 121, 604-620.

Egger, J., 1996. Volume conservation in phase space: A fresh look at numerical integration schemes, Mon. Wea. Rev., 124, 1955-1964.

Elliassen, A. and Palm, E., 1960. On the transfer of energy in stationary mountain waves, Geofys. Publ., 22, 1-23.

Fritts, D.C., 1979. The Excitation of Radiating Waves and Kelvin-Helmholtz Instabilities by the Gravity Wave-Critical Level Interaction, J. Atmos. Sci, 36, 12-23.

Fujita, T.T., 1986. DFW Microburst, SMRP research paper No. 217, Univ. of Chicago

Fujita, T.T., 1985. The downburst microburst and macroburst, SMRP research paper No. 210, Univ. of Chicago

Fulton, R., Zrnic, D.S. and Doviak, R.J., 1990. Initiation of a solitary wave family in the demise of a nocturnal thunderstorm density current, J. Atmos. Sci., 47, 319-337.

Gardner, C.S., Greene, J.M., Kruskal, D.M., and Miura, R.M., 1967. Method for solving the Korteweg-de Vries Equation, Phys. Rev. Lett., 19, 1095-1097.

Gear, J.A, and Grimshaw, R., 1983. A second-order theory for solitary waves in shallow fluids, Phys. Fluids, 26, 14-29.

Grimshaw, R. 1981a. Evolution equations for long, nonlinear internal waves in stratified shear flows., Stud. Appl. Math., 65, 159-88.

Grimshaw, R. 1981b, A second order theory for solitary waves in deep fluids, Phys. Fluids, 24, 1611-1618.

Grimshaw, R.H.J., He, J.M., Ostrovsky, L.A., 1998. Terminal damping of a solitary wave due to radiation in rotational systems, Stud. Appl. Math., 101, 197-210.

Haase, S. P. and Smith, R.K. 1989a. The numerical simulation of atmospheric gravity currents, Part I. Neutrally-stable Environments, Geophys. Astro. Phys. Fluid Dyn., 46, 1-33.

Haase, S.P. and Smith, R.K. 1989b. The Numerical Simulation of atmospheric gravity currents, Part 2. Environments with stable layers., Geophys, Astro. Phys. Fluid Dyn., 46, 35-51.

Haase, S.P. and Smith, R.K. 1984. Morning Glory wave-clouds in Oklahoma: A case study, Mon. Wea. Rev., 112, 2078-2089.

Hammack, J.L., 1973. A note on tsunamis: their generation and propagation in an ocean of uniform depth, J. Fluid Mech., 60, 769-799.

Hammack, J.L., and Segur, H., 1974, The Korteweg-de Vries equation and water waves. Part 2. Comparison with experiments, J. Fluid Mech., 65, 289-314.

Holloway, P.E., 1987. Internal hydraulic jumps and solitons at a shelf break region on the Australian north-west shelf, J. Geophys. Res., 92, 5405-5416.

Honji, H., Matsunaga, N., Sugihara, K., and Sakai, K., 1995. Experimental observation of internal symmetric solitary waves in a two-layer fluid, Fluid Dyn. Res., 15, 89-102.

Hunkins, K., and Fliegel, M., 1973. Internal undular surges in Seneca lake: A natural occurance of solitons, J. Geophys. Res., 78, 539-548.

Kim, Y., Kar, S.K., and Arakawa, A., 1993. A Nonreflecting Upper Boundary Condition for Anelastic Nonhydrostatic Mesoscale Gravity-Wave Models, Mon. Wea. Rev., 121, 1249-1261.

Klemp, J.B. and Wilhelmson, R.B. 1978. The simulation of three- dimensional convective storm dynamics, J. Atmos. Sci., 35, 1070-1096.

Klemp, J.B. and Durran, D.R. 1983. An upper boundary condition permitting internal gravity wave radiation in numerical mesoscale models., Mon. Wea. Rev., 111, 430-444.

Klemp, J.B. and Lilly, D.K. 1978. Numerical simulation of hydrostatic mountain waves, J. Atmos. Sci., 35, 78-107.

Koop, C.G., and Butler, G., 1981. An investigation of internal solitary waves in a two-fluid system. J. Fluid Mech., 112, 225-251.

Koop, C.G., 1981. A preliminary investigation of the interaction of internal gravity waves with a steady shearing motion, J. Fluid Mech., 113, 347-386.

Korteweg D.J. and de Vries, G., 1895. On the change of form of long waves advancing in a rectangular canal, and on a new type of long stationary wave, Phil. Mag., 39, 422-443.

Lilly, D.K., 1965. Numerical solutions for the shape preserving two dimensional thermal convection element, J. Atmos. Sci., 21, 83-98.

Lilly, D.K., and Klemp, J.B., 1979. The effects of terrain shape on nonlinear hydrostatic mountain waves, J. Fluid. Mech., 95, 241-263.

Liu, C. and Mitchell, W.M., 1996. A Numerical Study of the Effects of Ambient Flow and Shear on Density Currents, Mon. Wea. Rev., 124, 2282-2303.

Liu, C., and Moncrieff, M.W., 1996. A numerical study of the effects of ambient flow and shear on density currents, Mon. Wea. Rev., 124, 2282-2303.

Liu, A.K., Pereira, N.R., and Ko, D.R.S. 1982. Weakly interacting internal solitary waves in neighbouring pycnoclines, J. Fluid Mech., 122, 187-194.

Liu, A.K., Holbrook, J.R., and Apel, J.R., 1985. Nonlinear internal wave evolution in the Sulu Sea., J. Phys. Ocean., 15, 1613-1624.

Lin and Goff, 1988. A study of a mesoscale solitary wave in the atmosphere originating near a region of deep convection, J. Atmos. Sci., 45, 194-205.

Linden, 1973. The interaction of vortex rings with a sharp density interface: a model for turbulent entrainment, J. Fluid. Mech., 60, 467-480.

Long, R., 1965. The Boussinesq approximation and its role in the theory of internal waves, Tellus, 17, 46-52.

Long, R., 1953. Some aspects of the flow of stratified fluids. I. A theoretical investigation., Tellus, 5, 42-57.

Macaskill, C., Bewick B.M., 1995. The use of hyperviscosity in simulations of nonlinear geophysical fluid flows, 12th Australian fluid mechanics conference, proceedings, 415-418.

Mahapatra, P.R., Doviak, R.J., Zrnic, D.S., 1991. Multisensor Observation of an Atmospheric Undular Bore, Bul. Amer. Met. Soc., 72, 1468-1480.

Manasseh, R. and Middleton, J.H., 1995. Boundary-layer oscillations from thunderstorms at Sydney Airport, Mon. Wea. Rev., 123, 1166-1177.

Manasseh, R., Chang-Yun Ching, Fernando, H., 1998. The transition from density-driven to wave-dominated isolated flows, J. Fluid Mech., 361, 253-274.

Maslowe, S.A. and Redekopp, L.G. 1980. Long nonlinear waves in stratified shear flows., J. Fluid Mech., 101, 321-48.

Maxworthy, T., 1980. On the formation of nonlinear internal waves from gravitational collapse of mixed regions in two and three dimensions, J. Fluid Mech., 96, 47-64.

Miller, M.J. and Thorpe, A.J., 1981. Radiation conditions for the lateral boundaries of limited-area numerical models., Quart. J. R. Met. Soc., 107, 615-628.

Mitchell, K.E. and Hovermale, J.B., 1977. A Numerical Investigation of the severe thunderstorm gust front, Mon. Wea. Rev., 105, 657-675.

Mitsudera, H. and Grimshaw, R. 1991. Effects of radiative damping on resonantly generated internal gravity waves., Stud. Appl. Math., 84, 183- 206.

Monaghan, J.J, 1996. Gravity currents and solitary waves, Physica D, 98, 523-533.

Nakamura, A. and Chen, H., 1981. Soliton Solutions of the Cylindrical KdV Equation, J. Phys. Soc. Japan, 50, 711-718.

Noh, Y., Fernando, H.J.S., and Ching, C.Y., 1992. Flows induced by the impingement of a two-dimensional thermal on a density interface, Journal of Physical Oceanography, 22, 1207-1220.

Noonan, J.A. and Smith R.K., 1985. Linear and Weakly Nonlinear Internal Wave Theories Applied to "Morning Glory" Waves, Geophys. Astrophys. Fluid Dynamics, 33, 123-143.

Ono, H., 1975. Algebraic solitary waves in stratified fluids., J. Phys. Soc. Jap., 39, 1082-1091.

Orlanski, I. 1976. A simple boundary condition for unbounded hyperbolic flows, J. Comp. Phys., 21, 251-269.

Pearson, R.A., 1974. Consistent Boundary Conditions for Numerical Models of Systems that Admit Dispersive Waves, J. Atmos. Sci., 31, 1481-1489.

Pereira, N.R. and Redekopp, L.G. 1980. Radiation damping of long, finite- amplitude internal waves., Phys. Fluids, 23, 2182-3.

Piacsek, S.A., and Williams, G.P. 1970. Conservation properties of convection difference schemes, J. Comp. Phys., 6, 392-405.

Proctor, F., 1988. Numerical Simulations of an Isolated Microburst. Part I: Dynamics and Structure, J. Atmos. Sci, 45, 3137-3160.

Pullin, D.I., and Grimshaw, R.H.J, 1988. Finite amplitude solitary waves at the interface between two homogeneous fluids., Phys. Fluids, 31, 3550-3559.

Roache, P.J., 1985. Computational Fluid Dynamics, Hermosa Publishers, pp 446.

Robert, A.J., 1966. Integration of a low order spectral form of the primitive meteorological equations., J. Met. Soc. Jap., 44, 237-245.

Rottman, J.W. and Einaudi, F., 1993. Solitary Waves in the Atmosphere, J. Atmos. Sci., 50, 2116-2136.

Rottman, J.W. and Koch, S.E., 1992. Numerical simulations of gravity currents in stratified shear flows, 5th conference on mesoscale processes, Proceedings AMS.

Rottman, J.W., and Simpson, J.E., 1989. The formation of internal bores in the atmosphere: A laboratory model, Quart. J. Roy. Meteor. Soc., 115, 941-963.

Richards, J.M., 1961. Experiments on the penetration of an interface by buoyant thermals, J. Fluid Mech., 11, 369-384.

Scorer, R.S., 1949. Theory of waves in the lee of mountains., Quart. J. Royal Met. Soc., 75, 41-56.

Scorer, R.S., 1957. Experiments on convection of isolated masses of buoyant fluid, J. Fluid Mech., 2, 583-594.

Shapiro, R., 1970. Smoothing, filtering, and boundary effects, Rev. Geophys. Space Phys., 8, 359-387.

Shreffer and Binkowsi, 1981. Observations of pressure jump lines in the Midwest 10-12 August 1976, Mon. Wea. Rev., 109, 1713-1725.

Simpson, J.E., 1987. Gravity Currents: In the environment and in the laboratory, Ellis Horwood Limited, pp 244.

Simpson, J.E., 1972. Effects of the lower boundary on the head of a gravity current, J. Fluid Mech., 53, 759-768.

Simpson, J.E. and Britter, R.E., 1979. The dynamics of the head of a gravity current advancing over a horizontal surface, J. Fluid Mech., 94, 477-495.

Simpson, J.E. and Britter, R.E., 1980. A laboratory model of an atmospheric mesofront, Quart. J. Roy. Metero. Soc., 106, 485-500.

Skyllingstad, E.D. 1991. Critical layer effects on atmospheric solitary and cnoidal waves, J. Atmos. Sci., 48, 1613-1624.

Smagorinsky, J., 1963. General circulation experiments with the primitive equations: 1. The basic experiment, Mon. Wea. Rev., 91, 99-164.

Smith, R.K., 1988. Travelling Waves and Bores in the Lower Atmosphere: The 'Morning Glory' and Related Phenomena, Earth Science Reviews, 25, 267-290.

Tung, K.K., Ko, D.R.S., and Chang, J.J., 1981. Weakly nonlinear internal waves in shear., Stud. Appl. Math., 65, 189-221.

Tung, K.K., Chan, T.F., and Kubota, T., 1982. Large amplitude internal waves of permanent form, Stud. Appl. Math., 66, 1-44.

Turkington, B., Eydeland, A., and Wang, S., 1991. A computational method for solitary internal waves in a continuously stratified fluid., Stud. Appl. Math., 85, 93-107.

Turner, J.S., 1963. Model experiments relating to thermals with increasing buoyancy, Quart. J. Roy. Met. Soc., 89, 62-74.

Turner, J.S., 1973. Buoyancy effects in fluids, Cambridge University Press.

Young, J.W. and Lane, F.D., 1989. The effect of a ground-based inversion layer on an impacting microburst, 27th Aerospace sciences meeting, AIAA-89-0810.

Wolfson, M.M, 1990. Understanding and Predicting Microbursts., PhD thesis MIT.

Wiin-Nielson, A., 1965. On the propagation of gravity waves in a hydrostatic compressible fluid with vertical wind shear, Tellus, 17, 306-320.

Wu, 1969. Mixed region collapse with internal wave generation in a density-stratified medium, J. Fluid. Mech., 56, 265-276.